CONTACT RECOMBINATION IN SILICON SOLAR CELLS

ir. Jan DECKERS

Supervisor:
prof. dr. ir. J. Poortmans

Members of the Examination Committee:
prof. dr. ir. R. Puers
prof. dr. A. Stesmans
prof. dr. ir. C. Claeys
emer. prof. dr. ir. R. P. Mertens
dr. ir. M. Debucquoy
prof. dr. J. Schmidt
prof. dr. ir. H. Hens

Dissertation presented in partial fulfilment of the requirements for the degree of Doctor in Engineering Science

Uitgegeven in eigen beheer, Jan Deckers, Gemeentestraat 160, 3010 Kessel-Lo (Leuven), België

ISBN 978-94-6018-969-2
D/2015/7515/25

“The sun will rise and set regardless. What we choose to do with the light while it's here is up to us.”

- Alexandra Elle

Acknowledgements

Jan Van Hoeymissen and Jef Poortmans have my thanks for introducing me to the field of silicon solar cells during my master's thesis. While I was waiting for a porous silicon etching tool that, like Godot, would never come, I started modelling the optics of thin-film silicon solar cells. In this context, I would like to thank Koen Van Wichelen who has always been generous in sharing his extraordinary knowledge in the field of semiconductor device modelling. During the work on my master's thesis, I got specifically fascinated by thin film silicon solar cells. So I applied for a Ph.D. on thin-film polycrystalline silicon solar cells with n-type (as opposed to p-type) silicon absorbers.

I am once more indebted to Jef Poortmans, who was willing to be my promotor. I would also like to acknowledge the contribution of Robert Mertens, who often took the role of a proxy-promotor. The presence of both resulted in monthly follow-up meetings which are quite memorable as they were akin to audiences with two kings at the same time; though slightly less formal, and – I imagine – significantly more wrought with semiconductor physics.

I am also grateful to Dries Van Gestel, who provided guidance in the face of adversity during this early stage of my Ph.D. In addition, I would like to thank the colleagues with whom I collaborated in the field of polycrystalline silicon thin-film solar cells: Anja Vanleenhoven, Srisaran Venkatachalam, Ivan Gordon, Valerie Depauw, Christos Trompoukis, Ounsi El Daif, and especially Yu Qiu who taught me how to make thin-film polycrystalline silicon solar cells, and Kris Van Nieuwenhuysen for countless epitaxial depositions. I am also indebted to the partners with whom I collaborated within the context of funded projects; in the first place Andre Stesmans, Mihaela Jivanescu, Emilie Bourgeois, and Aimi Abbass.

At this point, I would like to thank the attentive reader who may have noticed something rotten in the state of this text. I have been elaborating in the past tense about a Ph.D. in the field of thin-film polycrystalline silicon solar cells whereas the topic of the present dissertation is contact recombination, which is a subject mostly studied in the context of high efficiency silicon solar cells. The explanation for this discrepancy is a re-orientation of the research done in this Ph.D., which was motivated on economic grounds: following a crash in the price of raw silicon, and an increasing importance of "soft", non-hardware related costs; the incentive to strive for very thin silicon absorber layers dwindled and the incentive for high efficiency solar cells was enhanced. Research in the field of contact recombination currents is motivated by contact recombination currents being one of the major

power loss mechanisms in high efficiency silicon solar cells featuring diffused junctions.

I am indebted to Niels Posthuma for introducing me to the field of high-efficiency interdigitated back contact (IBC) solar cells, and for allowing me to take the opportunity to start working on a new characterization method of contact recombination in silicon solar cells. I am also grateful to Xavier Loozen, who – just before he left imec – showed me sketches of an interesting test structure for the characterization of contact recombination currents by means of photo conductance measurements. This test structure, proposed by Xavier Loozen himself and Pierre Verlinden, was the precursor of the test structure which is developed in the present dissertation.

My gratitude also goes to the technicians and operators who keep the tools up and running, and process samples in the meantime: Didier Dehertoghe, Andre Janssens, Reinoud Moors, Dirk Hendrickx, Stefan Van Den Broeck and their leader and lab manager: Giovanni Flamand.

I would like to thank Kris Paulussen, Olivier Richard and Hugo Bender for TEM measurements, Danielle Verhaeren for SSRM measurements, Alain Moussa for AFM measurements, Trudo Clarysse for help with SRP measurements, and I would like to thank Bastien Douhard for SIMS measurements.

I am indebted to the colleagues with whom I collaborated in the field of IBC silicon solar cells: in the first place Maarten Debucquoy, for taking over Niels Posthuma's role during the last year of my Ph.D. Bartosz Zielinski is acknowledged for expert help related to light trapping, Jo Robbelein and Barry O'Sullivan for lithography-related help. Jo Robbelein is also acknowledged for helping me to learn the Cadence software for mask design. I am indebted to Sukhvinder Singh for countless metal depositions, and for teaching me how to use the oxidation furnaces. I would like to acknowledge Emanuele Cornagliotti's help with aluminum oxide depositions. I'd like to thank Patrick Choulat for learning me about diffusions and Angel Uruena De Castro for teaching me how to use a laser. I'd also like to thank Manabu Kyozo for great company in the nearly best office ever during the last months of my PhD. In addition, my thanks go to Monica Aleman, Maria Recaman Payo, Jozef Szlufcik, Loic Tous, Chi Dang Thi Thuy, Jia Chen, Twan Bearda, Stefano Granata, Roberto Martini, Michael Haslinger and to many others who have been of great help.

I would finally like to thank my family for being there and for helping in which every way they could; and above all, the resident lagomorpha for not devouring all essential parts of this dissertation and Fleur Deboutte for love, empowerment, linguistic editing, graphical artistry, and graphical magic.

Jan Deckers (Heverlee, August 11, 2014;
adapted on October 7, 2014)

Abstract

As solar cells become ever cheaper to make, costs not directly related to the solar cell manufacturing process comprise an ever increasing share of the total cost of a solar cell [DOE 2014]. These costs can be reduced on a per unit energy basis by making more efficient solar cells. Therefore, there is a strong incentive for research in the field of high-efficiency solar cells. Specifically silicon solar cells are of great practical interest as they presently have a dominant market position. Contact recombination currents are one of the major power loss mechanisms in certain types of high efficiency silicon solar cells, for example interdigitated back contact silicon solar cells featuring diffused junctions. Therefore, reducing contact recombination currents can result in efficiency gains. However, the characterization of contact recombination losses is convoluted, and many present technologies for the characterization of contact recombination currents are imperfect. This provided the incentive for this work on a novel characterization method for contact recombination currents. The characterization method developed in this dissertation is based on photo conductance measurements on lattices of point contacts on otherwise passivated wafers.

Chapter one features a general introduction. This includes a discussion the context in which this dissertation is performed is performed. Then, various sources of efficiency loss in solar cells are discussed. The focus is on silicon solar cells, and Interdigitated Back Contact (IBC) silicon solar cells in particular. Finally, various types of passivated contacts are discussed.

In chapter two, an introduction to carrier recombination in silicon solar cells is provided. Chapter two also features an introduction to radio-wave detected quasi steady state photo conductance (QSSPC) measurements. QSSPC measurements lie at the basis of the characterization method for contact recombination measurements which is developed in this dissertation. The result of chapter two is a mathematical framework for a number of basic concepts in the field of silicon solar cells, and particularly in the field of silicon solar cell characterization.

In chapter three, an overview of contemporary methods for contact recombination current measurements is given, and it is argued why the development of a novel method for contact recombination measurements is desirable. This method is subsequently described in detail. This detailed description covers the physics that lies at the basis of the method. It also covers design rules, error analysis, parasitic effects, and experimental results. The focus is on test structures based on lattices

of point contacts, but at the end of chapter three, alternative test structure embodiments are described.

In chapter four, point contact based test structures are applied to the optimization of n^+ diffusions which are used as back surface fields (BSF) in interdigitated back contact (IBC) silicon solar cells. In addition, various front surface field oxidations are investigated. The use of the $J_{0,met}$ test structure developed in chapter three for a classical junction optimization problem allows for further experimental confirmation of the characterization method. Certainly, the consistency of the trends observed between contact resistance, contact saturation current density and saturation current density of passivated junctions is a strong experimental confirmation of the novel characterization method described in this dissertation.

In the final chapter, thin dielectric Al_2O_3 layers grown using thermal atomic layer deposition (ALD) are investigated for the passivation of the interface between aluminum contacts and n^+ or p^+ silicon. Specific attention is paid to the effect of specific surface treatments prior to the formation of Al_2O_3 contact passivation layers: ALD Al_2O_3 contact passivation layers on HF-last and HNO_3-last silicon are investigated. ALD Al_2O_3 contact passivation layers are found to effectively passivate aluminum contacts on n^+ silicon surfaces, but they are found to be ineffective at passivating aluminum contacts on p^+ silicon surfaces. In addition, it is found that pin-holes associated with HF-last ALD Al_2O_3 contact passivation layers can improve the trade-off between contact resistance and contact recombination associated with passivated contacts. However, the reproducibility of pinhole formation in ALD Al_2O_3 contacts remains an open question.

Nederlandse samenvatting

De siliciumzonnecellentechnologie gaat al enkele jaren met rasse schreden vooruit en de productie van silicium zonnecellen wordt steeds goedkoper. Dat brengt met zich mee dat de globale kost van een fotovoltaïsch systeem steeds meer wordt bepaald door kosten die niets te maken hebben met de kost van de eigenlijke zonnecellen. Zo bepaalt bijvoorbeeld de installatiekost intussen voor een groot stuk het globale prijskaartje van een zonnecelinstallatie. Zulke kosten dalen per eenheid geleverde energie wanneer de zonnecellen efficiënter worden. Daarom is er een sterke drijfveer voor onderzoek naar hoog efficiënte silicium-zonnecellen.

In bepaalde zonneceltechnologieën, zoals hoog efficiënte silicium-zonnecellen met gediffundeerde juncties, zijn contactrecombinatiestromen een grote bron van energieverlies. Daarom kunnen nieuwe technologieën voor de vermindering van contactrecombinatiestromen een efficiëntieverhoging met zich meebrengen. De karakterisatie van contactrecombinatiestromen is echter ingewikkeld, en heel wat moderne technologieën voor de karakterisatie van contactrecombinatiestromen laten nog ruimte voor verbetering. Daarom werd in deze dissertatie een nieuwe methode ontwikkeld voor de karakterisatie van contactrecombinatiestromen. Die methode is gebaseerd op fotoconductantiemetingen op twee dimensionele roosters van puntcontacten op gepassiveerde silicium plakken.

Na een algemene inleiding in hoofdstuk een, wordt in hoofdstuk twee een inleiding tot ladingsdrager-recombinatie in silicium-zonnecellen gegeven. Hoofdstuk twee introduceert vervolgens radiogolf-gedetecteerde fotoconductantiemetingen in de gestage toestand (QSSPC), waarop de contactrecombinatiestroom-karakterisatiemethode die in deze dissertatie wordt ontwikkeld is gebaseerd. Hoofdstuk twee brengt bovendien een wiskundig kader aan voor een aantal basisconcepten met betrekking tot QSSPC-metingen.

In hoofdstuk drie geven we een overzicht van moderne contactrecombinatiestroom-karakterisatiemethodes. Bovendien wordt beargumenteerd waarom de ontwikkeling van een nieuwe contactrecombinatiestroom-karakterisatiemethode nuttig is. Die nieuwe methode voor de karakterisatie van contactrecombinatiestromen beschrijven we vervolgens in detail in hoofdstuk drie. Eerst komt de fysica die aan de basis van de methode ligt aan bod. Daarna behandelt hoofdstuk drie ook ontwerpregels, een foutenanalyse, en een bespreking van parasitaire effecten. Vervolgens ondersteunen de experimentele resultaten de eerder gegeven theoretische beschrijving. In dit proefschrift ligt de nadruk op teststructuren die gebaseerd zijn

op roosters van puntcontacten, maar aan het einde van hoofdstuk drie bespreken we ter volledigheid ook alternatieve vormen van de teststructuur.

In hoofdstuk vier werken we uit hoe de teststructuren, gebaseerd op roosters van puntcontacten, gebruikt worden voor de optimalisatie van n^+ diffusies. Die n^+ diffusies dienen als achterzijdeveld (BSF) in IBC-silicium-zonnecellen. Daarnaast behandelt dit hoofdstuk ook enkele voorzijdeveld (FSF) oxidaties. De aanpak van een klassiek junctie-optimalisatieprobleem met de teststructuur uit hoofdstuk drie laat een verdere experimentele bevestiging toe van de nieuwe contactrecombinatiestroom-karakterisatiemethode. In het bijzonder levert de consistentie van de trends tussen contactweerstanden, contactrecombinatiestromen en recombinatiestromen in gepassiveerde juncties een sterk experimenteel bewijs voor de karakterisatiemethode die voor dit proefschrift ontwikkeld is.

Het laatste hoofdstuk onderzoekt de passivatie van aluminium contacten op n^+- en p^+-silicium. Specifiek behandelen we het gebruik van dunne Al_2O_3 lagen, gegroeid via thermische atomaire laagdepositie (ALD). Het hoofdstuk besteedt bijzondere aandacht aan het effect van de oppervlaktebehandeling die voorafgaat aan de depositie van de Al_2O_3 contactpassivatielagen. Daarbij bespreken we zowel behandelingen die eindigen met een onderdompeling in verdund fluorwaterstofzuur als behandelingen die eindigen met een onderdompeling in azeotropisch salpeterzuur. Uit die studie blijkt dat ALD Al_2O_3-contactpassivatielagen aluminium contacten op n^+-silicium oppervlakken efficiënt passiveren, maar dat de passivatie van aluminium contacten op p^+-silicium oppervlakken ineffectief is. Bovendien komen pinvormige perforaties voor bij de Al_2O_3 contactpassivatielagen, wanneer die lagen gedeponeerd zijn op plakken die als laatste oppervlaktebehandelingsstap een onderdompeling in verdund fluorwaterstofzuur hebben gekregen. Deze perforaties zijn afwezig voor Al_2O_3 contactpassivatielagen die gedeponeerd zijn op wafers die als laatste oppervlaktebehandelingsstap een dip in azeotropisch salpeterzuur ondergingen. De aanwezige perforaties in Al_2O_3 contactpassivatielagen zorgen voor een gunstigere afweging tussen contactweerstand en contactrecombinatie in vergelijking met Al_2O_3 contactpassivatielagen waarbij die perforaties afwezig zijn. Tot slot moet worden toegevoegd dat de reproduceerbaarheid van die perforatievorming in ALD Al_2O_3 contacten een vraagteken blijft.

Table of contents

1. Introduction

1.1. Context

Conventional energy sources are increasingly replaced by renewable energy sources for a variety of reasons: to reduce global CO_2 emissions to curb global warming; to reduce emissions of SO_x, NO_x and particulate matter; for energy security issues; to lower fossil-fuel import bills; and for concerns with regard to the reliability of foreign energy suppliers [CEC 2007, Fthenkakis 2008, IEA 2013, Turner 1999, WEO 2009, Wooley 2001]. In addition, renewable energy sources in general, and solar power in particular, are also useful for providing electric power in remote locations, where grid access is difficult and costly. Examples include applications in the mining industry, where photovoltaic systems are used to complement traditional fossil fuel-powered generators [First Solar 2014]; offshore drilling [IPM 2010] where solar panels and small rechargeable batteries replace large and expensive non-rechargeable batteries. Solar power is also used in Antarctic research [BAS 2014]. Finally, in military settings, photovoltaic systems can be very valuable as well, for example in the form of foldable solar arrays which replace batteries and portable generators, and thereby eliminating the need for vulnerable supply lines [Johnson 2011].

In Europe, the push for renewable energy is part of a wider commitment to a low-carbon economy, which is set-out in the climate and energy package. The climate and energy package is a set of binding legislation which sets the “20-20-20” targets for 2020. The 20-20-20 targets set-out objectives for greenhouse gas emission reduction, renewable energy production, and energy efficiency improvement [EU 2014]. The role of renewable energy in a carbon-free energy future is now more significant than ever as the share of nuclear power in the global energy mix has become the lowest since the 1980s [DNA 2014]. This can be partly explained by the nuclear renaissance losing some of its luster in the wake of the Fukushima Daiichi accident which displaced more than 150,000 people from their homes [Saito 2014, Schwägerl 2011, Verbruggen 2014].

Solar photovoltaic energy is now one of the major renewable energy sources and modern solar photovoltaic systems are very environmentally friendly [Peng 2013]. Indeed, the solar photovoltaic industry has come a long way since the manufacture of the first practical, 6% efficient silicon solar cell in 1954 by Bell labs [Chapin 1954]. The strides that have been taken during the last decades are especially spectacular; in the 1970’s, a decade wrought with oil crises, the state of the photovoltaic energy conversion technology was still described as: “We probably know only slightly more about generating energy from photovoltaic devices than

James Watt knew about producing mechanical energy from steam" [Kelly 1978]. At present, solar photovoltaic power has reached grid parity in at least 19 markets globally, and is therefore competitive without subsidies in these markets. More markets are expected to reach grid parity as the cost of photovoltaic systems further decreases, and a new gold rush has been predicted in the solar industry for the coming years [Chase 2014, Shah 2014].

Even though the solar photovoltaic industry seems to be set for a rosy future, many challenges remain. Because the solar photovoltaic energy landscape is very diverse, some challenges apply only for specific solar cell technologies, whereas other challenges are more general. A first, very general challenge is related to the solar power being an intermittent energy source, for which the output is difficult to predict. The same challenges arise in the context of another major renewable energy source: wind power. The intermittency of renewable energy sources such as wind and solar powers entails difficulties in balancing electricity supply and demand which are being tackled through the introduction of smart grid technologies, including energy storage; see for example [Strasser 2013]. Further challenges are related to the lobbying of vested interests, and to confusion about the extent to which governments are willing to support or accommodate renewable energy sources; see e.g. [Schwarzenegger 2010]. This is closely related to recurring questions about the about the amount societies are willing to pay for the social and environmental benefits of clean, renewable energy sources [Kelly 1978]. Yet another challenge is related to health hazards related to the use of materials such as cadmium which are featured in the absorber of CdTe (cadmium telluride) solar cells and in the CdS window layer of some CIGS (copper indium gallium selenide) solar cells [MSDS 2014]. Finally, there are concerns related to the availability of certain materials such as indium and tellurium, which are used in the absorbers of CIGS and CdTe solar cells, respectively [DOE 2004, Feltrin 2008]. Conversely, these concerns have been countered by other authors [Phipps 2008, Zweibel 2010]. With respect to the availability and toxicity of the component materials of solar cells, silicon solar cells are an ideal technology since silicon is a relatively non-toxic and readily available material [Turekian 1961, MSDS 2014b]. However, the toxicity argument should be strongly nuanced as the emissions from both cadmium telluride and silicon photovoltaics are negligible compared to those from fossil fuels. In addition, the life-cycle cadmium emissions for CdTe photovoltaic systems are actually lower than those for crystalline silicon photovoltaic systems. The latter, highly counter-intuitive fact is due to silicon solar cells using less energy in their life cycle than cadmium telluride solar cells [Fthenakis 2008].

Silicon solar cells currently dominate the solar photovoltaic market with a 91% market share; of which 6% features n-type Czochralski silicon substrates and the

remaining 85% feature multi- and monocrystalline p-type silicon substrates [Kopecek 2014]. Different silicon solar cell technologies can be categorized according to the efficiency of the resulting modules. A detailed overview of contemporary solar photovoltaic technologies is beyond the scope of this dissertation, but the interested reader is referred to a number of reviews: [Bagnall 2008, Parida 2011, De Wolf 2012]. High efficiency silicon solar cells provide the context for this dissertation and will be described in some detail in chapter one.

As this doctoral dissertation is completed in the context of the development of novel technologies, its motivation is based on economic grounds. However, motivations based on economic grounds have a tendency to be volatile. Around 2010, the material cost of silicon continued to be a major contributing factor to the final cost of a crystalline silicon photovoltaic module: 40-50% [Depauw 2009, O'Rourke 2009, O'Rourke 2010]. This was the case despite advances in silicon production technology and an increased production capacity which had resulted in a significantly reduced cost of the silicon base material [Taylor 2010]. As a result, there was a very strong argument for focusing research in the field of silicon solar cells to solar cell concepts that involve a reduced material use compared to the State-of-the-Art

However, the situation has changed dramatically since then. In particular, the price of the polysilicon feedstock material for silicon solar cells is expected to continue its decreasing trend, and drop to a mere 11-12$/kg in the near term [Shah 2014]. Due to the significant drop in the cost of photovoltaic system components, non-hardware related costs comprised over 50% of the total cost of a photovoltaic system in 2012 [DOE 2014, Friedman 2013]. As solar cells are becoming ever cheaper to make, costs which have nothing to do with the solar cell manufacturing process itself comprise an ever increasing share of the total cost of a photovoltaic system. These costs can be reduced on a per unit energy basis by making more efficient solar cells. Therefore, there is a strong rationale for research in the field of high-efficiency silicon solar cells. Contact recombination currents are one of the major power loss mechanisms in certain types of high efficiency silicon solar cells, for example interdigitated back contact silicon solar cells featuring diffused junctions [Verlinden 2012]. Therefore, reducing contact recombination currents will result in efficiency gains. This provides a strong rationale for their study. However, the characterization of contact recombination losses is convoluted, and present technologies for the characterization of contact recombination currents are imperfect. This provided the incentive for this work on a novel characterization method for contact recombination currents.

1.2. Theoretical, multi junction and single junction solar cells

The ultimate efficiency of photovoltaic devices is discussed for the case of multi junction and single junction devices, and we compare record efficiencies to the maximum attainable efficiency of photovoltaic devices in their respective class. We first discuss the thermodynamic (reversible) efficiency limit, which follows directly from the first and second laws of thermodynamics. Then, we discuss the limiting efficiency of multi junction solar cells under more realistic, irreversible operating conditions. We then compare this limit to the highest efficiency obtained in real world multi junction solar cells at the time of writing. Subsequently, we discuss single junction solar cells, which are significantly cheaper to make than multi junction solar cells. This benefit offsets their lower conversion efficiencies in many practical settings. Finally, we shortly discuss the efficiency limits of single junction silicon-based solar cells, which are currently the most widely used class of solar cells. Their success is related to the favorable tradeoff between efficiency and cost for terrestrial applications. In addition, silicon is a non-toxic and readily available material.

1.2.1. The thermodynamic limit

Energy conversion devices are generally benchmarked by comparing their efficiency to the maximum efficiency that could be attained from a theoretical point of view. From the point of view of thermodynamics, the theoretical maximum efficiency of any heat engine is only dependent on the temperatures of the hot and cold heat reservoirs that are used to feed the engine [De Vos 1981]:

$$\eta = \frac{T_h - T_c}{T_h}, \tag{1.1}$$

in which η is the solar cell efficiency, T_h is the temperature of the hot heat reservoir, and T_c is the temperature of the cold heat reservoir. Now let the solar cell be the cold heat reservoir with a temperature of $300\ K$, and let the sun be the hot heat reservoir with a temperature of $6000\ K$, then the maximum efficiency η equals 95%.

1.2.2. Multi junction solar cells

The thermodynamic limit corresponds to reversible operation. In reality, power cannot be extracted under reversible operation. Instead, solar cells operate at the maximum power point, which corresponds to irreversible operation. Under concentrated light, the maximum efficiency for an ideal multi junction device is 86.8%. At 1 sun light intensity, the maximum efficiency of an ideal multi junction solar cell is further lowered to 54% [De Vos 1981]. These efficiencies were calculated assuming that the solar cell is a blackbody at $300\ K$ which is illuminated by the sun which is modelled as a blackbody at $6000\ K$.

The most efficient solar cell made to date is a multi-junction solar cell featuring a monolithic InGaP/GaAs/InGaAs triple junction. This device, made by Sharp Solar, has an efficiency of 44.4% under concentrated light [Green 2014]. Multi junction solar cells are generally very expensive to make such that their applicability is limited to niche markets such as space exploration, where their superior efficiency justifies the cell's high cost. For terrestrial applications, their cost per unit of produced energy can be lowered by using the solar cells under concentration. Concentrated photovoltaic systems have the advantage that the technology allows for co-generation of heat and electricity, see e.g. [Chow 2010]. Unfortunately, the operation of concentrated photovoltaics requires direct sunlight which renders concentrating photovoltaic systems ineffective in generally cloudy countries, for example: Belgium.

1.2.3. Single junction solar cells

Single junction solar cells are less efficient than multi junction solar cells, but for many applications, this efficiency deficit is made up for by their significantly lower cost. Single junction solar cells are commonly used in non-concentrating systems. The maximum efficiency of single junction solar cells under unconcentrated light is given by the Shockley-Queisser limit [Shockley 1961]. The Shockley-Queisser limit follows from a detailed balance calculation, taking only radiative recombination into account. It models both the sun and the solar cells as ideal blackbodies.

The most common semiconductor used for the manufacture of solar cells is silicon [Kopecek 2014]. Silicon has a band gap of $1.1\ eV$, which is close to the optimum band gap. For solar cells manufactured from a semiconductor with a band gap of $1.1\ eV$, the Shockley-Queisser limit is an efficiency of ca. 30%, when the solar cell is taken to be a blackbody at $300\ K$ and the sun is taken to be a blackbody at $6000\ K$. A further refinement of the Shockley-Queisser limit for the case of silicon

solar cells is the calculation by Tiedje et al. [Tiedje 1984]. This calculation takes the following additional phenomena into account: free carrier absorption, Auger recombination, the actual AM1.5 spectrum instead of blackbody radiation, and imperfect light trapping in silicon solar cells. This calculation yields a limiting efficiency of 29.8% for silicon solar cells at $300\ K$. The most efficient silicon solar cells manufactured so far are interdigitated back contact (IBC) silicon solar cells with an efficiency of 25.6% [Green 2014, Panasonic 2014]. This dissertation was completed in the context of the study and improvement of IBC silicon solar cells.

1.3. Losses in silicon solar cells

In this section, we provide a brief description of the major power loss categories in silicon solar cells. First, we provide an intuitive explanation of various categories of losses in solar cells. Then, we provide a qualitative power loss analysis which is based on heuristic grounds. This power loss analysis method is based on [Debucquoy 2013]. The motivation for providing this qualitative power loss analysis in the present dissertation lies in that it provides an elegant indication of the effect of different power loss categories on the major solar cell figures of merit.

Many power loss analysis methods and tools are described in the literature, some of which are listed here as guidance for the interested reader. A simple analytical power loss analysis method for high-efficiency interdigitated back contact silicon solar cells is given in [Verlinden 2012]. Another simple model, directed modelling the saturation current of point contacted solar cells is provided in [Plagwitz 2006], which expands on the work of B. Fischer [Fischer 2003]. Many solar cell simulation programs can be used to perform power loss analysis, such as Quokka [Fell 2013] and PC1D [Clugson 1997]. An excellent resource where many freely available resources can be found is [PV Lighthouse 2014].

1.3.1. Intuitive discussion of power loss mechanisms

A first type of power losses in silicon solar cells are those which are fundamentally related to the solar cells being based on silicon absorbers. The choice of silicon as an absorber material implies that absorption of photons with an energy smaller than silicon's band gap, 1.1 eV, do not give rise to electron-hole pair generation and therefore do not contribute to the solar cell's power output. Also, for photons with an energy larger than silicon's band gap, which are usefully absorbed, only the band gap energy is needed for electron-hole pair generation and the remainder is lost as thermal energy. As explained in the previous section, these band-gap related limitations can be overcome by employing multi-junction solar cells.

The imperfect optics of silicon solar cells results in another class of power loss mechanisms which primarily affect the short circuit current: the refractive index mismatch between silicon and the environment gives rise to reflection losses, and photons that do enter the silicon semiconducting layer may escape before being absorbed. These losses related to imperfect optics can be tackled through any of a variety of patterning methods, and through the application of anti-reflective coatings, see e.g. [Oh 2012, Trompoukis 2012, Vazsonyi 1999, Zhao 1991]. Additionally, there are parasitic absorption mechanisms, for example free carrier

absorption [Falk 1998] and parasitic absorption at back contacts [Duerinckx 2014], which also lower the short circuit current.

A third type of power losses are resistive losses. Resistive losses themselves fall in two categories: losses associated with shunt resistance and losses associated with series resistance. Series resistance losses are of particular interest in the context of this dissertation as there is a trade-off between power loss related to contact resistance and power loss related to contact recombination. Contact recombination is one of the recombination mechanisms of yet another category of power losses: recombination losses.

Recombination losses primarily affect the voltage of solar cells, although they also affect the fill factor and excessive recombination losses can give rise to significant current losses. Current losses in silicon solar cells due to recombination losses occur when the recombination current is sufficiently substantial such that the recombination current comprises a significant part of the maximally attainable short circuit current.

Voltage losses due to carrier recombination are most easily explained in a simplified setting: we consider the absence of resistive effects and we also assume the absence of space charge recombination currents. In this case, the voltage across the solar cell terminals equals the difference between the minority carrier quasi Fermi levels at the p-n junction. Quasi Fermi level splitting is lowered by recombination currents, and the quasi Fermi level splitting at the pn-junction equals the voltage over the solar cell in the absence of resistive effects. Therefore, the voltage increases with increasing excess carrier density; and the higher the recombination rate for a given generation rate (that is, for a given amount of light reaching the solar cell), the lower the steady-state excess carrier density, and the lower the voltage.

Recombination currents occur at the semiconductor surfaces and in the semiconductor bulk. Bulk recombination may occur through radiative recombination, through the Auger process, or through mediation of electronic states in silicon's band gap: Shockley-Read-Hall recombination. With respect to a discussion of surface recombination, contacted and non-contacted areas must be distinguished. Non-contacted areas are passivated by thick dielectric layers, for example silicon oxide, in order to reduce the density of defect states, thereby limiting Shockley-Read-Hall recombination at those surfaces. In contacted areas on the other hand, there is a very large amount of surface states resulting in a large amount of Shockley-Read-Hall recombination at the metal-semiconductor interface. In addition, minority carrier injection from the semiconductor into the metal also results in a very large recombination current, even in the absence of surface states. This dissertation is performed in the context of techniques to

reduce the recombination current at contacted areas. These techniques are generally referred to as contact passivation techniques.

Contact passivation techniques differ from techniques for the passivation of non-contacted areas in the sense that passivated contacts must still allow for majority carrier transport, whereas there is no such requirement for passivation layers designed for non-contacted areas.

1.3.2. Qualitative power loss analysis

The efficiency η of a solar cell is a function of the illumination conditions: i.e. of the spectral power distribution and the intensity of the incident light. For any given illumination conditions, a solar cell's efficiency η is the ratio between the maximum power density that can be delivered by the solar cell P_{mpp}, and the power density of the incident light P_{inc}:

$$\eta = \frac{P_{mpp}}{P_{inc}}. \tag{1.3.2.1}$$

The voltage at the maximum power point is the maximum power point voltage V_{mpp} and the current density at the maximum power point is the maximum power point current density J_{mpp}. The J_{mpp} - V_{mpp} pair is commonly referred to as the maximum power point on a solar cell's $J-V$ characteristic. P_{mpp}, V_{mpp} and J_{mpp} are related by:

$$P_{mpp} = J_{mpp} \cdot V_{mpp}. \tag{1.3.2.2}$$

Alternatively, the power output at the maximum power point can be written in terms of the solar cell's open circuit voltage V_{OC} and the solar cell's short circuit current density J_{SC} through the introduction of a new quantity, the fill factor FF. The fill factor is defined by:

$$FF \equiv \frac{J_{mpp} \cdot V_{mpp}}{J_{SC} \cdot V_{OC}}, \tag{1.3.2.3}$$

i.e. the fill factor is the ratio of the solar cell's true output power density and the solar cell's output power if the solar cell would be able to yield the short circuit current density J_{SC} and the open circuit voltage V_{OC} at the same time.

Through substitution of Equation 1.3.2.3 in Equation 1.3.2.2, the following equality is seen to be trivially satisfied:

$$P_{mpp} = J_{SC} \cdot V_{OC} \cdot FF, \tag{1.3.2.4}$$

i.e. the power density delivered by a solar cell at its maximum power point equals the product of the short circuit current density, the open circuit voltage and the fill factor.

The power loss ΔP is defined as the difference between the maximum power density output of an ideal solar cell with minimal losses from a theoretical point of view, P_{ideal}, and the maximum power density output of the solar cell being analyzed P_{mpp}, subject to the same test conditions:

$$\Delta P = P_{ideal} - P_{mpp} = V_{ideal} \cdot J_{ideal} \cdot FF_{ideal} - V_{OC} \cdot J_{JC} \cdot FF, \quad (1.3.2.5)$$

in which V_{ideal} is the maximum power point voltage of the ideal solar cell, J_{ideal} is the maximum power current density of the ideal solar cell, and FF_{ideal} is the fill factor of the ideal solar cell.

The total power loss ΔP can be written as the sum of three power loss components: current power loss ΔP_J, voltage power loss ΔP_V and fill factor power loss ΔP_{FF}:

$$\Delta P = \Delta P_J + \Delta P_V + \Delta P_{FF}, \quad (1.3.2.6)$$

in which

$$\Delta P_J = (J_{ideal} - J) \cdot V_{ideal} \cdot FF_{max}, \quad (1.3.2.7)$$

$$\Delta P_V = J \cdot (V_{ideal} - V) \cdot FF_{ideal}, \quad (1.3.2.8)$$

$$\Delta P_{FF} = J \cdot V \cdot (FF_{ideal} - FF). \quad (1.3.2.9)$$

Roughly speaking, the physical interpretation of the different power loss components is found as follows: ΔP_J is the power loss due to imperfect light trapping, parasitic absorption and imperfect carrier collection, ΔP_V is the power loss due to recombination currents that lead to less-than-maximum open circuit voltages and ΔP_{FF} is the power loss due to resistive effects or non-ideal diode characteristics.

This model has several major advantages. First, it is very easy to use due to its simplicity. Second, it only uses essential solar cell figures of merit which can be generally found in literature. For more detailed power loss analyses, more detailed, most likely proprietary information would be required. In addition, the more detailed a power loss analysis, the more intricate any comparison between different technologies becomes.

The downside of this simple model is that it is purely based on heuristic grounds and that it only allows to make general, qualitative statements about power losses in the devices under investigation. Nevertheless, it is a useful tool to investigate at a glance whether power losses are mostly due to optical effects (ΔP_J), due to excessive recombination currents (ΔP_V) or due to non ideal diode currents or resistive effects (ΔP_{FF}); in which the interpretation must be done with due care.

As an ideal solar cell, we take the model calculation by Tiedje et al. [Tiedje 1984], which yields: $V_{ideal} = 769\,mV$, $J_{ideal} = 42.2 mA \cdot cm^2$, $FF_{ideal} = 0.89$ and $P_{ideal} =$

$289\ Wm^{-2}$. We consider the power losses in one of the most efficient mono-crystalline silicon wafer-based solar cell technologies currently in industrial production [Cousins 2010]. This interdigitated back-contact silicon solar cell has the following figures of merit: $\eta = 24.2\%$, $J_{SC} = 40.5mA \cdot cm^2$, $V_{OC} = 721\ mV$, $FF = 82.9\%$, in which η denotes efficiency, J_{SC} short circuit current density and V_{OC} open circuit voltage. This leads to the power-loss distribution shown in Figure 1.3.2.1. From the figure, it is clear that the losses are limited compared to the ideal case, and are approximately equally distributed between the three major power loss categories for this particular type of solar cell.

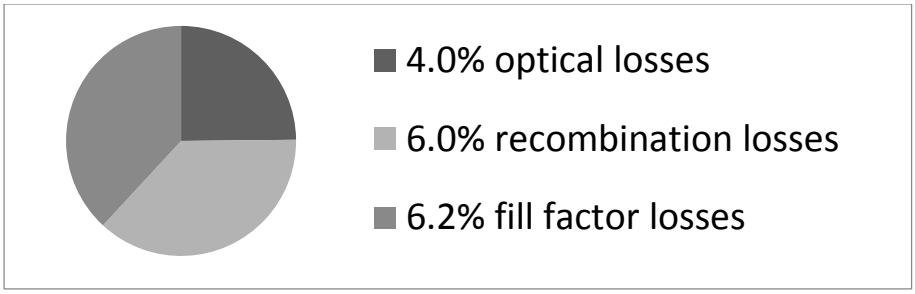

Figure 1.3.2.1: Power losses in a highly efficient wafer-based mono crystalline silicon solar cell used as a benchmark [Cousins 2010].

The solar cell for which the different power loss components are shown in Figure 1.3.2.1 is an Interdigitated Back Contact (IBC) silicon solar cell. IBC silicon solar cells are discussed in the next section.

1.4. IBC Silicon Solar Cells

This dissertation is completed in the context of studying and reducing power losses in Interdigitated Back Contact (IBC) silicon solar cells. IBC silicon solar cells have several advantages over two-side contacted solar cells. First, all contacts are at the back, which eliminates shading losses associated with front contacts. In addition, the IBC solar cell's front surface can be optimized to minimize recombination losses, whereas in front contact solar cells, there is a trade-off between recombination losses and resistive losses. A final advantage of IBC solar cells compared to two-side contacted silicon solar cells lies in the use of single side contacts facilitates the incorporation of the solar cells into modules, thereby reducing cell-to-module losses as a result [Greulich 2014]. A schematic cross section of the essential features of IBC solar cells is shown in Figure 1.4.1.

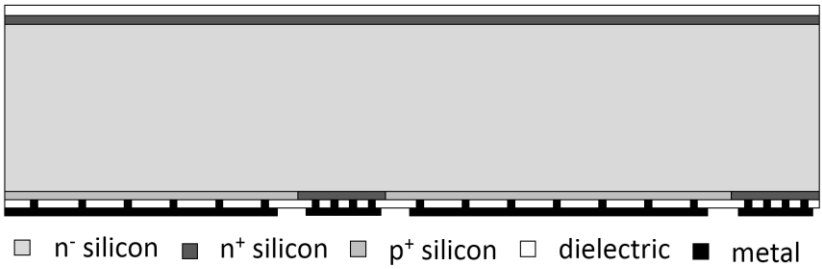

Figure 1.4.1. Schematic cross section of a simple IBC silicon solar cell. The solar cell's upper side in the picture is its illuminated side.

The down side associated with the IBC structure is its cost. The higher cost is related to two distinct causes. First, IBC solar cells require more patterning steps than 2-side contacted solar cells. Second, high-lifetime substrates, and high lifetime cell processing techniques are required due to the rather challenging charge carrier collection in IBC solar cells structures compared to two side contacted solar cell structures. The challenges related to charge carrier collection have two distinct causes. We discuss these causes for n-type wafers, which are commonly used as substrates for IBC silicon solar cells.

The first cause for the challenging minority carrier collection in IBC solar cells is related to the all contacts in an IBC solar cell being at the cell's back side, while a large portion of the AM 1.5G spectrum, especially the short wavelengths, is absorbed close to the illuminated (front) surface. This is shown for a specific example in Figure 1.4.2. Most light being absorbed close to the front surface results in a larger average distance that minority charge carriers must travel before they are collected compared to two side contacted solar cells featuring a front emitter. The larger average charge carrier traveling distance results in additional

recombination losses unless electrically thin, high-lifetime substrates are used along with surface passivation techniques that yield very low effective surface recombination velocities.

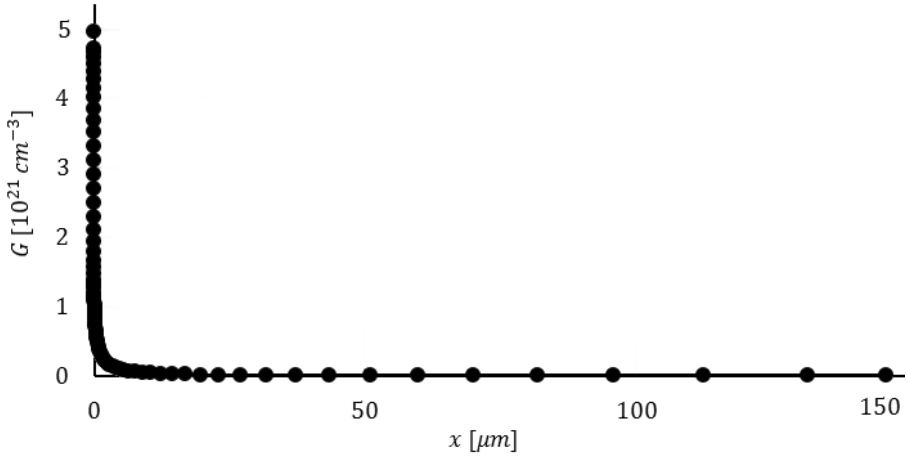

Figure 1.4.2. Electron-hole pair generation rate as a function of distance from the front surface in a 150 µm thick silicon solar cell.

Figure 1.4.2 shows the results from a simulation which was performed using OPAL 2, which is an online calculator freely available on www.pvlighthouse.com.au, using the following parameters: random surface morphology featuring upright pyramids with a characteristic angle of 54.74º. The solar spectrum was taken to be the AM1.5g spectrum according to [Guemyard 1995], the zenith angle was 0º. The path length enhancement factor was taken to be $Z = 4 + (ln(n^2 + (1 - n^2)e^{-4\alpha W}))/(\alpha W)$. The silicon solar cell was simulated under air. The antireflective coating consisted of a 65 nm thick PECVD SiN_x antireflective coating, and an underlying 20 nm thick passivating SiO_2 layer which has a parasitic optical effect. The optical constants for the PECVD SiN_x layer were taken from [Baker-Finch 2011]. The optical constants for the SiO_2 layer were taken from [Palik 1985]. The optical constants of silicon were taken from [Green 2008].

A second cause for the challenging minority carrier collection in IBC silicon solar cells is due to the requirement of lateral charge carrier transport. For IBC solar cells featuring n-type wafers, n^+ back surface fields and p^+ emitters; holes generated above the BSF diffusion must travel laterally in order to be collected in the emitter regions, and electrons generated above the emitter regions must travel laterally to be collected in the BSF regions. The lateral minority carrier transport can cause electrical shading, which results in current losses [Hermle 2008], [Kluska 2010]. Avoiding electrical shading is done through using BSF regions which are thin compared to the BSF's effective diffusion length, through the use

of excellent surface passivation, and through the use of high-lifetime substrates which tend to have an above-average cost.

We now proceed by giving a literature overview of the technologies that have been proposed to overcome the challenges associated with the IBC cell concept. Then, we give an overview of the IBC cell structure that was under development during the time when this dissertation was performed at imec and which provided the context for the work that is completed in this dissertation.

1.4.1. IBC silicon solar cell literature overview

Many different specific technologies have been proposed to fully exploit the benefits of the IBC solar cell structure, and to overcome the challenges associated with single side contacted solar cells. A detailed review of several back contact silicon solar cell technologies until 2005, including IBC solar cells, can be found in [Van Kerschaver 2006]. Recently, several notable IBC silicon solar cell technologies have emerged, which are discussed next.

The first example are IBC silicon solar cells that feature emitter and BSF (Back Surface Field) regions comprising a thin silicon oxide layer and doped polysilicon; see [De Ceuster 2014, Dennis 2012, Dennis 2014, Smith 2014], and the references therein. The technology leader in polysilicon-based IBC solar cells is Sunpower Corp. The record efficiency of IBC silicon solar cells featuring polysilicon-based contacts is 25% [Green 2014].

At the time of writing, the highest efficiency single junction silicon solar cells have an efficiency of 25.6% [Green 2014, Panasonic 2014]. These record solar cells are IBC silicon solar cells in which amorphous silicon junctions are used. These amorphous silicon junctions comprise a thin intrinsic amorphous silicon layer and a highly doped amorphous silicon layer that serves to induce the junction. This is Panasonic's HIT concept; HIT stands for *Heterojunction with Intrinsic Thin layer*.

Polysilicon and amorphous silicon based IBC silicon solar cells achieve very high efficiencies through the introduction of materials and processes that are new to the field of silicon solar cells. There is also considerable effort going into the development of IBC solar cells manufactured using common, "industry standard" processes. For example, Hareon solar presented 19.65% efficient IBC silicon solar cells made using alkaline texturing, $POCl_3$ and BBr_3 diffusions, and screen printing [Dong 2014]. Another low cost approach to IBC solar cells is ECN's Mercury concept [Cesar 2014] in which screen printed contacts are used to keep processing costs down. In order to avoid electrical shading losses, a conductive front floating junction is used, which collects minority carriers in the BSF region and facilitates transport to the (contacted) emitter region, where they can be

collected by the contacted back side emitter. At the time of writing, the Mercury solar cell concept yielded an efficiency of 19%. Other examples of low-cost IBC silicon solar cell approaches are the Zebra cell from the University of Konstanz [Galbiati 2012] and Hanwha Solar's p-type absorber IBC cell [Basore 2013].

1.4.2. IBC silicon solar cells at imec

In this section, we briefly describe how the IBC silicon solar cells featured in this dissertation are made. These IBC solar cells are produced following imec's lithography-based baseline process, which is a variation on the process described in [Verlinden 2012]. The substrates are Czochralski (Cz) silicon wafers with a bulk resistivity in the range of $1-5\ \Omega\cdot cm$. Relatively lowly doped n-type Czochralski silicon substrates are used to ensure a large bulk diffusion length. Note that compared to p-type Czochralski silicon, n-type Czochralski silicon has the advantage of the absence of boron-oxygen complexes, which are a dominating defect type in p-type (boron doped) Czochralski silicon [Bothe 2005].

The first step in imec's IBC solar cell process is saw damage removal using tetramethyl ammonium hydroxide (TMAH) at 80°C, which yields a relatively smooth, chemically polished surface. Prior to TMAH saw damage removal, a dip in a diluted aqueous HF/HCl solution (HF(aq):HCl:H_2O 5:5:70) is performed to remove the native oxide. Optionally, an SPM clean (H_2SO_4:H_2O_2 4:1, 90-120°C) is performed prior to the HF-dip to remove organic contaminants.

After saw damage removal, wafers are cleaned and subsequently receive a BBr_3 diffusion to form the p^+ emitter. Subsequently, the borosilicate glass (BSG) is removed and after a clean, a passivating oxide is grown using wet oxidation. This yields the structure depicted in Figure 1.4.2.1.

Figure 1.4.2.1. Schematic representation of the state of a device wafer during IBC solar cell processing, after emitter oxidation.

After emitter oxidation, the oxide is locally etched on one side of the wafer to define the n^+ back surface field (BSF). A BSF is a highly doped region in a high-low

junction on a solar cell's non-illuminated side used for surface passivation and base contacting.

The wafer is subsequently exposed to a silicon etchant such that the emitter is etched in the BSF openings. Then, n^+ BSF regions are formed using $POCl_3$ diffusion. The phosphosilicate glass (PSG) formed during the $POCl_3$ diffusion is subsequently removed, the wafers are cleaned, and a passivating oxide is formed on the BSF regions using dry oxidation. This yields the structure shown in Figure 1.4.2.2.

Figure 1.4.2.2. Schematic representation of the state of a device wafer during IBC solar cell processing, after BSF oxidation.

After BSF oxidation, the front oxide, which is shown on the top side of the wafer in Figure 1.4.2.2, is etched using HF vapor. Then, the front side of the wafer is textured, which also removes the p^+ emitter diffusion on the front side. Subsequently, the wafers receive a $POCl_3$ diffusion forming a front surface field. The front surface field is optimized for passivation and is lower doped than the back surface field used for contacting the base. After the front surface field diffusion, the phosphosilicate glass (PSG) is removed, the wafers are cleaned and a thin passivating oxide is formed for front surface field passivation. Then, a silicon nitride anti-reflective coating is deposited on the front surface field oxide. This yields the structure shown in Figure 1.4.2.3.

Figure 1.4.2.3. Schematic representation of the state of a device wafer during IBC solar cell processing, after FSF oxidation.

1. *Clean*
2. *Saw damage removal*
3. *Laser labeling*
4. *Clean*
5. *BBr_3 diffusion*
6. *BSG removal*
7. *Clean*
8. *Wet oxidation*
9. *Lithography*
10. *Silicon Etch*
11. *Resist removal*
12. *Clean*
13. *$POCl_3$ diffusion*
14. *PSG removal*
15. *Clean*
16. *Dry oxidation*
17. *1 side oxide etch*
18. *Texturing*
19. *Clean*
20. *$POCl_3$ diffusion*
21. *PSG removal*
22. *Clean*
23. *Dry oxidation*
24. *SiN_x deposition*
25. *Lithography*
26. *Oxide etch*
27. *Metal deposition*
28. *Lithography*
29. *Resist removal*
30. *Metal etch*
31. *Forming Gas anneal*
32. *Laser dicing of small cells*

Figure 1.4.2.4. Coarse-grained overview of the major process steps of an IBC silicon solar cell process, as performed in imec's photolithography baseline in December 2013. This baseline process was used for the manufacture of the solar cells discussed in chapter 4.

After FSF oxidation, contact openings are lithographically defined. The wafer is subsequently exposed to a silicon oxide etching solution. After resist removal, the metal contacts are sputtered. The metal contacts are aluminum alloyed with 1% silicon. Silicon is used as an alloying element in aluminum to prevent aluminum spiking during the forming gas anneal at the end of solar cell processing. After metal deposition, an interdigitated finger pattern is defined lithographically. The exposed metal regions are then etched to create the bus bar and interdigitated finger pattern. After resist removal and a silicon-dust etch (the silicon dust

originates from the Al:1% silicon alloy for contacting), a final forming gas anneal is done for 30 minutes at 400℃ to remove sputter damage and to improve surface passivation. This yields the structure shown in Figure 1.4.1. A course grained overview of the steps of the solar cell production process used in the present dissertation is given in Figure 1.4.2.4.

1.5. Passivated Contacts

In this section, an overview is provided of various types of technologies and methods that are designed to reduce recombination currents at solar cell contacts, while allowing majority carriers to pass through and therefore having low contact resistance. In this thesis, we use the term passivated contacts to denote these technologies. Note that the term passivated contacts may also refer to corrosion protection of solar cell contacts, see e.g. [Fischer 1971]. An alternative name for passivated contacts is carrier selective contacts [Feldmann 2014]. The term carrier selective contacts is commonly used in the field of excitonic photovoltaics, in which it refers to contacting methods designed to boost their efficiency [Gregg 2003]. There are ample examples of passivated contacts. We provide an extensive, though not exhaustive, overview below.

One type of passivated contacts is the semiconductor-oxide-semiconductor structure, shown schematically in Figure 1.5.1.

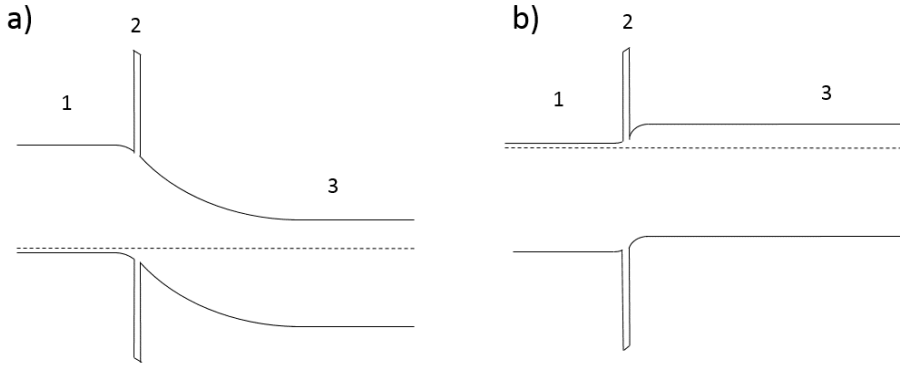

Figure 1.5.1. Schematic equilibrium band diagram of semiconductor (1) – dielectric (2) -semiconductor (3) passivated contacts (not to scale). Area (1) is a contacted highly doped semiconductor region. Area (2) is the interfacial tunnel oxide. Area (3) is a lowly doped semiconductor. The lower solid line is the valence band, the upper solid line is the conductance band, and the dotted line is the Fermi level. The drawings have been made for the case in which semiconductor areas (1) and (3) have the same band gap. a) p^+ semiconductor – oxide – n^- semiconductor structure; usable, for example, as an emitter. b) n^+ semiconductor – oxide – n^- semiconductor structure; usable, for example, as a back surface field (BSF).

In Figure 1.5.1, the conductance and valence band offsets between semiconductor and dielectric are shown to be equal. However, asymmetric band offsets are rather the rule than the exception. For most dielectrics; for example SiO_2, HfO_2, ZrO_2, Lu_2O_3, and Al_2O_3; the conductance band offset with silicon is smaller than the valence band offset with silicon [Bersch 2008, Seguini 2004]. The band offset asymmetry results in unequal barriers for electron and hole tunneling

through the oxide, which has been observed for e.g. silicon oxide tunnel barriers on silicon [Ng 1979]. We also explain some of our experimental results, specifically the observed trends in contact resistance and contact recombination current for MIS (metal-insulator-semiconductor) contacts featuring Al_2O_3 tunnel layers, from the valence band asymmetry of Al_2O_3 on silicon (chapter 5). Also, we note that the band structure of very thin tunnel oxides has been observed to depend on film thickness [Keister 1999]; which is a notion which is not explored any further in this dissertation. Apart from the symmetric band offsets, there is another simplification in Figure 1.5.1: Figure 1.5.1 shows the case in which both semiconductors have the same band gap, which is the case for, for example, polycrystalline silicon – silicon oxide – silicon passivated contacts. However, when regions (1) and (3) are made from different semiconductors, regions (1) and (3) generally have a different band gap.

1.5.1. Polycrystalline silicon

A first type of passivated contacts which are discussed in detail are polycrystalline silicon contacts. Polycrystalline silicon contacts were first discovered by IBM, and have been used in IBM's bipolar transistors since 1981 [Ning 2001]. The first applications of polycrystalline silicon for contacts in silicon solar cells were published around the mid-1980's [Lindholm 1985, Tarr 1985]. It was realized relatively soon that the trade-off between contact resistance and contact recombination can be improved through controlled break-up of the interfacial oxide between the polysilicon contact and the crystalline silicon base. This controlled interfacial oxide break-up can be done without detrimentally affecting the dopant profile by using a two-step annealing sequence: one anneal to break up the oxide, and a separate anneal for dopant diffusion [Gan 1990]; this avoids excessive dopant out diffusion, and the associated Auger recombination that comes with high thermal budgets after dopant incorporation.

When the interfacial oxide has been partially broken up, the contact structure for silicon solar cells with polycrystalline silicon contacts features passivated areas and unpassivated areas. When the interfacial oxide in the passivated areas is sufficiently thin, tunneling through the interfacial oxide can occur. When the interfacial oxide is sufficiently thick (more than ca. 2 nm), and when the surface area of the perforations is sufficiently large, the tunnel current in the passivated contact areas is much smaller than the current in the perforated areas. The latter structure is reminiscent to the structure of contacts on diffused junctions for which the junction surface is partially passivated with a thick dielectric layer and partially contacted using unpassivated contacts. In fact, the physics of such passivated contacts with partially broken up interfacial dielectric layers can be explained

within the framework of classical p-n junctions for passivated, locally contacted junctions [Peibst 2014].

Polysilicon contacts have gained significant attention after the achievement of 24.2% efficient solar cells with “passivated contacts” by Sunpower Corp [Cousins 2010]. Given a subsequent flurry of patent publications in the field of tunnel oxide - polysilicon contacts by the same company, this record is very likely to have been achieved using poly-Si / (SiO_2) / c-Si junctions; see [De Ceuster 2014, Dennis 2012, Dennis 2014, Smith 2014], and references therein. Another remarkable recent result in the field of poly-Si / (SiO_2) / c-Si junctions is the achievement of implied Voc’s of 732 mV for Si-SiO_2-n-type polysilicon and 711 mV for Si-SiO_2 p-type polysilicon [Römer 2014]. This investigation also featured the investigation of various chemical tunnel oxides as part of the passivated contact.

Note that polycrystalline silicon thin films have also been extensively studied as absorbers in thin-film solar cells. It could be possible to apply technologies that have been investigated in this domain to the field of passivated contacts for high efficiency, crystalline silicon solar cells. Notable achievements in the field of thin-film polycrystalline silicon solar cells are: solid phase crystallized, 9.2% efficient n-type polycrystalline silicon absorber solar cells on steel substrates [Baba 1995]; 10% efficient, solid phase crystallized, polycrystalline silicon absorbers on glass [Keevers 2007]; 8.5% efficient polycrystalline silicon solar cells on aluminum oxide substrates, featuring epitaxial absorbers on a template formed by aluminum-induced crystallization of amorphous silicon [Qiu 2010]; thin-film solar cells featuring 9% electron beam crystallized polycrystalline silicon absorbers on glass substrates [Amkreutz 2014]; and finally, 11.7% efficient laser-crystallized thin-film polycrystalline silicon solar cells on glass [Dore 2014].

The polycrystalline silicon layer in polycrystalline silicon passivated contacts can be replaced by another material such as amorphous or microcrystalline silicon. This yields a structure recently named TOPCon [Feldmann 2014, Feldmann 2014b, Feldmann 2014c, Feldmann 2014d, Moldovan 2014]. A hybrid, 2-side contacted cell with selective diffused emitter on the front and an n-type TOPcon layer on the back featured an efficiency of 24.4% [Feldmann 2014c]. In [Feldmann 2014b], the TOPcon structure is defined as being “based on the poly-silicon technology but makes use of a wide band gap layer placed above the tunnel oxide which can be more transparent than a-Si due to its crystalline phases”. This could be specifically advantageous for frontside contacts, but it is less critical for backside contacts. In [Felmann 2014d], the semiconducting layer is disclosed to be amorphous, microcrystalline or polycrystalline silicon, depending on the annealing temperature.

1.5.2. Semi insulating oxygen doped polycrystalline silicon

Semi insulating oxygen doped polycrystalline silicon (SIPOS) is another semiconducting material used for contact passivation that stems from the field of bipolar transistors [Matsushita 1979]. In this reference, SIPOS is defined as a CVD film made of SiH_4 and N_2O, with N_2 as a carrier gas at 650°C. SIPOS is a mixture of silicon crystallites, amorphous silicon, and silicon dioxide. Many material properties are described in detail in [Pan 1993]. One of the advantages of SIPOS is that its absorption coefficient can be lowered by increasing the oxygen concentration, thereby reducing parasitic absorption [Pan 1993b]. An early application of SIPOS to photovoltaics resulted in an excellent open circuit voltage of 720 mV, but low fill factor [Yablonovitch 1985]. Both polycrystalline silicon and SIPOS emitters can yield emitter saturation current densities lower than 20 fA/cm^2 in their optimized form [Kwark 1987].

1.5.3. Amorphous silicon

Another contact passivation method makes use of amorphous silicon. The use of amorphous silicon heterojunctions also stems from the field of bipolar transistors [IMEC 1984, Ghannam 1992]. Crystalline silicon solar cells featuring amorphous silicon emitters have been commercialized by Sanyo (now Panasonic) [Tanaka 1992]. Panasonic's amorphous silicon based HIT (heterojunction with intrinsic thin layer) concept features an intrinsic amorphous silicon passivation layer, and a highly doped, field-inducing amorphous silicon layer. This structure provides excellent contact passivation resulting in a 24.7% efficient, two-side contacted silicon solar cell with an open circuit current of 750 mV [Taguchi 2014]. The efficiency of this solar cell was limited by the relatively low short circuit current of 39.5 mA/cm^2. The short circuit current limitations in the two-side-contacted solar cell lay-out have been overcome by moving towards an IBC solar cell design, resulting in efficiencies of 25.6% under AM 1.5G illumination [Panasonic 2014], which is the most efficient silicon solar cell produced up to now [Green 2014]. Note that like polycrystalline silicon films, amorphous silicon films have been used as absorbers for thin-film solar cells, see for example [Schropp 2007]. It could be possible to apply technologies that have been investigated in this domain to the field of passivated contacts for high efficiency, crystalline silicon solar cells.

1.5.4. Undisclosed materials

We finally mention a variation on the semiconductor – dielectric – semiconductor passivated contact structure that features an undisclosed semiconducting material, Silevo's Triex solar cells, which have a 22.1% efficiency for cells with an area of 155 cm^2 [Heng 2013]. These solar cells feature a silicon oxide tunnel layer and a highly doped semiconducting layer which is described a "graded doped silicon-based thin film".

1.5.5. Metal-Insulator-Semiconductor Structures

The function of metal-insulator-semiconductor (MIS) contacts is conceptually similar to that of semiconductor-insulator-semiconductor contacts. There is a notable difference though, namely that the effective surface recombination velocity at the metal-insulator interface is infinite; there are no minority carriers in a metal. Therefore, any minority carriers that tunnel from the semiconductor to the metal through the dielectric layer are lost in MIS structures. In the semiconductor-insulator-semiconductor structures on the other hand, the highly doped semiconductor region can have a finite minority carrier lifetime. Therefore, minority carriers that tunnel from the lowly doped semiconductor, through the dielectric, to the highly doped semiconductor do not immediately recombine, and they are therefore not necessarily lost.

An early discussion of the theory of MIS solar cells can be found in [Green 1974], and early experiments by the same authors are described in [Shewchun 1974].

One application of MIS structures to solar cells are inversion layer solar cells. In an ideal world, Al-SiO_2-p Si MIS solar cells have been predicted to have an efficiency potential of 21% [Shewchun 1977], which is an efficiency that has not materialized so far. For MIS-inversion layer devices, thermal stability has been a major concern [Beyer 1996, Hezel 1984]. The efficiencies of such MIS- inversion layer devices have been mostly limited by their low open circuit voltages, see e.g. [Bartels 1995].

Recently, a new line of research has emerged in the field of MIS structures for solar cells. Rather than attempting to induce a junction through appropriate choice of metal work function and charged dielectrics, attempts have been made to reduce the recombination currents of contacted p-n or high-low junctions. One example is the passivation of aluminum contacts on n^+ silicon surfaces by Al_2O_3 or SiO_2 [Zielke 2011, Bullock 2013]. Other examples are the passivation of indium-tin oxide on n-type silicon by SiO_2 tunnel layers [Young 2014], and Al_2O_3 passivated aluminum-doped ZnO stacks for passivated contacts [Garcia-Alonso

2013]. Also, an interesting MIS passivated contact could be formed using a stack of intrinsic amorphous silicon and magnesium, as magnesium is known to form a good Ohmic contact with undoped a-Si:H [Matsuura 1989]. An Ohmic contact is a low-resistance junction with non-rectifying behavior [Warwick 2014]. However, it must be noted that for MIS contacts featuring amorphous silicon, there are likely temperature stability concerns as many metals; such as nickel, palladium and aluminum are known to induce the crystallization of amorphous silicon at low temperatures [Yoon 2001]. Also, the processing temperature would be additionally limited because of concerns related to hydrogen retention.

A MIS-contact based device architecture which is conceptually particularly appealing is a structure for which a band diagram is shown in Figure 1.5.2. For simplicity, no band bending is considered. The center are in Figure 1.5.2 shows a semiconductor. The left- and right-hand areas, denoted (1) and (2) respectively, are metal contacts.

The left-hand contact in Figure 1.5.2 is shielded from the semiconductor by means of a dielectric layer having a very small conductance band offset with the semiconductor, but a very large valence band offset. Therefore, the dielectric layer between the semiconductor and the left-hand metal contact shields holes from the left hand contact but allows electrons to readily pass through.

Conversely, the right hand contact (2) in Figure 1.5.2 is shielded from the semiconductor by means of a dielectric layer which has a large conductance band offset but a small valence band offset with the semiconductor. Therefore, the dielectric layer between the semiconductor and the right-hand metal contact shields electrons from the right-hand contact but allows holes to readily pass through.

When carriers are excited in the semiconductor under the influence of light with an above-bandgap energy, electrons will flow to the left hand contact and holes will flow through the right hand contact because of the band-offset asymmetry of the dielectric layers between contacts and semiconductor. When the left-hand and the right-hand contacts are connected through an electrical circuit, the asymmetry between hole and electron current flow can be exploited to do work.

The device structure shown in Figure 1.5.2 is particularly appealing because the device structure does not feature any highly doped semiconductor regions; thereby avoiding the associated Auger recombination or effective bandgap narrowing. The challenge associated with the practical realization of this device architecture lies in finding material systems and processing sequences which result in the band diagram shown in Figure 1.5.2.

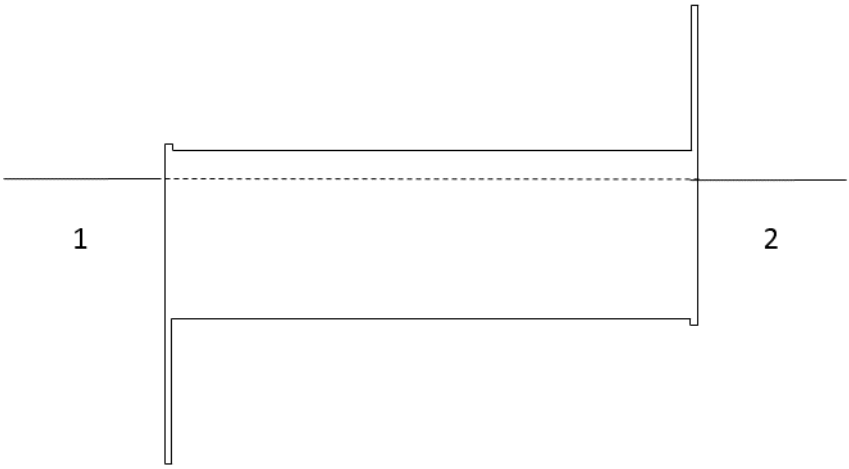

Figure 1.5.2. Solar cell device structure featuring MIS-contacts with dielectric layers having asymmetric band offsets.

1.5.6. Surface state passivation

A final type of passivated contacts that is discussed here are metal-semiconductor structures for which interface states have been passivated, thereby avoiding Fermi level pinning at metal-semiconductor interfaces, and allowing band bending at metal-semiconductor junctions to be controlled by the metal's work function. For example, passivation at the metal (titanium) – n-type silicon interface can be accomplished by for using selenium [Osvald 2004, Tao 2004, Tao 2004b, Tao 2004c]. For metals with an appropriate work function, the resulting band bending can repel minority carriers from the metal-semiconductor interface, thereby reducing parasitic minority carrier flow from semiconductor to metal. However, there is no report on the effect of surface passivation on the effective surface recombination velocity in the aforementioned references.

2. Basic concepts

In this chapter, several basic aspects of semiconductor device physics are introduced in a simplified way. This introductory discussion is included for two reasons. First, it serves as a useful introduction to subsequent chapters on recombination current measurements. Second, it provides a summary of several key concepts, which will be used as a basis for future reference. For the sake of conciseness, this chapter is limited to the essential theory that is required for understanding further chapters. An excellent introduction to semiconductor device physics, aimed at the layperson, can be found in [Shockley 1956]. A detailed technical discussion of a great variety of semiconductor devices can be found in [Sze 2007, Van Overstraeten 1998].

Charger carrier recombination in silicon solar cells is discussed first (section 2.1). Subsequently, an introduction is given to radio-wave detected quasi steady state photoconductance (QSSPC) measurements (section 2.2). QSSPC measurements lie at the basis of the characterization method for contact recombination measurements treated in this dissertation. We end this chapter with a treatment of how the minority carrier concentration varies over the wafer thickness (section 2.3) in blanket test structures during QSSPC measurements under uniform illumination. The resulting mathematical framework forms the basis for the discussion of the novel characterization method for contact recombination currents introduced in this dissertation.

2.1. Recombination and Current Flow

Recombination is a process by which the carrier concentration in an excited semiconductor returns to its equilibrium value. Therefore, the equilibrium carrier concentration in semiconductors is discussed first. Then, departure from equilibrium and the associated recombination processes are described.

2.1.1. Equilibrium

Consider a large and uniform semiconductor volume such that boundary effects are of no importance. The semiconductor contains freely moving electrons and holes. In thermal equilibrium, the electron and hole concentration is determined by a naturally occurring balance between two continually occurring processes: generation and recombination. The first process, generation, is due to the thermal excitation of electrons from their lower energy states in the valence band to higher energy states in the conduction band, where they are free to move. In this process, a hole remains in the valence band which, in turn, acts as a freely moving positively charged species. In the second process, recombination, electrons and holes annihilate each other. The balance between generation and recombination processes can be described as a chemical equilibrium:

$$n + p \leftrightarrow [], \tag{2.1.1.1}$$

in which n is the electron concentration in the conduction band, p is the hole concentration in the valence band and [] denotes the absence of either free charge carrier. Equation 2.1.1.1 states that free electrons and free holes are antiparticles; when they react, they annihilate each other. In equilibrium, the product of electron and hole concentrations equals a constant:

$$n_0 \cdot p_0 = n_i^2, \tag{2.1.1.2}$$

in which n_0 is the equilibrium electron concentration, p_0 is the equilibrium hole concentration and n_i^2 is the square of the intrinsic carrier concentration, n_i. In its simplest definition, n_i is the carrier concentration in an intrinsic semiconductor. An intrinsic semiconductor is a semiconductor to which no doping elements are added. In an intrinsic semiconductor, the electron and hole concentrations are equal and therefore in thermal equilibrium, they equal the intrinsic concentration:

$$n = p = n_i. \tag{2.1.1.3}$$

Note that the quantity n_i^2 is analogous to the concept of a chemical equilibrium constant [Shockley 1956].

Apart from intrinsic semiconductors, extrinsic semiconductors exist as well. In the simplest picture of an extrinsic semiconductor, impurities (dopants) are added that either lack electrons or have an excess of electrons in their valence shell. The case of excess electrons corresponds to an n-type semiconductor and the case of an electron deficit corresponds to the case of a p-type semiconductor. For group IV semiconductors such as silicon, group III elements are p-type dopants and group V elements are n-type dopants. When the concentration of one charge carrier type is increased through incorporation of donor or acceptor impurities in the silicon lattice, the concentration of its antiparticle is decreased such that Equation 2.1.1.2 still holds.

For example, take the case of an n-type semiconductor that contains a concentration of active electron donor atoms N_D. In this case, the equilibrium electron concentration n approximately equals the donor concentration N_D:

$$n_0 \approx N_D, \tag{2.1.1.4}$$

Combining Equations 2.1.1.2 and 2.1.1.4, the equilibrium hole concentration p approximately equals n_i^2/N_D:

$$p_0 \approx n_i^2/N_D, \tag{2.1.1.5}$$

In most practical settings, $N_D \gg n_i$. Therefore, there are many more electrons than holes in an n-type semiconductor in equilibrium, and electrons are called majority carriers and holes are called minority carriers.

The preceding discussion established that electron and hole concentrations are linked in equilibrium. For a given material, this relation is elegantly described by the Fermi level, E_F. The Fermi level is the electrochemical potential. As electrons and holes are Fermions, their energy distribution follows Fermi-Dirac statistics. For low doping concentrations, the Fermi-Dirac distribution is equivalent to the mathematically simpler Maxwell-Boltzmann distribution, and the free electron and hole concentration are:

$$n = N_C exp\big((E_F - E_C)/kT\big), \tag{2.1.1.6}$$

$$p = N_V exp\big((E_V - E_F)/kT\big), \tag{2.1.1.7}$$

in which N_C and N_V are electron and hole effective density of states, respectively, E_F is the Fermi level, E_C is the conductance band energy, E_V is the valence band energy, k is Boltzmann's constant, and T is absolute temperature. Note that by combination of Equations 2.1.1.2, 2.1.1.6 and 2.1.1.7; the intrinsic carrier concentration is linked to the effective density of states and the difference between conduction and valence band energy as:

$$n_i^2 = N_C N_V exp\big((E_V - E_C)/kT\big). \tag{2.1.1.8}$$

$E_V - E_C$ is the semiconductor's band gap, ΔE_g.

2.1.2. Departure from equilibrium

We first describe how departure from equilibrium is described in a semiconductor. Then, we discuss how the balance between generation and recombination processes results in steady state carrier concentrations in an out of equilibrium situation. We will continue to arbitrarily consider the case of an n-type semiconductor. The p-type semiconductor case is readily found by analogy.

Excess carrier density

The simplest, most intuitive way to describe departure from equilibrium in a semiconductor is through the concept of excess carrier density. By definition, the excess carrier density is the amount by which the carrier concentration exceeds the equilibrium carrier concentration. For an n-type semiconductor:

$$p = p_0 + \Delta p \approx \Delta p, \quad (2.1.2.1)$$

$$n = n_0 + \Delta n \approx N_D + \Delta n, \quad (2.1.2.2)$$

in which Δp is the excess hole concentration, N_D is the electron donor concentration, Δn is the excess electron concentration, n_0 is the equilibrium electron concentration, and p_0 is the equilibrium hole concentration.

Quasi neutrality

In uniformly doped, electrically neutral semiconductor regions, the excess electron concentration equals the excess hole concentration:

$$\Delta n = \Delta p. \quad (2.1.2.3)$$

The assumption of electrical neutrality is useful in the analysis of the properties of certain regions in various semiconductor devices. One example is the bulk absorber of a typical pn junction silicon solar cell. However, the assumption of electrical neutrality is often not exact such that the term "quasi neutrality" is used instead of the term "electrical neutrality".

The assumption of quasi neutrality allows the description of the carrier concentrations in a semiconductor by considering only one charge carrier: the concentration of the other charge carrier is determined by the concentration of the first charge carrier and the condition of quasi neutrality (i.e. the assumption that Δn approximately equals Δp). As a result, the behavior of only one charge carrier type must be considered in the analysis of electrically neutral semiconductor

regions, which greatly simplifies the mathematical treatment of the quasi neutral semiconductor region.

In particular, the quasi neutrality concept allows an elegant analysis of the flow of electrons and holes in a semiconductor through the concept of the ambipolar diffusion coefficient, as discussed for example in [Baliga 2008]. The ambipolar diffusion coefficient is discussed in the next paragraphs.

In order to preserve quasi neutrality over time, the quasi neutrality concept requires that at any position in a quasi neutral semiconductor region, the electron flux equals the hole flux such that the electron current density exactly cancels the hole current density:

$$J_p + J_n = 0. \tag{2.1.2.4}$$

The electron and hole current densities are given by:

$$J_n = q\mu_n nE + qD_n \nabla n; \text{ and} \tag{2.1.2.5}$$

$$J_p = q\mu_p pE - qD_p \nabla p; \tag{2.1.2.6}$$

in which J_n is the electron current density, q is elementary charge, μ_e is electron mobility, n is electron concentration, E is electric field, D_n is electron diffusion constant, J_p is hole current density, μ_p is hole mobility, p is hole concentration, and D_p is hole diffusion coefficient. In a uniformly doped semiconductor, spatial variations in electron and hole concentrations can only occur through spatial variations in the excess carrier density. By Equation 2.1.2.3, the excess carrier densities are equal in quasi neutral semiconductor regions, and therefore, the electron and hole concentration gradients are equal as well. Taking this into account and combining Equations 2.1.2.4 to 2.1.2.6 yields:

$$E = \frac{D_p - D_n}{\mu_n n + \mu_p p} \nabla p, \tag{2.1.2.7}$$

which provides an expression for the electrical field in the quasi neutral region as a function of the hole concentration gradient, which equals the excess carrier concentration gradient.

Substitution of Equation 2.1.2.7 in Equation 2.1.2.6 yields:

$$J_p = -q\left(\frac{(n+p)D_n D_p}{D_n n + D_p p}\right)\nabla p, \tag{2.1.2.8}$$

which has the form of a hole diffusion current. The quantity within brackets is the ambipolar diffusion coefficient D_a for quasi neutral regions in a semiconductor:

$$D_a = \frac{(n+p)D_n D_p}{D_n n + D_p p}. \tag{2.1.2.9}$$

The ambipolar diffusion coefficient D_a is a modified diffusion coefficient which takes interactions between electrons and holes in quasi neutral regions into

account. It is a function of the electron and hole concentrations. For an n-type semiconductor in low injection ($p \ll N_D \approx n$):

$$D_a \approx D_p. \tag{2.1.2.10}$$

Similarly, for a p-type semiconductor in low injection, ($n \ll N_A \approx p$):

$$D_a \approx D_n. \tag{2.1.2.11}$$

Therefore, the ambipolar diffusion coefficient equals the minority carrier diffusion coefficient in the low injection limit. Throughout the remainder of this dissertation, we assume that the low injection limit is valid for the purpose of determining diffusion coefficients in quasi neutral regions. The reason for this is pragmatic: using the ambipolar diffusion coefficient instead would introduce injection level dependence in the diffusion coefficient, which would make the transport equations used herein more difficult to solve.

We now analyze the worst-case error which is introduced in the diffusion coefficient for holes in n-type quasi neutral regions. We assume that the hole diffusion coefficient of silicon is $12\ cm^2/s$ and that the electron diffusion coefficient of silicon is $36\ cm^2/s$. In that case, the low injection limit ($n \gg p$) of the ambipolar coefficient is the hole diffusion coefficient, $12\ cm^2/s$. The high injection limit ($n \approx p$) of the ambipolar diffusion coefficient is $18\ cm^2/s$; resulting in an error of 50% if the low injection value of the ambipolar diffusion coefficient is used in the high injection limit instead of the actual value of the ambipolar diffusion coefficient.

Quasi Fermi level splitting

Quasi Fermi level splitting is an alternative way to describe departure from equilibrium in semiconductors. When excess carriers are generated, the electron and hole distributions are no longer in thermal equilibrium with one another. However, it is assumed that the electron and hole distributions are in thermal equilibrium with themselves, separately. Therefore, the electron energy distribution is a Fermi-Dirac distribution described by an “electron quasi Fermi level” and the hole energy distribution is described by a separate Fermi-Dirac distribution, with its own “hole quasi Fermi level”. Analogous to the equilibrium case, the Fermi-Dirac distributions reduce to Maxwell-Boltzmann distributions for low doping levels and low excess carrier densities:

$$n = N_C exp\big((E_{Fn} - E_C)/kT\big), \tag{2.1.2.12}$$

$$p = N_V exp\left(\big(E_V - E_{Fp}\big)/kT\right), \tag{2.1.2.13}$$

in which E_{Fn} is the electron quasi Fermi level, and E_{Fp} is the hole quasi Fermi level. The difference between the electron and hole quasi Fermi level, also known as

the quasi Fermi level splitting V, is a measure of the amount by which a semiconductor is out of equilibrium, similar to the excess carrier density. Combination of Equations 2.1.1.8, 2.1.2.1, 2.1.2.2, 2.1.2.12, and 2.1.2.13 yields the following relation between excess carrier density Δp and quasi Fermi level splitting V:

$$np = \Delta p(N_D + \Delta p) = n_i^2 exp(qV/kT), \quad (2.1.2.14)$$

in which $V = \left(E_{Fn} - E_{Fp}\right)/q$, with q elementary charge.

Generation, recombination and current

In uniform semiconductors out of equilibrium, and in the absence of electric fields, the electron and hole concentrations are determined by a balance between generation and recombination processes, analogous to the equilibrium case. For non-uniform semiconductors, so-called “diffusion currents” flow which tend to even out any non-uniformities in the carrier profile. In addition, in the presence of electric fields, the electric field induces currents to flow as well. Electrical current flow under influence of electric fields is referred to as “drift current”. In this subsection, we focus on holes in an n-type semiconductor, but an analogous derivation holds for electrons in a p-type semiconductor.

Consider an elementary volume of semiconductor in Cartesian coordinates. A two dimensional analogue is shown in Figure 2.1.2.1 for the purpose of defining the symbols used.

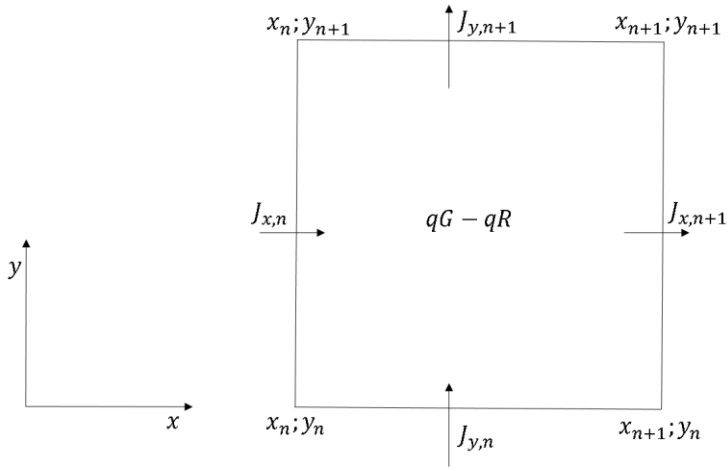

Figure 2.1.2.1. Two dimensional representation of an elementary semiconductor volume (i.e. one spatial dimension is suppressed).

A mass balance for holes in a small semiconductor volume yields:

$$qG\Delta x\Delta y\Delta z - qR\Delta x\Delta y\Delta z - \Delta J_x\Delta y\Delta z - \Delta J_y\Delta x\Delta z - \Delta J_z\Delta x\Delta y = q\frac{\Delta p}{\Delta t}\Delta x\Delta y\Delta z,$$

(2.1.2.15)

in which $\Delta J_x = J_{x,n+1} - J_{x,n}$, $\Delta x = x_{n+1} - x_n$. ΔJ_y, ΔJ_z, Δy and Δz are defined analogously. The semiconductor volume is small in the sense that current densities J_x, J_y and J_z do not vary significantly in the plane perpendicular to the direction of current flow, for the volume under consideration. In addition, for Equation 2.1.2.15 to hold, the volume under consideration must be sufficiently small such that the generation rate G and the recombination rate R do not vary appreciably over the volume.

Division of Equation 2.1.2.15 by the small volume element $\Delta x\Delta y\Delta z$ yields:

$$qG - qR - \frac{\Delta J_x}{\Delta x} - \frac{\Delta J_y}{\Delta y} - \frac{\Delta J_z}{\Delta z} = q\frac{\Delta p}{\Delta t}. \quad (2.1.2.16)$$

Taking the limit of Equation 2.1.2.16 for infinitesimally small distances and times, the fractions of finite differences in Equation 2.1.2.16 become partial derivatives:

$$qG - qR - \frac{\delta J_x}{\delta x} - \frac{\delta J_y}{\delta y} - \frac{\delta J_z}{\delta z} = q\frac{\delta p}{\delta t}. \quad (2.1.2.17)$$

Using the del symbol ∇ to denote a gradient, Equation 2.1.2.17 can be written in a condensed form:

$$qG - qR - \nabla \mathrm{J_p} = q\frac{\delta p}{\delta t}, \quad (2.1.2.19)$$

in which $\mathrm{J_p}$, the hole current density is the vector quantity (J_x, J_y, J_z).

The hole current density J_p has two components: the diffusion current which tends to annihilate carrier profile inhomogeneity, and the drift current in which carriers move under influence of an electric field. The total current is given by the sum of the two:

$$\mathrm{J_p} = \mathrm{q}\mu_\mathrm{p} pE - \mathrm{q}\mu_\mathrm{p}\frac{kT}{q}\nabla \mathrm{p}, \quad (2.1.2.20)$$

in which μ_p is hole mobility, and E is the electric field. The first term in Equation 2.1.2.20 is the drift current and the second term in Equation 2.1.2.20 is the diffusion current. The recombination rate in Equation 2.1.2.19 is commonly expressed by means of the excess carrier density Δp and the bulk lifetime τ_b:

$$R = \frac{\Delta p}{\tau_b}. \quad (2.1.2.21)$$

Substitution of Equations 2.1.2.20 and 2.1.2.21 in Equation 2.1.2.19 yields:

$$G - \frac{\Delta p}{\tau_b} - \nabla\left[\mu_\mathrm{p} pE - \mu_\mathrm{p}\frac{kT}{q}\nabla \mathrm{p}\right] = \frac{\delta p}{\delta t}. \quad (2.1.2.22)$$

The assumption of constant mobility, quasi neutrality, low injection, and the identification of the bulk diffusion length as $L_D = \sqrt{\tau_b D_p}$, with $D_p = \mu_p \, kT/q$, yields:

$$\tau_b G - \Delta p - L_D^2 \nabla^2 p = \tau_b \frac{\delta p}{\delta t}. \quad (2.1.2.23)$$

Throughout this dissertation, the steady-state form of this equation will be commonly used to analyze the behavior of charge carriers in quasi neutral regions.

Surface recombination

Semiconductor surfaces act as catalysts for carrier recombination in semiconductors. The simplest description of surface recombination currents J_R makes use of an effective surface recombination velocity S_{eff}:

$$J_R = qS_{eff}(p - p_0). \quad (2.1.2.24)$$

At any boundary of a semiconductor volume, current continuity, the assumption of only a diffusion current flowing to the surface and the description of surface recombination using an effective surface recombination velocity S_{eff} yields the following well-known boundary condition for Equation 2.1.2.23:

$$D_p \nabla p \cdot \vec{n} = S_{eff}(p - p_0) = J_R/q, \quad (2.1.2.25)$$

in which $\vec{n}$ is an outward pointing unit vector perpendicular to the surface, J_R is the surface recombination current, and "·" denotes the dot product. Equation 2.1.2.25 is the statement that the diffusion current flowing towards a semiconductor surface equals the recombination current at that surface. In one dimension, Equation 2.1.2.25 becomes:

$$D_p \frac{dp}{dx} = \pm S_{eff}(p - p_0), \quad (2.1.2.26)$$

in which the sign is determined by the relative orientation of semiconductor and surface in a particular coordinate system.

Junction recombination

Consider recombination currents in p-n or high-low junctions shielding minority carriers in the semiconductor bulk, for example emitters and back surface fields, from recombining surfaces. These recombination currents are generally lumped together with recombination currents at the respective surfaces. Such lumped recombination currents are often expressed by means of saturation current densities J_0 instead of by effective surface recombination velocities S_{eff} (Equation 2.1.2.25):

$$J_R = J_0 exp\left(\frac{qV}{mkT}\right), \quad (2.1.2.27)$$

in which J_R is the surface recombination density, J_0 is the saturation current density, q is elementary charge, V is quasi Fermi level splitting, k is Boltzmann's constant, T is absolute temperature, and m is the ideality factor. In this work, we

will be mostly dealing with junctions for which the recombination current has unit ideality factor at the relevant injection levels such that:

$$J_R = J_0 exp\left(\frac{qV}{kT}\right). \quad (2.1.2.28)$$

Using the relation between the p-n product and quasi Fermi level splitting, Equation 2.1.2.14, the junction recombination current according to Equation 2.1.2.28 can be expressed in terms of the excess carrier density:

$$J_R = J_0 \frac{\Delta p(N_D+\Delta p)}{n_i^2}. \quad (2.1.2.29)$$

Note that the excess carrier density in Equation 2.1.2.29 is the excess carrier density at the bulk side of the space charge region between the semiconductor bulk and the highly doped region under consideration.

The saturation current density J_0 is a central concept throughout this dissertation. The next section is dedicated to providing the interested reader with a means to obtain an intuitive understanding of this quantity.

2.1.3. Saturation current density J_0

In order to gain some physical understanding of the saturation current density J_0, we consider a uniformly doped n⁺ silicon back surface field (BSF) on an n-type wafer that shields minority carriers (holes) from a recombining surface with effective surface recombination velocity S_W.

Other cases are readily found by analogy. With respect to the analogy, the bulk doping type is immaterial (i.e. it does not influence the resulting equations for J_0). When recombination in a p⁺ region instead of an n⁺ region is considered, the following substitutions are made: the hole diffusion coefficient D_p is substituted for by the electron diffusion coefficient D_n, the hole diffusion length L_p is substituted for by the electron diffusion length L_n, and the donor concentration N_D is substituted for by the acceptor concentration N_A.

The minority carrier concentration in the n⁺ BSF under consideration is schematically depicted in Figure 2.1.3.1 as a function of position x. In the present example $\mathrm{d}\Delta\mathrm{p}/dx = \mathrm{dp}/dx$ as $\Delta\mathrm{p} = \mathrm{p} - \mathrm{p}_0$ and p_0 is a constant because N_D is a constant.

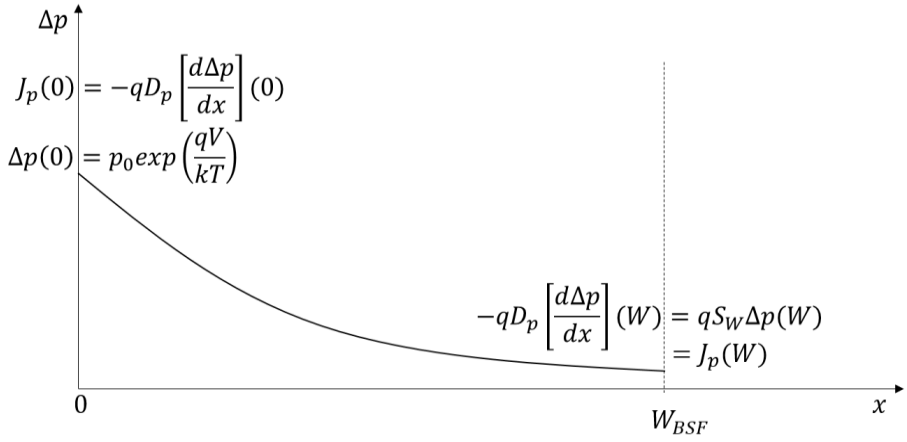

Figure 2.1.3.1. Schematic representation of the excess minority carrier (hole) concentration in an n⁺ BSF in a silicon solar cell. The same picture applies for other quasi neutral regions in which minority carriers are injected at one surface (here x=0) and where minority carriers recombine at another surface (here x=W).

Intuitively, Figure 2.1.3.1 should be read as follows: the excess minority carrier (hole) concentration $\Delta\mathrm{p}$ at the edge of a space charge region $x = 0$ is determined by the equilibrium minority carrier concentration p_0 at that position and by the quasi Fermi level splitting V at that position. When the only source of minority carriers in the BSF is minority carrier injection at $x = 0$ (i.e. there is negligible minority carrier

generation in the BSF region), the total recombination current density in the BSF, $J_R = J_0 exp(qV/kT)$, is equal to $J_p(0)$, $J_p(0)$ being the hole current density at $x = 0$. $J_p(0)$ is determined by the hole diffusion coefficient D_p and by the hole excess carrier density gradient $\mathrm{d}\Delta\mathrm{p}/dx$ at $x = 0$.

The excess carrier density gradient is the mathematical description of how the excess carrier density changes with position. In general, the local change of $d\Delta p/dx$ (i.e. the second derivative of Δp with respect to position) is determined by the local balance between generation and recombination currents, and by the local transport properties (i.e. D_p). In the present example, generation currents are of no importance because for highly doped regions (such as a BSF or emitter) on the back side of typical wafer-based silicon solar cells, most light is absorbed near the front surface (Refer to section 1.4, Figure 1.4.2). Therefore, the local change in $\mathrm{d}\Delta\mathrm{p}/dx$ is only determined by local transport and recombination processes. The occurrence of bulk recombination currents in the present example explains why the absolute value of $\mathrm{d}\Delta\mathrm{p}/dx$ decreases with increasing position: as minority carriers recombine, fewer minority carriers are available to contribute to the diffusion current density, such that the diffusion current density decreases with increasing position. The diffusion current density is proportional to $\mathrm{d}\Delta\mathrm{p}/dx$ such that decreasing diffusion current densities with position correspond to decreasing $|\mathrm{d}\Delta\mathrm{p}/dx|$, in which $|\ \ |$ denotes the absolute value of the quantity within vertical lines.

Despite the bulk recombination, some minority carriers injected at $x = 0$ still reach the junction's surface at $x = W$. This surface features a certain number of surface states where recombination may occur. The resulting surface recombination current density is expressed as the product of the elementary charge q, an effective surface recombination velocity S_W, and the excess carrier density Δp. A basic mass balance requires that the diffusion current density flowing towards the surface equals the recombination current density at that surface. Therefore, the effective surface recombination velocity S_W determines the slope of Δp at $x = W$, and indirectly the slope of Δp at $x = 0$. Therefore, S_W indirectly determines J_0. However, this is only the case when W_{BSF}/L_p is not much bigger than one, because in the latter case all minority carriers recombine before they reach the back surface and as a result, the properties of the back surface do not have any influence on J_0 in this case.

Mathematically, J_0 can be found as follows: solve Equation 2.1.2.14 for the steady state case (solar cells are devices which operate in steady state), i.e. $\delta\Delta p/\delta t = 0$, with boundary conditions $\Delta\mathrm{p}(0) = \mathrm{p}_0 \exp(qV/kT)$ and $S_W \Delta\mathrm{p}(W) = -D_p\, d\Delta p/dx\,(W)$. Then use the obtained minority carrier profile to obtain J_0 from:

$$J_R = J_0 exp\left(\frac{qV}{kT}\right) = -qD_p \frac{d\Delta p}{dx}(0). \quad (2.1.3.1)$$

For the present example, this yields for the saturation current density J_0 [Verlinden 2010]:

$$J_0 = \frac{qD_p n_i^2}{L_p N_{D,BSF}} \left[\frac{\frac{S_W L_p}{D_p} + tanh\left(\frac{W_{BSF}}{L_p}\right)}{1 + \frac{S_W L_p}{D_p} \tanh\left(\frac{W_{BSF}}{L_p}\right)}\right], \quad (2.1.3.2)$$

in which q is elementary charge, D_p is the hole diffusion coefficient in the uniformly doped BSF, n_i is the intrinsic carrier concentration, L_p is the hole diffusion length in the BSF, $N_{D,BSF}$ is the dopant concentration in the BSF, and W_{BSF} is the BSF thickness.

Equation 2.1.3.2 is a function of the ratio W_{BSF}/L_D and it has two interesting limits. The first limit is for $W_{BSF}/L_D \gg 1$. In this case, the factor between brackets is equal to one, and Equation 2.1.3.2 becomes:

$$\lim_{W_{BSF}/L_D \gg 1} J_0 = \frac{qD_p n_i^2}{L_p N_{D,BSF}}. \quad (2.1.3.3)$$

Equation 2.1.3.3 corresponds to the case of an electrically opaque junction; minority carriers injected at the space charge region at $x = 0$ (see Figure 2.1.3.1) recombine before reaching the recombining surface at $x = W$ such that the effective surface recombination velocity S_W does not influence J_0.

The other limit of Equation 2.1.3.2 is for $W_{BSF}/L_D \ll 1$. In this case, the factor between brackets is equal to $S_W L_p/D_p$, and Equation 2.1.3.2 becomes:

$$\lim_{W_{BSF}/L_D \ll 1} J_0 = \frac{qn_i^2 S_W}{N_{D,BSF}}. \quad (2.1.3.4)$$

Equation 2.1.3.4 corresponds to the case of an electrically transparent junction; minority carriers injected at the space charge region at $x = 0$ (see Figure 2.1.3.1) do not recombine before reaching the recombining surface at $x = W$ such that the bulk diffusion length or the bulk diffusion coefficient do not influence J_0. The doping level $N_{D,BSF}$ does influence J_0 because by combination of Equation 2.1.2.28 and Equation 2.1.2.29, the excess carrier density is inversely proportional to the doping level for a given amount of quasi Fermi level splitting (this is true for moderate doping levels, i.e. as long as n_i does not increase due to effective bandgap narrowing). The smaller the effective carrier density for a given amount of quasi Fermi level splitting, the smaller the recombination current for a given amount of quasi Fermi level splitting and the smaller J_0.

Figure 2.1.3.2 is an elegant representation of Equation 2.1.3.2, which has been adapted from [Verlinden 2010]. It is a plot of a first dimensionless number, $J_0 \cdot \left[\left(L_p N_{D,BSF}\right)/qD_p n_i^2\right]$, as a function of a second dimensionless number, W_{BSF}/L_p,

for various values of a third dimensionless number, $[S_W L_p]/[D_p]$. In essence, the picture is an elegant representation of how J_0 changes as a function of the most relevant parameters. $J_0 \cdot [(L_p N_{D,BSF})/qD_p n_i^2]$ is a measure of J_0, W_{BSF}/L_p is a measure of the electrical opacity of the junction, and $[S_W L_p]/[D_p]$ is a measure of the magnitude of surface recombination with respect to bulk recombination. W_{BSF}/L_p and $[S_W L_p]/[D_p]$ are discussed in detail in the next paragraphs.

W_{BSF}/L_p is a measure of the extent to which minority carriers at $x = 0$ are shielded from the surface at $x = W_{BSF}$. W_{BSF}/L_p is the ratio of two characteristic lengths: W_{BSF} is the characteristic length of the spatial extension of the region under consideration and L_p is the characteristic length over which minority carriers travel before they recombine. The higher the W_{BSF}/L_p ratio, the more minority carriers recombine before they reach the surface. Therefore, surface recombination contributes less to J_0 for higher W_{BSF}/L_p ratios. In other words, electrical opacity explains why $J_0 \cdot [(L_p N_{D,BSF})/qD_p n_i^2]$ does no depend on $[S_W L_p]/[D_p]$ for high W_{BSF}/L_p ratios. Conversely, electrical transparency explains why $[(L_p N_{D,BSF})/qD_p n_i^2]$ is strongly dependent on $[S_W L_p]/[D_p]$ for low W_{BSF}/L_p ratios.

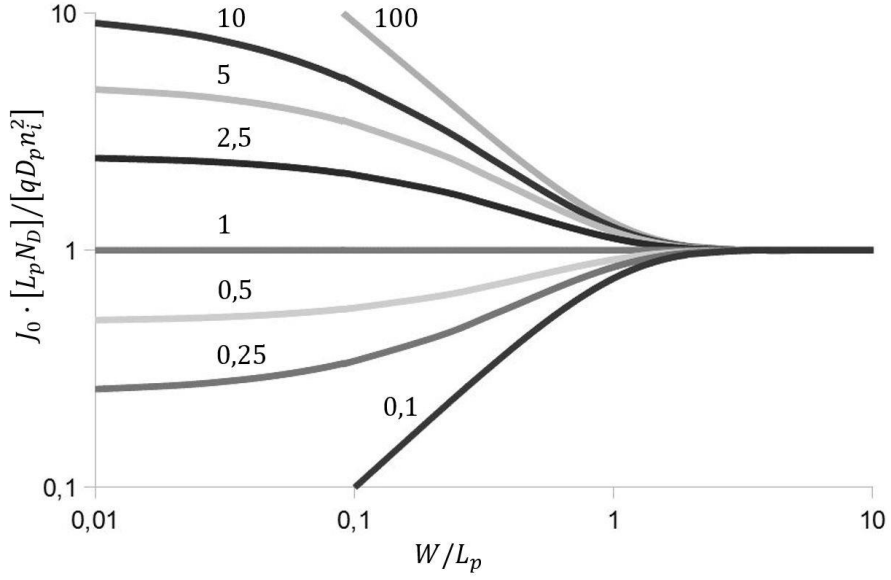

Figure 2.1.3.2. Intuitive representation of the saturation current density of a quasi neutral region, for example a BSF or emitter region, in a silicon solar cell; adapted from [Verlinden 2010]. $J_0 \cdot [(L_p N_{D,BSF})/qD_p n_i^2]$ is plotted as a function of W_{BSF}/L_p, for various values of $[S_W L_p]/[D_p]$. The number above each curves indicates the $[S_W L_p]/[D_p]$ value corresponding to that particular curve.

The last dimensional number, $[S_W L_p]/[D_p]$, is a measure of the magnitude of the effective surface recombination velocity S_W, normalized to a measure for the importance of bulk recombination and the ease at which minority carriers traverse through the bulk: L_p/D_p. In essence, $[S_W L_p]/[D_p]$ is a figure of merit that determines whether or not it is useful to shield minority carriers from a recombining surface using a particular junction. When $[S_W L_p]/[D_p]$ is larger than one, surface recombination currents dominate J_0 and as a result, J_0 can be reduced by further shielding minority carriers from the surface by making the junction thicker; i.e. J_0 decreases with increasing W_{BSF}/L_p in this case. On the other hand when $[S_W L_p]/[D_p]$ is smaller than one, bulk recombination currents are dominating and J_0 can be reduced by reducing the junction's thickness. The peculiar case of $[S_W L_p]/[D_p]$ being equal to one corresponds to the case when J_0 is independent of W_{BSF}/L_p.

Apart from the dimensionless numbers, also the pre-factor $qD_p n_i^2/L_p N_{D,BSF}$ on the right-hand side of Equation 2.1.3.2 influences J_0. Naively, one could think that J_0 could be made arbitrarily small by increasing the doping level $N_{D,BSF}$ to an arbitrarily high value. Unfortunately the hole diffusion length L_p and especially the intrinsic concentration n_i are adversely affected as $N_{D,BSF}$ becomes large. In particular, L_p decreases due to increased Auger recombination, which increases proportional to $N_{D,BSF}^2$ in the highly doped BSF. Also, n_i increases dramatically at high doping levels due to effective bandgap narrowing, which is for example discussed in [Lanyon 1979, Slotboom 1976].

As a result of these various competing factors, J_0 is a complex function of the junction shape, surface concentration, and surface passivation. In the context of planning experiments in the field of contacted or passivated diffused junctions, the J_0 contours in [King 1990] can be used as a guidance.

2.2. QSSPC measurements

In quasi steady state photoconductance (QSSPC) measurements [Sinton 1996], the photoconductance of a wafer is measured using inductive coupling between a coil and the wafer. From the difference between conductance measurements in the dark and under illumination, the wafer's photoconductance is obtained. During a photoconductance measurement under illumination, light intensity is measured using a photodiode. Using a calibration factor, the photoconductance is translated into the photoconductivity, and using the electron and hole mobility, the photoconductivity is translated into the excess carrier concentration. Also, light intensity is translated into a generation rate using optical modeling. The generation rate and excess carrier concentration are used to define an effective lifetime, which is a figure of merit for minority carrier recombination.

In this chapter, we discuss the basics of QSSPC measurements. Selected main features of a QSSPC lifetime tester are schematically drawn in Figure 2.2.1.

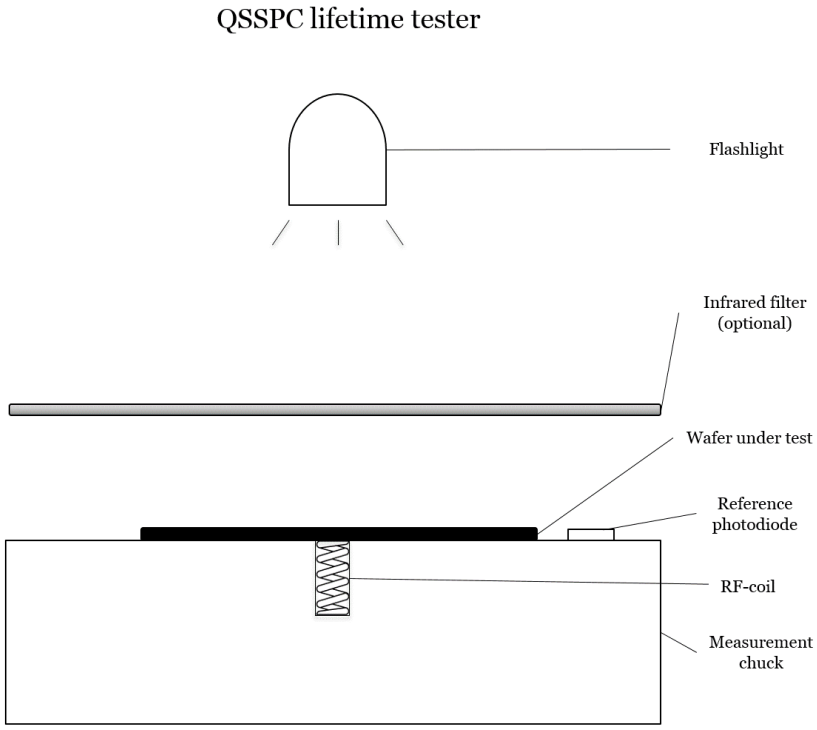

Figure 2.2.1. Schematic representation of selected main features of a QSSPC lifetime tester.

A QSSPC lifetime tester comprises a measurement chuck housing an RF-coil which is inductively coupled to the sample under test. The coil induces eddy currents in the sample under test, and the resulting Ohmic losses result in a measurable signal from which the conductance of the sample under test is obtained. More specifically, typical operating frequencies are in the range of 10s of MHz: operating frequencies of 8 to 10 MHz are reported in [Sinton 1996b], operating frequencies of 11 MHz are reported in [King 1990], and operating frequencies of 25 MHz are reported in [Fischer 2003]. In the present dissertation, an operating frequency of 11 MHz is taken as a typical operating frequency for the purpose of qualitative reasoning. In [Sinton 1996b], the coil is described as being in a bridge (presumably a Wheatstone Bridge). The electrical circuitry which comprises the coil yields a signal which is proportional to the conductance of the sample under test [King 1990]. Therefore, with an appropriate calibration factor, the RF-coil can be used to probe the conductance of a sample under test which is put on the measurement chuck. By measuring a sample's conductance under illumination and in the dark, the sample's photo conductance is obtained. Sample illumination is generally done using a flashlight. High-powered LEDs that emit light in the infrared range, for example light with a wavelength of 875 nm, can be used as an alternative for the flashlight [Fischer 2003, p. 56]. The light intensity is measured concurrently using a reference photodiode. Optionally, an infrared filter can be used to filter out short wavelength light from the flashlight's spectrum. Infrared light is only weakly absorbed in silicon such that the use of infrared light for carrier excitation ensures a uniform generation rate.

A uniform generation rate is often desirable in QSSPC measurements because a uniform generation rate helps to obtain uniform excess carrier densities throughout the wafer's quasi neutral bulk. Uniform excess carrier densities throughout the quasi neutral bulk make the measurement interpretation easier. This can be intuitively understood from the fact that only in the case of uniform excess carrier densities, the measured injection level equals *the* injection level. In addition, the various recombination current components are strongly injection level dependent such that the occurrence of injection level inhomogeneity complicates the measurement interpretation. As a result, uniform bulk injection levels are highly desirable.

In the remainder of this section, we explore the physics of photoconductance-based effective lifetime measurements in detail. First, we discuss the physics of photoconductance measurements per se. Then, we consider the transfer of light and dark conductance to photoconductance in detail. We proceed to discuss the concept of "effective lifetime". Finally, we discuss how the effective lifetime is extracted from photoconductance measurements.

2.2.1. Conductance measurements

In a QSSPC measurement, the photoconductance is obtained through a sequence of two conductance measurements. First, the conductance under dark conditions S_0 is measured, and subsequently the conductance under uniform illumination S_L is measured. From the difference between light and dark conductance, the measured photoconductivity is calculated. Then, the average injection level is calculated from the average photoconductivity. By concurrently measuring the generation rate using a reference photodiode, the effective lifetime is obtained. These different steps are now considered one-by-one.

Consider a wafer's conductivity σ. It is related to the excess carrier density as:

$$\sigma = q(\mu_e n + \mu_p p), \tag{2.2.1.1}$$

in which q is elementary charge, μ_e is electron mobility, n is electron concentration, μ_p is hole mobility, and p is hole concentration.

For the sake of clearness, we mention that the derivations in this section should not be confused with the discussion of quasi neutrality in section 2.1.2. In this section, we treat current flow under the influence of externally applied electric fields. Conversely, in our treatment of quasi neutrality in section 2.1.2, we discuss the effect of interactions between electrons and holes on diffusion currents in "quasi neutral regions". The only electric field considered in section 2.1.2 is the electric field that arises from interactions between electrons and holes in quasi neutral regions.

A blanket wafer has uniform properties throughout the wafer plane, but its properties may vary in the direction perpendicular to the wafer plane. The position in the wafer is described by an associated Cartesian coordinate system. The x-axis is aligned with the direction perpendicular to the wafer plane and perpendicular in-plane directions are aligned with the y- and z- axis. The wafer and the associated coordinate system are shown in Figure 2.2.1.1.

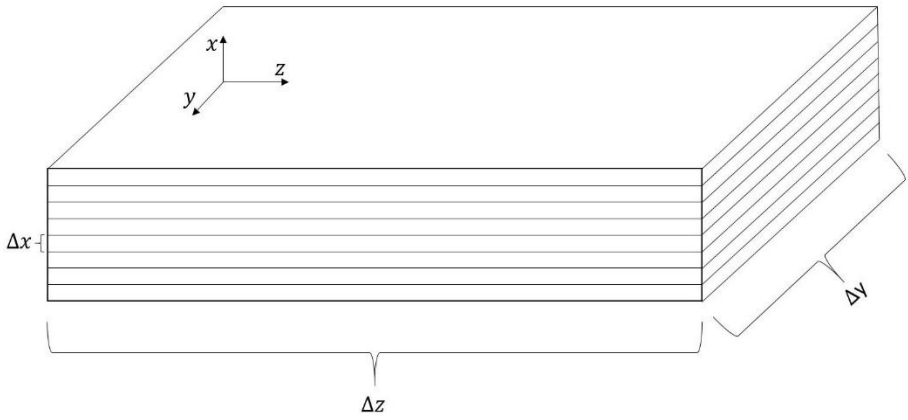

Figure 2.2.1.1. A silicon wafer piece with lateral dimensions Δy and Δz, subdivided in thin wafer slices parallel to the wafer plane with thickness Δx.

We now consider the conductance of a thin wafer slice parallel to the wafer plane, with in-plane dimensions Δy and Δz in the y and z directions respectively, and with thickness Δx. Its conductance in the y-and z-directions is:

$$\Delta S_y = \sigma \frac{\Delta x \Delta z}{\Delta y}, \qquad \Delta S_z = \sigma \frac{\Delta x \Delta y}{\Delta z} \tag{2.2.1.2}$$

with ΔS_y and ΔS_z the slap's conductance in the y- and z- directions, respectively. From now, we focus solely on the conductance in the y-direction, with the conductance in the z direction found by interchange of the y and z labels. In fact, by rotational symmetry in the wafer plane, the exact choice of coordinate axis is arbitrary for a blanket structure and the y-axis can denote any direction in the wafer plane.

Now consider an in-plane conductance measurement on a wafer, and assume that the measurement is set-up such that current transport perpendicular to the wafer plane is of no importance for the conductance measurement. This is the case in a QSSPC measurement, in which the eddy currents used to probe the wafer's conductance in the wafer plane.

A wafer piece can be thought of as consisting of a stack of many thin slices, which all contribute in parallel to the wafer's in-plane conductance. When the conductance of all thin wafer slices spanning the wafer's thickness is summed, an approximation for the wafer piece's in-plane conductance is obtained:

$$S_y = \sum_i \sigma_i \frac{\Delta z}{\Delta y} \Delta x_i, \tag{2.2.1.3}$$

in which S_y is the wafer's conductance in the y-direction, i is an index that distinguishes different wafer slices, Δx_i is the thickness of the ith wafer slice, and σ_i is the conductivity in the middle of the ith wafer slice. Equation 2.2.1.3 is a

Riemann sum. In the limit of infinitesimal Δx_i, it becomes an integral for wafer's the in-plane conductance:

$$S_y = \int_W \sigma \frac{\Delta z}{\Delta y} dx, \tag{2.2.1.4}$$

with W wafer thickness. Because Δy and Δz are constants, they can be moved out of the integral:

$$S_y = \frac{\Delta z}{\Delta y} \int_W \sigma \, dx. \tag{2.2.1.5}$$

From the mean value theorem of integral calculus, there exists a number σ_a such that:

$$\int_W \sigma \, dx = W \sigma_a, \tag{2.2.1.6}$$

in which σ_a is the mean value of σ over the wafer thickness W. From inspection of Equations 2.2.1.5 and 2.2.1.6, a measurement of a wafer's in-plane conductance is equivalent to a measurement of the average conductivity over the wafer's thickness σ_a.

2.2.2. Photoconductivity

Now consider a wafer which is illuminated with sufficiently energetic light such that excess minority carriers are generated, i.e. there is a non-zero excess carrier density. The electron and hole concentrations can be written as the sum of two components: their equilibrium concentration and an excess carrier density:

$$\sigma = \sigma_0 + \Delta\sigma = q\left(\mu_e n_0 + \mu_p p_0\right) + q\left(\mu_e \Delta n + \mu_p \Delta p\right), \tag{2.2.2.1}$$

in which σ_0 is the dark conductivity, $\Delta\sigma$ is photoconductivity, n_0 is the equilibrium electron concentration, p_0 is the equilibrium hole concentration, Δn is the excess electron concentration, and Δp is the excess hole concentration. Combining Equations 2.2.1.6 and 2.2.2.1 yields:

$$\sigma_a = \frac{1}{W} \int_W \sigma_0 dx + \frac{1}{W} \int_W q\left(\mu_e \Delta n + \mu_p \Delta p\right) dx, \tag{2.2.2.2}$$

or:

$$\Delta\sigma_a = \frac{1}{W} \int_W q\left(\mu_e \Delta n + \mu_p \Delta p\right) dx. \tag{2.2.2.3}$$

That is:

$$\Delta\sigma_a = \sigma_a - \frac{1}{W} \int_W \sigma_0 \, dx. \tag{2.2.2.4}$$

Applying the mean value theorem of integral calculus to Equation 2.2.2.3, $\Delta\sigma_a$ can be interpreted as the mean value of $\Delta\sigma$ over the wafer thickness.

2.2.3. Excess carrier density

The integral in Equation 2.2.2.3 runs over the wafer's thickness. For a typical photoconductance measurement on a blanket test wafer, three regions can be typically discerned in the wafer: quasi neutral bulk, diffused regions, and intermediary regions in which band bending occurs. This is the structure we will be considering in this section and we will show that only the quasi neutral bulk contributes to photoconductance. Other cases (e.g. a uniform wafer with no diffused regions) are readily found by analogy.

To discuss why only the quasi neutral bulk has a contribution to photoconductance, we focus on n-type samples with p^+ diffusions on both sides. For simplicity, we assume constant quasi Fermi level splitting, quasi neutrality ($\Delta n = \Delta p$) and we assume that in all quasi neutral regions, the injection level is much higher than the respective equilibrium minority carrier concentrations.

For constant quasi Fermi level splitting across the space charge region between emitter and bulk, the following equality holds:

$$\Delta p_{bulk}\left(N_{D,bulk} + \Delta p_{bulk}\right) = \Delta p_{emitter}\left(N_{A,emitter} + \Delta p_{emitter}\right), \qquad (2.2.3.1)$$

in which the subscripts "bulk" and "emitter" denote the quantities at the bulk and emitter side of the space charge region between bulk and emitter, respectively; N_D is the donor concentration in the bulk and N_A is the acceptor concentration in the emitter. Typically, the doping level in diffused regions is several orders of magnitude higher than the doping level in the quasi neutral bulk, such that Equation 2.2.3.1 requires $N_{A,emitter} \gg \Delta p_{emitter}$. Reordering then yields:

$$\Delta p_{emitter} = \Delta p_{bulk} \frac{N_{D,bulk} + \Delta p_{bulk}}{N_{A,emitter}}. \qquad (2.2.3.2)$$

Therefore, $\Delta p_{emitter}$ is orders of magnitude smaller than Δp_{bulk}, as long as $\Delta p_{bulk} \ll N_{A,emitter}$, which is definitely the case in the relevant injection level range for common terrestrial silicon solar cells operating at 1 sun illumination. Because of this, and because the emitter is much thinner than the quasi neutral bulk region in a silicon solar cell (e.g. 1 µm versus 150µm), the emitter's photoconductance is negligible compared to the bulk photoconductance. Also, since the space charge regions are less than 1 micrometer wide for typical solar wafers, and since the excess carrier concentration in the space charge region is definitely not bigger than in the quasi neutral bulk, the photoconductance of space charge regions is negligible compared to the bulk photoconductance. In addition, because space charge region thickness and the thickness of diffused regions are much smaller than wafer thickness, the quasi neutral region thickness is approximately equal to the wafer thickness. Therefore, Equation 2.2.2.3 can be written as:

$$\Delta\sigma_a = \frac{1}{W_b}\int_{W_b} q\left(\mu_e \Delta n_b + \mu_p \Delta p_b\right) dx \,, \qquad (2.2.3.3)$$

in which the subscript "b" denotes the respective quantity in the quasi neutral bulk. From now on, we omit the subscript b for ease of notation.

In the quasi neutral wafer bulk, $\Delta n \approx \Delta p$. As such, and approximating μ_e and μ_p as constants, Equation 2.2.3.3 becomes:

$$\Delta\sigma_a = q\left(\mu_e + \mu_p\right)\frac{1}{W}\int_W \Delta p dx. \qquad (2.2.3.4)$$

Note that the subscript "b" has been omitted. Using the mean value theorem of integral calculus, there exists a value Δp_a such that:

$$\Delta p_a = \frac{1}{W}\int_W \Delta p dx, \qquad (2.2.3.5)$$

with Δp_a the mean value of Δp over the quasi neutral region thickness W. Combining Equations 2.2.3.4 and 2.2.3.5 yields:

$$\Delta\sigma_a = q\left(\mu_e + \mu_p\right)\Delta p_a. \qquad (2.2.3.6)$$

Therefore, the measured injection level in a QSSPC measurement is the average injection level in the quasi neutral bulk.

Note that we have made a number of assumptions regarding the structure of the device under test which are valid for the structures investigated in the present dissertation. For more exotic test structures, more arcane contributions to photoconductance might be important. Examples of such rather arcane contributions to photoconductance are for example volume trapping, photoconductance from p-n junctions, and photoconductance from charged surfaces, as discussed for example in [Fischer 2003, p. 64-66].

2.2.4. Effective lifetime

Consider an n-type silicon wafer during a steady state measurement of the in-plane photoconductance. A wafer piece is depicted in Figure 2.2.4.1. It spans the entire wafer thickness and distances Δx and Δy in the in-plane x and y directions, respectively. One in-plane dimension is suppressed in Figure 2.2.4.1.

We focus on the behavior of minority carriers (holes) in the quasi neutral bulk and assume that the majority carrier concentration is determined by the minority carrier concentration and the requirement of quasi neutrality. An approximate mass balance yields the following approximate equation:

$$q\int_W G\, dz\Delta x\Delta y - q\int_W R_B\, dz\Delta x\Delta y + \int_W J_x\, dz\Delta y - \int_W J_{x+dx}\, dz\Delta y$$

$$+\int_W J_y\,dz\Delta x-\int_W J_{y+dy}\,dz\Delta x-J_{S,1}\Delta x\Delta y-J_{S,2}\Delta x\Delta y=q\int_W\frac{\delta p}{\delta t}dz\Delta x\Delta y,$$

(2.2.4.1)

in which q is elementary charge, G is the volumetric generation rate, R_B is the bulk recombination rate, W is cell thickness, dx is an elementary distance in the wafer plane, dy is an elementary distance in the wafer plane in a direction perpendicular to x, J_x is the net current density flowing into the wafer region of size dx on the left side of the respective region (low x), J_{x+dx} is the net current flowing out of on the right side of the respective region (high x), $J_{S,1}$ is the recombination current density at the top wafer surface, $J_{S,2}$ is the recombination current density at the lower wafer surface, p is the minority carrier concentration, and t is time. J_y and J_{y+dy} are defined analogously to J_x and J_{x+dx}, respectively.

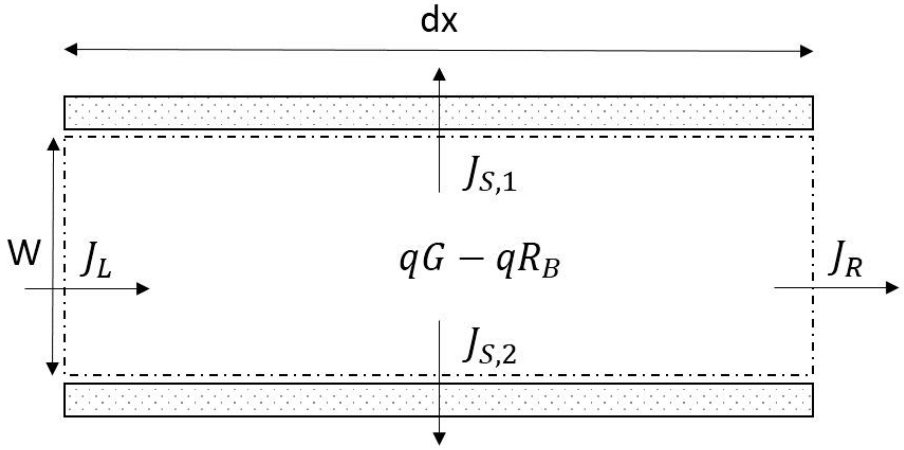

Figure 2.2.4.1. Volume element in a silicon wafer spanning the entire thickness of its quasi neutral bulk. Its dimensions in the x and y directions are Δx and Δy, respectively. One dimension (the y-direction out of the picture's plane) is suppressed.

Equation 2.2.4.1 is approximate in the sense that $\int_W\frac{\delta p}{\delta t}dz$, $\int_W G\,dz$, $\int_W R_B\,dz$, $J_{S,1}$, and $J_{S,2}$ are approximated as constants over the area $\Delta x\Delta y$. Equation 2.2.4.1 is also approximate in the sense that $\int_W J_x\,dz$ and $\int_W J_{x+dx}\,dz$ are assumed to be constant over the interval Δy, and that $\int_W J_y\,dz$ and $\int_W J_{y+dy}\,dz$ are assumed to be constant over the interval Δx.

We now use the mean value theorem of integral calculus to replace all integrals by their average values over W. The subscript "a" is used to denote an average quantity over W:

$$qG_aW\Delta x\Delta y-qR_{a,B}W\Delta x\Delta y+J_{a,x}W\Delta y-J_{a,x+dx}W\Delta y$$

$$+J_{a,y}W\Delta x - J_{a,y+dy}W\Delta x - J_{S,1}\Delta x\Delta y - J_{S,2}\Delta x\Delta y = q\frac{\delta p_a}{\delta t}W\Delta x\Delta y. \quad (2.2.4.2)$$

Division of Equation 2.2.4.2 by $W\Delta x\Delta y$ yields:

$$qG_a - qR_{a,B} - \frac{\Delta J_{a,x}}{\Delta x} - \frac{\Delta J_{a,y}}{\Delta y} - \frac{J_{S,1}+J_{S,2}}{W} = q\frac{\delta p_a}{\delta t}, \quad (2.2.4.3)$$

in which $R_{a,B}$ is the average bulk recombination rate and in which we used the following notation: $\Delta J_{a,x} = J_{a,x+dx} - J_{a,x}$, and $\Delta J_{a,y} = J_{a,y+dy} - J_{a,y}$. Now take the limit for Δx and Δy going to zero such that the finite differences in Equation 2.2.4.3 become differentials, and the expression becomes exact rather than approximate:

$$qG_a - qR_{a,B} - \frac{\delta J_{a,x}}{\delta x} - \frac{\delta J_{a,y}}{\delta y} - \frac{J_{S,1}+J_{S,2}}{W} = q\frac{\delta p_a}{\delta t}. \quad (2.2.4.4)$$

By Equation 2.2.4.4, $R_{a,B}$ can be expressed in terms of the excess carrier concentration and bulk lifetime:

$$R_{a,B} = \frac{1}{w}\int_W \frac{\Delta p}{\tau_b}dz = \left[\frac{\Delta p}{\tau_b}\right]_a \approx \frac{\Delta p_a}{\tau_b}, \quad (2.2.4.5)$$

in which the last equality holds true when τ_b is constant over the thickness of the wafer's quasi neutral bulk.

With Equation 2.2.4.5, and when we write the surface recombination currents in terms of the excess carrier concentration and effective surface recombination velocities at the surfaces, Equation 2.2.4.4 can be written as:

$$qG_a - \frac{\delta J_{a,x}}{\delta x} - \frac{\delta J_{a,y}}{\delta y} - q\frac{\Delta p_a}{\tau_b} - q\frac{S_1\Delta p_1 + S_2\Delta p_2}{W} = q\frac{\delta p_a}{\delta t}, \quad (2.2.4.6)$$

in which S_1 and S_2 are the effective surface recombination velocities of surfaces 1 and 2, respectively, and Δp_1 and Δp_2 are excess carrier concentrations at surfaces 1 and 2, respectively.

We now introduce the effective lifetime τ_{eff}:

$$\frac{1}{\tau_{eff}} = \frac{1}{\tau_b} + \frac{S_1\frac{\Delta p_1}{\Delta p_a} + S_2\frac{\Delta p_2}{\Delta p_a}}{W}, \quad (2.2.4.7)$$

and introduce the notation:

$$\nabla J_a = \frac{\delta J_{a,x}}{\delta x} + \frac{\delta J_{a,y}}{\delta y}. \quad (2.2.4.8)$$

Equation 2.2.4.6 then becomes:

$$qG_a - \nabla J_a - q\frac{\Delta p_a}{\tau_{eff}} = q\frac{\delta p_a}{\delta t}, \quad (2.2.4.9)$$

which has the same form as Equation 2.1.2.19, with $\Delta p_a \tau_{eff}^{-1}$ identified as the recombination rate. The only differences are the suppression of one spatial dimension, bulk lifetime is substituted by effective lifetime and local quantities are substituted by average quantities over the wafer thickness. In the next section, the

extraction of effective lifetimes τ_{eff} from photoconductance measurements is discussed in detail.

2.2.5. Effective lifetime measurements.

By reordering the different terms, Equation 2.2.4.9 can be rewritten as:

$$q\frac{\delta p_a}{\delta t} = -\nabla J_a + q\left[G_a - \frac{\Delta p_a}{\tau_{eff}}\right]. \quad (2.2.5.1)$$

We assume that ∇J_a is negligible compared to the net recombination term. The assumption of negligible ∇J_a is met when electric fields are slowly varying or zero and when minority carrier concentrations vary linearly or are constant in space.

The requirement of slowly varying or zero electric fields holds true because it follows from the assumption of quasi neutrality which implies very small electric fields in the semiconductor bulk. The diffusion current is zero in the wafer plane since the average carrier concentration is constant in a blanket test structure due to translational symmetry. Also, the electric field used in a radio-wave detected photoconductance measurement to probe the wafer is the only electric field present in the wafer's quasi neutral bulk during the measurement. This electric field oscillates with a frequency of around 11 MHz [King 1990], that is the timescale in which the field oscillates is about $0.1\,\mu s$. The timescales of QSSPC measurements are much larger than this very short timescale. Therefore, the effect of this field is found from its average value over the timescale of a QSSPC measurement, which is zero.

For negligible ∇J_a, and using that the time-rate of change of the minority carrier concentration equals the time-rate of change of the excess minority carrier density, Equation 2.2.5.1 becomes:

$$\frac{1}{\tau_{eff}} = \frac{G_a}{\Delta p_a} - \frac{1}{\Delta p_a}\frac{\delta \Delta p_a}{\delta t}. \quad (2.2.5.2)$$

Note that by Equation 2.2.4.7, τ_{eff} is a parameter which describes all recombination processes in the wafer. Depending on the time rate of change of the excess minority carrier density compared to the generation rate, photoconductance measurements fall in different categories. First, when τ_{eff} is much longer than the characteristic decay time of the generation term, the photoconductance measurement is said to be done in transient mode. Second, when the characteristic decay time of the generation term is much longer than minority carrier lifetime, the photoconductance measurement is done in (quasi) steady state mode (QSSPC). Finally, in the in-between case, the photoconductance measurement is said to be done in the generalized mode.

We proceed to summarize how effective lifetimes are extracted from photoconductance measurements in different cases. In this dissertation, the focus lies on steady state photoconductance measurements (QSSPC), but for the merit

of completeness, we shortly discuss the transient and generalized case [Nagel 1999] as well.

Transient measurements

When the generation term decays much faster than the characteristic time in which minority carrier concentration changes, the generation term is zero during the effective lifetime measurement such that only the second term on the right hand side of Equation 2.2.5.2 is important such that:

$$\tau_{eff} = -\Delta p_a \left[\frac{\delta \Delta p_a}{\delta t}\right]^{-1}. \quad (2.2.5.3)$$

The effective lifetime obtained from transient photoconductance measurements is discussed in more detail in [Fischer 2003, p. 59].

Steady state measurements (QSSPC)

In a steady state photoconductance measurements, changes in excess minority carrier density are assumed to occur in much faster time scales than changes in the generation term. Therefore, the first term on the right hand side of Equation 2.2.5.2 is dominating in the steady state regime:

$$\tau_{eff} = \frac{\Delta p_a}{G}. \quad (2.2.5.4)$$

Generalized measurements

Generalized effective lifetimes are found directly from Equation 2.2.5.2, i.e. no assumption is made about the timescale of the effective generation rate and the transient excess carrier concentration:

$$\frac{1}{\tau_{eff}} = \frac{G}{\Delta p_a} - \frac{1}{\Delta p_a}\frac{\delta \Delta p_a}{\delta t}. \quad (2.2.5.5)$$

In the present dissertation, we focus on steady state measurements (QSSPC).

2.3. Minority carrier concentration over wafer thickness

In section 2.2, we showed that the measured minority carrier concentration in a photoconductance measurement on a blanket test structure is the average minority carrier concentration over the wafer thickness. In this section, we derive the minority carrier variations over the thickness of the quasi neutral bulk in a planar test structure. The derivation is done for a constant generation rate, and bulk lifetime is assumed to be constant with injection level. The boundary conditions are written in terms of effective surface recombination velocities.

Minority carrier concentrations in a wafer's quasi neutral bulk under illumination are found from Equation 2.1.2.14; which we repeat here for the steady-state case:

$$-D_p \nabla^2 p + G - R = 0, \tag{2.3.1}$$

in which $D_p = \mu_p \, kT/q$. We describe bulk recombination with an effective lifetime τ_b, we identify the minority carrier diffusion length $L_D = \sqrt{D_p \tau_b}$, and we use that in a planar test structure, translational symmetry causes the minority carrier concentration to change in only one dimension (i.e. perpendicular to the wafer plane). This yields:

$$-L_D^2 \frac{\mathrm{d}^2 p}{dx^2} - p + p_0 + \tau_b G = 0. \tag{2.3.2}$$

Solutions of this equation are of the form:

$$p = C_1 sinh\left(\frac{x}{L_D}\right) + C_2 cosh\left(\frac{x}{L_D}\right) + p_0 + \tau G, \tag{2.3.3}$$

in which C_1 and C_2 are constants which are found by taking the boundary conditions for Equation 2.3.2 into consideration. We define the x-coordinate to have its origin at the front surface, and to have the value W at the back surface, with W wafer thickness.

As x can take on values from 0 to W, Equation 2.3.3. is a constant in the limit of $L_D \gg W$ (for $L_D \gg W$, the argument of the $sinh$ and $cosh$ terms is zero, and $\sinh(0) = 0$ and $\cosh(0) = 1$). However, as we shall see in a moment, very large surface recombination currents can cause significant excess carrier density variations, even when the bulk diffusion length is much bigger than wafer thickness. The influence of surface recombination currents manifests itself through the prefactors C_1 and C_2 and is incorporated via appropriate boundary conditions.

In the chosen coordinate system, the boundary conditions are:

$$S_1[p - p_0]_{x=0} = D_p \left[\frac{dp}{dx}\right]_{x=0}, \tag{2.3.4}$$

$$S_2[p - p_0]_{x=W} = -D_p \left[\frac{dp}{dx}\right]_{x=W}, \tag{2.3.5}$$

in which S_1 and S_2 are effective surface recombination velocities at the front and back surfaces, respectively. With these boundary conditions, the constants in the solution of Equation 2.3.2 are found to be:

$$C_1 = \tau G S_1 \frac{L_D}{D_p}\left[1 - \frac{S_2+S_1\cosh\left(\frac{W}{L_D}\right)+S_1S_2\frac{L_D}{D_p}\sinh(\frac{W}{L_D})}{(S_1+S_2)\cosh\left(\frac{W}{L_D}\right)+\left(\frac{D_p}{L_D}+S_1S_2\frac{L_D}{D_p}\right)\sinh\left(\frac{W}{L_D}\right)}\right], \tag{2.3.6}$$

$$C_2 = -\tau G \frac{S_2+S_1\cosh\left(\frac{W}{L_D}\right)+S_1S_2\frac{L_D}{D_p}\sinh(\frac{W}{L_D})}{(S_1+S_2)\cosh\left(\frac{W}{L_D}\right)+\left(\frac{D_p}{L_D}+S_1S_2\frac{L_D}{D_p}\right)\sinh\left(\frac{W}{L_D}\right)}. \tag{2.3.7}$$

When $S_1 = S_2$, the boundary value problem 'Equation 2.3.2, 2.3.4, 2.3.5' is symmetric around the center of the wafer. Therefore, the solution of the boundary value problem, Equation 2.3.3, is mirror symmetric around the center of the wafer as well. This case is shown in Figure 2.3.1.

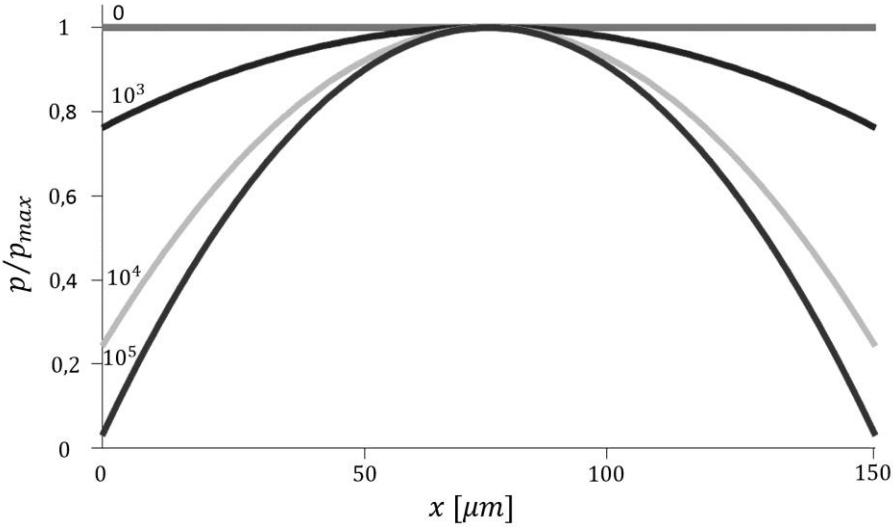

Figure 2.3.1. Normalized minority carrier concentration as a function of position (in the direction perpendicular to the wafer plane), for a wafer thickness of 150 µm, and for symmetric structures; i.e. structures in which $S_1 = S_2$. The value of S_1 and S_2 used in each simulation is indicated above each curve.

In Figure 2.3.2, we show the normalized minority carrier concentration as a function of position (in the direction perpendicular to the wafer plane), for asymmetric structures; i.e. for structures in which $S_1 = 0$ and for which S_2 has the value indicated next to each curve. Note that in the case shown in Figure 2.3.2, there is no symmetry associated with the minority carrier concentration profile.

By comparison of figures 2.3.1 and 2.3.2, the minority carrier concentration is less constant in the asymmetric case compared to the symmetric case. Otherwise stated: the normalized minority carrier concentration is lower near the recombining

surface in the asymmetric compared to the symmetric case. This observation is the underlying reason for a well-known mantra in the field of QSSPC measurements: symmetric test structures are preferable over asymmetric test structures because the minority carrier concentration is more constant for symmetric test structures.

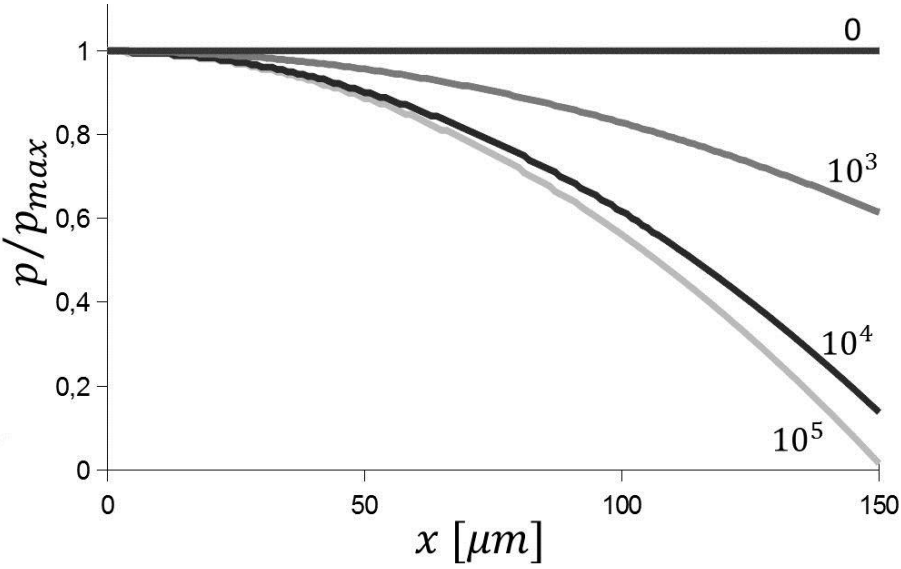

Figure 2.3.2. Normalized minority carrier concentration as a function of position (in the direction perpendicular to the wafer plane), for asymmetric structures in which $S_1 = 0$ and S_2 has the value indicated next to each curve.

Figures 2.3.1 and 2.3.2 are plots of Equation 2.3.3 with C_1 and C_2 given by Equations 2.3.6 and 2.3.7, respectively. In the simulations, the following parameters were used: $W = 150\,\mu m$, $G = 1.67 \cdot 10^{19} cm^{-3}$ (ca. 1 sun), $D_p = 12 cm^2 \cdot s^{-1}$, $p_0 = 9.4 \cdot 10^4 cm^{-3}$, $L_D = 1000\,\mu m$. S_1 and S_2 were equal for the simulations shown in Figure 2.3.1 and are shown next to each curve. In Figure 2.3.2, $S_1 = 0$ and S_2 was varied, wich each value of S_2 shown next to the corresponding curve.

Note that in all simulations, the bulk diffusion length $\mathrm{L_D}$ was kept constant and was always much larger than the wafer thickness $\mathrm{L_D}$; $L_D = 1000\ \mu\mathrm{m}$ and $W = 150\ \mu\mathrm{m}$, respectively. As we will show in sections 3.5 and 3.6, significant excess carrier variations throughout the wafer's quasi neutral bulk have detrimental effects on contact recombination current measurements done using the test structure developed in the present dissertation, and should therefore be avoided.

In conclusion, the minority carrier concentration can vary appreciably over the wafer thickness, even when the bulk diffusion length is much larger than the wafer

thickness. However, for $L_D \gg W$ and $S \approx 0$, the minority carrier concentration is approximately constant over a wafer's thickness.

3. Contact recombination current measurements

In this chapter's first section, an overview is given of contemporary methods for contact recombination current measurements, and it is argued why the development of a novel method for contact recombination current measurements is desirable. This novel method for contact recombination current measurements is subsequently described in detail. We cover the basic physics that underlies the method and we discuss design rules, error analysis, parasitic effects, and experimental results. The focus is on test structures based on lattices of point contacts on otherwise passivated wafers. Such a lattice of point contacts is shown in Figure 3.1. At the end of this chapter, alternative test structure embodiments are described.

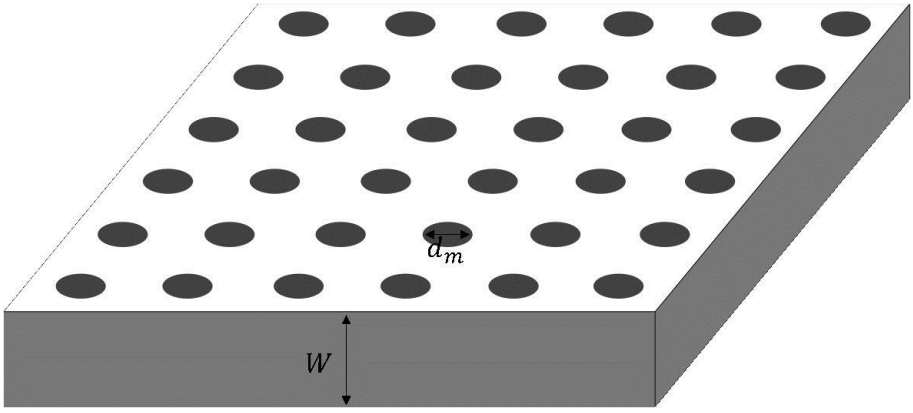

Figure 3.1. Simple square lattice of point contacts on an otherwise passivated wafer.

Our test structure is based on photoconductance measurements on different areas with different contact fractions. Each area is a simple square lattice of point contacts on an otherwise passivated wafer (figure 3.1.). In order to perform accurate contact recombination current measurements using our test structure, a number of design rules must be followed. These design rules, summarized in Table 3.1, are formulated to ensure the elimination of two types of parasitic effects.

The first parasitic effect type is related to current flow through the point contacts instead of through the semiconductor, and causes underestimations of contact saturation current densities. It is discussed in section 3.4. The transfer length – contact diameter ratio, L_T / d_m, is the primary figure of merit that determines whether parasitic current flow through point contacts affects the contact

recombination current measurement. When L_T is much bigger than d_m, current does not flow through the point contacts and the parasitic effect is avoided.

Parasitic Effect	Discussed in section	Figure of merit	Design rule
Current Flow Through Point Contacts	3.4	L_T/d_m	$L_T/d_m \gg 1$
In-Plane Injection Level Variations (Contacted Areas)	3.5	L_m/d_m	$L_m/d_m \gg 1$
In-Plane Injection Level Variations (Passivated Areas)	3.5	L_p/d_p	$L_p/d_p \gg 1$
Out-of-plane injection level variations	3.6	L_D/W S_{eff}	$L_D/W \gg 1$ $S_{eff} \approx 0$

Table 3.1. Summary of design rules for contact recombination current measurement test structures.

The second type of parasitic effect is related to injection level variations, and is discussed in sections 3.5 and 3.6.

Injection level variations in the wafer plane are discussed in section 3.5 and a distinction can be made between in-plane injection level variations in contacted areas and in-plane injection level variations in passivated areas. In-plane injection level variations in passivated areas can be avoided by making the characteristic size of passivated areas, d_p, much smaller than the effective diffusion length in passivated areas, L_p. Similarly, in-plane injection level variations in contacted areas can be avoided by making the characteristic size of contacted areas, d_m, much smaller than the effective diffusion length of contacted areas, L_m.

Out-of plane injection level variations are discussed in section 3.6 in the context of our test structure. In addition, they have been discussed in section 2.3 in a general context. In order to avoid out-of-plane injection level variations, two conditions have to be met. First, the bulk diffusion length L_D must be much bigger than the wafer thickness W. Second, effective surface recombination velocities must be small.

In sections 3.7 to 3.9, we provide additional guidance for the design of photoconductance-based test structures for contact recombination measurements.

In section 3.7, we discuss the importance of using the correct doping level when using our test structure to extract contact saturation current densities, especially when the arbitrary injection level technique (Equation 3.2.2.7) is used.

In section 3.8, we discuss the effect of non-unit ideality factors on extracted saturation current densities. This includes a proposed method for fitting the extracted contact recombination current using a two-diode model.

In section 3.9, we discuss the effect of using incorrect contact fractions on extracted saturation current densities, with a focus on errors in the point contact diameter, which was particularly difficult to control in the lithography-defined test structures used in the present dissertation.

In section 3.10, we discuss alternative test structure embodiments. In some experimental settings, the use of point contact lattice- based test structures may be inconvenient or downright unfeasible. Therefore, we discuss the design of test structures featuring line-shaped or circle-shaped contacts. The use of these test structures in practice would require the development of new tools though, and is therefore beyond the scope of the present dissertation.

3.1. Methods for the characterization of contact recombination currents[1]

There exists a variety of methods for the extraction of contact recombination currents. Their merits and flaws are shortly discussed in this section.

One well-known method for contact saturation current density $J_{0,met}$ measurements is based on short circuit current-open circuit voltage or suns-V_{oc} data for solar cells, in which contact fractions of emitter or back surface fields are varied [Fellmeth 2011]. As this is a device-level measurement, a positive result has the advantage of being the ultimate proof that a contact passivation scheme is successful at reducing the contact recombination current in the finished device. However, the $J_{0,met}$ measurement is only possible after all cell process steps are complete, which makes it the most laborious measurement technique. In addition, care must be taken to ensure that the contact recombination current of interest is limiting the open circuit voltage in the device structure under test. If the contact recombination current of interest does not limit the open circuit voltage, no detection of contact passivation can be expected. Finally, saturation current densities extracted from current-voltage characteristics are highly temperature dependent (see section 3.2.4, intrinsic concentration), such that excellent temperature control is required during the measurement.

Photoluminescence based techniques have the advantage of spatial resolution and allow for effective lifetime measurements on unfinished devices. However, extraction of injection levels at which lifetimes are measured is convoluted using photoluminescence data alone. This issue has been circumvented by using QSSPC calibrated photoluminescence measurements, including the use of both low- and high-pass filters in front of the detector [Mueller 2012]. However, this technique is limited to the characterization of contacts on thick wafers. For thin wafers, elimination of parasitic effects due to back reflection with a short pass filter would involve cutting off the entire band-to-band photoluminescence peak in silicon. In the context of J_0 measurements, the use of thin wafers is desirable since the bigger the bulk minority carrier diffusion length to wafer thickness ratio, the more constant the minority carrier concentration is over the wafer thickness. Non-constant injection levels over the wafer thickness result in errors in the J_0 measurement. More specifically, J_0 will be underestimated (see section 3.6 for a discussion on this subject in the context of the test structure developed in the present dissertation). Such errors may be overcome through the use of numerical

[1] This section is adapted from [Deckers 2013]

modelling techniques, for example similar to those described in [Fell 2013b]; in which numerical modelling using the Quokka device simulator was used to enhance the accuracy of contact recombination currents extracted from photoluminescence measurements. Analogous methods could also be applied to the characterization method proposed in the present dissertation.

Photoconductance measurements allow for effective lifetime extraction at specific injection levels. For photoconductance measurements to be feasible, special care must be taken to prevent wafer conductivity to be dominated by the metal layer, as has successfully been done in the past for microwave-detected and inductively detected photoconductance measurements on wafers covered by a ca. 1 nm thick aluminum layer [Cuevas 1996]. A disadvantage of the use of very thin metal layers is that many metallization techniques do not allow for the deposition of such thin metal layers, and the contact surface recombination characteristics may well depend on the contacting method. In addition, unless specific precautions are taken, such thin aluminum layers could be fully oxidized before measurements are done since aluminum is well known to react fast with oxygen in ambient air to form aluminum oxide.

Microwave detected photoconductance decay measurements (μW-PCD) have also been used by Plagwitz et al. for the characterization of contact recombination currents [Plagwitz 2006]. In μW-PCD measurements, minority carrier properties are extracted from the reflected microwave power form a sample under test. The test structure used in [Plagwitz 2006] is reminiscent to the test structure proposed in this dissertation. The test structure is based on a silicon wafer which is passivated by a 50 nm aSi:H passivation layer on both wafer sides. On one side of the wafer features circular aluminum contacts (unknown thickness) with diameters between 120 and 920 μm. After a three hour anneal at 210°C, the amorphous silicon under the aluminum contacts is dissolved in the aluminum, while the amorphous silicon in the passivated contacts is not affected. During the microwave detected photoconductance measurement, the test structure is illuminated on the non-contacted side. However, the interpretation of microwave detected photoconductance decay measurements is convoluted, as eloquently put by B. Fisher: “Interpretation of the measured decay time constants as effective lifetimes is not straightforward. Microwave reflectance is not linear in wafer conductance and is sensitive to the geometrical arrangement of sample, microwave antennae and metallic 'short circuit' behind the wafer. The sensitivity even changes sign and must be optimised by adjusting the rear short circuit or the microwave frequency for each sample. In addition, according to [Schöfthaler 1995], the measurement interpretation is further complicated by the measured reflected microwave power decay only mirroring the minority carrier decay in low

injection, for homogeneous carrier generation, and for an appropriately positioned detector.

An alternative to photoconductance on test structures that comprise metal layers is to avoid the use of a metal layer during photoconductance measurements, and to assume that the surface recombination velocity at the silicon-air interface equals the surface recombination rate at the silicon-metal interface. Unfortunately, this approach is not applicable for the investigation of passivated contacts, e.g. MIS (metal-insulator-semiconductor) contacts, in which interactions between the insulator and metal layer are essential to take into account, see for example [Manole 2005]. In addition, taking recombination currents at the semiconductor-air interface as a proxy for semiconductor-metal recombination currents is oblivious to the fact that different contacts lead to different band bending and surface states at the metal-semiconductor interface, which may significantly affect contact recombination currents.

Although the aforementioned methods certainly have their merits, and have contributed to the understanding of contact recombination currents, their flaws are sufficiently significant to motivate the investigation of a novel characterization method for contact recombination currents. The main subject of this dissertation is the development of such a method.

3.2. $J_{0,met}$ test structures: Fundamentals

We developed a test structure that allows for effective lifetime measurements as a function of contact fraction using photo conductance measurements [Deckers 2013, Deckers 2013b]. Under relatively high injection conditions, saturation current densities of metallized junctions can be extracted from the slope of the saturation current density as a function the contact fraction. At arbitrary injection levels, the difference between the saturation current density at metallized junctions and the saturation current density at passivated junctions is extracted from the slope of inverse effective lifetime versus contact fraction. If bulk recombination is negligible compared to junction recombination, saturation current densities at the Si-metal and at the passivated silicon surface can be independently determined for arbitrary injection levels.

3.2.1. Test structure lay-out

Our test structure is a two-side passivated wafer which is divided in numerous areas with different contact fractions. Each area comprises circular metal point contacts arranged in a simple square lattice. A top view and cross section of a part of our test structure is schematically depicted in Figure 3.2.1.1.

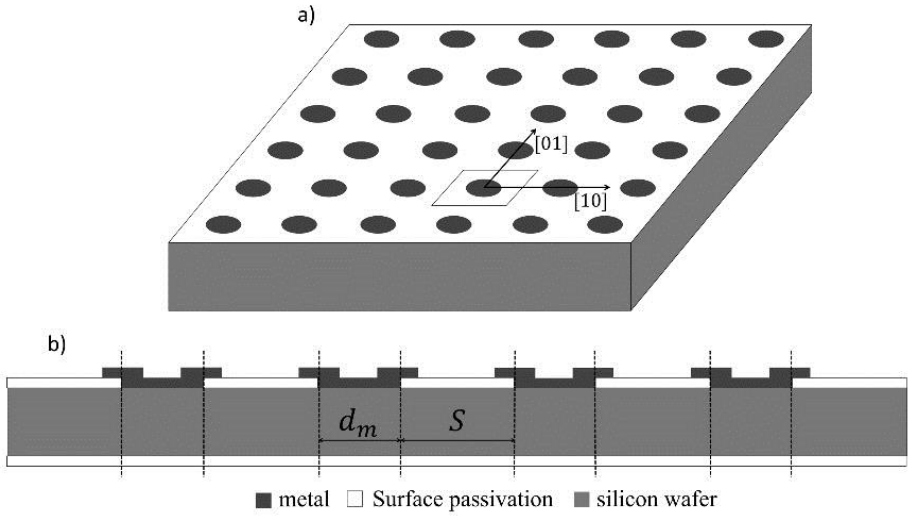

Figure 3.2.1.1. Our test structure for contact recombination current measurements, adapted from [Deckers 2013]. a) top view. b) cross section along one of the [10] directions.

A top view optical micrograph of one of the point contact lattices in our test structure is shown in Figure 3.2.1.2. Two approximately concentric circles are

observed in the point contacts. The inner circles are the contact openings in the oxide passivation layer. The outer circles are defined by the edge of the metal layers that cover the contact openings.

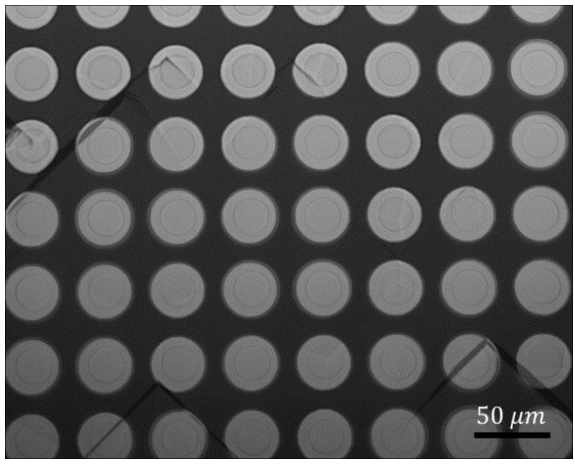

Figure 3.2.1.2. Optical micrograph of a part of one of the point contact lattices in our test structure.

A picture of a finished test structure in a sample box is shown in Figure 3.2.1.3. The test structure consists of nine 4 cm by 4 cm simple square point contact lattices with different contact fractions between 0 and 20%. For the test structures we manufactured, contact openings have a diameter of approximately $15\ \mu m$ and the pitch is typically in the order of $30 - 120\ \mu m$. The as-designed dimensions of the test structure used in the experiments shown in the present dissertation are summarized in Table 3.2.1.2.

C_{met} [%]	0	1,25	2,5	5	7,5	10	12,5	15	17
S [μm]	-	118,9	84,1	59,4	48,5	42	37,6	34,3	32,2

Table 3.2.1.2. Design parameters of the test structure used in the experiments shown in the present dissertation. The inter-contact point distance (pitch) is shown as a function of contact fraction. The contact hole diameter is $15\ \mu m$ *for all contact fractions.*

East test structure area with a given contact fraction can contain up to millions of very small, closely packed point contacts. Because the point contacts are very small and very closely packed, they are not visible by the naked eye. With the naked eye, lattices of point contacts look like the uniformly colored areas in Figure 3.2.1.3. In Figure 3.2.1.3, the lighter and darker areas correspond to areas with higher and lower contact fractions, respectively. The test structure shown in Figure 3.2.1.3 is designed such that different squares with different contact fractions are scattered across the wafer. This is done to avoid measurement artifacts related to

bulk lifetime variations across the wafer. Such lifetime variations could cause errors in extracted contact recombination currents if areas with similar contact fractions would be grouped together.

As stated before, our test structure is based on effective lifetime measurements on different wafer areas with different contact fractions. The effective lifetime measurements are performed with the QSSPC technique which is explained in section 2.2.

For the specific test structures used in the present dissertation, each wafer area on which a QSSPC measurement is done consists of a simple square lattice of point contacts on an otherwise passivated wafer. In addition, the specific test structure used in the present dissertation is contacted on one side only. In each area with a given contact fraction, two distinct regions can be discerned. The first region consists of passivated patches. The passivated patches in our test structure are for example passivated on both sides with a thermal SiO_2 layer. The second region consists of metallized patches. The metallized patches of our test structure have the same surface passivation as the first patches on one side, and the surface on the other side can be anything with different recombination characteristics such as a silicon-metal interface, a passivated contact, or a silicon-air interface.

The test structures should be designed such that minority carrier concentrations are approximately constant throughout the wafer's quasi neutral bulk. In section 3.5.1, we show that minority carrier concentrations are exactly constant when the bulk diffusion length is infinite and when all effective surface recombination velocities are zero. We also show in section 3.5.1 that the larger the bulk diffusion length and the smaller the effective surface recombination velocities, the smaller the excess carrier density variations in the wafer's quasi neutral bulk.

In the present dissertation, we do not strive for a general quantitative mathematical expression for when the minority carrier concentration can be considered to be constant in the context of our present test structure. Instead, we provide a qualitative treatment of the effect of in-plane excess carrier density variations in section 3.5 and we provide a qualitative treatment of the effect of out-of-plane excess carrier density variations in section 3.6. In these sections, we show how to design test structures such that bulk excess carrier density variations are avoided. In short, both passivated and contacted areas should have characteristic feature sizes much smaller than their respective effective diffusion lengths such that the minority carrier concentration can be considered to be approximately constant throughout the test structure plane. Also, relatively thin wafers are used to limit out-of-plane excess carrier density variations: the excess carrier dependency of Equation 2.3.3, which describes out-of-plane excess carrier density variations in

blanket test structures, depends on the ratio of W/L_D; the smaller W compared to L_D for the same surface recombination velocities, the smaller the out-of-plane excess carrier density variations.

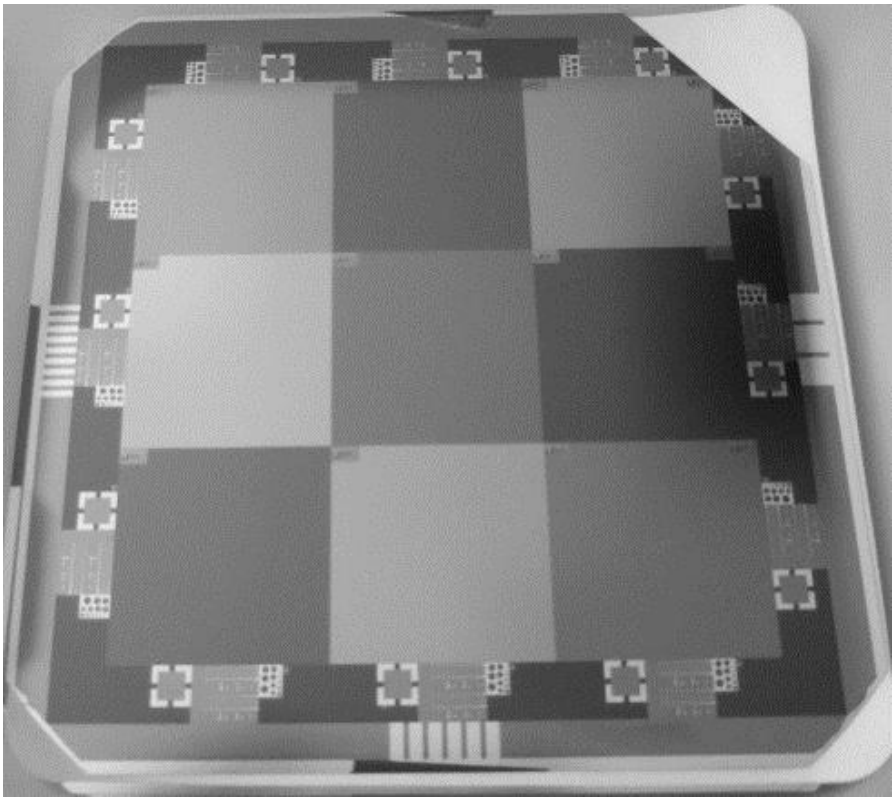

Figure 3.2.1.3. A silicon wafer on which a point contact-based test structure for contact recombination current measurements is made. The sides of the semi-square wafer have a length of 156 mm.

In addition, the contacts should be designed such that their transfer length is much larger than the contact size such that no current flows through the point contacts. The effect of current flow through the point contacts is discussed in section 3.4.

Throughout the remainder of section 3.2, we consider ideal test structures with constant bulk excess carrier densities and in which no current flows through the point contacts. Also, we assume that the bulk doping level is well-known. Furthermore, we assume that when we are treating recombination currents at surfaces featuring p-n or high-low junctions, the recombination currents are characterized by having a unit ideality factor. Finally we assume that the contact

fraction is well-known as well. The effect of the break-down of these assumptions is discussed throughout sections 3.4 to 3.9.

3.2.2. $J_{0,met}$ extraction[1]

$J_{0,met}$ is extracted from effective lifetime measurements as a function of the contact fraction. For a wafer piece comprising different areas with different recombination characteristics, the total recombination rate per unit area R is the area-weighted sum of the recombination rates per unit area in those areas, R_1 and R_2.

$$R = \frac{A_1}{A} R_1 + \frac{A_2}{A} R_2 \quad (3.2.2.1)$$

in which A_1/A is the fractional coverage of the first area and A_2/A is the fractional coverage of the second area. This equation holds when the recombination rate is a constant throughout each area separately.

We consider a wafer piece which has the same surface passivation layer on both sides. One side is contacted in contact openings. The semiconductor surface exposed to the contact openings has a different surface passivation. Therefore, two different areas can be discerned in the wafer piece: area one features two passivated surfaces and area two features one passivated surface and one contacted surface. When the excess carrier density is assumed to be constant throughout the wafer piece, the recombination rate in area 1 is given by:

$$R_1 = R_{bulk} + 2R_{diel}, \quad (3.2.2.2)$$

in which R_{bulk} and R_{diel} are recombination rates per unit area in the bulk and at the passivated surfaces, respectively.

The recombination rate in area 2 is given by:

$$R_2 = R_{bulk} + R_{diel} + R_{met}, \quad (3.2.2.3)$$

in which R_{met} is the recombination rate per unit area at the silicon-contact interface.

Combination of Equations 3.2.2.1-3.2.2.3, and renaming A_2/A to C_{met}, i.e. metal contact fraction, yields an expression for the overall recombination rate per unit area in the test structure as a function of the metal contact fraction:

$$R = R_{bulk} + 2R_{diel} + C_{met}[R_{met} - R_{diel}]. \quad (3.2.2.4)$$

Therefore, the difference between recombination rates per unit area at the metallized and passivated surfaces can be extracted from the slope of the recombination rate versus contact fraction.

We now consider the case of an n-type wafer with an emitter diffusion on both sides. The assumption of constant injection levels in the entire wafer piece's quasi neutral bulk is a reasonable assumption if wafer thickness, contact opening size,

[1] This section is partly based on [Deckers 2013].

and inter-contact opening distance are smaller than bulk minority carrier diffusion length, effective minority carrier diffusion length in the contacted regions and effective minority carrier diffusion length in passivated regions between contacts, respectively. The general reasoning behind the approach to write the recombination rate as a function of its components is similar to the approach in [Cuevas 1999], but it is applied here specifically to the point contact based test structure studied in this dissertation. Emitter recombination can be described by a saturation current density J_0 which is defined from:

$$R_{emitter} = \frac{J_0}{qn_i^2}\Delta p(N_D + \Delta p), \tag{3.2.2.5}$$

in which a recombination mechanism characterized by a unit ideality factor is assumed and in which Δp is the injection level at the bulk-side of the space charge region between emitter and bulk. Bulk recombination is described by a bulk lifetime τ_{bulk}. In section 2.2.4, we showed that the bulk lifetime is related to the average bulk recombination rate $R_{a,B}$ by $R_{a,B} \approx \Delta p_a/\tau_b$, in which the expression is exact when τ_b is independent of Δp in the relevant range. In this section, we have assumed constant excess carrier densities throughout the quasi neutral bulk. Therefore, the average injection level equals *the* injection level ($\Delta p_a = \Delta p$) and we can identify a bulk recombination rate per unit area R_{bulk} such that $R_{bulk} = \Delta p\, W/\tau_{bulk}$, in which W is the distance between the emitter space charge regions at the front and at the back of the test structure, which is approximately equal to the wafer thickness. From the total recombination rate, a global effective lifetime τ_{eff} is defined: $R \equiv \Delta p\, W/\tau_{eff}$. This yields the following expression for τ_{eff}:

$$\frac{1}{\tau_{eff}} = \frac{1}{\tau_{bulk}} + J_{0,tot}\frac{\Delta p(N_D+\Delta p)}{qn_i^2 W}, \tag{3.2.2.6}$$

in which we once again used that in this section, we assume that the bulk excess carrier density is constant. Using Equation 3.2.2.4 and Equation 3.2.2.5, Equation 3.2.2.6 can we written explicitly as a function of C_{met}:

$$\frac{1}{\tau_{eff}} = \frac{1}{\tau_{bulk}} + 2J_{0,diel}\frac{N_D+\Delta p}{qn_i^2 W} + C_{met}\left[J_{0,met} - J_{0,diel}\right]\frac{N_D+\Delta p}{qn_i^2 W}. \tag{3.2.2.7}$$

$J_{0,met}$, $J_{0,diel}$ and $J_{0,tot}$ are saturation current densities at the metallized surface, at the passivated surface and the total saturation current density, respectively. Δp is the injection level, n_i is the intrinsic carrier concentration, q is elementary charge, N_D is the base doping level. At arbitrary injection levels, $J_{0,met} - J_{0,diel}$ can be extracted from the slope of inverse effective lifetime versus contact fraction. If recombination at the passivated surface dominates bulk recombination, $J_{0,diel}$ can be extracted from the intercept of inverse effective lifetime versus contact fraction with the $C_{met} = 0$ axis. Otherwise, only $J_{0,met} - J_{0,diel}$ and an upper limit for $J_{0,diel}$ can be extracted at arbitrary injection levels.

An alternative method for $J_{0,met}$ extraction exists. This method is based on the extraction of $J_{0,met}$ from the slope of $J_{0,tot}$ as a function of contact fraction. For this method to be applicable, it must be possible to extract $J_{0,tot}$ from the effective lifetime data at each contact fraction. One way to extract $J_{0,tot}$ from the effective lifetime data at each contact fraction is by using Kane and Swanson's method [Cuevas 1999, Kane 1985]:

$$J_{0,tot} = qn_i^2 W \frac{d\tau_{eff,A}^{-1}}{d\Delta p}, \tag{3.2.2.8}$$

in which $\tau_{eff,A}$ is Auger-corrected effective lifetime, which is defined such that:

$$\frac{1}{\tau_{eff,A}} = \frac{1}{\tau_{eff}} - \frac{1}{\tau_A}, \tag{3.2.2.9}$$

with τ_A the carrier lifetime that describes Auger recombination. After correction for Auger-recombination, τ_{bulk} is assumed to be constant with injection level. This assumption is commonly, though not exclusively, met in the high injection regime. In the range of injection levels where the assumption of constant Auger-recombination-corrected bulk lifetimes is valid, $J_{0,met}$ and $J_{0,diel}$ can be extracted from $J_{0,tot}$ versus contact fraction data irrespective of the relative magnitude of bulk recombination and recombination at the passivated surface. In particular, substituting τ_{eff}^{-1} as given by Equation 3.2.2.7 in Equation 3.2.2.9, and extracting $J_{0,tot}$ from $\tau_{eff,A}$ using Equation 3.2.2.8 yields:

$$J_{0,tot} = 2\,J_{0,diel} + C_{met}\left[J_{0,met} - J_{0,diel}\right], \tag{3.2.2.10}$$

in which additionally, the following fact was used: $\tau_b^{-1} - \tau_A^{-1}$ is approximately constant as a function of the injection level, at sufficiently high injection levels. The above discussion has focused on extraction of saturation current densities of contacted emitters. However, the method is equally applicable to extraction of saturation current densities of contacted back surface fields. In Figure 3.2.2.1, experimental measurements of τ_{eff}^{-1} and $J_{0,tot}$ as a function of C_{met} are shown for test structures featuring aluminum contacts on an n^+ silicon diffusion. The substrate is a high lifetime, $145\ \mu m$ thick, n-type Czochralski silicon wafer with a bulk resistivity of $4\ \Omega \cdot cm$. The sheet resistance of the resulting n^+ n n^+ structure was $43\ \Omega/square$.

A photoluminescence image of a $J_{0,met}$ test structure is shown in Figure 3.2.2.2. Darker and lighter areas correspond to regions with higher and lower contact fractions, respectively. Higher contact fractions correspond to lower effective lifetimes, and therefore to a higher fraction of non-radiative recombination processes compared to radiative recombination processes. As a result, higher contact fractions correspond to lower photoluminescence signals.

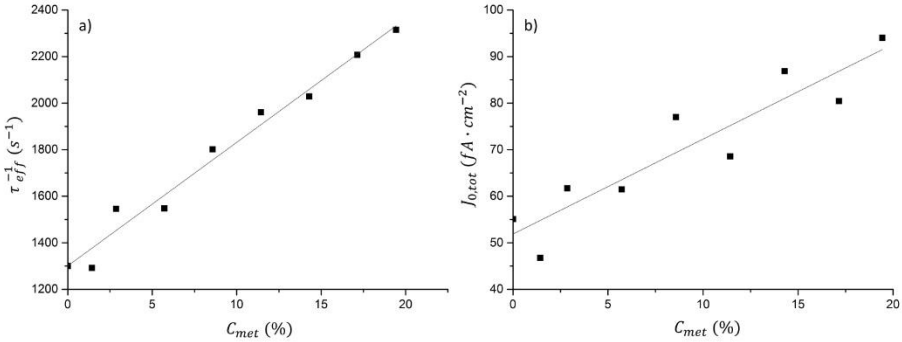

Figure 3.2.2.1. Experimental data used for contact recombination current extraction. The data are shown for unpassivated aluminum contacts on an n-type Czochralski silicon wafer with thermal oxide-passivated n^+ diffusions ($POCl_3$) on both sides. The symbols are experimental data and the lines are least square fits of Equations 3.2.2.7 and 3.2.2.10, for panels a) and b), respectively. Panel a) shows the inverse lifetime as a function of contact fraction, extracted at an excess carrier density of $1 \cdot 10^{15} cm^{-3}$. Panel b) shows the total saturation current density as a function of contact fraction.

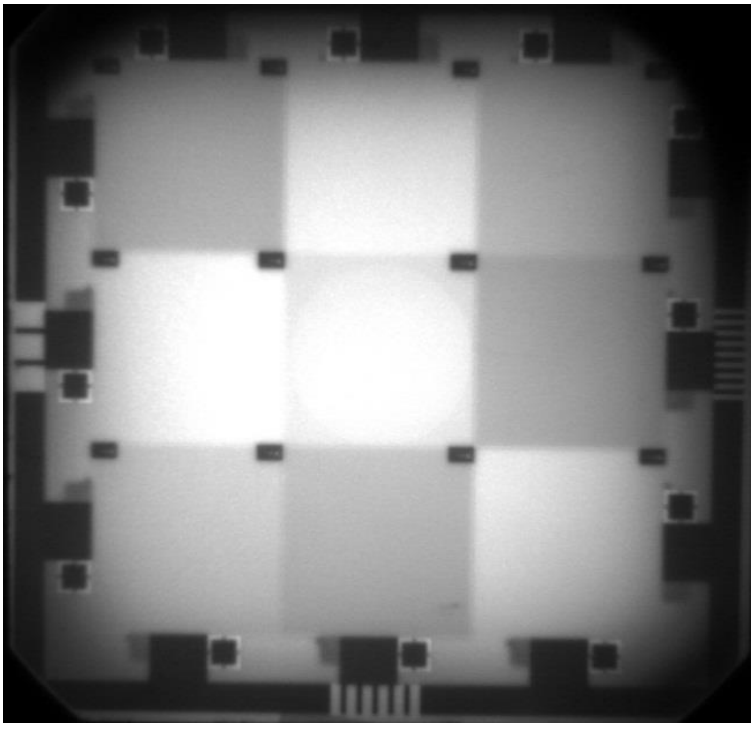

Figure 3.2.2.2. Photoluminescence image of a $J_{0,met}$ test structure based on simple square lattices of point contacts. The measurements are done with the non-contacted side facing the camera such that the pattern is the mirror image of the pattern shown in Figure 3.2.1.3.

The circular feature in the middle of Figure 3.2.2.2 is the QSSPC coil used in the measurement. The QSSPC coil is visible because the coil is placed in a circular orifice in the measurement chuck which has different optical properties than the rest of the measurement chuck.

3.2.3. Other measures for contact recombination[1]

Equation 3.2.2.7 is readily modified to allow for effective surface recombination velocity extraction as a function of injection level. This is accomplished by writing the surface recombination rate per unit area in terms of an effective surface recombination velocity times injection level ($R_{surface} = S_{eff}\Delta p$) and following a derivation similar to the derivation of Equation 3.2.2.7. This yields:

$$\frac{1}{\tau_{eff}} = \frac{1}{\tau_{bulk}} + \frac{2S_{diel}}{W} + \frac{C_{met}}{W}[S_{met} - S_{diel}], \tag{3.2.3.1}$$

in which S_{diel} is the surface recombination velocity at passivated surfaces and S_{met} is the surface recombination velocity at contacted surfaces. The interpretation of Equation 3.2.3.1 is analogous to that of Equation 3.2.2.7. It shows that $S_{met} - S_{diel}$ can be derived from the slope of inverse lifetime as a function of the contact fraction. If bulk recombination is negligible compared to surface recombination in the passivated areas, S_{diel} can be derived from the intercept of inverse lifetime with the $C_{met} = 0$ axis. If bulk recombination is significant compared to surface recombination, an upper limit for S_{diel} can be derived from the intercept of inverse lifetime with the $C_{met} = 0$ axis.

Finally, Equation 3.2.2.4 can also be written in terms of effective lifetimes of contacted and passivated areas, yielding yet another alternative for Equation 3.2.2.7:

$$\frac{1}{\tau_{eff}} = \frac{1}{\tau_p} + C_{met}\left[\frac{1}{\tau_m} - \frac{1}{\tau_p}\right], \tag{3.2.3.2}$$

in which τ_m is the effective lifetime of contacted areas and τ_p is the effective lifetime of passivated areas.

3.2.4. Intrinsic concentration

Contactless photoconductivity measurements actually provide a measurement of J_0/n_i^2 instead of J_0, when Kane and Swanson's method is used for J_0 extraction [King 1990]. Similarly, when $J_{0,met} - J_{0,diel}$ is extracted using Equation 3.2.2.7, the

[1] This section is based on [Deckers 2013]

quantity that is actually measured is $(J_{0,met} - J_{0,diel})/n_i^2$ instead of $J_{0,met} - J_{0,diel}$. Both J_0 and n_i depend strongly on temperature, but the temperature dependence of J_0/n_i^2 is much less. This has several interesting and useful consequences. First, the relative temperature independence of J_0/n_i^2 causes temperature control to be much less critical than for the case of $J_{0,met}$ extraction from suns-Voc measurements [Fellmeth 2011] or from current-voltage characteristics. Second, J_0/n_i^2 is rather temperature independent. Therefore, the exact choice of intrinsic concentration used to report J_0 values measured from contactless photoconductance measurements is rather arbitrary. That is, the exact choice of n_i is not predetermined by the measurement.

In this work, we consistently use $n_i = 7.4 \cdot 10^9 cm^{-3}$ for our room temperature $J_{0,tot}$ measurements. According to [Green 1990], this corresponds to a measurement temperature of 23°C. However, the saturation current densities reported in this work can be transferred at leasure to saturation current densities corresponding to different values of the intrinsic concentration, as long as the J_0/n_i^2 does not change too much in the relevant temperature range. This can be accomplished using the following procedure:

Let $J_{0,a}$ and $n_{i,a}$ represent the actual saturation current density and the actual intrinsic carrier concentration at the measurement conditions, respectively. The quantity $J_{0,a}/n_{i,a}^2$ is the measured figure of merit for the contact recombination current density during the photoconductance measurement.

Let $J_{0,b}$ be a saturation current density that is extracted from the photoconductance measurement assuming an intrinsic concentration $n_{i,b}$. Therefore:

$$J_{0,b} = n_{i,b}^2 \frac{J_{0,a}}{n_{i,a}^2} \tag{3.2.4.1}$$

Let $J_{0,c}$ be a saturation current density that is extracted from the photoconductance measurement assuming an intrinsic concentration $n_{i,c}$. Therefore:

$$J_{0,c} = n_{i,c}^2 \frac{J_{0,a}}{n_{i,a}^2}. \tag{3.2.4.2}$$

Combination of Equations 3.2.4.1 and 3.2.4.2 yields:

$$J_{0,c} = \frac{n_{i,c}^2}{n_{i,b}^2} J_{0,b}. \tag{3.2.4.3}$$

Equation 3.2.4.3 can be used to recalculate saturation current densities that correspond to any given value of the intrinsic carrier concentration to saturation current densities corresponding to a preferred intrinsic carrier concentration. The intrinsic carrier concentration in crystalline silicon is discussed in the following references: [Altermatt 2003, Green 1990, Misiakos 1993, Sproul 1991, Vankemmel 1993].

The recalculation of J_0 from one arbitrary n_i value to another can be done provided that J_0/n_i^2 does not change significantly with temperature in the relevant temperature range. In order to investigate the remaining temperature dependence of J_0/n_i^2, we take Equation 2.1.3.2 and reorder:

$$\frac{J_0}{n_i^2} = \frac{qD_p}{L_p N_{D,BSF}} \left[\frac{\frac{S_W L_p}{D_p} + tanh\left(\frac{W_{BSF}}{L_p}\right)}{1 + \frac{S_W L_p}{D_p} \tanh\left(\frac{W_{BSF}}{L_p}\right)} \right]. \quad (3.2.4.4)$$

Whereas J_0 and n_i both depend exponentially on temperature (Equation 2.1.1.8), the right hand side of Equation 3.2.4.4 depends only on terms which depend comparatively softly on temperature.

In order to verify this, we investigate the temperature dependence of Equation 3.2.4.4 in two extreme cases: the opaque junction limit and the transparent junction limit. For the opaque junction limit (i.e. $W_{BSF}/L_p \gg 1$, see section 2.1.3):

$$\frac{J_0}{n_i^2} = \frac{qD_p}{L_p N_{D,BSF}}, \quad (3.2.4.5)$$

and for the transparent junction limit (i.e. $W_{BSF}/L_p \ll 1$, see section 2.1.3):

$$\frac{J_0}{n_i^2} = \frac{qS_W}{N_{D,BSF}}. \quad (3.2.4.6)$$

In order to investigate the temperature dependence in the right hand sides of Equations 3.2.4.5 and 3.2.4.6, we consider the temperature dependence of each of the individual factors.

First, q is a universal constant and is therefore temperature independent.

Assuming (quasi) complete dopant atom ionization, $N_{D,BSF}$ can be considered to be a constant as well at room temperature. This assumption is reasonable for the present qualitative discussion on the temperature dependence of J_0/n_i^2 around room temperature because for phosphorous and boron, the dopant ionization fraction is above 70% at room temperature in the doping concentration range of $10^{15}\ cm^{-3}$ to $10^{20}\ cm^{-3}$ [Schenk 2006].

As q and $N_{D,BSF}$ can be considered to be roughly constant around room temperature, the remaining temperature dependence in Equations 3.2.4.5 and 3.2.4.6 is in the ratio D_p/L_p and S_W, respectively.

We first consider the remaining temperature dependence in Equation 3.2.4.5. As $L_D = \sqrt{\tau_p D_p}$, the ratio D_p/L_p equals $\sqrt{D_p/\tau_p}$, with τ_p the minority carrier (hole) lifetime in the highly doped region under consideration. $D_p = \mu_p\, kT/q$ and μ_p can be found from [Van Overstraeten p. II-24]:

$$\frac{1}{\mu_p} = \sum_k \frac{1}{\mu_k}, \quad (3.2.4.7)$$

in which μ_k is the mobility due to a specific scattering mechanism and comprises the mobility related to ionized impurity scattering μ_i and the mobility due to acoustic phonon scattering μ_{ap}, in which:

$$\mu_i \propto \frac{T^{3/2}}{\sqrt{m^* N_D}} \tag{3.2.4.8}$$

and

$$\mu_{ap} \propto \frac{1}{(m^*)^{5/2} T^{3/2}}. \tag{3.2.4.9}$$

For the highly doped regions under consideration, ionized impurity scattering dominates at room temperature such that the temperature dependence of the mobility is:

$$\mu_p \propto T^{3/2}. \tag{3.2.4.10}$$

The hole lifetime τ_p is dominated by Auger recombination in the highly doped regions under consideration, which is not very temperature dependent because the Auger coefficients C_n and C_p are not very temperature dependent: $C_n = (2.3; 2.8;\ 2.8) \cdot 10^{-31} cm^6 s^{-1}$ at $(75;\ 300; 400)K$ and $C_p = (0.78; 0.99; 1.2) \cdot 10^{-31}$ $cm^6 s^{-1}$ at $(75;\ 300;\ 400)K$ [Dziewior 1977], in which C_n is the Auger coefficient for the electron-electron-hole process and C_p is the Auger coefficient for the electron-hole-hole process.

As $L_p = \sqrt{\tau_p D_p}$, the D_p/L_p ratio in Equation 3.2.4.5. equals $\sqrt{D_p/\tau_p}$ and as τ_p is approximately constant for the case being considered, the main temperature dependence left in Equation 3.2.4.5 is the temperature dependence of $\sqrt{D_p}$, and from the preceding discussion, $\sqrt{D_p} \propto T^{5/4}$ when ionized impurity scattering dominates mobility.

The primary source of temperature dependence in Equation 3.2.4.6 is S_W. For the n-type semiconductor surface under consideration, and assuming a constant density of surface states throughout the bandgap as a function of energy, $S_W = \sigma_p v_{th} N_{SS}$ [Van Overstraeten p. II-14], in which σ_p is the capture cross section for holes, v_{th} is the thermal velocity and N_{SS} is the density of surface states. The main source of temperature dependence in S_W is v_{th}, which is proportional to $\sqrt{T}$ [Van Overstraeten p. II-12].

In conclusion around room temperature and for sufficiently highly doped semiconductors such that ionized impurity scattering dominates mobility:

$$\lim_{W_{BSF}/L_D \gg 1} \frac{J_0}{n_i^2} \propto T^{5/4}, \tag{3.2.4.11}$$

Also, around room temperature and assuming a constant density of surface states as a function of energy throughout the band gap:

$$\lim_{W_{BSF}/L_D \ll 1} \frac{J_0}{n_i^2} \propto T^{1/2}. \quad (3.2.4.12)$$

Therefore, the temperature dependence of J_0/n_i^2 is estimated to be supralinear at most ($T^{5/4}$), which is much less than the exponential temperature dependence of J_0. Therefore, J_0/n_i^2 can be considered to be approximately constant over a limited temperature range, thereby justifying the applicability of Equation 3.2.4.3. The extent of the limited temperature range is determined by the accuracy which is demanded by the experimentalist; a detailed treatment of which is beyond the scope of the present dissertation.

3.3. $J_{0,met}$ test structure process flow

In this section, the fabrication of $J_{0,met}$ test structures is explained for the characterization of passivated contacts on diffused junctions. For the sake of relevance and conciseness, we limit the scope of our discussion of $J_{0,met}$ test structure manufactor to the scope of this dissertation's experimental part. However, the usefulness of $J_{0,met}$ test structures is not limited to this specific case, and $J_{0,met}$ test structures can also be used to characterize other types of contacts. Process flows for these other types of contacts are readily found by analogy.

In particular, a process flow is considered for the following case: passivated metal contacts on diffused junctions following the metal-insulator-semiconductor (MIS) route for contact passivation. The contact pattern is defined using lithography.

$J_{0,met}$ test structures are made starting from a bare silicon wafer. The substrate should have a high bulk lifetime such that the bulk diffusion length is much larger than the wafer thickness. In this dissertation, we used n-type Czochralski silicon wafers with a bulk resistivity around $3\ \Omega \cdot cm$ and with a typical bulk lifetime of at least several milliseconds.

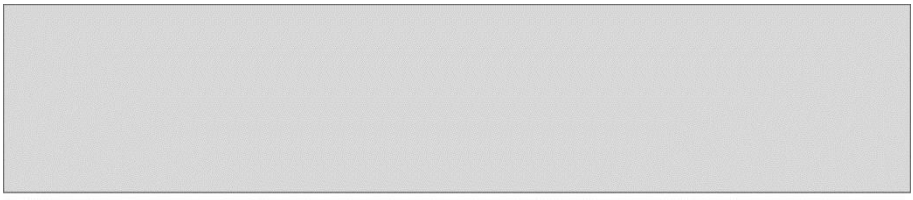

Figure 3.3.1. Cross section of an n-type silicon wafer prior to $J_{0,met}$ test structure processing (not to scale).

An n-type silicon wafer prior to $J_{0,met}$ test structure processing is shown in Figure 3.3.1. The first process step is saw damage removal. After saw damage removal, the wafers are cleaned prior to a diffusion step. In our experiments, $POCl_3$ and BBr_3 were used for phosphorous and boron diffusions, respectively. The diffusions were followed by phosphosilicate glass (PSG) or borosilicate glass (BSG) removal, for $POCl_3$ and BBr_3 diffusions, respectively. Then the wafers are thermally oxidized. In Figure 3.3.2, the wafer is shown after oxidation for the case of a boron diffusion.

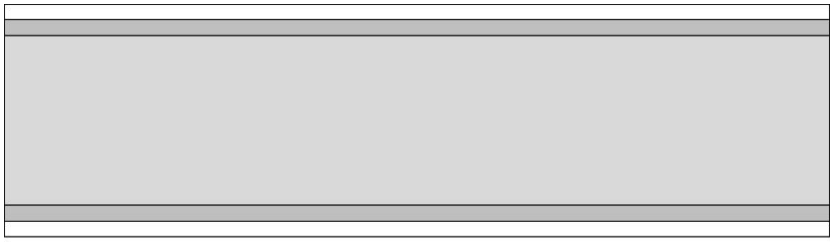

Figure 3.3.2. Cross section of an n-type silicon wafer during $J_{0,met}$ test structure processing, after BBr_3 diffusion and thermal oxidation (not to scale).

Subsequent to thermal oxidation, the contact opening pattern is defined lithographically. Then, contact openings are etched, and the wafers are cleaned, resulting in the structure schematically shown in figure 3.3.3.

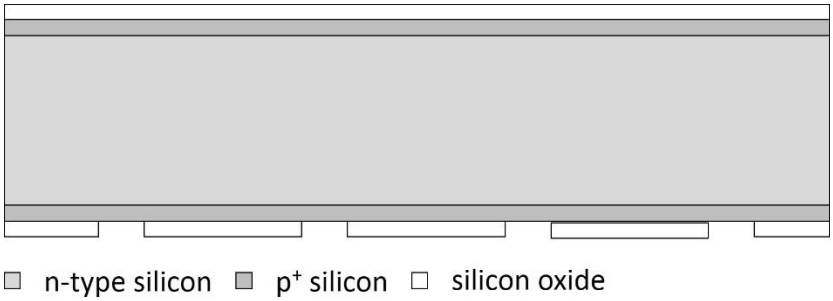

Figure 3.3.3. Cross section of an n-type silicon wafer during $J_{0,met}$ test structure processing, after contact opening lithography (not to scale).

After contact opening lithography, the contacts are formed. For the passivated contacts in this thesis, a thin Al_2O_3 layer is deposited using thermal atomic layer deposition (ALD) prior to metal deposition. As a metal, we use sputtered aluminum, alloyed with 1% silicon. Then, the metal pattern is lithographically defined and the metal layer is etched such that only the contact openings remain covered with metal. The wafers are subsequently cleaned to remove the resist and are finally given a forming gas anneal to improve surface passivation. This results in the structure schematically shown in Figure 3.3.4.

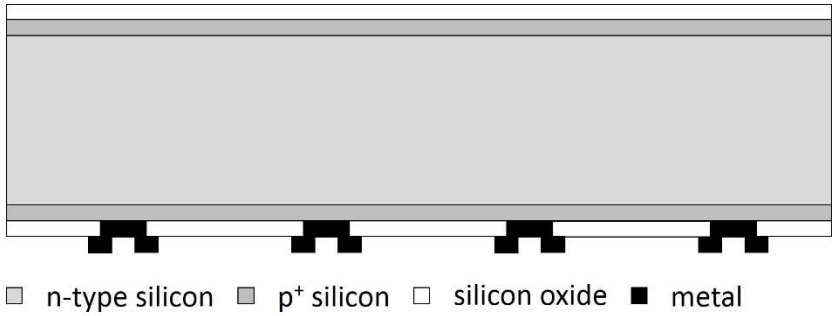

Figure 3.3.4. Cross section of finished $J_{0,met}$ test structure after processing (not to scale).

3.4. Parasitic current flow through point contacts[1]

The effect of metal contacts in the $J_{0,met}$ test structure is two-fold. First, the metal contacts introduce an additional recombination current, which is the quantity of interest. Second, part of the eddy currents induced during the radio wave-detected photoconductance measurement may flow through the metal point contacts instead of through the semiconductor, which is a parasitic effect since it influences the test structure's photoconductance in a way that is not related to the excess minority carrier density.

The influence of this parasitic effect on extracted lifetimes, injection levels, and contact saturation current densities is discussed. The present analysis yields the remarkable result that for test structures featuring point contacts with a characteristic size smaller than the contact's transfer length, there are negligible parasitic effects related to current flow through the point contacts instead of through the semiconductor. Finally, this prediction is proven experimentally.

3.4.1. Influence on measured conductivity

In our test structure, contact openings and contact opening spacing should both be much smaller than the effective diffusion lengths in contacted and passivated areas, respectively. These requirements arise from the fact that the minority carrier concentration has to be constant for our simple analysis to be valid. Therefore, in realistic embodiments of our test structure, both point contact size and point contact spacing are well in the sub-millimeter range. Typical coil frequencies used to probe wafer conductance during contact less photoconductance measurements are around 11 MHz [King 1990], which corresponds to probing wafers with electromagnetic radiation that has a wavelength of ca. 27m. Since the wavelength of radiation by which the photoconductance in our test structure is probed is many orders of magnitude larger than the characteristic size of its metal features, the equivalent resistance of our test structure's partly metallized areas can be derived using ordinary electric circuit theory.

We now derive the influence of point contacts on photoconductance measurements for a simple square lattice of circular contacts. For simplicity, we do not consider current flow in the bulk of the wafer perpendicular to the wafer plane. Consider a unit cell of our test structure as in Figure 3.4.1.1. A lumped-circuit analysis of the conductance along one of the <10> directions in the point

[1] Parts of this section are adapted from [Deckers 2013] and [Deckers 2014].

contact lattice is performed. The <10> directions are chosen because the symmetry of a simple square lattice allows for a simple analysis in these directions (note that we refer to the symmetry of the point contact lattice, not to the symmetry of the semiconductor's crystal lattice; throughout the present dissertation, silicon is approximated as an isotropic material). Qualitatively, our analysis also holds true for other directions. This is motivated in some detail at the end of this section. Due to coarse lumping in the equivalent circuit, it is assumed that part of the current can flow through the metal inside the smallest squares that enclose the circular contacts. Resistances R_1 and R_2, as defined in Figure 3.4.1.1, are given by:

$$R_1 = \frac{2R_S S}{S-d_m} \text{ and } R_2 = \frac{R_S(S-d_m)}{2d_m}, \tag{3.4.1.1}$$

in which R_s is the wafer's sheet resistance in the absence of metal contacts, S is point contact spacing (pitch) and d_m is the point contact diameter.

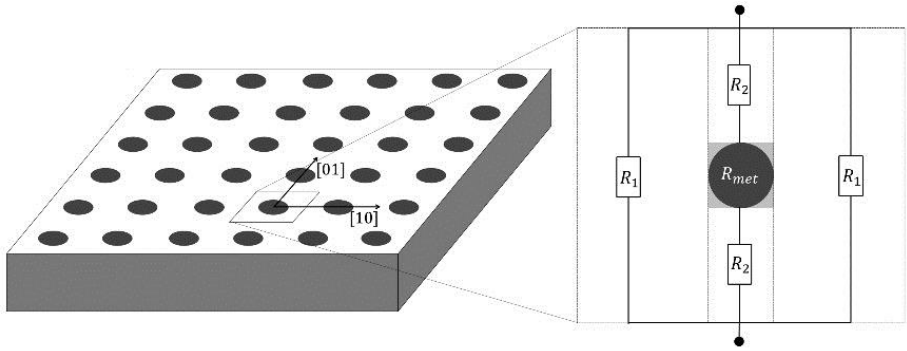

Figure 3.4.1.1. Definition of the <10> directions in the simple square lattice of point contacts in our test structure and equivalent lumped circuit for in-plane current flow in the <10> directions for a unit cell in our test structure's simple square lattices of point contacts [Deckers 2013].

The impedance of a contacted semiconductor region is called R_{met}. To calculate R_{met}, we first approximate the circular contacts by the smallest square contacts that entirely contain them. Then, we assume that electrical current flow through the semiconductor in the contacted area can be described by a transmission line. We subsequently solve for the spatial distribution of current and voltage in the semiconductor under metal contacts and use this information to obtain contacted area resistance. The metal layers are assumed to be perfect conductors, the semiconductor is described by its sheet resistance R_S, the metal-semiconductor interface is described by the specific contact resistance ρ_c, and the specific capacitance associated with the metal-semiconductor space charge region C_j. For this case, the well-known telegrapher's Equations read [Berger 1972]:

$$\frac{\delta V(x)}{\delta x} = -R\, I(x), \tag{3.4.1.2}$$

$$\frac{\delta I(x)}{\delta x} = -G_c V(x), \tag{3.4.1.3}$$

with $G_c = d_m\left(\rho_c^{-1} + j\omega C_j\right)$ and $R = R_S/d_m$, in which x is the position coordinate in the test structure plane along a <10> direction, I is the current flowing in the semiconductor under the contact, V is the voltage in the semiconductor under the contact, ω is angular velocity, and C_j is the specific metal-semiconductor contact capacitance. Note that the AC behavior of contact resistance may be important for the point contacts in our test structure because QSSPC contact recombination current measurements are typically done at a frequency of about 11 MHz [King 1990].

For the sake of conciseness, the following notation is used:

$$\rho'^{-1}_c = \rho_c^{-1} + j\omega C_j. \tag{3.4.1.4}$$

Selected parameters from the present transfer length model are defined in Figure 3.4.1.2.

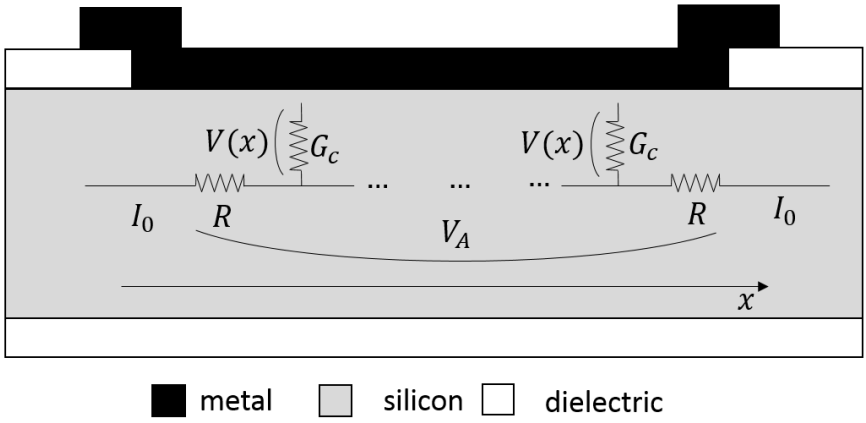

Figure 3.4.1.2. Schematic representation of one of the point contacts in a point contact-based test structure for QSSPC contact recombination current measurements, including an indication of selected parameters from the present transfer length model.

Whether or not the frequency dependence of contact resistance ρ_c' has to be taken into account obviously depends on the relative magnitude of the DC contact resistance ρ_c and the angular frequency – junction capacitance product ωC_j. H. H. Berger [Berger 1972] states the problem as follows: "*Whether the frequency dependence of the contact has to be considered depends on the cut-off frequency* ω_c … [$\omega_c = \left(\rho_c C_j\right)^{-1}$, red.]. *By estimating* C_j*, taking the silicon lattice constant …* [$\approx 0.5\, nm$, red.] *as an absolute minimum for the depletion layer thickness and by*

using experimentally determined ρ_c values, this [cut-off, red.] *frequency has been found to lie at least in the range of GHz for typical aluminum-silicon contacts. Therefore, for these the frequency dependence usually need not be considered. This might not be true for other metal-semiconductor pairs.*"

The problem with the particular line of reasoning pertaining the importance of the ac-behavior of contact resistance followed in [Berger 1972] is that typical aluminum-silicon contacts do not exist. This is the case for unpassivated aluminum-silicon contacts and it is a fortiori the case for passivated aluminum-silicon contacts.

A first reason why typical aluminum-silicon contacts do not exist is that the contact resistance changes dramatically with doping level for aluminum contacts on both n- and p-type silicon [Berger 1972b].

Second, the metal-semiconductor contact's space charge region capacitance depends on both the doping level and the built-in voltage [Sze 2007 p. 175]:

$$\frac{1}{C_j^2} = \frac{2[\psi_{bi} - V(x) - kT/q]}{q\varepsilon_s N_D}, \tag{3.4.1.5}$$

in which ψ_{bi} is the built-in potential, V_{app} is the (local) potential difference between the semiconductor and the metal, ε_s is the semiconductor's dielectric constant and all other parameters have been defined before. In our test structure, no voltage is deliberately applied between the semiconductor and point contacts. As a result, it is not unreasonable to assume that V_{app} is small compared to ψ_{bi}, and therefore:

$$\frac{1}{C_j^2} \approx \frac{2[\psi_{bi} - kT/q]}{q\varepsilon_s N_D}. \tag{3.4.1.6}$$

The built-in potential ψ_{bi} depends on the metal work function and on charge trapping at interface states at the metal-semiconductor junction, with the latter influence often dominating the former influence. Such charge trapping at interface states can be very difficult to control. Therefore, ψ_{bi} is variable.

We have now given a rough idea of how to analyze the relative importance of junction capacitance and DC contact resistance for the contacts under investigation in this dissertation. More specifically, the ideas developed in the previous paragraphs will be used in the experimental part of this chapter, section 3.4.5, to estimate in which cases the consideration of the ac-contact resistance behavior is necessary or not. It will turn out that for unpassivated aluminum contacts on the investigated n^+ diffusions, AC current transport across the metal-semiconductor junction is estimated to be significant whereas for unpassivated aluminum contacts on the investigated p^+ diffusions, only the DC component of the contact resistance is estimated to be significant.

For passivated contacts, the AC-behavior of contact resistance could be of particular importance: the DC-contact resistance of passivated contacts is often relatively high because of the resistance of the passivating layers between metal and semiconductor. Also, because these passivating layers are often very thin, the passivated contacts can still have a very high contact capacitance. As the cut-off frequency ω_c from which the AC-behavior of contact resistance becomes of importance equals $\left(\rho_c C_j\right)^{-1}$, this combination of high contact resistance and high contact capacitance results in a situation at which the AC-behavior of contact resistance becomes of importance at particularly low frequencies.

With respect to the passivated contacts investigated in chapter 5, we note that the transfer length of the investigated passivated metal-insulator-semiconductor (MIS) contacts is at least as high as the transfer length of the unpassivated contacts. The contact size was the about same in all our experiments. Therefore, parasitic current flow through the point contacts is of no importance for the investigated passivated aluminum contacts on n^+ silicon, but could have affected the measurements on the investigated passivated aluminum contacts on p^+ silicon.

After this digression on the motivation of including an AC-analysis of contact resistance, we return to the simultaneous solution of Equations 3.4.1.2-3.4.1.3 for a one dimensional model of a point contact in our test structure. We remind the reader that the most important parameters have been defined in Figure 3.4.1.2.

The x-axis is chosen to have its origin in the middle of a contacted region. Substitution of Equation 3.4.1.2 in Equation 3.4.1.3 yields:

$$\frac{\delta^2 V(x)}{\delta x^2} - \frac{R_S}{\rho'_c} V(x) = 0 \qquad (3.4.1.7)$$

We call the voltage over the contacted area V_a and without loss of generality, we choose the voltage at $x = -d_m/2$ to be $-V_a/2$. Solving Equation 3.4.1.7 with these boundary conditions yields for V(x):

$$V(x) = -V_a/2\, cosh\left(\sqrt{R_S/\rho'_c}\,(x - d_m/2)\right) - \frac{V_a[1+cosh(\sqrt{R_S/\rho'_c}d_m)]}{2sinh(\sqrt{R_S/\rho'_c}d_m)} sinh\left(\sqrt{R_S/\rho'_c}\,(x - d_m/2)\right) \qquad (3.4.1.8)$$

We substitute Equation 3.4.1.8 in Equation 3.4.1.2, work out the derivative, and evaluate the resulting equation at $x = -d_m/2$ and use that $I(-d_m/2) = I_0$, with I_0 the current flowing in/out of the contacted area. Also, we identify $\sqrt{\rho'_c/R_S}$ as L_T, the contact transfer length. This yields the ratio of V_a to I_0 which is readily identified as the impedance of a contacted area:

$$\frac{V_a}{I_0} = R_{met} = R_S \frac{L_T}{d_m} \frac{2sinh(d_m/L_T)}{[1+cosh(d_m/L_T)]}. \qquad (3.4.1.9)$$

Equation 3.4.1.9 states that the resistance of point contacts in our test structure is only a function of the semiconductor's sheet resistance R_S and of the ratio of point contact size and the contact transfer length. For the experiments in the present dissertation, typical values of R_S are in the range of $10-100\,\Omega/square$, d_m is typically around $15\,\mu m$ and L_T is typically in the order of $10-100\mu m$, although deviations from these ranges occur as well.

The equivalent impedance of a unit cell in our test structure along a <10> direction is found from:

$$R_{eq} = R_1//(2R_2 + R_{met}\ )//\ R_1, \tag{3.4.1.10}$$

in which // denotes parallel circuit elements. We now combine Equations 3.4.1.9 and 3.4.1.10 and use that for a test structure with circular point contacts, the contact fraction is given by $C_{met} = \pi d_m^2 4^{-1} S^{-2}$. This yields:

$$S'_{eq}\ = S_s Q' \tag{3.4.1.11}$$

in which $S'_{eq} = {R_{eq}}^{-1}$, i.e. S'_{eq} is the admittance of a unit cell in our test structure in the presence of metal, S_s is the conductance of the wafer under test in the absence of metal, and Q' is a factor which depends on C_{met} and d_m/L_T. Q' is given by:

$$Q' = 1 + 2\sqrt{\frac{C_{met}}{\pi}}\left[\left[1 - 2\sqrt{\frac{C_{met}}{\pi}} + 4\sqrt{\frac{C_{met}}{\pi}}\frac{L_T}{d_m}\frac{sinh(d_m/L_T)}{[1+cosh(d_m/L_T)]}\right]^{-1} - 1\right]. \tag{3.4.1.12}$$

From Equation 3.4.1.11, Q' is the ratio S'_{eq} and S_s; i.e. Q' is a measure for the influence of current flow through the point contacts in a point contact lattice on a wafer's in-plane admittance.

The measured conductance is the norm of Equation 3.4.1.12. Using that S_s is a real number:

$$S_{eq}\ = S_s Q, \tag{3.4.1.13}$$

with $Q = |Q'|$, and $S_{eq} = \left|S'_{eq}\right|$, in which the symbol | | denotes the norm of the quantity inside the vertical lines. Therefore, Q is a measure for the influence of a point contact lattice on a wafer's in-plane conductance. Note that $Q = Q'$ in DC, i.e. for $\omega C_j \ll \rho_c^{-1}$.

Q depends on C_{met} and the ratio of d_m and L_T. Q is shown as a function of these parameters in Figure 3.4.1.3. In the limit of $L_T/d_m = 0$, Equation 3.4.1.13 reduces to Equation 10 in [Deckers 2013].

Also, note that Q equals one in the limit of transfer lengths much larger than the contact size, as long as adjacent point contacts do not touch, i.e. for $C_{met} < \pi/4$:

$$\lim_{L_T/d_m \to \infty}(Q) = 1. \tag{3.4.1.14}$$

In fact, for the contact fractions shown in Figure 3.4.1.3, Q is only significantly different from one when $L_T/d_m < 1$, which means that it is possible to design test structures such that current flow through the metal contacts does not influence the photoconductance measurement. It is quite remarkable that even for $L_T/d_m = 1$, Q is undescernable from one on the scale of Figure 3.4.1.3.

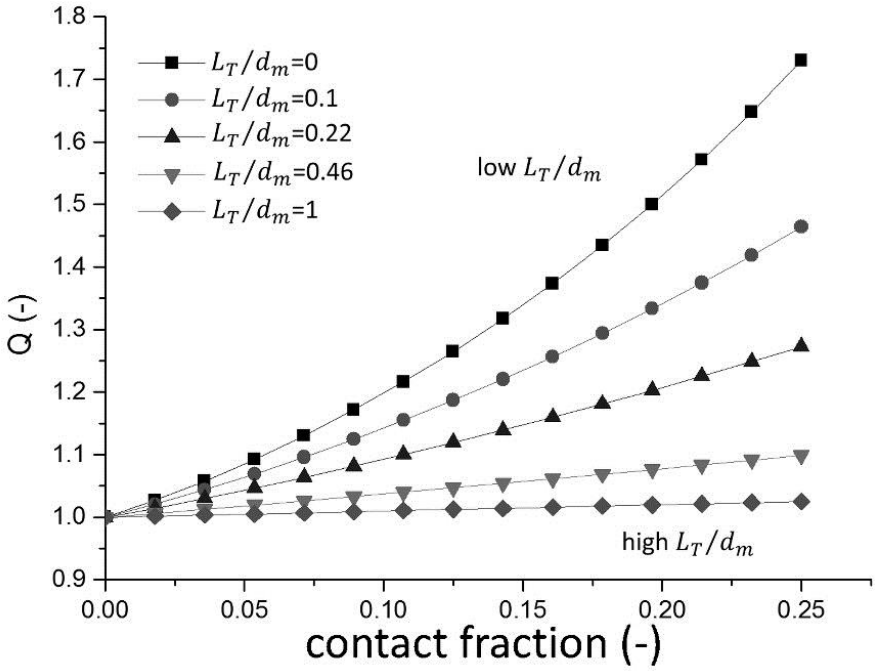

Figure 3.4.1.3. Q in the <10> directions of a simple square lattice of circular contacts as a function of C_{met} and L_T/d_m, for DC ($\omega C_j \ll \rho_c$) [Deckers 2014]. Q is close to unity for high L_T/d_m which means that current flow through the point contacts in our test structure negligibly influences the photoconductance measurement in this limit.

The observation that $Q \approx 1$ for $L_T/d_m > 1$ is a very significant prediction because designing test structures in a way such that this condition is fulfilled allows for a very simple interpretation of the measurement results. In section 3.4.5, we show experimental data which support the prediction that current flow through the metal contacts does not influence the photoconductance measurement when $L_T/d_m > 1$. Also, we give a specific example in the next paragraph.

The example we consider is a test structure for the characterization of unpassivated aluminum contacts on a typical n^+ diffusion used in our baseline IBC (Interdigitated Back Contact) solar cell process flow. The contacts have a contact resistance of $5.8 \cdot 10^{-4} \Omega \cdot cm^2$, the junction has a sheet resistance of 29 $\Omega/square$ and as a result, the contacts have a transfer length of 45 μm. Typical contact

openings in our test structure have a diameter of 15 μm, and we consider a test structure with a maximum contact fraction of 15%. For this specific example, Q is between 1 and 1.0018 for all contact fractions, which is identical to one for all practical purposes. Therefore, parasitic current flow through the point contacts instead of through the semiconductor does not constitute a parasitic effect for the specific example considered here.

It is useful to note that current flow through the point contacts does not constitute a significant parasitic effect for $L_T/d_m > 1$, independent of the direction in the test structure. This can be understood intuitively for test structures with circular point contacts, which we used in our experiments: the effect of metal on conductance in contacted areas is independent of orientation due to the circular symmetry. Equation 3.4.1.9, which describes this behavior, reduces to $R_{met} = R_S$ in the limit of $d_m/L_T \ll 1$. Therefore, the observation that the presence of point contacts does not disrupt photoconductance measurements in this limit is true regardless of the direction in the two dimensional lattice of our test structure. This is true regardless of the contact fraction, as long as the contact fraction is sufficiently small such that adjacent contacts do not overlap.

The exact form of Q' depends on the details of the test structure geometry. For example, consider a test structure that consists of simple square arrays of square metal dots, with the sides of the square contacts aligned with the <10> directions. For this structure, Q' for current flow along the <10> directions is given by:

$$Q'_{sq} = 1 + \sqrt{C_{met}}\left[\left[1 + \sqrt{C_{met}}\left[\frac{L_T}{z}\,\frac{2sinh(z/L_T)}{[1+cosh(z/L_T)]} - 1\right]\right]^{-1} - 1\right], \qquad (3.4.1.15)$$

in which z is the length of the sides of the square contacts. Analogous to the case of simple square lattices of circular contacts, Equation 3.4.1.15 reduces to $Q'_{sq} = 1$ in the limit of z/L_T small. This indicates that the notion that the lattice of point contacts does not corrupt the photoconductance measurement in the limit of transfer lengths much bigger than contact size is true independent of the exact test structure geometry. Our discussion of linear test structures in 3.10 further corroborates this notion; please refer to Equation 3.10.2.6 in particular.

3.4.2. Influence on Measured Injection Level

The average injection level in the wafer's quasi neutral bulk is related to the average photoconductivity by Equation 2.2.3.6, which is repeated here:

$$\Delta\sigma_a = q(\mu_e + \mu_p)\Delta p_a. \qquad (3.4.2.1)$$

When the injection level is extracted from a photoconductance measurement on our test structure, the influence of current flow through the point contacts on the photoconductance measurement is disregarded. Since this influence is disregarded, the measured photoconductivity and the measured injection level are found by an analogous equation:

$$\Delta\sigma_{eq} = q(\mu_e + \mu_p)\Delta p_{eq}, \tag{3.4.2.2}$$

in which Δp_{eq} is the measured injection level.

The measured photoconductance is overestimated by a factor Q (Equation 3.4.1.13) due to current flow through point contacts in our test structure. As the measured photoconductance is proportional to the measured average photoconductivity (see sections 2.2.1 and 2.2.2), the average photoconductivity is overestimated by the same factor:

$$\Delta\sigma_{eq} = \Delta\sigma_a Q. \tag{3.4.2.3}$$

Substitution of Equations 3.4.2.1 and 3.4.2.2 in Equation 3.4.2.3 yields:

$$\Delta p_{eq} = Q\Delta p_a, \tag{3.4.2.4}$$

i.e. the measured injection level is overestimated compared to the injection level in the quasi neutral bulk by a factor Q due to the presence of current flow through the point contacts in our test structure.

3.4.3. Influence on Measured Effective Lifetime

In section 2.2.5, it was derived that for negligible current gradients, the continuity Equation in terms of the average minority carrier concentration in the wafer plane can be written as:

$$\frac{1}{\tau_{eff}} = \frac{G_a}{\Delta p_a} - \frac{1}{\Delta p_a}\frac{\delta\Delta p_a}{\delta t}. \tag{3.4.3.1}$$

The following discussion is inspired by the work of Nagel et al. [Nagel 1999], but it is specifically applied to the analysis of the influence of currents flowing through contacts in $J_{0,met}$ test structures on extracted lifetimes.

τ_{eff} is a parameter that describes all recombination processes in the wafer. Depending on the time rate of change of the excess minority carrier density compared to the generation rate, either a transient analysis (minority carrier lifetime much longer than the characteristic decay time of the generation term), a steady state analysis (the characteristic decay time of the generation term is much longer than minority carrier lifetime) or a generalized analysis (the in-between case) applies. We proceed to discuss errors in measured effective lifetimes due to errors in extracted injection levels.

Transient measurements

When the generation term decays much faster than the characteristic time in which the minority carrier concentration changes, only the second term on the right hand side of Equation 3.4.3.1 is important. Combination of Equations 3.4.2.4 and 3.4.3.1 readily yields the fact that metal contacts short part of the wafer has no influence on measured effective lifetimes, as long as Q is not injection level dependent (which is not expected to be the case). However, the injection level is underestimated, as explained before, which has an indirect effect since recombination currents are injection level dependent.

Steady state measurements (QSSPC)

In a steady state analysis, changes in excess minority carrier density are assumed to occur in much faster time scales than changes in the generation term. The measurement occurs in the timescale of changes in the generation term, and the minority carrier concentration adapts to changes in the generation term in much shorter timescales, which are not resolved. Therefore, only the first term on the right hand side of Equation 3.4.3.1 needs to be considered in the steady state regime. Inspection of Equations 3.4.2.4 and 3.4.3.1 readily yields:

$$\tau_{eq} = \tau_{eff} Q. \tag{3.4.3.2}$$

As $Q \geq 1$, the presence of point contacts results in over estimations of minority carrier lifetimes extracted from QSSPC measurements when Q is significantly different from one, or equivalently when $L_T/d_m < 1$.

Generalized analysis

For a generalized analysis, combination of Equations 3.4.2.4 and 3.4.3.1 yields:

$$\tau_{eq}^{-1} = \frac{G}{Q\Delta p} - \frac{1}{\Delta p}\frac{\delta \Delta p}{\delta t}; \tag{3.4.3.3}$$

that is, the effective lifetime is over estimated, but by less than a factor Q.

In conclusion, the effective lifetime measurement is not affected by current flow through the point contacts when $L_T/d_m > 1$, irrespective of the type of photoconductance measurements; i.e. irrespective of whether steady-state, transient, or generalized photoconductance measurements are performed.

3.4.4. Influence on Measured $J_{0,met}$ (QSSPC)

In this section, the effect of injection level and effective lifetime over estimations on extracted contact saturation current densities is investigated for the case of (quasi) steady state photoconductance (QSSPC) measurements. First, it is recalled that contact saturation current densities are either extracted from the

slope of inverse effective lifetime as a function of contact fraction (the arbitrary injection level technique, Equation 3.2.2.7):

$$\frac{1}{\tau_{eff}} = \frac{1}{\tau_{bulk}} + 2J_{0,diel}\frac{N_D+\Delta p}{qn_i^2W} + C_{met}\left[J_{0,met} - J_{0,diel}\right]\frac{N_D+\Delta p}{qn_i^2W}, \quad (3.4.4.1)$$

or from the slope of the total saturation current density as a function of contact fraction (Equation 3.2.2.10):

$$J_{0,tot} = 2\,J_{0,diel} + C_{met}\left[J_{0,met} - J_{0,diel}\right] \quad (3.4.4.2)$$

From Equation 3.4.2.4, injection levels measured using photoconductance measurements on our test structure are over estimated by a factor Q:

$$\Delta p_{eq} = Q\Delta p_a. \quad (3.4.4.3)$$

In quasi steady state photoconductance (QSSPC) measurements, effective lifetimes are over estimated by the same factor:

$$\tau_{eq} = \tau_{eff}Q. \quad (3.4.4.4)$$

This section is devoted to quantifying this over estimation. First, the underestimation of $J_{0,met} - J_{0,diel}$ extracted using the arbitrary injection level technique, Equation 3.2.2.7, is investigated. Then, a similar analysis is applied to saturation current densities extracted using the high injection level technique, Equation 3.2.2.10. Finally, a comparison is made of the influence of current flow through metal contacts on saturation current densities extracted using these two methods.

Arbitrary injection level extraction

We first introduce a slight change of notation for simplicity. In the remainder of this section, a subscript “m” is used for measured quantity, and a subscript “r” is used for the actual physical quantity.

For simplicity, we assume negligible bulk recombination. Since $J_{0,diel}$ is extracted at $C_{met} = 0$ and $Q = 1$ at $C_{met} = 0$:

$$J_{0,diel,m} = J_{0,diel,r}, \quad (3.4.4.5)$$

in which $J_{0,diel,m}$ is the measured value of $J_{0,diel}$ and $J_{0,diel,r}$ is the actual value of $J_{0,diel}$. We recall that $J_{0,diel}$, as extracted from Equation 3.2.2.7, is overestimated when bulk recombination is not negligible.

We now investigate how $J_{0,met} - J_{0,diel}$ is influenced by current flow through point contacts. We make the simplifying assumption that $J_{0,met} - J_{0,diel}$ is found from the derivative of inverse effective lifetime with respect to C_{met} whereas in practice, we use a large C_{met} range for $J_{0,met} - J_{0,diel}$ extraction because of enhanced numerical stability. Inspection of Equation 3.2.2.7 yields:

$$\left[J_{0,met} - J_{0,diel}\right]_m = \frac{qn_i^2 W}{N_D + \Delta p_m} \frac{d\tau_m^{-1}}{dC_{met}}, \quad (3.4.4.6)$$

in which $\left[J_{0,met} - J_{0,diel}\right]_m$ is the measured value of $J_{0,met} - J_{0,diel}$, Δp_m is measured injection level and τ_m is measured effective lifetime. However, the injection level and effective lifetime are actually over estimated by a factor Q. Substitution of Equations 3.4.4.3 and 3.4.4.4 in Equation 3.4.4.6 yields:

$$\left[J_{0,met} - J_{0,diel}\right]_m = \frac{qn_i^2 W}{N_D + Q\Delta p_r} \left[\frac{1}{Q} \frac{d\tau_r^{-1}}{dC_{met}} - \frac{1}{Q^2} \frac{dQ}{dC_{met}} \frac{1}{\tau_r}\right]. \quad (3.4.4.7)$$

τ_r^{-1} is equal to τ_{eff}^{-1} as given in Equation 3.4.4.1. We use this information in combination with Equation 3.4.4.7 while assuming that bulk recombination is negligible compared to surface recombination. This last assumption is not essential to the point being made but it does greatly simplify the resulting equation, Equation 3.4.4.8.

$$\left[J_{0,met} - J_{0,diel}\right]_m = \frac{1}{Q} \frac{N_D + \Delta p_r}{N_D + Q\Delta p_r} \left[\left[J_{0,met} - J_{0,diel}\right]_r - \frac{1}{Q} \frac{dQ}{dC_{met}} \left[2J_{0,diel,r} + C_{met}\left[J_{0,met} - J_{0,diel}\right]_r\right]\right], \quad (3.4.4.8)$$

in which $\left[J_{0,met} - J_{0,diel}\right]_r$ is the actual value of $J_{0,met} - J_{0,diel}$.

High injection $J_{0,met}$ extraction

We investigate the relation between the measured total saturation current density $J_{0,m}$ and the actual saturation current density $J_{0,r}$ for any contact fraction. Applying Kane and Swanson's [Kane 1985] method for J_0 extraction, and using Equations 3.4.4.3 and 3.4.4.4:

$$J_{0,m} = qn_i^2 \frac{d1/\tau_m}{d\Delta p_m} = \frac{J_{0,r}}{Q^2}, \quad (3.4.4.9)$$

in which $J_{0,m}$ is the total measured saturation current density and $J_{0,r}$ is the actual total saturation current density. $J_{0,diel}$ is obtained from the value of $J_{0,m}$ at $C_{met} = 0$, and $Q = 1$ at $C_{met} = 0$, which yields:

$$J_{0,diel,m} = J_{0,diel,r}, \quad (3.4.4.10)$$

in which $J_{0,diel,m}$ is the measured value of $J_{0,diel}$ and $J_{0,diel,r}$ is the actual value of $J_{0,diel,r}$. We make the simplifying assumption that $J_{0,met} - J_{0,diel}$ is found from the derivative of J_0 with respect to C_{met} whereas in practice, we use a large range of contact fractions because it results in enhanced numerical stability. Using $\left[J_{0,met} - J_{0,diel}\right]_m = dJ_{0,m}/dC_{met}$ yields:

$$\left[J_{0,met} - J_{0,diel}\right]_m = \frac{1}{Q^2}\left[J_{0,met} - J_{0,diel}\right]_r$$

$$-\frac{2}{Q^3}\frac{dQ}{dC_{met}}\left[2J_{0,diel,r}+C_{met}\left[J_{0,met}-J_{0,diel}\right]_r\right]. \quad (3.4.4.11)$$

Comparison between arbitrary and high injection level $J_{0,met}$ extraction

Since $Q > 1$ for $C_{met} > 0$, both injection levels and effective lifetimes tend to be overestimated due to this parasitic effect. As Q is a monotonously increasing function with C_{met}, these overestimations are worse for higher contact fractions. As a result, the slope of inverse lifetime versus contact fraction is underestimated, and by Equation 3.4.4.8, this results in an underestimation of $J_{0,met} - J_{0,diel}$ as extracted by the arbitrary injection level technique, Equation 3.2.2.7. A similar reasoning leads to the conclusion that also $J_{0,met}$ extracted using the high injection technique, Equation 3.2.2.10, is underestimated due to parasitic current flow through point contacts in our test structure.

In figures 3.4.4.1 and 3.4.4.2, the effect of parasitic current flow through the point contacts is shown for $J_{0,met} - J_{0,diel}$ extracted using the arbitrary injection level technique, Equation 3.2.2.7; and the high injection level technique, Equation 3.2.2.10. We used the following parameters in the simulations: the doping level was $10^{15} cm^{-3}$, the injection level was $5 \cdot 10^{15} cm^{-3}$, the actual value of $J_{0,met}$ was $200\ fA/cm^2$ and the actual value of $J_{0,diel}$ was $50\ fA/cm^2$. We used the expression for Q' that corresponds to a simple square lattice of circular point contacts, Equation 3.4.1.12. The parasitic effect is worse for $J_{0,met} - J_{0,diel}$ extraction at higher contact fractions and for lower L_T/d_m ratios. In extreme cases, extracted $J_{0,met} - J_{0,diel}$ values can even be negative. Fortunately, the figures clearly show that the parasitic effect can be avoided all together by making the contact size smaller than the transfer length because $Q \approx 1$ and $dQ/dC_{met} \approx 0$ in this case.

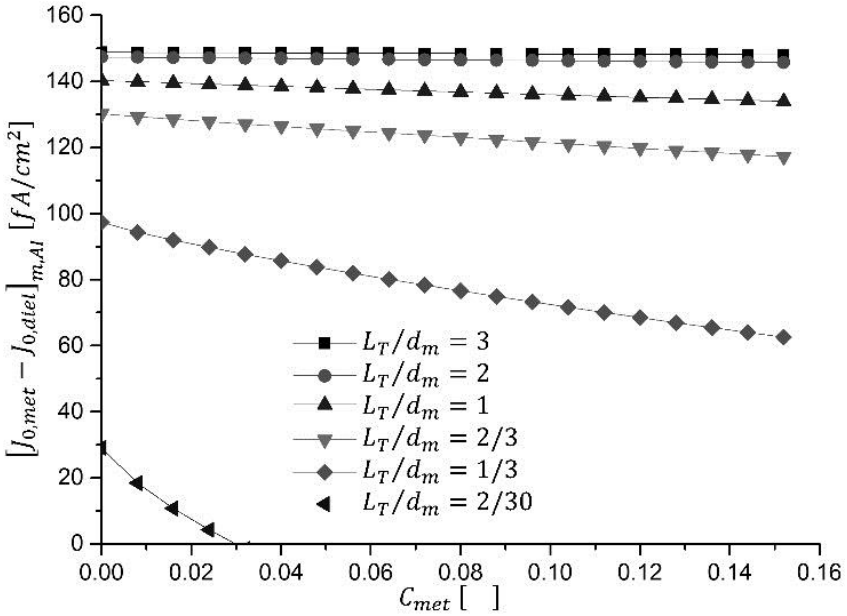

Figure 3.4.4.1. Effect of current flow through metal contacts instead of through the semiconductor on $J_{0,met} - J_{0,diel}$ extracted using the arbitrary injection level technique (Equation 3.2.2.7). The actual value of $J_{0,met} - J_{0,diel}$ is $150 fA \cdot cm^{-2}$ [Deckers 2014].

We now compare the influence of current flow through metal contacts on saturation current densities extracted using Equations 3.2.2.7 and 3.2.2.10. Comparison of Equations 3.4.4.8 and 3.4.4.11 yields:

$$\left[J_{0,met} - J_{0,diel}\right]_{m,AI} - \left[J_{0,met} - J_{0,diel}\right]_{m,HI} > \frac{1}{Q^3}\frac{dQ}{dC_{met}}\left[2J_{0,diel,r} + C_{met}\left[J_{0,met} - J_{0,diel}\right]_r\right], \quad (3.4.4.12)$$

in which the subscripts AI and HI denote values of $\left[J_{0,met} - J_{0,diel}\right]_m$ extracted using the arbitrary and high injection level techniques, respectively. In order to proof this, we required that $2N_D > Q(N_D - \Delta p_r)$. This is always true in high injection and it is not relevant in low injection because Equation 3.2.2.10 should not be used in that regime. Since Equation 3.4.4.12 requires that $\left[J_{0,met} - J_{0,diel}\right]_{m,AI} > \left[J_{0,met} - J_{0,diel}\right]_{m,HI}$, this parasitic effect is less severe when Equation 3.2.2.7 is used compared to when Equation 3.2.2.10 is used for $J_{0,met}$ extraction. Therefore, this parasitic effect will tend to make $J_{0,met}$ extracted using the arbitrary injection level technique higher than $J_{0,met}$ extracted using the high injection technique.

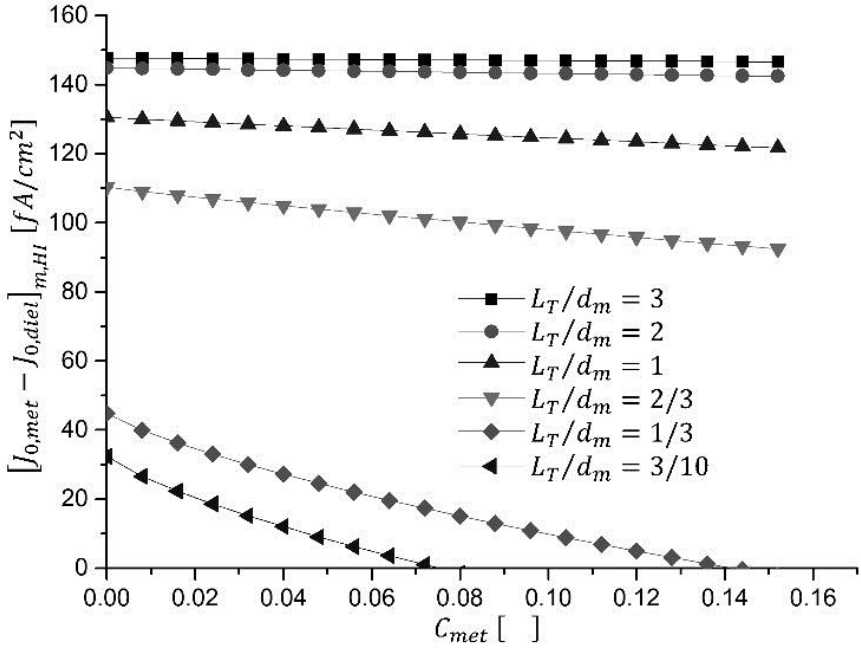

Figure 3.4.4.2. Effect of current flow through metal contacts instead of through the semiconductor on $J_{0,met} - J_{0,diel}$ extracted using the high injection level technique (Equation 3.2.2.10). The actual value of $J_{0,met} - J_{0,diel}$ is $150\ fA \cdot cm^{-2}$.

3.4.5. Experimental

We verify the applicability of our model by comparison with experiment. We focus on experimentally verifying the following predictions: 1) There is no parasitic effect associated with the presence of metal point contacts in our test structure when the transfer length is larger than the point contact size. 2) When the transfer length is smaller than the point contact size, extracted contact saturation current densities are underestimated. We defer an experimental comparison between contact saturation current densities extracted using the high injection and arbitrary injection techniques to a later chapter because this comparison also depends on injection level variations in the test structure's quasi neutral bulk.

We manufactured test structures for contact recombination current measurements on multiple wafers (n-type Czochralski silicon with a bulk resistivity around $4\Omega \cdot cm$). Either a boron emitter (sample a) or a phosphorous back surface field (samples b and c) was formed on both wafer sides using a BBr_3 or $POCl_3$ diffusion, respectively. Surface passivation and dopant drive-in was accomplished using thermal oxidation. After thermal oxidation, test structures were made according to the procedure outlined in section 3.3, with circular contact openings arranged in a

simple square lattice. Contact fractions between 0 and 20% were used. The metal contacts were 0.5 µm thick aluminum layers alloyed with 1% silicon. Effective lifetime measurements were done in QSSPC mode. As we showed before, this corresponds to a worst case scenario in terms of the effect of current flow through the point contacts on the photoconductance measurement. All saturation current densities were extracted assuming an intrinsic concentration of $7.4 \cdot 10^9 cm^{-3}$. $J_{0,diel}$ was measured using Kane and Swanson's method [Kane 1985], at an injection level of $1 \cdot 10^{16} cm^{-3}$, and $J_{0,met} - J_{0,diel}$ was obtained from Equation 3.2.2.7 at $\Delta p = 1 \cdot 10^{15} cm^{-3}$.

The experiment we show here is designed to show that current flow through point contacts does not distort the contact recombination current measurement when $L_T/d_m > 1$. A similar measurement has been shown in [Deckers 2013], but that particular experiment was done on a test structure with very small contact fractions of 0-2%. This resulted in only a very small trend of effective lifetime as a function of the contact fraction, which in turn resulted in a large uncertainty on the extracted contact recombination currents. Here, this issue has been overcome by using a significantly larger range of contact fractions, namely 0-20%.

We compare contact saturation current densities in which the contact holes are either contacted ($J_{0,met}$), or not ($J_{0,open}$). For $J_{0,open}$ measurements, the exposed contact regions have a very high surface recombination velocity due to the lack of surface passivation, which mimics the recombination characteristics of the silicon-metal interface. However, due to the absence of metal, any effects related to current flow through the metal contacts instead of through the semiconductor are avoided. Therefore, the comparison between these two types of measurements enables the evaluation of the effect of current flow through point contacts on saturation current densities extracted from photo-conductance measurements on our test structure.

The high surface recombination velocity needed for $J_{0,open}$ measurements was achieved using a ten minute dip in a hot ($90 - 120$℃) SPM solution (1 H_2O_2 : 4 H_2SO_4) prior to the effective lifetime measurements. This yields a poorly passivated surface, which was verified by effective lifetime measurements of $150\ \mu m$ thick saw damage removed wafers with high bulk lifetime (at least 1ms at $\Delta p = 1 \cdot 10^{15} cm^{-3}$) that were given an SPM dip. The effective lifetime of these wafers was below the resolution of our lifetime tester ($\sim 1\ \mu s$) which yields an effective surface recombination velocity of at least 15000 $cm \cdot s^{-1}$.

For sample a, $J_{0,met}$ was measured first. Then, the metal contacts were etched and $J_{0,open}$ was subsequently measured. For samples b and c, $J_{0,open}$ was measured after contact hole opening, and $J_{0,met}$ was then measured after metallization. For

all samples, a forming gas anneal was performed after metallization. For samples b and c, a forming gas anneal was performed after contact opening as well.

Experimentally measured contact saturation current densities are shown in Table 3.4.5.1, corrected contact saturation current densities are shown in Table 3.4.5.2, and other relevant sample parameters are listed in Table 3.4.5.3. The indicated uncertainties are 95% confidence intervals indicating the precision of the measurements. Sample a has a boron diffusion forming n^-p^+ junctions on both sides of the wafer. Samples b and c have phosphorous diffusions forming n^-n^+ junctions on both sides.

Sample	$J_{0,open} - J_{0,diel}$ (uncovered contact holes)	$J_{0,met} - J_{0,diel}$ (metal covered contact holes)
a	680±55	584±32
b	356±70	317±43
c	308±63	326±54

Table 3.4.5.1. Experimental data based on as-measured effective lifetimes and injection levels. A comparison is shown between the saturation current density of uncontacted and contacted contact openings, $J_{0,open}$ and $J_{0,met}$, respectively, in $fA \cdot cm^{-2}$.

Sample	$J_{0,met} - J_{0,diel}$ (using measured L_T)	$J_{0,met} - J_{0,diel}$ (assuming $L_T = 0$)
a	753±52	1374±221
b	319±43	876±132
c	328±55	793±113

Table 3.4.5.2. Experimental data extracted from corrected effective lifetimes and injection levels. $J_{0,met} - J_{0,diel}$ is extracted from effective lifetime measurements that were corrected according to Equations 3.4.2.4 and 3.4.3.2. In the first column, the actual transfer length (calculated using the DC contact resistance) was taken into account. In the second column, the transfer length was assumed to be zero.

Sample	$J_{0,diel}$	ρ_c	L_T	R_{sheet}	d_m
a	40	$(4 \pm 10) \cdot 10^{-5}$	6±9	106±5	17
b	54	$(1.9 \pm 0.5) \cdot 10^{-3}$	66±8	43±2	16
c	47	$(9 \pm 3) \cdot 10^{-4}$	46±6	43±1	15

Table 3.4.5.3. Various properties of samples a, b and c. The corresponding units are: $[J_{0,diel}] = fA/cm^2$, $[\rho_c] = \Omega \cdot cm^2$, $[L_T] = \mu m$, $[R_{sheet}] = \Omega/square$, $[d_m] = \mu m$. *Error bars are 95% confidence intervals.* $J_{0,diel}$ *was measured on test structures without metal.*

In Table 3.5.3.1, $J_{0,open}$ is compared to $J_{0,met}$ extracted from as-measured effective lifetimes and injection levels. For sample a, $J_{0,met}$ is significantly lower than $J_{0,open}$, but for samples b and c, $J_{0,met}$ is equal to $J_{0,open}$ within the experimental precision. This can be explained using our model. In table 3.4.5.3, we show L_T, R_{Sheet}, ρ_c and d_m for samples a, b and c. From table 3.4.5.3, sample a is the only sample for which $L_T/d_m < 1$. Therefore, effective lifetimes and injection levels measured on contacted regions of sample a are over estimated. This over estimation is worse for higher contact fractions. Also, for our samples, and at the relevant injection levels, the effective lifetime was either constant or decreasing with injection level. As a result, the slope of inverse lifetime versus contact fraction is underestimated, and by Equation 3.4.4.8, this results in an underestimation of $J_{0,met} - J_{0,diel}$. For samples b and c on the other hand, $L_T/d_m > 1$ such that $Q \approx 1$ and current flow through the point contacts does not influence the photo conductance measurement.

In Figure 3.4.5.1, experimentally measured inverse lifetimes are shown as a function of contact fraction for sample c, both in the presence and absence of metal contacts. The slope of τ_{eff}^{-1} as a function of C_{met} is identical for the measurements in the presence and absence of metal, which is consistent with the data in Table 3.4.5.1.

The expressions we derived for Q can be used as a simple model for the effect of parasitic current flow on photoconductance measurements. Therefore, the derived expressions for Q can be used to correct measured effective lifetime and injection level data for the effect of parasitic current flow through the point contacts. Saturation current densities extracted from such corrected data are shown in Table 3.4.5.2. However, given the simplicity of the models, the corrections can only be expected to qualitatively agree with experiment when Q is significantly different than one.

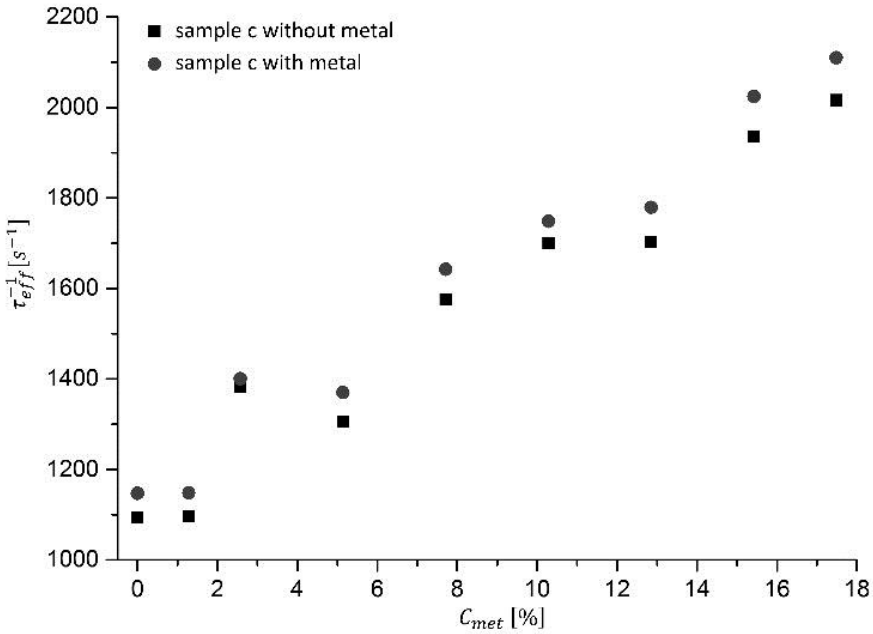

Figure 3.4.5.1. Inverse effective lifetime at $\mathbf{1 \cdot 10^{15} cm^{-3}}$ *as a function of contact fraction measured on test structures with contacted (squares) and uncontacted (circles)* contact openings. The data are shown for sample c.

In the first column of Table 3.4.5.2, the correction was done taking the contact's actual transfer length into account. For samples b and c, $Q \approx 1$ since $L_T/d_m > 1$ and as expected, the correction has negligible influence on the extracted value of $J_{0,met} - J_{0,diel}$. For sample a, $L_T/d_m < 1$ and as expected, the correction has significant influence on the extracted value of $J_{0,met} - J_{0,diel}$. However, application of the correction causes an over estimation compared to $J_{0,open} - J_{0,diel}$. As $J_{0,open} - J_{0,diel}$ is a measure for the same recombination current as $J_{0,met} - J_{0,diel}$, but $J_{0,open} - J_{0,diel}$ is (due to the absence of metal) not influenced by parasitic current flow through the point contacts, we can conclude from experiment that our model for Q yields an overestimation of the effect of parasitic current flow through point contacts on the photoconductance measurements. In other words, our models correctly predict that $Q \approx 1$ when $L_T/d_m > 1$ but the expressions for Q only yield qualitative measures for the effect of parasitic current flow on photoconductance measurements when $L_T/d_m < 1$ and Q is significantly bigger than one.

In the second column in Table 3.4.5.2, saturation current densities are shown which were extracted from effective lifetime data that were corrected for current flow through the point contacts assuming the contact's transfer length is zero. In

other words, Q was calculated assuming $L_T = 0$. Measured effective lifetimes and injection levels were corrected using this particular expression for Q, and the saturation current densities extracted from these corrected data are shown in the second column in Table 3.4.5.2. The correction factor is much larger in this case, and this causes $J_{0,met} - J_{0,diel}$ to be significantly overestimated when this correction factor is used. Note that this is the correction factor which was proposed in [Deckers 2013]. We can conclude that this expression for the correction factor should not be used to correct effective lifetime – injection level data measured on our test structure. Instead, test structures must be designed such that the effect of parasitic current flow on the photoconductance measurement is negligible.

Note that the DC contact resistance was used for the calculation of the correction factors. As discussed elaborately in section 3.4.1, this is only valid when $\omega \rho_c C_j \ll 1$ (note that ω is the angular frequency at which the photoconductance measurement is done, ρ_c is the contact resistance of the metal-semiconductor contact and C_j is the junction capacitance of the metal-semiconductor junction). To check this assumption, we calculated the space charge capacitance of a metal-semiconductor junction (Equation 3.4.1.6) using a built-in voltage of 0.6 eV for aluminum on n-type silicon, taken from experimental barrier heights from [Van Overstraeten 2000, p. VII-8]. The built-in voltage for aluminum on p-type silicon was taken to be 0.5 eV, which was calculated from the barrier height on n-type silicon and the rule of thumb which states that the barrier heights on n- and p-type silicon add up to the band gap. The surface doping level of sample a (p-type) was ca. $1 \cdot 10^{19} cm^{-3}$ and for samples b and c (n-type), it was ca. $3 \cdot 10^{19} cm^{-3}$. For a measurement frequency of 11 MHz (which is a typical measurement frequency for QSSPC measurements taken from [King 1990]), this yields $\omega \rho_c C_j = 0.06$ for sample a, 2.9 for sample b, and 1.3 for sample c. Therefore, using the DC analysis is only valid for sample a. However, the AC transfer lengths at 11 MHz for samples b and c were still estimated to be 39 and 36 μm respectively, which is still significantly bigger than the corresponding point contact diameters of 17 and 15 μm, respectively. Therefore, $L_T / d_m > 1$ and $Q \approx 1$ for samples b and c, also in AC, which explains why $J_{0,met} \approx J_{0,open}$ for these samples.

3.4.6. Conclusions

In conclusion, closed form analytical expressions were derived for parasitic effects related to current flow through metal point contacts on effective lifetimes and injection levels from photoconductance measurements in the context of our test structure. The model predicts that parasitic effects related to current flow through the point contacts in the test structure are only significant when $L_T/d_m < 1$. This means that when test structures are designed such that the contact's transfer length is larger than the contact size, metal contacts do not cause parasitic effects in the photoconductance measurement. We verified this prediction experimentally.

3.5. In-plane injection level variations[1]

Recombination currents are strongly injection level dependent. Therefore, injection level and lifetime measurements performed on regions with different C_{met} must be performed at the same injection level when they are used for the extraction of contact recombination characteristics using Equation 3.2.2.7. For the same reason, it is absolutely essential that the injection level is approximately constant throughout the quasi neutral bulk of a test structure area with a given contact fraction for a simple interpretation of the measurement results to apply. We first show that injection levels become constant on a relative basis in the limit of high minority carrier diffusion lengths L_D and small effective surface recombination velocities S. Then, we use a one-dimensional model to investigate minority carrier variations in the wafer plane and their effect on extracted lifetimes in a simple context.

3.5.1. Requirements for constant excess carrier densities – general case

We consider injection level variations in the bulk of an n-type wafer for an arbitrary test structure geometry. An analogous analysis has been done for photoconductance measurements on blanket test structures, that is the one-dimensional case, in [Cuevas 1999]. In our present analysis, we provide proof for the constancy of injection levels under certain conditions in a much more general case. This is useful in the context of our test structure because injection levels can vary in three dimensions, and not just one. We use the continuity equation and combine it with the current equation to yield the following well known expression:

$$-q\mu_p\nabla\left[pE-\frac{kT}{q}\nabla p\right]+q[G-R]=q\frac{\delta p}{\delta t}, \qquad (3.5.1.1)$$

in which p is minority carrier (hole) concentration, ∇ is the del operator, q is elementary charge, μ_p is minority carrier mobility, E is the electric field, k is Boltzmann's constant, T is temperature, R is the volumetric recombination rate, G is the volumetric generation rate, and t is time. As argued in section 2.2.5, the field term is of no importance in the wafer's bulk during a photoconductance measurement. Also, we assume that the timescale in which minority carrier concentrations change (that is the effective minority carrier lifetime) is much

[1] This section is based on [Deckers 2014b].

shorter than the timescale on which the measurement is done, which is equivalent to assuming steady state. This yields:

$$D_p \nabla^2 p + G - R = 0, \tag{3.5.1.2}$$

in which $D_p = \mu_p \, kT/q$. We describe bulk recombination with an effective lifetime τ_b, and identify the minority carrier diffusion length $L_D = \sqrt{D_p \tau_b}$. Reordering yields:

$$\frac{\nabla^2 p}{p - p_0 - \tau_b G} = \frac{1}{L_D^2}, \tag{3.5.1.3}$$

with p_0 the equilibrium minority carrier concentration. For a uniform generation rate G, the quantity $p - p_0 - \tau_b G$ is the amount by which the excess carrier concentration differs from the value it would have in the absence of edge effects. It is, for all intents and purposes, the amount of driving force for spatial minority carrier gradient variations. Therefore, the Laplacian of p gets small on a relative basis (per unit driving force) in the limit of large L_D. As a result, relative changes in ∇p become small in the limit of large L_D.

In order to investigate the requirements for small minority carrier concentration gradients, we consider the boundary conditions. At any boundary during a photoconductance measurement, current continuity, the assumption of only a diffusion current flowing to the surface and the description of surface recombination using an effective surface recombination velocity S yields the following well-known boundary condition for Equation 3.5.1.3:

$$D_p \nabla p \cdot \vec{n} = S(p - p_0), \tag{3.5.1.4}$$

in which $\vec{n}$ is an outward pointing unit vector perpendicular to the surface, and "$\cdot$" denotes the dot product. Reordering Equation 3.5.1.4, and using $p - p_0 \approx p$ yields:

$$\frac{D_p \nabla p \cdot \vec{n}}{p} = S. \tag{3.5.1.5}$$

Therefore, the gradient of the minority carrier concentration perpendicular to any surface becomes smaller on a relative basis as that surface gets better passivated (small S). Since any finite volume is bounded from all sides by surfaces, this constraint is applied to the minority carrier gradient in any arbitrary direction. We now combine this observation with the previously derived notion that relative changes in minority carrier concentration gradient become small for L_D large. This yields that on a relative basis, minority carrier concentrations become approximately constant for low S and high L_D, independent of the exact test structure geometry.

3.5.2. One dimensional model for in-plane injection level variations

In order to investigate under which conditions minority carrier concentrations can be considered to be constant in practice, we use a simple model. It is linear analogue of our test structure for the extraction of contact recombination characteristics using QSSPC. Linear test structures are shortly discussed in section 3.10.2. The model is sufficiently elaborate to qualitatively capture some of the essential physics of the actual test structure but it is simple enough to allow for analytical solutions for the minority carrier concentrations. The closed form expressions we obtain allow for a clear and intuitive interpretation of the effects of non-constant injection levels in the test structure. Also, as we will show in section 3.5.4, our model shows excellent agreement with experimental photoluminescence measurements on interdigitated back contact (IBC) solar cells.

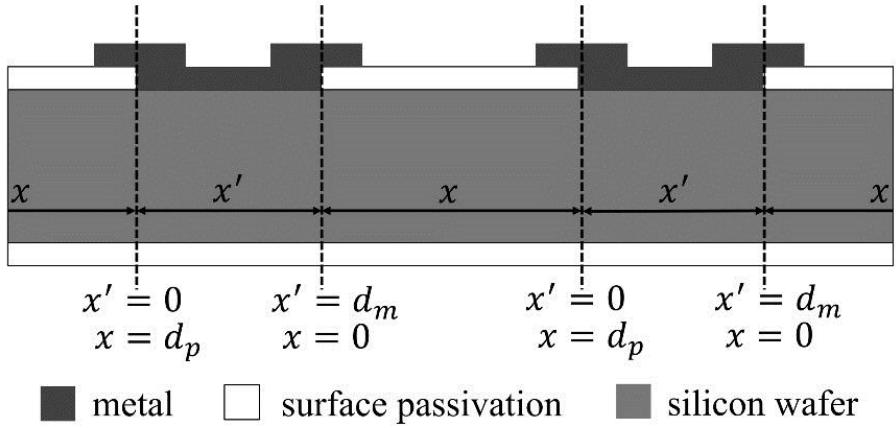

Figure 3.5.2.1. Cross section of a one-dimensional model of our test structure. This model is used as the basis for our calculations of in-plane excess carrier density variations.

Our one dimensional model consists of an infinite array of long contact fingers with width d_m on a passivated wafer. The contacts are separated by fully passivated areas with width d_p. A cross section of this model structure in the direction perpendicular to the contact lines is drawn in Figure 3.5.2.1.

Also, the bulk diffusion length is assumed to be much larger than the wafer thickness W. In this case, minority carrier concentrations are approximately constant over the wafer thickness. This is a commonly used assumption in the extraction of saturation current densities on blanket structures. This assumption and the consequences of its breakdown are discussed in [Cuevas 1999] in the context of saturation current density extraction from QSSPC measurements on blanket test structures for a number of simple cases. From our preceding discussion, and from our discussion in section 2.3, we can conclude that the

assumption of constant injection levels over a wafer's thickness is also more accurate for S_1 and S_2 small.

Within the scope of the further discussion in the present section, we assume constant injection levels over the wafer thickness. Out-of-plane injection level variations are discussed in section 3.6.

In the model that we introduce in this section, the recombination characteristics of passivated areas and contacted areas are described by effective lifetimes τ_p and τ_m, respectively. τ_p and τ_m are effective lifetimes which lump all recombination current components in the bulk and at the surfaces: $\tau_m^{-1} = \tau_b^{-1} + (S_{met} + S_{diel})W^{-1}$ and $\tau_p^{-1} = \tau_b^{-1} + 2S_{diel}W^{-1}$, with τ_b bulk lifetime, S_{diel} effective surface recombination velocity of passivated surfaces, and S_{met} effective surface recombination velocity of contacted surfaces.

For simplicity, we limit ourselves to a steady-state analysis. From a basic mass balance, the current equation and the assumption of quasi neutrality, it follows that finding the minority carrier concentration in the test structure plane amounts to concurrently solving Equations 3.5.2.1 (for p in contacted areas) and 3.5.1.7 (for p in passivated areas). For contacted areas:

$$-L_{D,m}^2 \frac{d^2 p_m}{dx'^2} + p_m - p_0 - \tau_m G = 0, \tag{3.5.2.1}$$

in which $L_{D,m}$ is an effective diffusion length in contacted areas, p_m is the minority carrier concentration in contacted areas and τ_m is the effective lifetime in contacted areas. The x' coordinate is used for simplicity in contacted areas. It is defined such that $x' = 0$ at the left hand side of contacted areas and $x' = d_m$ (contacted area width) on the right hand side of contacted areas. A similar equation holds for the passivated areas:

$$-L_{D,p}^2 \frac{d^2 p_p}{dx^2} + p_p - p_0 - \tau_p G = 0, \tag{3.5.2.2}$$

in which $L_{D,p}$ is the effective diffusion length in passivated areas, p_p is minority carrier concentration in passivated areas and τ_p is the effective lifetime in passivated areas. The x coordinate is used for simplicity in passivated parts. It is defined such that $x = 0$ at the left hand side of a passivated area and $x = d_p$ (passivated area width) at the right hand side of a passivated area. Note that x is related to x' by:

$$x = x' + \frac{d_m + d_p}{2}. \tag{3.5.2.3}$$

Because of translational symmetry, minority carrier concentrations are identical in all contacted and passivated areas. Therefore, we do not need to distinguish between different contacted and passivated areas in our equations. Due to mirror

symmetry around the center of contacted and passivated patches the solutions of Equations 3.5.2.1 and 3.5.2.2 are symmetric around the center of contacted and passivated areas, respectively. Therefore, they can be written in the general form:

$$p_m = C_a cosh\big((x' - d_m/2)L_m^{-1}\big) + p_0 + \tau_m G, \tag{3.5.2.4}$$

$$p_p = C_b cosh\left(\big(x - d_p/2\big)L_p^{-1}\right) + p_0 + \tau_p G, \tag{3.5.2.5}$$

with d_p passivated area width and d_m contacted area width. Boundary conditions determine the constants C_a and C_b in Equations 3.5.2.4 and 3.5.2.5. The first set of boundary conditions arises from requiring charge carrier density continuity at the boundaries between contacted and passivated areas:

$$p_m(\,x' = 0) = p_p\,\big(x = d_p\big)\,, \tag{3.5.2.6}$$

$$p_m(\,x' = d_m) = p_p\,(x = 0)\,. \tag{3.5.2.7}$$

Because of mirror symmetry around the center of contacted and passivated areas, these boundary conditions are equivalent. The second set of boundary conditions arises from the requirement of current density continuity at the boundaries between contacted and passivated areas:

$$\frac{dp_m}{dx'}(\,x' = 0) = \frac{dp_p}{dx}\,\big(x = d_p\big)\,, \tag{3.5.2.8}$$

$$\frac{dp_m}{dx'}(\,x' = d_m) = \frac{dp_p}{dx}\,(x = 0). \tag{3.5.2.9}$$

Again, mirror symmetry causes these boundary conditions to be equivalent. With boundary conditions 3.5.2.6-3.5.2.9, the solutions to Equations 3.5.2.1 and 3.5.2.2 are found to be:

$$p_m = \frac{G_0(\tau_p - \tau_m)cosh\left(\frac{x' - d_m/2}{L_m}\right)}{\frac{L_p}{L_m}\frac{sinh\left(\frac{d_m}{2L_m}\right)}{tanh\left(\frac{d_p}{2L_p}\right)} + cosh\left(\frac{d_m}{2L_m}\right)} + p_0 + \tau_m G, \tag{3.5.2.10}$$

$$p_p = \frac{G_0(\tau_m - \tau_p)\cosh\left(\frac{x - d_p/2}{L_p}\right)}{\frac{L_m}{L_p}\frac{sinh\left(\frac{d_p}{2L_p}\right)}{tanh\left(\frac{d_m}{2L_m}\right)} + cosh\left(\frac{d_p}{2L_p}\right)} + p_0 + \tau_p G. \tag{3.5.2.11}$$

We provide two numerical examples to elucidate the physical interpretation of Equations 3.5.2.10 and 3.5.2.11. In the first example (Figure 3.5.2.2), we consider the ratio of the minimum and maximum minority carrier concentration for various contacted area diffusion lengths. The minimum minority carrier concentration is achieved in the center of contacted areas and the maximum minority carrier concentration is achieved in the center of passivated areas. In our simulation: $\tau_p = 200\mu s$, $d_m = 15\mu m$, $d_p = 100\mu m$, and $D_p = 12cm^2s^{-1}$. For $L_m \gg d_m$, the minority carrier concentration is constant throughout the test structure. However, for L_m of

order d_m or smaller, the minority carrier concentration varies strongly in the test structure plane.

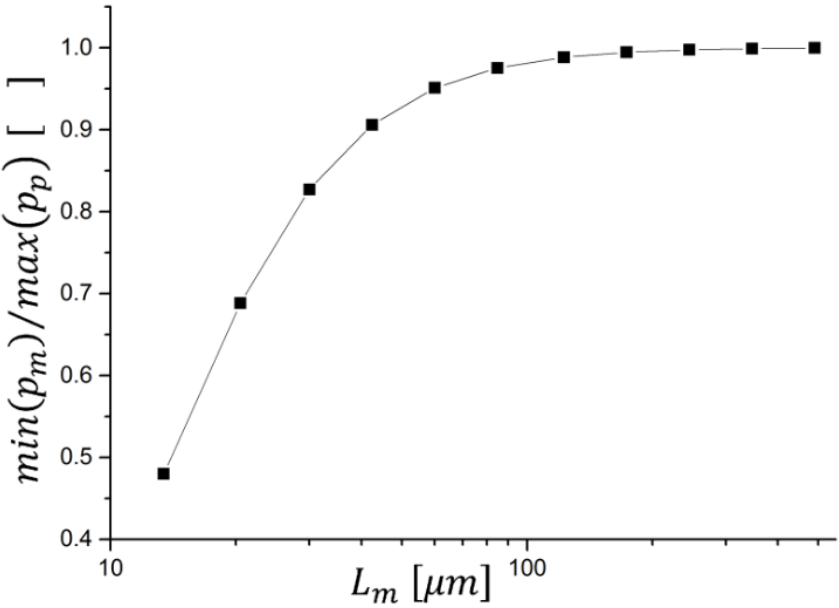

Figure 3.5.2.2. Ratio of the minimum minority carrier concentration in the contacted areas and the maximum minority carrier concentration in the passivated areas. The parameters used in the simulation were: $\tau_p = 200\mu s$, $d_m = 15\mu m$, $d_p = 100\mu m$.

The second example (Figure 3.5.2.3) tells a similar story as the first in a different way. This time, we vary both τ_p and τ_m simultaneously and we plot normalized minority carrier concentrations for three different scenarios. Normalized minority carrier concentrations are defined as p/p_{max}, with p_{max} the maximum minority carrier concentration for a given scenario. For high minority carrier lifetimes (high diffusion lengths), the injection level is approximately constant in the test structure plane, for low minority carrier lifetimes (low diffusion lengths), there are significant injection level variations. Note that the results we obtain are reminiscent of electrical shading effects in IBC (Interdigitated Back Contact) silicon solar cells (see for example [Hermle 2008, Kluska 2010]). In section 3.5.4, we show the applicability of our one dimensional model to the study of injection level variations in IBC solar cells.

Our results are also in line with the 'scaling effect' of effective lifetimes observed in [Schöfthaler 1994], in which microwave-detected photoconductance decay measurements were performed on samples with lattices of point contacts.

Therefore, the qualitative observations made in this section can be extrapolated to the point-contact based test structures at the heart of this dissertation.

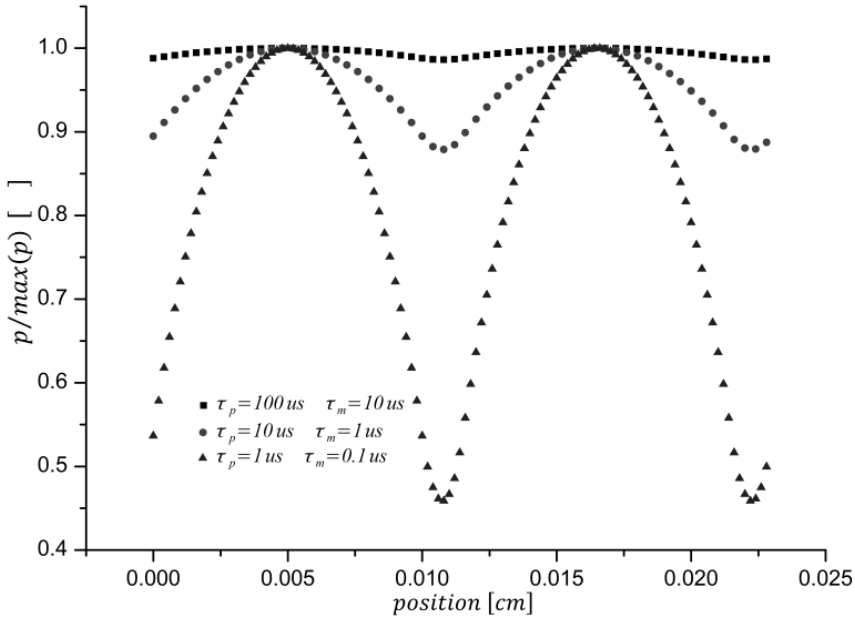

Figure 3.5.2.3. Injection level variations in the direction perpendicular to the metal contact fingers, for several combinations of minority carrier lifetimes in the passivated regions and in the contacted regions. The origin of the position coordinate is the boundary between a passivated and a contacted area. Subsequent maxima (minima) are centers of passivated (contacted) areas. Simulation for $d_m = 15\mu m$ *and* $d_p = 100\mu m$.

3.5.3. One dimensional model: limiting cases

We now investigate Equations 3.5.2.10 and 3.5.2.11 in a number of interesting limiting cases. First, we take the limit of these equations for all diffusion lengths much larger than the relevant characteristic feature sizes, that is $L_m \gg d_m$ and $L_p \gg d_p$. A first order Taylor series expansion in d_m/L_m and d_p/L_p readily yields:

$$p_m - p_0 = G_0 \left[\frac{1}{\tau_p} + C_{met}\left[\frac{1}{\tau_m} - \frac{1}{\tau_p}\right]\right]^{-1} = p_p - p_0. \qquad (3.5.3.1)$$

Therefore, the injection level is constant in the wafer plane in the limit of $L_m \gg d_m$ and $L_p \gg d_p$. This the desirable case because in this limit, the expression for the excess carrier density reduces to a very simple form, namely Equation 3.5.3.1.

This form is equivalent to the expressions for the extraction of contact recombination characteristics proposed in [Deckers 2013] (Equations 3.2.2.7 and 3.2.2.10).

In the limit of $L_m \gg d_m$ and $L_p \gg d_p$, the measurement interpretation is very straightforward. For example, the measurement may be interpreted in terms of effective surface recombination velocities of contacted and passivated areas, S_{met} and S_{diel}:

$$\frac{1}{\tau_{eff}} = \frac{1}{\tau_b} + \frac{2S_{diel}}{W} + \frac{C_{met}}{W}[S_{met} - S_{diel}], \tag{3.5.3.2}$$

in which τ_b is bulk effective lifetime, and τ_{eff} is the overall effective lifetime which is measured in the QSSPC measurement.

The other limit we investigate is the limit of diffusion lengths much smaller than the relevant characteristic feature sizes. We first consider Equation 3.5.2.10, take the limit of $d_m \gg L_m$, and reorder:

$$p_m - p_0 = \frac{G_0 L_m(\tau_p - \tau_m)}{L_p cotanh\left(\frac{d_p}{2L_p}\right) + L_m} \frac{cosh\left(\frac{x' - d_m/2}{L_m}\right)}{exp\left(\frac{d_m}{2L_m}\right)} + \tau_m G_0. \tag{3.5.3.3}$$

The maximum value of the $cosh([x' - d_m/2]/L_m)$ factor is reached at the edges of the contacted regions, where it is approximately equal to $exp(d_m/2L_m)$ for $L_m \ll d_m$. However, when $L_m \ll d_m$, the cosh factor becomes much smaller than $exp(d_m/2L_m)$ even at relatively small distances from the edge of the contacted areas. Therefore, the ratio of $cosh((x' - d_m/2)/L_m)$ to $exp(d_m/(2L_m))$ is exponentially smaller than one in the entire contacted area except very close near the contact edges. The other factors in the first term do not diverge as d_m/L_m goes to zero. Therefore, the first term in Equation 3.5.3.3 is negligible compared to the second term in most of the contacted area. As a result, the excess minority carrier concentration in the contacted area is given by:

$$p_m - p_0 = \tau_m G_0, \tag{3.5.3.4}$$

which is (not surprisingly) equal to the steady state excess minority carrier concentration in a uniformly contacted semiconducting slap under illumination. This means that the minority carrier concentration in the contacted area is not influenced by the region outside the contacts. This is illustrated in Figure 3.5.3.1.

An analogous derivation yields for the minority carrier concentration in the passivated areas in the limit of $L_p \ll d_p$:

$$p_p - p_0 = \tau_p G_0, \tag{3.5.3.5}$$

that is the excess minority carrier concentration in the passivated areas is the same as what would be expected for an infinitely large passivated area. Therefore,

in the limits of $L_m \ll d_m$ and $L_p \ll d_p$ respectively, contacted areas are not influenced by passivated areas and vice versa. Also, the injection level is constant throughout each area separately. In this limit, and assuming $L_T \gg d_m$, with L_T the contact's transfer length, the measured injection level from a photoconductance measurement in the x-direction would be the area-weighed harmonic average of the injection levels in contacted and passivated areas. This is found from a lumped circuit analysis, the relation between photoconductance and injection level, and Equations 3.5.3.4 and 3.5.3.5. On the other hand, when $L_T \ll d_m$, the photoconductance measurement would not be influenced at all by the minority carrier properties in the contacted areas because they would be fully shorted by the metal contacts. In intermediate cases, the injection level is given by Equations 3.5.2.10 and 3.5.2.11, and the measured injection level is a complicated function of the diffusion lengths, contact transfer length and characteristic feature sizes.

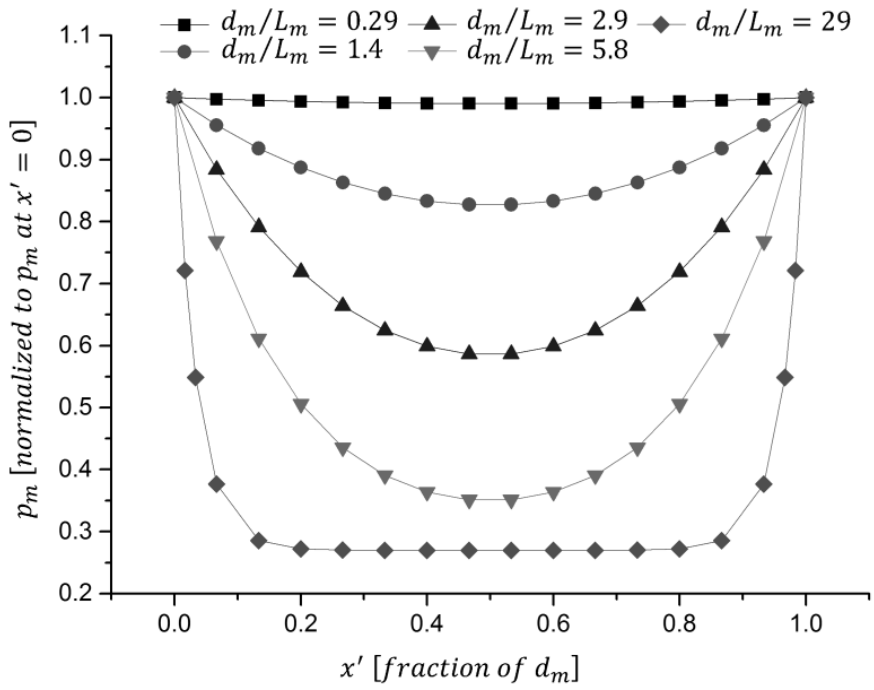

Figure 3.5.3.1. Minority carrier concentration as a function of position in contacted areas. Minority carrier concentration is normalized to the minority carrier concentration at the edge of contacted areas. Position is normalized to contacted area width. Parameters used in the simulation were: $G_0 = 1.05 \cdot 10^{19} cm^{-3} s^{-1}$, $\tau_p = 100 \mu s$, $\tau_m = 1 \mu s$, $D_p = 12 cm^2 \cdot s^{-1}$, $p_0 = 7.7 \cdot 10^4 cm^{-3}$. *Contacted area width is varied.*

Note that the limits of effective diffusion lengths much smaller and much larger than the relevant characteristic sizes are analogous to the small-scale and large-scale limits identified in [Schöfthaler 1994], respectively.

In conclusions, the observations made in this section strongly justify the design rule that all characteristic feature sizes must be much smaller than the relevant diffusion lengths.

3.5.4. Experimental

We performed steady state photoluminescence (PL) imaging measurements on finished IBC (interdigitated back contact) solar cells to experimentally validate our model calculations. The structure and manufacturing process of these solar cells is described in section 1.4.2. In Table 3.5.4.1, we summarize several key performance parameters of the investigated samples.

Sample	$V_{oc}\ [mV]$	$J_{sc}\ [mA \cdot cm^{-2}]$	$FF\ [\%]$	$\eta\ [\%]$
a	690	41.0	80.4	22.7
b	687	41.5	80.2	22.9

Table 3.5.4.1. Key performance parameters of the samples used for validation of our one dimensional model (in-house measurements). Sample a has a low BSF contact fraction (2%), and sample b has a high BSF contact fraction (8%).

The solar cells have an asymmetrical structure consisting of an oxide passivated lowly doped front surface field on the front, and alternating highly doped emitter and back surface field (BSF) regions on the back. Both regions are contacted by point contacts, but the individual point contacts are small and very closely spaced, such that the corresponding contact recombination current can be lumped together with the recombination current of oxide passivated BSF and emitter areas. As a result, the recombination properties of the BSF and emitter regions can be described by the corresponding effective lifetimes. In addition, the BSF has a significantly higher J_0 than the emitter. Therefore, the interdigitated BSF and emitter areas form alternating regions with low and high effective lifetime, such that this structure corresponds to the structure modelled in our one dimensional model.

We performed photoluminescence measurements on such a structure. Since the radiative band-to-band recombination rate is proportional to the pn product, the photoluminescence (PL) signal coming from any small wafer area is proportional to the average pn product over the wafer thickness in that area. Therefore, the ratio of the PL signal at two different locations equals the ratio of the average pn product at those locations.

The use of infrared light for carrier excitation during photoluminescence imaging results in a uniform carrier generation rate, and the use of high lifetime wafers and adequate surface passivation ensures that the assumption of constant minority carrier concentrations over wafer thickness is reasonable. Therefore, during photoluminescence measurements the minority carrier concentration in the BSF and emitter fingers of our IBC cells can be described using Equations 3.5.2.10 and 3.5.2.11, with the low-lifetime BSF regions analogous to contacted regions, and the high lifetime emitter regions analogous to passivated regions. This allows the comparison of experimental photoluminescence data to model calculations.

Figure 3.5.4.1 shows such a comparison for two samples that are identical except for their BSF contact fraction. Sample a has a low BSF contact fraction (2%), and sample b has a high BSF contact fraction (8%). The symbols in Figure 3.5.4.1 are experimental data, the solid lines are simulations using our one dimensional model that have been calibrated to fit the experimental data. The only fitting parameters that were used were τ_m (here: effective lifetime of the BSF region) and τ_p (here: effective lifetime of the emitter region). For both samples, τ_p was found to be 1 ms, which a reasonable value, and it is consistent with the fact that the emitter was identical for both samples. τ_m was 700 μs for sample a and 550 μs for sample b, which is consistent with the fact that our BSF has a higher saturation current density than our emitter. It is also consistent with sample a having a smaller BSF contact fraction than sample b and that consequentially, sample a has a lower BSF saturation current density than sample b. Therefore, we have proved that our model shows excellent agreement with experiment.

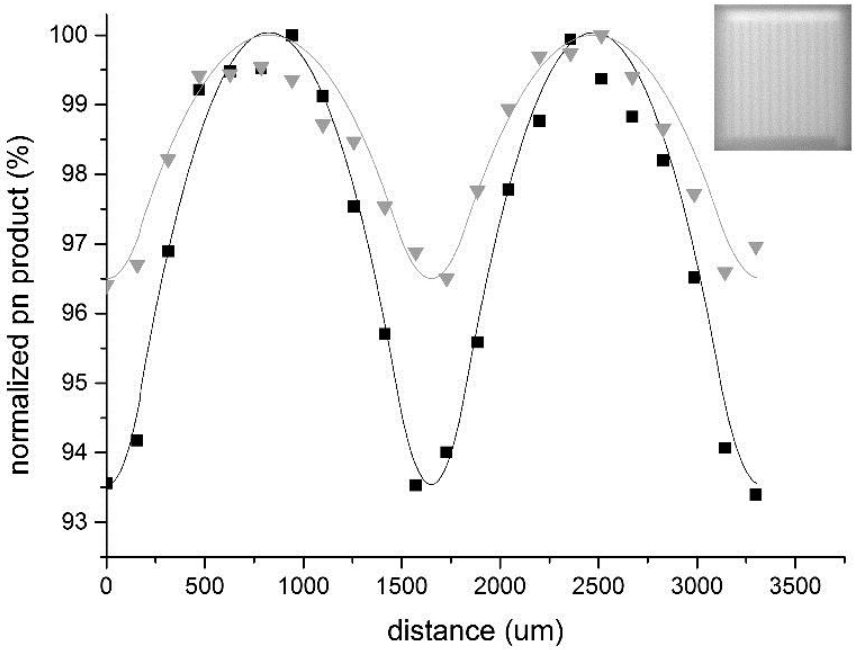

Figure 1 3.5.4.1. Normalized pn product as a function of position. The inset shows a photoluminescence image of sample a. The origin of the position coordinate is chosen to be the center of a BSF region. The symbols are experimental data, the lines are simulations from our one dimensional model that have been calibrated to fit the experimental data.

3.5.5. Conclusions

In conclusion, we analyzed injection level variations in test structures for the extraction of recombination characteristics of metal contacts on semiconducting substrates from photoconductance (QSSPC) measurements. We first made a very general derivation to show that injection levels are constant in the limit of small effective surface recombination velocities and large minority carrier diffusion lengths. The usefulness of this treatment lies in it showing how our method works best for high lifetime wafers with low surface recombination currents, irrespective of test structure geometry. Then, we used a simple one dimensional model to analyze minority carrier concentration variations in a practical setting, in the context of test structures for contact recombination current extraction from photoconductance measurements.

We showed how the injection level becomes constant in the wafer plane when effective diffusion lengths are much larger than the relevant characteristic feature sizes. Also, we discussed how minority carrier concentrations vary with position

when this limit is not satisfied, and we qualitatively described how such injection level variations influence the photoconductance measurement depending on the ratio of contact transfer length and contact size.

Because these results are based on a one dimensional model, they are only expected to qualitatively agree with experiments on test structures based on two dimensional lattices of point contacts. However, the simplicity of the expressions we derive from the one dimensional model make them useful tools for understanding the physics of point contact based test structures for the extraction of the recombination characteristics of metal contacts on semiconducting substrates from photoconductance measurements. In addition, the modelled structure accurately reflects the structure of the linear test structures described in section 3.10 such that the developed models could be directly applied to the analysis of such linear test structures. Finally, the excellent fit of our one dimensional model with experimental photoluminescence data suggests that it could also be a useful tool to study injection level variations in IBC silicon solar cells.

3.6. Out-of-plane injection level variations

3.6.1. Theory

As we have stressed before, recombination currents at the surfaces of silicon wafers depend on the excess carrier density at the surface. Therefore, the constancy of injection levels in the wafer bulk is a critical requirement in the context of QSSPC measurements on our test structure. It is only in the case of uniformly constant injection levels throughout the test structure bulk that the measurements can be easily interpreted because only in this case, *"the"* injection level is well defined. Roughly speaking, injection levels may vary either over wafer thickness or in the wafer plane. We discussed in-plane injection levels in section 3.5. The effect of out-of-plane injection level variations in blanket test structures during QSSPC measurements is discussed in [Cuevas 1999]. In this chapter, we investigate out-of-plane injection level variations in the context of our test structure.

In typical test structures, the design rules laid out in the previous section are followed such that the contacted area size and the contact area spacing are much smaller than the effective diffusion lengths in contacted and passivated areas, respectively. For a representative example for the experimental structures considered in the present dissertation, wafer thickness is about $150\,\mu m$, the effective lifetime in passivated areas is in the order of 1 ms and the effective lifetime in contacted areas is in the order of 0.1 ms. This corresponds to effective hole diffusion lengths in passivated areas of order 1 mm and to effective hole diffusion lengths in contacted areas of order 300 µm. Typically, the contact area spacing is in the order of 100 µm or less, and the size of the point contacts is typically around 15 µm.[1] Accordingly, the effective diffusion lengths in contacted and passivated areas are much larger than the size of the contacted areas. Extrapolating the findings of section 3.5 to test structures based on simple square lattices of point contacts, we can conclude that in-plane excess carrier density variations are mitigated in this typical example. However, from the simulations in section 2.3, out-of-plane excess carrier density variations may be significant in this typical example, especially for large effective surface recombination velocities (e.g. because of large contact fractions and/or high injection levels) and/or for asymmetric test structures (as used in the present dissertation).

[1] Note that the contact area spacing is smaller for higher contact fractions in the test structures used in this dissertation. Also, for the lithography-based test structures, the diameter of the circular contacts was kept fixed at approximately 15 µm.

The choice for asymmetric, single side contacted test structures, was primarily made because of difficulties related to the alignment of features on opposite sides of a wafer. Also, the generation profile changes with changing contact fraction for two-side contacted test structures, which complicates the measurement interpretation. In addition, partial shading in 2 side contacted test structures could introduce additional in-plane excess carrier density variations due to inhomogeneous in-plane excess carrier density generation profiles.

We now discuss the influence of injection level variations on extracted saturation current densities for typical test structures, with properly designed contact size and pitch such that in-plane injection level variations are avoided. The test structure is based on a passivated wafer. One side of the wafer, denoted front (f), is passivated and the other side, denoted back (b), is partly passivated and partly contacted. The passivation is imperfect though such that there is still some recombination in the passivated areas; as is the case with, for example, the passivation of silicon surfaces with thermal silicon oxide layers. We express surface recombination currents in terms of saturation current densities and the pn product.

First, we consider the steady state recombination current in passivated and contacted areas separately. Note that because we assume constant in-plane excess carrier concentrations, and we because we consider a quasi-neutral region, only current transport in the out-of-plane direction needs to be considered.

Following a basic mass balance, the steady state recombination current in passivated areas is given by:

$$J_{R,diel} = \frac{q\Delta p_a W}{\tau_p} = q\int_W R_B\, dx + qS_{diel}\Delta p(f) + qS_{diel}\Delta p(b), \tag{3.6.1.1}$$

in which Δp_a is the average carrier concentration over the wafer thickness, τ_p is the effective lifetime in passivated areas, R_B is the volumetric bulk recombination rate, and S_{diel} is the effective surface recombination velocity at the passivated surfaces. The x-direction is the out-of-plane direction.

Using Equation 2.2.4.5,

$$\int_W R_B\, dx \approx W\frac{\Delta p_a}{\tau_b}. \tag{3.6.1.2}$$

A combination of Equations 3.6.1.1 and 3.6.1.2 yields:

$$\frac{1}{\tau_p} = \frac{1}{\tau_b} + \frac{S_{diel}}{W}\frac{\Delta p(f) + \Delta p(b)}{\Delta p_a}. \tag{3.6.1.3}$$

Again following a basic mass balance, the steady-state recombination current in contacted areas is given by:

$$J_{R,met} = \frac{q\Delta p_a W}{\tau_m} = q\int_W R_B\, dx + qS_{diel}\Delta p(f) + qS_{met}\Delta p(b), \quad (3.6.1.4)$$

which can be rewritten as:

$$\frac{1}{\tau_m} = \frac{1}{\tau_b} + \frac{S_{diel}\Delta p(f) + S_{met}\Delta p(b)}{\Delta p_a W}. \quad (3.6.1.5)$$

The recombination current in the test structure is the area-weighted average of the recombination current in contacted and passivated areas:

$$J_{R,tot} = \frac{q\Delta p_a W}{\tau_{eff}} = J_{R,diel} + C_{met}\left[J_{R,met} - J_{R,diel}\right], \quad (3.6.1.6)$$

in which τ_{eff} is the effective lifetime describing the recombination behavior of the entire test structure.

Combination of Equations 3.6.1.1 to 3.6.1.6 yields:

$$\frac{1}{\tau_{eff}} = \frac{1}{\tau_p} + C_{met}\left[\frac{1}{\tau_m} - \frac{1}{\tau_p}\right], \quad (3.6.1.7)$$

which has the same form as Equation 3.2.3.2.

Effective surface recombination velocities S_{eff} can, in some cases, be more elegantly written as saturation current densities J_0 over a wider range of injection levels. This is for example the case for the description of recombination currents in contacted or passivated diffused junctions. Combination of Equations 2.1.2.24 and 2.1.2.29 yields the following relation between S_{eff} and J_0:

$$S_{eff} = J_0 \frac{\Delta p(N_D + \Delta p)}{qn_i^2}, \quad (3.6.1.8)$$

in which Δp denotes the recombination current at the relevant surface. Combination of Equations 3.6.1.3, 3.6.1.6, 3.6.1.7, and 3.6.1.8 now yields:

$$\frac{1}{\tau_{eff}} = \frac{1}{\tau_b} + J_{0,diel}\left[\frac{\Delta p(f)}{\Delta p_a}\frac{N_D + \Delta p(f)}{qn_i^2 W} + \frac{\Delta p(b)}{\Delta p_a}\frac{N_D + \Delta p(b)}{qn_i^2 W}\right]$$

$$+C_{met}\left[J_{0,met} - J_{0,diel}\right]\frac{\Delta p(b)}{\Delta p_a}\frac{N_D + \Delta p(b)}{qn_i^2 W}. \quad (3.6.1.9)$$

Note that we used that the average injection level Δp_a equals the measured injection level Δp_m, which is used in defining the steady state effective lifetime ($\tau_{eff} \equiv \Delta p_m / G$), with G the generation rate. $\Delta p(f)$ is the injection level at the front, $\Delta p(b)$ is the injection level at the back and all other symbols have been defined before.

We now assume for simplicity that the recombination current is dominated by recombination in the junctions (τ_b^{-1} negligible), and we use the following notation: a subscript m denotes a measured quantity, a subscript r denotes the actual quantity, the suffix $\{AI\}$ denotes an arbitrary injection level measurement (application of Equation 3.2.2.7), and the suffix $\{HI\}$ denotes a high injection level

measurement (application of Equation 3.2.2.10). Using the arbitrary injection level technique (Equation 3.2.2.7), the measured value of $J_{0,diel}$ is found as:

$$J_{0,diel,m}\{AI\} = \frac{qn_i^2 W}{2(N_D+\Delta p_a)}\tau_{eff}^{-1}(C_{met}=0), \tag{3.6.1.10}$$

and therefore:

$$\frac{J_{0,diel,m}}{J_{0,diel,r}}\{AI\} = \frac{pn(f)+pn(b)}{2pn_a}, \tag{3.6.1.11}$$

in which $pn_a = \Delta p_a(N_D + \Delta p_{av})$, $pn(f)$ is the pn product at the front surface and $pn(b)$ is the pn product at the back surface. Using the high injection level technique, $J_{0,diel}$ is found as:

$$J_{0,diel}\{HI\} = \frac{qn_i^2 W}{2}\frac{d\tau_m^{-1}}{d\Delta p_a}(C_{met}=0), \tag{3.6.1.12}$$

and therefore:

$$\frac{J_{0,diel,m}}{J_{0,diel,r}}\{HI\} = \frac{d}{d\Delta p_a}\left[\frac{pn(f)+pn(b)}{2\Delta p_a}\right]. \tag{3.6.1.13}$$

We now discuss how $J_{0,met} - J_{0,diel}$ is influenced by non-constant injection levels. We make the simplifying assumption that $J_{0,diel}$ is sufficiently small such that the change in the term comprising $J_{0,diel}$ of Equation 3.6.1.9 with C_{met} (because the injection level ratios vary with C_{met}) has negligible influence on the slope of τ_{eff}^{-1} as a function of C_{met}. Using the arbitrary injection level technique (Equation 3.2.2.7), $J_{0,met} - J_{0,diel}$ is found from:

$$\left[J_{0,met} - J_{0,diel}\right]_m\{AI\} = \frac{qn_i^2 W}{N_D+\Delta p_a}\frac{d\tau_{eff}^{-1}}{dC_{met}}, \tag{3.6.1.14}$$

which yields:

$$\frac{\left[J_{0,met}-J_{0,diel}\right]_m}{\left[J_{0,met}-J_{0,diel}\right]_r}\{AI\} = \frac{pn(b)}{pn_a}, \tag{3.6.1.15}$$

For the high injection level technique (Equation 3.2.2.10):

$$\left[J_{0,met} - J_{0,diel}\right]_m\{HI\} = qn_i^2 W\frac{d}{dC_{met}}\left[\frac{d\tau_{eff}^{-1}}{d\Delta p_a}\right], \tag{3.6.1.16}$$

and therefore:

$$\frac{\left[J_{0,met}-J_{0,diel}\right]_m}{\left[J_{0,met}-J_{0,diel}\right]_r}\{HI\} = \frac{d}{d\Delta p_a}\left[\frac{pn(b)}{\Delta p_a}\right]. \tag{3.6.1.17}$$

A critical observation derived from this analysis is that saturation current densities extracted using the high injection and arbitrary injection techniques are different when injection levels are not constant over the wafer thickness.

In order to evaluate the effect of non-constant injection levels on extracted saturation current densities, we solve for the minority carrier concentration over

the wafer thickness using Equation 2.3.2, which we repeat here for ease of reference:

$$L_D^2 \frac{d^2p}{dx^2} - p + p_0 + \tau_b G = 0, \tag{3.6.1.18}$$

with x the position coordinate perpendicular to the wafer plane. The boundary conditions are the statement that recombination currents at surfaces equal diffusion currents flowing towards those surfaces:

$$J_R = J_0 pn/qn_i^2 = qD_p \nabla p \cdot \vec{n}, \tag{3.6.1.19}$$

in which $\vec{n}$ is an outward-pointing unit vector normal to the surface.

Solving Equation 3.6.1.18 with boundary condition 3.6.1.19 applied to both surfaces (while also substituting the appropriate saturation current density) allows plotting $pn(b)/pn_a$ (Figure 3.6.1.1) and $d/d\Delta p_a\,[pn(b)/\Delta p_a]$ (Figure 3.6.1.2) as a function of Δp_a. By comparison with Equations 3.6.1.15 and 3.6.1.17, these are the ratios of the measured and actual values of $J_{0,met} - J_{0,diel}$ for extraction with the arbitrary injection level technique and for extraction with the high injection level technique, respectively. Note that we made the approximation that $J_{0,met} - J_{0,diel}$ is found from the derivative of inverse effective lifetime with respect to C_{met} whereas in practice, we use a large C_{met} range for $J_{0,met} - J_{0,diel}$ fitting because of enhanced numerical stability.

In the simulations, we take $J_{0,diel} = 0$ such that $J_{0,f} = 0$, with $J_{0,f}$ the saturation current density at the front surface. Also, $J_{0,b} = C_{met} J_{0,met}$ is varied, with $J_{0,b}$ the saturation current density at the back surface. Other parameters used in the simulations are: $W = 160\mu m$, $n_i = 7.4 \cdot 10^9 cm^{-3}$, $N_D = 1 \cdot 10^{15} cm^{-3}$, $\tau_b = 1ms$, and $D_p = 12 cm^2 s^{-1}$. Note that we merely show $d/d\Delta p_a\,[pn(b)/\Delta p_a]$ at relatively low injection levels for illustrative purposes and we do not intend to suggest that Kane and Swanson's method for J_0 extraction [Kane 1985] should be used at injection levels where Shockley-Read-Hall recombination may significantly affect the injection level dependence of the effective lifetime.

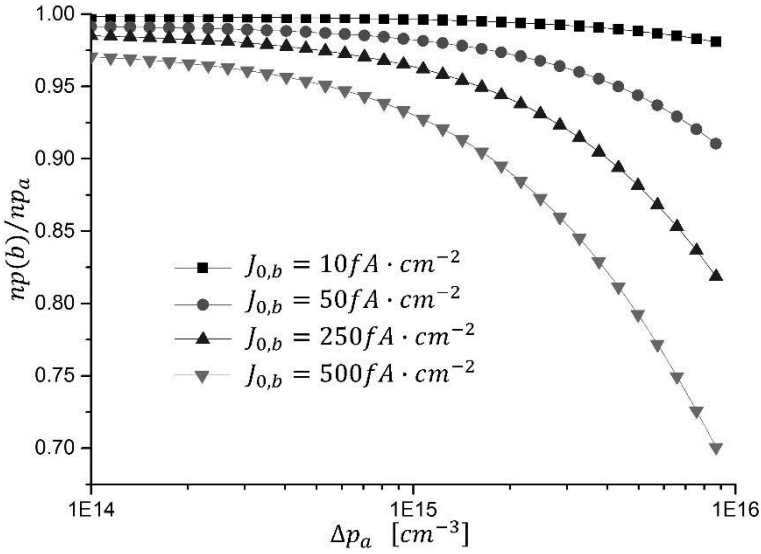

Figure 3.6.1.1. $np(w)/np_a$, *which equals* $[J_{0,met} - J_{0,diel}]_m / [J_{0,met} - J_{0,diel}]_r \{AI\}$, *as a function of* Δp_a, *for various values of* $J_{0,b}$.

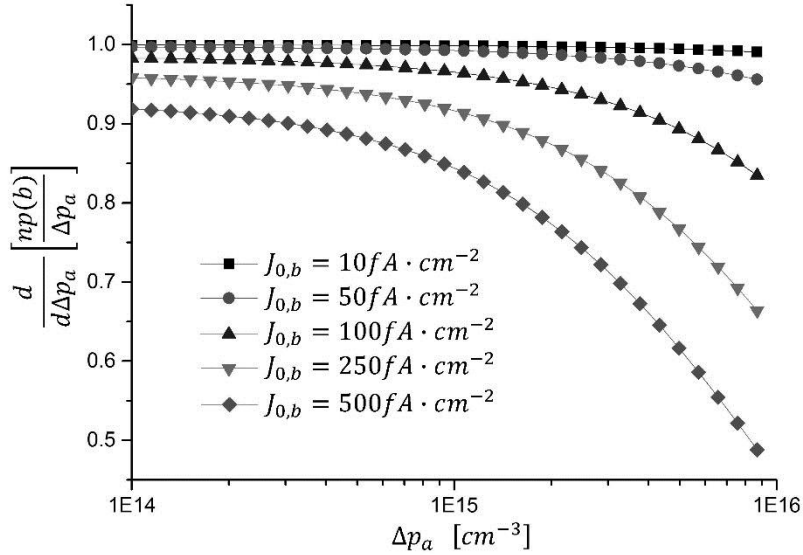

Figure 3.6.1.2. $d[np(w)/\Delta p_a]/d\Delta p_a = [J_{0,met} - J_{0,diel}]_m / [J_{0,met} - J_{0,diel}]_r \{HI\}$, *as a function of the average injection level* Δp_a, *for various values of* $J_{0,b}$.

Figures 3.6.1.1 and 3.6.1.2 show very similar trends. First, parasitic effects due to injection level variations over the wafer thickness are more severe for higher $J_{0,b}$,

which is consistent with the notion that injection level variations are more pronounced for higher effective surface recombination velocities (see section 2.3). Therefore this parasitic effect can be reduced by reducing the contact fraction (and thereby reducing $J_{0,b}$). Also, this parasitic effect is more severe at higher injection levels. This is related to effective surface recombination velocities of junctions characterized by constant saturation current densities and unit ideality factor going up with injection level as $S_{eff} = J_0 q^{-1} n_i^{-2}(N_D + \Delta p)$, with Δp the excess carrier concentration at the surface of interest. Finally, note that the vertical scale in Figure 3.6.1.1 is different from the vertical scale in Figure 3.6.1.2. A comparison between figures 3.6.1.1 and 3.6.1.2 clearly shows that the effect of injection level variations is generally more severe when saturation current densities are extracted using the high injection level technique, Equation 3.2.2.10, compared to when they are extracted using the arbitrary injection level technique, Equation 3.2.2.7.

In conclusion, non-ideal effects due to injection level variations cause underestimations of saturation current densities. These parasitic effects are more pronounced at high injection levels compared to low injection levels and saturation current densities extracted using the high injection level technique, Equation 3.2.2.10, are more prone to these parasitic effects than saturation current densities extracted using the arbitrary injection level technique, Equation 3.2.7. We show that non-ideal effects due to injection level variations over the wafer thickness can be reduced by reducing the contact fraction, and by extracting $J_{0,met} - J_{0,diel}$ at lower injection levels. From our discussion in sections 2.3 and 3.5.1, they can also be reduced by using thinner wafers.

3.6.2. Experimental

In Table 3.6.2.1, we show saturation current densities extracted on three samples with the same emitters, using the arbitrary injection level technique (Equation 3.2.2.7) and the high injection level technique (Equation 3.2.2.10). Measurements are shown for wafers in which oxide openings were covered with metal and for the same wafers after the metal layer had been etched. For the samples without metal, the exposed contact regions have a very high surface recombination velocity due to the lack of surface passivation, which mimics the recombination characteristics of the silicon-metal interface. However, due to the absence of metal, any parasitic effects related to current flow through the metal contacts instead of through the semiconductor are avoided. In that sense, this experiment is similar to the one presented in section 3.4.5, but the present focus is the effect of non-constant injection levels over the wafer thickness

rather than the effect of current flow through point contacts. The notation AI means that saturation current densities are extracted using the arbitrary injection technique, Equation 3.2.2.7. The notation HI means that saturation current densities are extracted using the high injection level technique, Equation 3.2.2.10. Measurements were done on samples in which oxide openings were covered with aluminum layers and on samples in which the aluminum layers were etched.

First note that there is significant spread in the contact saturation current density measurements. This spread is not expected to be related to variability in the emitter diffusion process. It is instead thought to be related to contact fraction-related errors. As we will show in section 3.9, the contact opening fraction has to be known accurately in order to allow for the reliable extraction of contact saturation current densities.

	$J_{0,met}$ - $J_{0,diel}$ [fA·cm^{-2}] AI	$J_{0,met}$ [fA·cm^{-2}] HI	$J_{0,diel}$ [fA·cm^{-2}] AI	$J_{0,diel}$ [fA·cm^{-2}] HI
Sample 1 with metal	441±55	381±115	22±3	21±7
Sample 1 after metal etch	479±90	441±149	23±6	21±9
Sample 2 with metal	471±46	349±108	25±3	22±7
Sample 2 after metal etch	516±52	378±112	26±3	22±7
Sample 3 with metal	497±112	379±212	25±8	21±15
Sample 3 after metal etch	562±140	405±288	25±10	21±20

Table 3.6.2.1. Saturation current density measurements on three n-type silicon wafers with the same emitter, extracted assuming an intrinsic concentration of $7.401 \cdot 10^{9} cm^{-3}$*. All saturation current densities were extracted at an injection level of* $6 \cdot 10^{15} cm^{-3}$*.*

$J_{0,met}$, or equivalently $J_{0,met} - J_{0,diel}$, extracted on samples with metal is consistently lower than $J_{0,met}$ extracted on samples without metal. This can be explained that for aluminum contacts on the emitters in these samples, the contact's transfer length was smaller than the contact diameter. Therefore, the effect of current flow through the point contacts is not negligible, which has been explained in section 3.4.

Also, $J_{0,met}$ extracted using the high injection level technique is consistently lower than $J_{0,met} - J_{0,diel}$ extracted using the arbitrary injection level technique. This is explained from the simulations in section 3.6.1: Figures 3.6.2.1 and 3.6.2.2 clearly show that excess carrier density variations over the wafer thickness result in more severe $J_{0,met}$ underestimations when the high injection technique is used. In section 3.4, we predicted that current flow through point contacts also results in $\left[J_{0,met} - J_{0,diel}\right]_{m,AI} > \left[J_{0,met} - J_{0,diel}\right]_{m,HI}$. Therefore, it would be expected that the difference between $\left[J_{0,met} - J_{0,diel}\right]_{m,AI}$ and $\left[J_{0,met} - J_{0,diel}\right]_{m,HI}$ would be larger for contacted samples than for uncontacted samples. However, the data in Table 3.6.2.1 do not support this prediction, which is suspected to be related to the uncertainty in the measurements being too large for this effect to be visible in the experiment.

Finally, $J_{0,diel}$ extracted using the arbitrary injection level technique is consistently larger than $J_{0,diel}$ extracted using the high injection level technique. This is suggested to be primarily due to $J_{0,diel}$ extracted using the arbitrary injection level technique being an upper bound on $J_{0,diel}$ because it has a contribution of bulk recombination.

In Figure 3.6.2.1, we show $J_{0,met} - J_{0,diel}$ for two samples. Sample a has a relatively shallow emitter with low surface concentration at both wafer surfaces, similar to samples a, b and c in Table 3.6.2.1. Therefore, sample a has a high $J_{0,met}$. Sample b has a relatively deep back surface field with a high surface concentration at both wafer surfaces. Therefore, sample b has a relatively low $J_{0,met}$. $J_{0,diel}$ is $41 fA \cdot cm^{-2}$ for sample a and $55\ fA \cdot cm^{-2}$ for sample b, as extracted by Kane and Swanson's method [Kane 1985] at an injection level of $1 \cdot 10^{16} cm^{-3}$.

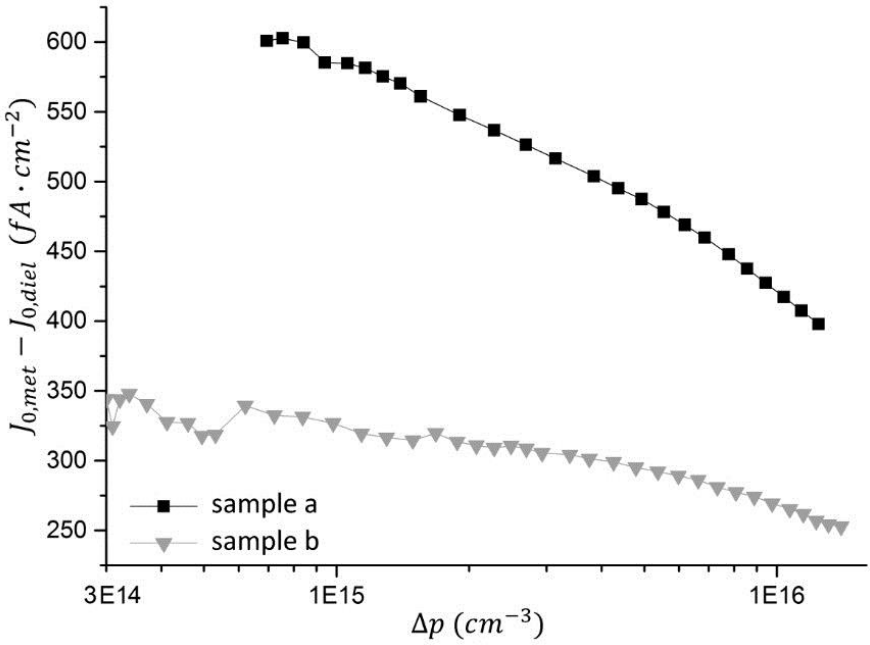

Figure 3.6.2.1. $J_{0,met} - J_{0,diel}$ as a function of the injection level. $J_{0,met} - J_{0,diel}$ was extracted from effective lifetime data using the arbitrary injection technique, Equation 3.2.2.7. $J_{0,met}$ test structures were made on n-type wafers. Samples a and b feature a shallow boron emitter and a deep phosphorous back surface field, respectively.

$J_{0,met} - J_{0,diel}$ decreases strongly with increasing injection level for sample a. By comparison with Figure 3.6.1.1, this is the hallmark injection level dependence introduced by non-constant injection levels. For sample b, $J_{0,met} - J_{0,diel}$ also decreases with the injection level, but the decrease is significantly less pronounced than for sample a. This is related to the $J_{0,met}$ being significantly lower for sample b. As a result, there are less injection level variations in the quasi neutral wafer bulk, and less associated artificial injection level dependence of extracted saturation current densities. In conclusion, the theory and experiments presented in this section show that the $J_{0,met}$ test structure proposed in [Deckers 2013] work better for lower $J_{0,met}$, and that $J_{0,met}$ (actually $J_{0,met} - J_{0,diel}$) is preferably extracted using the arbitrary injection level technique (Equation 3.2.2.7) at low injection levels.

3.7. Bulk doping level

In this section, we investigate the consequence of using incorrect bulk doping levels for the extraction of saturation current densities using the arbitrary and high injection level techniques, Equations 3.2.2.7 and 3.2.2.10 respectively. Since Equation 3.2.2.7 depends explicitly on the bulk doping level, it turns out that accurate knowledge of the bulk doping level is an essential prerequisite for the extraction of sensible contact saturation current densities using the arbitrary injection technique, Equation 3.2.2.7. We shall show that contact saturation current densities extracted using the high injection technique, Equation 3.2.2.10, are significantly less influenced by the use of incorrect bulk doping levels.

In our discussion, we disregard the fact that using incorrect doping levels results in the use of incorrect mobility during effective lifetime measurements, which does result in errors in measured injection levels and effective lifetimes. However, this effect is much smaller than the effect of incorrect doping levels on saturation current densities extracted using Equation 3.2.2.7 since the dependence of mobility on the doping level is only minor in the relevant doping level range ($\sim 10^{15} cm^{-3}$) [Li 1978, Masetti 1983].

Consider two contact saturation current densities $J_{0,met,1}$ and $J_{0,met,2}$ extracted using the arbitrary injection level technique, Equation 3.2.2.7. Both contact saturation current densities represent the same recombination current with unit ideality factor, but they have been extracted using different assumed doping levels $N_{D,1}$ and $N_{D,2}$, respectively. From Equation 3.2.2.7, it is readily found that:

$$\left[J_{0,met} - J_{0,diel}\right]_1 = \frac{qn_i^2 W}{N_{D,1}+\Delta p} \frac{d\tau_{eff}^{-1}}{dC_{met}}, \tag{3.7.1}$$

in which $\left[J_{0,met} - J_{0,diel}\right]_1$ is the value for $J_{0,met} - J_{0,diel}$ that was extracted assuming a bulk doping level $N_{D,1}$. $\left[J_{0,met} - J_{0,diel}\right]_2$ is found analogously:

$$\left[J_{0,met} - J_{0,diel}\right]_2 = \frac{qn_i^2 W}{N_{D,2}+\Delta p} \frac{d\tau_{eff}^{-1}}{dC_{met}}. \tag{3.7.2}$$

Division of Equation 3.7.1 by Equation 3.7.2 then yields:

$$\frac{\left[J_{0,met}-J_{0,diel}\right]_1}{\left[J_{0,met}-J_{0,diel}\right]_2} = \frac{\Delta p+N_{D,1}}{\Delta p+N_{D,2}}. \tag{3.7.3}$$

From Equation 3.7.3, we can draw the following conclusions regarding the use of incorrect doping levels in the extraction of $J_{0,met} - J_{0,diel}$ using Equation 3.2.2.7: $\left[J_{0,met} - J_{0,diel}\right]_1 = \left[J_{0,met} - J_{0,diel}\right]_2$ in the high injection limit but $\left[J_{0,met} - J_{0,diel}\right]_1 =$

$\left[J_{0,met} - J_{0,diel}\right]_2 N_{D,1}/N_{D,2}$ in the low injection limit. As a result, artificial injection level dependence is introduced in the intermediary regime.

For samples with negligible bulk recombination, Equation 3.2.2.7 can also be used to extract $J_{0,diel}$ as a function of the injection level. Following a derivation analogous to the derivation of Equation 3.7.3, it follows that the same artificial injection level dependence is introduced in $J_{0,diel}$ when the incorrect bulk doping level is used.

The assumed doping level during J_0 extraction does not influence saturation current densities extracted using Equation 3.2.10, except through the dependence of mobility on the doping level. This effect is much less significant since, as mentioned before, the doping dependence of mobility is not very significant in the relevant bulk doping level range ($\sim 10^{15} cm^{-3}$) [Li 1978, Masetti 1983]. The reason for this relative bulk doping independence of saturation current densities extracted using Equation 3.2.10 is that the slope inverse lifetime versus injection level is not directly influenced by the assumed bulk doping level.

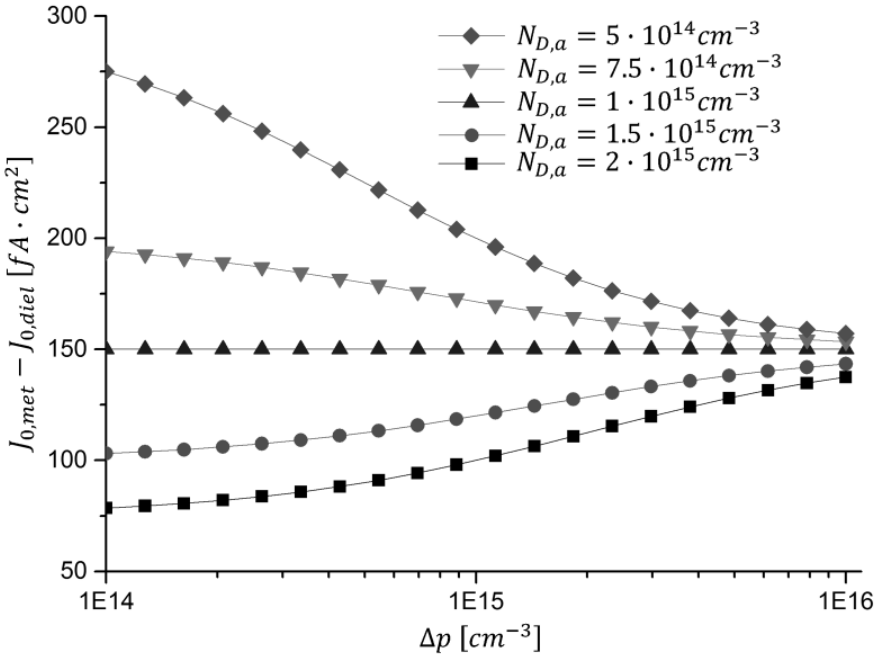

Figure 3.7.1. $J_{0,met} - J_{0,diel}$ extracted using Equation 3.2.2.7 assuming a variety of bulk doping levels. The actual doping level is $10^{15} cm^{-3}$, the actual value of $J_{0,diel}$ is $50 fA \cdot cm^{-2}$, and the actual value of $J_{0,met} - J_{0,diel}$ is $150 fA \cdot cm^{-2}$.

In Figure 3.7.1, the effect of the assumption of incorrect doping levels on J_0 extraction using Equation 3.2.2.7 is demonstrated for a number of assumed bulk

doping levels $N_{D,A}$. We simulated effective lifetimes as a function of injection level for a wafer with an actual bulk doping level of $10^{15} cm^{-3}$. The actual value of $J_{0,diel}$ is $50\ fA \cdot cm^{-2}$ and the actual value of $J_{0,met}$ is $200\ fA \cdot cm^{-2}$. Bulk recombination was taken to be negligible. As expected, the $J_{0,met}$ measurement is not corrupted when the correct doping level is used. When the doping level is over estimated, $J_{0,met} - J_{0,diel}$ is underestimated at low injection levels and vice versa. The assumed doping level has no influence on $J_{0,met} - J_{0,diel}$ in the high injection limit, which is consistent with Equation 3.7.3. In Figure 3.7.2, we show that the same artificial injection level dependence is introduced in $J_{0,met} - J_{0,diel}$ and $J_{0,diel}$ when bulk recombination is negligible such that $J_{0,diel}$ can be extracted using Equation 3.2.2.7.

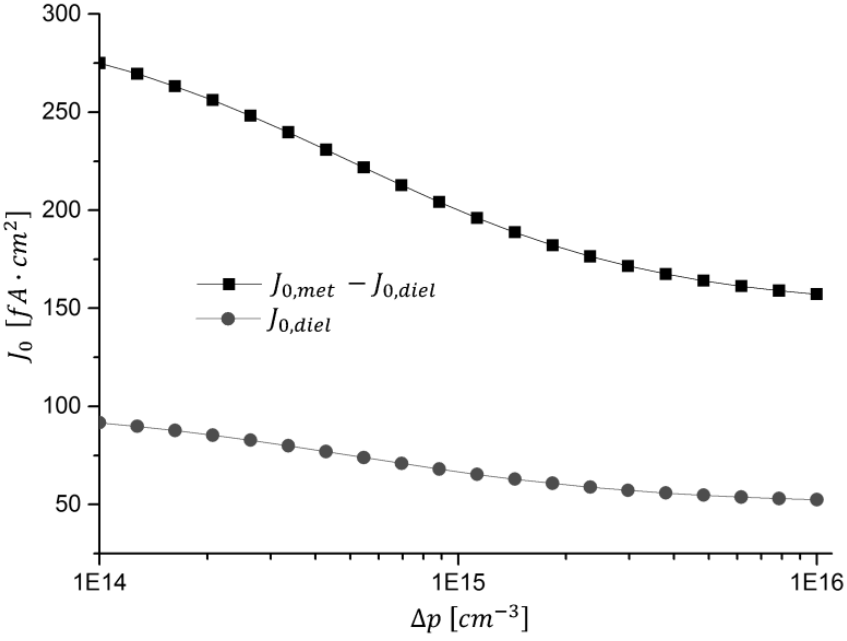

Figure 2.7.2. $J_{0,met} - J_{0,diel}$ and $J_{0,diel}$ extracted using Equation 3.2.2.7 assuming a doping level of $5 \cdot 10^{14} cm^{-3}$ whereas the actual doping level is $1 \cdot 10^{15} cm^{-3}$. Note that the artificially introduced injection dependence of both $J_{0,met} - J_{0,diel}$ and $J_{0,diel}$ is given by Equation 3.7.3.

3.8. Ideality factor[1]

In this dissertation, Equations 3.2.2.7 and 3.2.2.10; the arbitrary and high injection techniques, respectively; have been used almost exclusively for the description of recombination currents in contacted junctions. The validity of Equations 3.2.2.7 and 3.2.2.10 is limited to the case of junction saturation current densities featuring unit ideality factors. However, the assumption of unit ideality factors is by no means strictly necessary for the applicability of our method. In fact, at the heart of our method lies the more general Equation 3.2.2.4 ($R = R_{bulk} + 2R_{diel} + C_{met}[R_{met} - R_{diel}]$), which is simply the statement that the total recombination rate in the $J_{0,met}$ test structure is the area-weighed recombination rate in contacted and passivated areas. In this section, we study the application of our method to the characterization of contact recombination currents with non-unit ideality factors.

3.8.1. Local ideality factor

Specifically at low injection levels, space charge region recombination may be a significant part of the total junction recombination current J_R, resulting in ideality factors that are bigger than one. The presence of space charge region recombination is commonly modelled using the well-known two-diode model. In the two-diode model, the recombination current is modelled using two diodes in parallel. One diode has a unit ideality factor, and the other has an ideality factor 2, such that the recombination current J_R can be written as:

$$J_R = J_{0,1}\, exp\left(\frac{qV}{kT}\right) + J_{0,2}\, exp\left(\frac{qV}{2kT}\right), \tag{3.8.1.1}$$

in which $J_{0,1}$ is the saturation current density that corresponds to the recombination current with unit ideality factor, $J_{0,2}$ is the saturation current density that corresponds to the recombination current with ideality factor 2, and all other symbols have been defined before. With Equation 2.1.2.14, i.e. the relation between the pn product and the quasi Fermi level splitting, Equation 3.8.1.1 becomes:

$$J_R = J_{0,1}\frac{\Delta p(N_D+\Delta p)}{n_i^2} + J_{0,2}\sqrt{\frac{\Delta p(N_D+\Delta p)}{n_i^2}}. \tag{3.8.1.2}$$

Equation 3.8.1.1 can be rewritten in terms of a single exponential by introducing a function m which is defined such that:

[1] This section is partly based on [Chen 2014]

$$J_R = J_{0,m}\, exp\frac{qV}{mkT}. \quad (3.8.1.3)$$

m is the ideality factor which is a function of V, and $J_{0,m}$ is a constant. For a junction recombination current that consists partly of a diffusion current and partly of a space charge recombination current, $1 \leq m \leq 2$. Equation 3.8.1.3 can also be rewritten in terms of the pn product:

$$J_R = J_{0,m}\left[\frac{\Delta p(N_D+\Delta p)}{n_i^2}\right]^{\frac{1}{m}}. \quad (3.8.1.4)$$

The junction recombination current is assumed to have a unit ideality factor in Equation 3.2.2.7:

$$J_R = J_{0,1}\frac{\Delta p(N_D+\Delta p)}{n_i^2}. \quad (3.8.1.5)$$

Combination of Equations 3.8.1.4 and 3.8.1.5 yields:

$$J_{0,1} = J_{0,m}\left[\frac{\Delta p(N_D+\Delta p)}{n_i^2}\right]^{\frac{1-m}{m}}. \quad (3.8.1.6)$$

When $m > 1$, the exponent in Equation 3.8.1.6 is negative and $J_{0,1}$ is found to decrease with increasing injection level. This is illustrated in Figure 3.8.1.1.

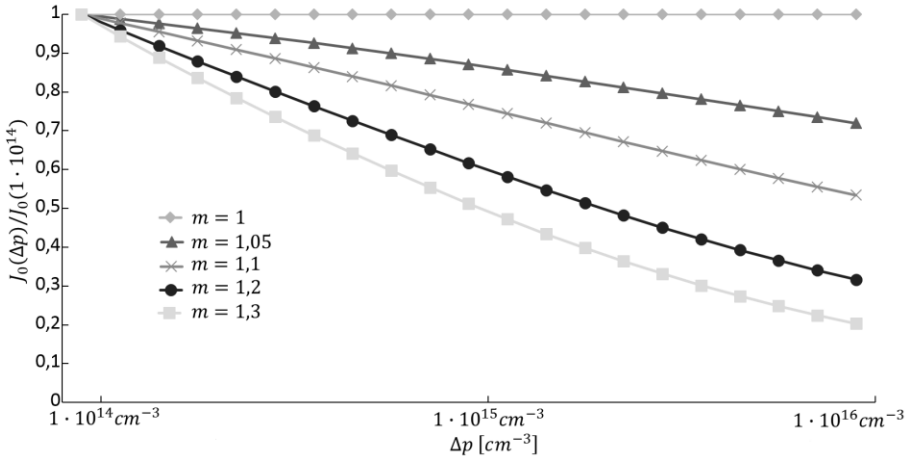

Figure 3.8.1.1. Normalized saturation current density as a function of the injection level, for recombination currents with ideality factors m which are greater or equal than one. The saturation current density was normalized at an injection level of $1\cdot 10^{14} cm^{-3}$.

In [Chen 2014], the observation that larger-than-unity ideality factors can give rise to seemingly decreasing saturation current densities was used for the interpretation of damage introduced during contact opening using laser ablation. Experimentally extracted contact saturation current densities from [Chen 2014]

are shown in Figure 3.8.1.2 and details on the laser ablation process can be found this reference.

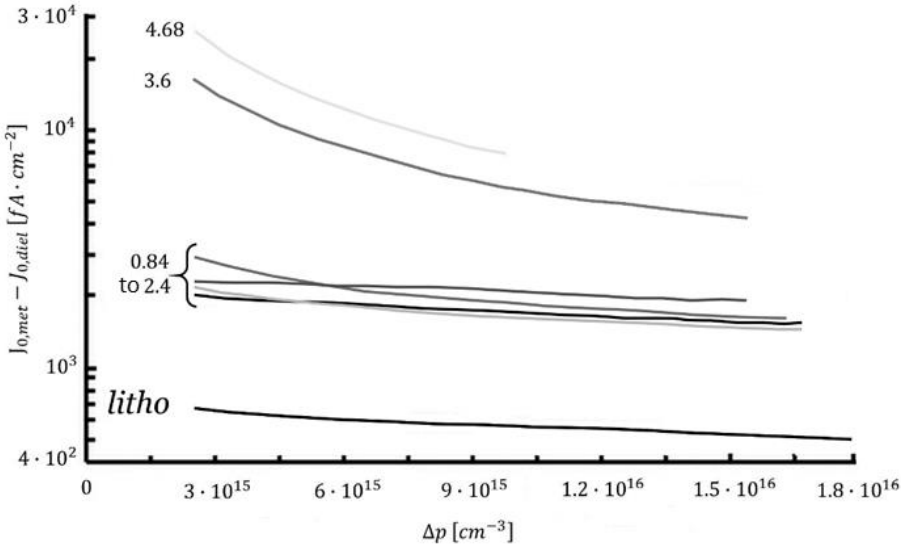

Figure 3.8.1.2. Contact saturation current densities for laser-opened contacts on Boron-diffused junctions (for the exact doping profile, refer to the emitter profile in Figure 4.1.1). The number next to the curves indicate the laser energy applied during ablation of the contact openings, in J/cm^2. A sample with contact openings defined using lithography (the bottom curve) is shown as a reference, reproduced and adapted with permission from [Chen 2014]. The saturation current densities in this graph are reported for $n_i = 9.7 \cdot 10^9\ cm^{-3}$.

The contact recombination current data shown in Figure 3.8.1.2 are shown for laser-opened and lithography-opened samples which underwent identical processing except for the contact opening step. The data relay that contact saturation current densities for the investigated laser-opened contacts are higher than contact saturation current densities for contacts opened using our baseline lithography process. In addition, there is a range of laser energies (0.84-2.4 J/cm^2) which yield similar contact recombination currents. Applied energies which are higher than this particular range result in higher contact recombination current densities, which indicates increased damage caused by the laser ablation process at higher energies.

In addition, the injection level dependence of $J_{0,met} - J_{0,diel}$ is much higher for the highest applied laser energies (3.6-4.68 J/cm^2) compared to the lower laser energies. As discussed before, this could be related to space charge region recombination resulting in higher-than-one ideality factors. However, it could also be an artifact related to non-constant injection levels over the wafer thickness, which has been discussed in section 3.6. Despite this reservation, it should be

noted that excess carrier density variations over wafer thickness cannot explain the cross-over of curves in Figure 3.8.12. The crossing over of the $J_{0,met} - J_{0,diel}$ curves seems to be a peculiar effect likely related to the presence significant space charge region recombination.

3.8.2. Two-diode fit of contact recombination currents

In this section, the application of a two-diode to the interpretation of recombination currents in junctions near surfaces is described. Reordering of Equation 3.8.1.2, and using $J_R = q\Delta p/\tau_{eff}$ when the junction recombination current is dominating yields an equation of the form:

$$y = J_{0,1}x + J_{0,2}, \tag{3.8.2.1}$$

in which

$$y = \frac{q\Delta p}{\tau_{eff}}\left[\frac{\Delta p(N_D+\Delta p)}{n_i^2}\right]^{-1/2}, \tag{3.8.8.2}$$

$$x = \sqrt{\frac{\Delta p(N_D+\Delta p)}{n_i^2}}. \tag{3.8.2.3}$$

When applied to the contact recombination term of Equation 3.2.2.4, these expressions could be a useful tool to assess the $J_{0,1}$ and $J_{0,2}$ components of contact recombination current losses.

However, injection level variations over the wafer thickness may complicate the use of Equations 3.8.2.1-3.8.2.3 for benchmarking the importance of space charge region and diffusion current contributions to the total contact recombination current. Non-constant injection levels due to large contact saturation current densities result in artificially induced injection level dependence of extracted saturation current densities, as derived in section 3.6. Recombination currents with $m > 1$ result in similar injection level dependence of $J_{0,1}$ extracted using Equation 3.2.2.7. This may render the effect of recombination currents with $m > 1$ indistinguishable from the effect of injection level variations, which significantly limits the applicability of Equations 3.8.2.1-3.8.2.3 to contacts with low effective surface recombination velocities such that the injection level is approximately constant. Most contact saturation current densities extracted in [Chen 2014] were very large. Therefore, it is likely that the corresponding measurements suffer from $J_{0,met}$ underestimations associated with non-uniform excess carrier densities which are difficult to separate from the hallmark injection level dependence introduced by non-unit ideality factors. This explains why we did not apply Equations 3.8.2.1-3.8.2.3 to the quantitative analysis of contact recombination currents in [Chen 2014].

3.9. Contact fraction

Typical $J_{0,met}$ test structures studied in this dissertation feature circular contacts arranged in a simple square lattice on an otherwise perfectly passivated wafer. The contact fraction is varied by changing the pitch. Since contact recombination currents are extracted from the slope of the recombination current plotted against the contact fraction, errors in contact fraction result in errors in extracted saturation current densities. Even though this issue is of a technological kind, and is not of principle interest, we include it here because understanding the issue at hand goes a long way to understanding the spread in the extracted contact saturation current densities. For example, the $J_{0,met} - J_{0,diel}$ values for samples b and c in Table 3.4.5.1 are supposed to be identical, however the extracted values are not exactly identical. This is probably due to errors in measured contact diameters on the test structures. Therefore, the discussion of the issue of contact fraction errors is particularly relevant, even though it could be considered to be a merely technological issue at first sight.

We focus our present discussion on typical errors incurred in photolithography defined contacts. This is motivated by the fact that most experimentally obtained contact recombination current measurements presented in this dissertation are obtained on lithographically defined test structures.

For lithographically defined test structures, the most significant source of errors in the contact fraction is the contact diameter which is not easy to control. In the discussion of these difficulties, we focus on the positive resist case since positive resist was used during the experiments presented in this thesis. The negative resist case is found by analogy.

A first source of difficulties in contact diameter control is related to the lithography process itself, in which there is a trade-off in resist thickness, illumination dose and development time: sufficient illumination and development is needed to develop all resist in the illuminated areas over the entire, rough solar cell wafer, but too much illumination and development leads to over-development. In addition, thicker resist layers are preferable to ensure uniform coverage of the rough solar cell wafer, whereas thin resist layers help to increase the pattern resolution. Second, there is also a trade-off during the etching of contact openings in the oxide passivation layers: sufficient etching is needed such that the contacts are opened over the entire wafer area, but too long etching leads to over etch. Both over etching and over development result in contact diameters that are larger than the design diameter. However, these effects do not influence the pitch.

We now proceed to the derivation of errors in extracted contact saturation current densities from effective lifetime measurements on $J_{0,met}$ test structures caused by poor contact diameter control. The contact diameter error is described by a relative error ε which is defined such that:

$$d_m = d_{m,0}(1+\varepsilon), \tag{3.9.1}$$

in which d_m is the actual contact diameter in the final test structure, and $d_{m,0}$ is the contact diameter value assumed in the extraction of contact recombination currents from effective lifetime measurements.

For a simple square lattice of circular contacts, the contact fraction C_{met} is related to the contact diameter d_m and the pitch S as:

$$C_{met} = \frac{\pi d_m^2}{4S^2}, \tag{3.9.2}$$

or in terms of $d_{m,0}$:

$$C_{met} = (1+\varepsilon)^2 \frac{\pi d_{m,0}^2}{4S^2}. \tag{3.9.3}$$

Since $(1+\varepsilon)^2 = 1 + 2\varepsilon + O(\varepsilon^2)$, with $O(\varepsilon^x)$ denoting terms containing ε to the power x and higher, small errors in the contact diameter d_m result in errors in the contact fraction C_{met} that are approximately twice as large. For $J_{0,met}$ obtained from fits of inverse lifetime versus contact fraction (Equation 3.2.2.7), $J_{0,met}$ is found from:

$$J_{0,met} = \frac{qn_i^2 W}{N_D + \Delta p} \frac{d\tau_{eff}^{-1}}{dC_{met}}, \tag{3.9.4}$$

or in terms of $d_{m,0}$:

$$J_{0,met} = (1+\varepsilon)^{-2} \frac{qn_i^2 W}{N_D + \Delta p} \frac{d\tau_{eff}^{-1}}{dC_{met,0}} = (1+\varepsilon)^{-2} J_{0,met,0}, \tag{3.9.5}$$

in which $C_{met,0} = \pi d_{m,0}^2 / 4S^2$, and $J_{0,met,0}$ is defined as:

$$J_{0,met,0} = \frac{qn_i^2 W}{N_D + \Delta p} \frac{d\tau_{eff}^{-1}}{dC_{met,0}}. \tag{3.9.6}$$

Since $(1+\varepsilon)^{-2} = 1 - 2\varepsilon + O(\varepsilon^2)$, relative errors in the contact diameter due to over (under) etch result in $J_{0,met}$ values which are under (over) estimated by a factor that is approximately twice as large.

For $J_{0,met}$ extracted from linear fits of $J_{0,tot}$ as a function of the contact fraction (Equation 3.2.2.10), an analogous reasoning yields that the same errors are introduced through contact diameters errors during $J_{0,met}$ extraction.

As a numerical example, consider a typical test structure used in our experiments. It has a design contact diameter of $15\ \mu m$. In an optimistic scenario, the increase in contact diameter due to over development and over etch is about $1\ \mu m$, or 6.7%.

If this over etch would not be taken into account, the corresponding error in $J_{0,met}$ would be 12.1%. Therefore, over etch has to be taken into account when contact recombination characteristics are extracted from lithographically defined test structures. This has been done in the present dissertation.

3.10. Alternative test structure embodiments

In this dissertation, we have focused on test structures based on lattices of point contacts. In this section, we suggest alternative embodiments of our test structure for contact recombination current measurements. These alternative embodiments are based on areas comprising thin contact fingers. The electrical current which is forced through the test structure during the photoconductance measurement is designed to flow perpendicular to the thin contact fingers.

Test structures based on lattices of point contacts have the advantage that they can be used for effective lifetime measurements using radio wave detected "contactless" photoconductance measurements, i.e. Sinton QSSPC lifetime testers [Sinton 1996] can be used. However, test structures based on lattices of point contacts also feature some limitations. In section 3.10.1, we discuss these limitations. In sections 3.10.2 and 3.10.3, we discuss alternative embodiments of our test structure, which allow to overcome these limitations.

However, the equipment for measuring the alternative test structure embodiments does not exist yet. Therefore, we limit ourselves in this dissertation to a brief, theoretical description of these test structures and their design rules. The required equipment is very similar to that for suns-Voc measurements [Sinton 2000]. In fact, as will become clear in sections 3.10.2 and 3.10.3, the hardware differences are related to the means for forcing currents between the test structure's outer contacts and measuring voltages on intermediate contacts. Evidently the data processing software has to be adapted as well.

3.10.1. Limitations of point contact based test structures

The contact recombination current depends in some contacting technologies on the precise morphology of the contact. One example are pulsed laser ablation-opened contacts in which the contact openings have a continuous line shape [Thuy 2014]. Such continuous line-shaped contact openings are for example useful in the context of plated nickel-copper contacts in which continuous contact between fingers and the silicon substrate is desirable because of improved contact adhesion [Tous 2014]. For pulsed-laser ablated contact openings, the continuous line shape of the contact openings is created by firing strong and short bursts of highly absorbed light at the dielectric covered silicon surface. The laser energy is absorbed in the silicon, near the silicon-dielectric interface. Subject to the absorbed laser energy, the silicon near the silicon-dielectric interface sublimates, evaporates or is converted to a plasma which causes a significant thermal expansion of the silicon near the silicon-dielectric interface. This causes a local

removal (ablation) of the dielectric layer. As a side-effect of the ablation process, damage in the form of various defects is introduced in- and around the contact opening. We refer to the regions where the ablation process resulted in the removal of dielectric layers as the ablated regions. We refer to the regions which were damaged by the laser ablation process but for which the dielectric layer was not removed as the heat-affected zone.

Line-shaped contact openings can be formed by using, for example, a pulsed laser. In each laser pulse, an ablated area and the associated heat-affected-zone are created. A line shaped contact is then formed by configuring the laser pulses such that adjacent ablated areas partially overlap. This is schematically shown for six partly overlapping laser pulses in figure 3.10.1.1. Regions in which the laser pulses do not overlap are referred to once-ablated areas whereas regions in which the laser pulses overlap are referred to as twice-ablated areas. The ablation process damages the ablated area, and therefore results in an increased recombination current in laser-opened contacts compared to lithography-opened contacts (see section 3.8). Because twice-ablated areas are subject to more damage, the recombination current density in twice-ablated areas is larger than the recombination current density in once-ablated areas. In addition, the heat affected zones associated with overlapping contact openings may overlap as well, which can also result in an influence on the associated recombination characteristic.

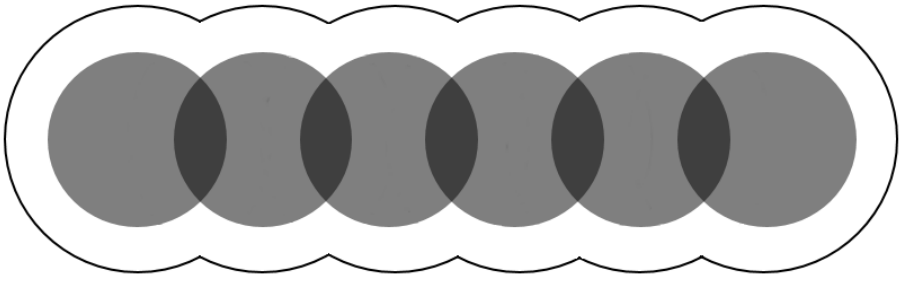

Figure 3.10.1.1. Schematic representation of a line-shaped contact opening made using pulsed laser ablation, featuring six partly overlapping contact openings. The white area within the surrounding line indicates non-ablated areas, which were nevertheless damaged during the ablation process; the heat-affected area. The light gray areas are ablated regions which were affected by a single laser pulse. The darker gray areas are ablated regions which were affected by two laser pulses, and are therefore more severely damaged than the areas which were affected by only one laser pulse.

Because the partial overlap of the ablated regions shown in Figure 3.10.1.1, and interactions in the heat affected zone, affect the contact recombination current, the point-contact based test structures studied throughout most of this dissertation are not ideally suited for the characterization of the contact recombination current

of the above line-shaped contact. Also, line-shaped contact are not compatible with QCCPC lifetime testers [Sinton 1996] because the line-shaped contacts would tend to short the underlying semiconductor, provided that the contact transfer length would be smaller than the length of the line-shaped contacts. This would make the measurement less sensitive to the properties of the wafer, which is evidently undesirable.

One possible alternative for the study of unpassivated contacts as in Figure 3.10.1.1, would be to characterize the contacts in the absence of metal, and simply providing a very poor surface passivation in the contacted regions. However, for some contacts, such as plated Nickel-Copper contacts, the metal deposition process itself can passivate defects in the laser-ablated contact openings [Tous 2014]. Because etching the metal layers prior to the characterization amounts to significant additional work, and because this process may influence the contact recombination current under investigation, it would be useful to modify the point-contact based test structures to allow for the characterization of line-shaped contacts.

Note that, in the field of passivated contacts, the entire contact stack should be present during contact characterization because interactions between the different layers in the contact passivation stack may significantly affect the contact recombination current.

A second, less important limitation of point contact based test structures is that rigorous modelling of our test structures based on lattices of point contacts tends to be complicated due to the three dimensional nature of the test structures. Rigorous modelling challenges include: three dimensional excess carrier density variations, the effect of three dimensional excess carrier density variations on in-plane photoconductance, and the effect of current flow through the point contacts on the photoconductance measurements, given the presence of three dimensional excess carrier density variations.

Another minor disadvantage of point contact based test structures is that the measurements can be relatively time consuming when performed manually. This is due to the fact that several separate photoconductance measurements have to be done for every measurement of contact recombination characteristics. Each photoconductance measurement requires careful aligning of the QSSPC measurement coil on the area under test. Manual alignment can take up to a minute for a single photoconductance measurement. Photoconductance measurements on multiple areas are required in order to obtain sufficient data points for a reliable linear fit of the inverse effective lifetime or the total saturation current density as a function of the contact fraction. A typical test structure features nine areas with different contact fractions. As a result, the total measurement time

needed for the characterization of a single wafer can easily be up to ten minutes. This disadvantage could be overcome by designing a measurement stage on which multiple photoconductance measurements can be done at the same time.

We finally draw the attention to a disadvantage of the use of radio wave detection in the contacts of contact recombination current extraction from photoconductance measurements. The radio waves that are used for the detection of the photoconductance have a typical frequency around 11 MHz. The contact resistance at these high frequencies can be smaller than the DC contact resistance, due to the effect of the metal-semiconductor junction capacitance. This is an undesirable effect because the higher the contact resistance, the higher the transfer length, and the less parasitic current flow through the metal contacts instead of through the semiconductor affects the contact recombination current measurement. In other words: when the DC contact resistance is higher than the AC contact resistance, parasitic effects related to current flow through the contacts could be reduced by performing DC contact recombination current measurements

We believe that this issue could be an important factor to take into account when characterizing passivated contacts: the DC-contact resistance of passivated contacts is often relatively high because of the resistance of the passivating layers between metal and semiconductor. Also, because these passivating layers are often very thin, the passivated contacts can still have a very high contact capacitance. As the cut-off frequency ω_c form which the AC-behavior of contact resistance becomes of importance equals $\left(\rho_c C_j\right)^{-1}$, this combination of high contact resistance and high contact capacitance results in a situation at which the AC-behavior of contact resistance becomes of importance at particularly low frequencies.

We have included a qualitative discussion of the AC contact resistance of selected unpassivated aluminum contacts on n+ and p+ silicon in the last paragraph of section 3.4.5; we found that parasitic current flow through the point contacts is of no importance for the investigated aluminum contacts on n+ silicon, but we found that it is an important parasitic for the investigated aluminum contacts on p+ silicon. With respect to the passivated contacts investigated in chapter 5, we note that the transfer length of the investigated passivated metal-insulator-semiconductor (MIS) contacts is at least as high as the transfer length of the unpassivated contacts. The contact size was about the same in all our experiments. Therefore, parasitic current flow through the point contacts is of no importance for the investigated passivated aluminum contacts on n+ silicon, but could have affected the measurements on some investigated passivated aluminum contacts on p+ silicon, especially those featuring no, or a small number of ALD Al_2O_3 layers.

3.10.2. Linear test structures & DC measurements

Said disadvantages could be overcome through the use of (quasi) DC photoconductance measurements on the linear test structure schematically drawn in Figure 3.10.2.1.

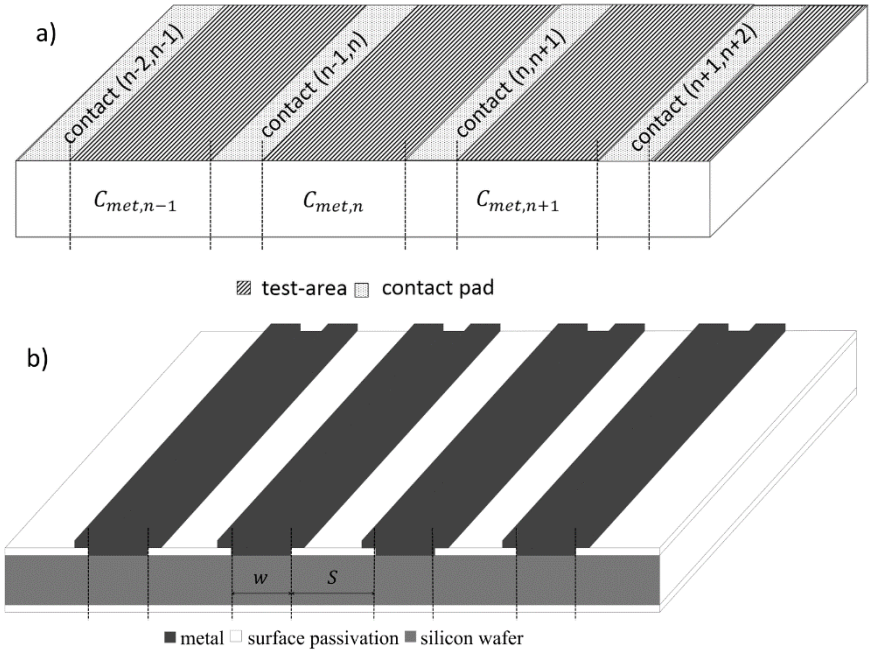

Figure 3.10.2.1. A linear test structure for contact recombination current measurements. Panel a) shows different areas under test (dashed areas) with differing contact fractions between contact pads. The contact pads are numbered as "contact (x,y)", with x and y numbers to indicate the areas under test adjacent to the bus bar. The test structure is illuminated from the non-contacted side. Panel b) shows a close-up of one area with a given contact fraction. The area consists of long fingers parallel to the bus bars, and thus perpendicular to the direction of current flow.

The linear test structure consists of several areas under test between parallel contact pads. Each area under test consists of equally spaced, parallel fingers. The fingers are also parallel to the contact pads. Every area under test has a different contact fraction, more specifically, the nth area has a contact fraction $C_{met,n}$. The contact fraction is varied by changing the pitch S. Every finger has a width w. In the linear test structure, bus bars are used as contacts to force currents and measure voltages. The current is forced to flow between the outer contacts. Voltages are measured on intermediate contacts, similar to the set-up of a four-point-probe measurement, as shown in 3.10.2.2. All areas between two

intermediate contact pads feature different contact fractions, as shown in Figure 3.10.2.1.

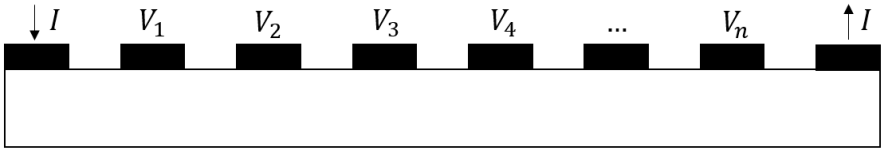

Figure 3.10.2.2. Macro cross sectional view of a linear test structure, showing that current flow is forced between two outer contact pads, and that voltages are measured on intermediate contact pads, analogous to the set-up in a four-point-probe measurement.

Because of translational symmetry in the direction of the fingers, the differential equations governing excess carrier density variations and current flow only depend on position in two directions: the direction perpendicular to the wafer plane, and the direction in the wafer plane, perpendicular to the contact fingers. Therefore, the analysis of excess carrier density and current flow is greatly simplified in this linear test structure compared to test structures based on two dimensional lattices of point contacts.

Influence of contact fingers on conductivity

Current flow in one area in our linear test structure, in the direction perpendicular to the contact fingers, can be described by a series circuit of the resistances of contacted areas and fully passivated areas:

$$R_{eq} = R_{met} + R_{pass}, \tag{3.10.2.1}$$

in which R_{eq} is the resistance of a unit cell (one passivated area and one contacted area) in the linear test structure, R_{met} is the resistance of a contacted area in the linear test structure, and R_{pass} is the resistance of a passivated area in the linear test structure. Note that the photoconductance measurement occurs in DC for linear test structures, such that the use of resistance instead of impedance is warranted. R_{met} is found through a derivation analogous to that of Equation 3.4.1.9:

$$R_{met} = R_S \frac{L_T}{w} \frac{2sinh(w/L_T)}{[1+cosh(w/L_T)]} \frac{w}{l}, \tag{3.10.2.2}$$

in which L_T is the contact's transfer length, R_S is the semiconductors' sheet resistance, w is the finger width, and l is finger length. The resistance of a passivated area is:

$$R_{pass} = R_S \frac{S}{l}. \tag{3.10.2.3}$$

For a linear test structure, the contact fraction is:

$$C_{met} = \frac{w}{s+w} \tag{3.10.2.4}$$

Combination of Equations 3.10.2.1 through 3.10.2.4 yields:

$$S_{eq,l} = S_s Q_l, \tag{3.10.2.5}$$

in which, analogous to the derivation in section 3.4, $S_{eq} = \left[R_{met}\frac{w}{l}\right]^{-1}$, $S_s = R_s^{-1}$, and Q_l is:

$$Q_l = \left[1 + C_{met}\left[2\frac{L_T}{w}\frac{sinh(w/L_T)}{1+cosh(w/L_T)} - 1\right]\right]^{-1}. \tag{3.10.2.6}$$

The influence of the point contacts on measured conductivities, injection levels, effective lifetimes and contact recombination characteristics, is found as in section 3.4, with Q substituted by Q_l. Taking the appropriate limit, it is found that $Q_l = 1$ for $L_T \gg w$. Therefore, it is possible to design this test structure such that the presence of the metal fingers does not disrupt the photoconductance measurement.

Design rules

As in test structures based on lattices of point contacts, all characteristic feature sizes in the area under test must be much smaller than the respective effective diffusion lengths. This requirement arises from the fact that excess carrier densities must be constant throughout the quasi neutral bulk. In addition, from sections 3.5 and 3.6, excess carrier densities are also more constant for small effective surface recombination velocities.

From our previous discussion, $Q_l = 1$ for $L_T \gg w$. Therefore, the finger width must be designed to be (much) smaller than the contact's transfer length.

The contact pads must be at the same electrical potential as the underlying semiconductor. This can be accomplished by forcing current through two outer contact pads, and measuring voltages on inner contact pads, as shown in Figure 3.10.2.2.

For single side contacted test structures, the measurement is ideally performed such that the semiconductor side without contacts is illuminated. This has two advantages. First and most important: it ensures a uniform generation rate, which aids achieving uniform excess carrier densities. Second, it has the advantage that shading does not have to be taken into account in calculating the generation rate in each area under test.

Two side contacted test structures have the advantage that excess carrier densities over the wafer thickness are more constant compared to single-side contacted test structures (see section 2.3). However, two side contacted test structures have the disadvantage that the generation profile is less constant in the

wafer plane due to shading, which can result in more severe in-plane excess carrier density variations. In addition, two side contacted test structures have the disadvantage that the exact amount of shading has to be known, and has to be taken into account in the calculation of the generation rate. Therefore, the finger width, including any overlap with the passivation layer outside the contact openings, must be accurately known.

The distance between two bus bars must be much larger than the effective diffusion length of the area under test such that the effect of excess carrier density variations at the edges of the test structure is negligible.

For linear test structures embedded in a much larger wafer, the length of the fingers must be much larger than the distance between two bus bars to minimize edge effects. These edge effects arise from the fact that at the edges of a linear test structure, part of the current between various bus bars inadvertently flows through the wafer, next to the fingers. This effect can be minimized on a relative basis by making the fingers much larger than the test structure size in the direction perpendicular to the wafer fingers.

Evidently, current flow outside the areas under test can be avoided by dicing the test structure out of the wafer. However, the resulting surface at the edges influences the minority carrier concentration near the edges, for a distance of the order of magnitude of the effective diffusion length in the area under test. Therefore, the finger length of the test structure must be much larger than the effective diffusion length in the area under test. For similar reasons, this requirement is also applicable to test structures embedded in a larger wafer.

3.10.3. Circular test structures

Edge effects due to the finite length of contact fingers can be avoided altogether by using circular test structures instead of linear test structures. This is similar to the use of circular transfer length method (TLM) test structures instead of linear TLM test structures to avoid edge effects in contact resistance measurements. Apart from design rules related to the finite finger length, similar design rules apply as for the linear case. A top view of a circular test structure is sketched in Figure 3.10.3.1. The operation of this test structure is analogous to the operation of the linear test structure. Current is forced to flow between the inner and outer bus bar. The voltages on intermediate bus bars are measured to obtain the voltage drops across the various areas under tests. Following an analysis similar to the analysis of cTLM measurements (see e.g. [Schroder 2006]), the sheet resistance of the semiconductor is obtained in the dark and under illumination. From the semiconductor's sheet resistance, the excess carrier density (averaged over the

wafer thickness) is obtained; and using an additional light intensity measurement with a reference photodiode, the effective lifetime is obtained. This results in effective lifetime measurements as a function of contact fraction, from which the contact recombination characteristics are obtained following the analysis introduced in section 3.2.

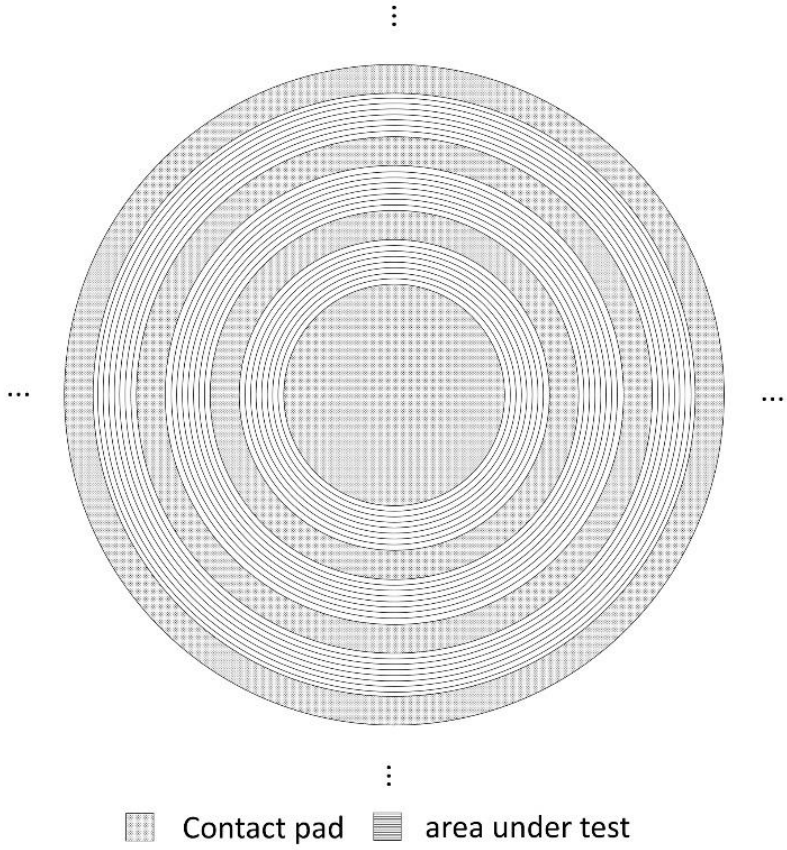

Figure 3.10.3.1. Schematic representation of a circular test structure.

3.11. Conclusions

In conclusion, we developed a photocondutance-based method for the characterization of contact recombination currents. This method is based on photoconductance measurements on different regions, having different contact fractions, on a dedicated test structure. A general description of the test structure and of its design rules is given in the introduction to this chapter.

In section 3.1, we discussed the State-of-the-Art with respect to the contact recombination current characterization methods at disposal of the experimentalist. We argued why, despite the merits of these characterization methods, the development of a new characterization method would be useful.

In section 3.2, we discuss the essence of our characterization method. In this chapter, we make the ansatz of constant excess carrier densities throughout the quasi neutral bulk. We also make the ansatz that the only influence of the point contacts in the test structure is the introduction of a recombining surface associated with the silicon-contact interface. These a-priori assumptions yield idealized expressions (Equations 3.2.2.7 and 3.2.2.10) which can be used for contact recombination current extraction from photoconductance measurements on properly designed test structures. Equation 3.2.2.7 is commonly referred to as the arbitrary injection technique and Equation 3.2.2.10 is commonly referred to as the high injection technique.

A typical process flow for test structure manufacture is given in section 3.3.

Design rules for proper test structure design summarized in the beginning of this chapter and are derived in sections 3.3 to 3.6. In short, the characteristic size of individual contacts in our test structure must be smaller than the contact's transfer length (section 3.4). In addition, all characteristic sizes must be much smaller than the relevant effective diffusion lengths (sections 3.4-3.6). Finally, the test structure is preferably applied to the characterization of contacts with low contact recombination currents (section 3.6). Failure to adhere to these design rules results in underestimations of extracted contact saturation current densities.

Accurate knowledge of the bulk doping level is required for the extraction of sensible contact saturation current densities using the arbitrary injection technique, Equation 3.2.2.7, but is less critical for contact saturation current extraction using the high injection technique, Equation 3.2.2.10. This is discussed in section 3.7.

In this dissertation, the focus lies on contact recombination currents with unit ideality factor. The application of our characterization method to the characterization of contact recombination currents with higher-than-unity ideality

factors is discussed in section 3.8. However, this must be done with care since parasitic effects related to non-homogeneous excess carrier densities roughly mimic the injection level dependence caused by larger-than-unity ideality factors.

Accurate knowledge of the contact fraction is essential for the extraction of sensible saturation currents with our test structure. Related errors are discussed in section 3.9.

For some contacting technologies, the characterization of line-shaped contacts as opposed to point-shaped contacts is desirable. Alternative test structure embodiments which allow for the characterization of line-shaped contacts are discussed in section 3.10.

When DC contact resistance is smaller than AC contact resistance, as is suspected to be the case for many passivated contacts, parasitic effects related to current flow through the contacts instead of through the wafer can be avoided by performing DC measurements instead of AC measurements. The test structures proposed in section 3.10 are suitable for DC contact recombination current measurements.

4. Optimization of IBC solar cells without contact passivation

In this chapter, point contact based test structures are applied to the optimization of n^+ diffusions which are used as back surface fields (BSF) in interdigitated back contact (IBC) silicon solar cells. In addition, various front surface field (FSF) oxidations are investigated. The figures of merit we investigate are the saturation current density of the passivated BSF and FSF, the saturation current density of the contacted BSF, and the contact resistance of the BSF contacts. This n^+ diffused region optimization has been done in an attempt to reduce recombination currents in non-contacted areas in imec's IBC silicon solar cells to a level at which a meaningful improvement of the total recombination current can be expected through the introduction of passivated contacts.

A schematic drawing of an IBC silicon solar cell is shown in Figure 4.1. The emitter, FSF and BSF is indicated in this picture.

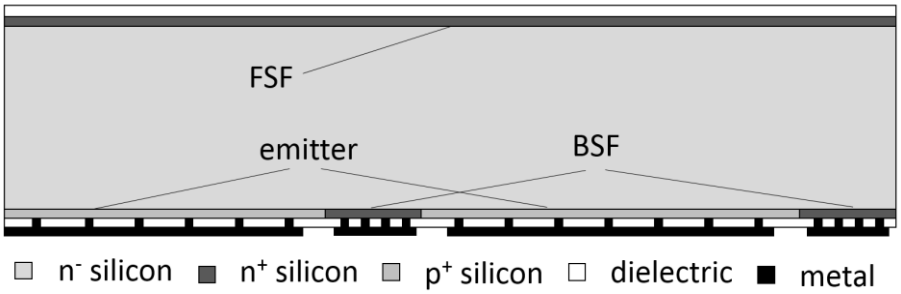

Figure 4.1. Schematic representation of an IBC silicon solar cell featuring diffused junctions, as investigated in the present chapter.

The use of the $J_{0,met}$ test structure proposed in [Deckers 2013] for a classical junction optimization problem allows for further experimental confirmation of the characterization method. Indeed, the consistency of the trends observed between process parameters, contact resistance, contact saturation current density and saturation current density of the passivated junction is a strong experimental confirmation of this novel characterization method.

Furthermore, the point contact based test structure is an elegant way to measure contact recombination currents, and test structure manufacture is done in parallel with the manufacture of the cTLM test structures for contact recombination current measurements. The only additional processing steps that are needed for $J_{0,met}$ test structure manufacture is the etching of metal, oxide, and diffused layers at the end

of the process to allow for a measurement of the bulk wafer resistivity, which is done for the purpose of bulk doping level extraction (see section 3.7).

The back surface field is chosen as the object of our contacted junction optimization even though the power losses at the emitter contacts are estimated to overshadow the recombination losses at the BSF contacts [Verlinden 2012]. This is done for two distinct reasons. First, the BSF processing is done after emitter diffusion (see section 1.4.2). Therefore, the thermal budget applied during BSF formation influences the emitter diffusion. As a result, the BSF must be optimized before the emitter can be optimized. The second reason for focusing on BSF optimization rather than emitter optimization is related to the fact that this diffused junction optimization was performed as a prelude to the introduction of Al_2O_3-passivated aluminum contacts in the solar cell flow. As will be shown in chapter 5, Al_2O_3 tunnel barriers have been found to only passivate aluminum contacts on n^+ silicon, and not aluminum contacts on p^+ silicon.

The junction optimization process is carried out starting from an existing diffusion profile, and then making motivated alterations in steps. This optimization of n^+ diffused regions has three branches. The first branch is modifying the $POCl_3$ diffusion parameters: diffusion and drive-in time and temperature. The second branch is an investigation of two different back surface field oxidations: a dry oxidation (with O_2 as the oxidizing species) and a wet oxidation (featuring H_2O as the oxidizing species). The wet oxidation is carried out at a lower temperature than the dry oxidation. In the third and final branch of the n^+ diffused region optimization, is lowering the front surface field (FSF) oxidation temperature. The details are discussed in the next sections.

Finally, an optimum set of process parameters is selected and verified through integration in an IBC silicon solar flow. This yielded 23.5% efficient IBC solar cells, which is an 0.2% absolute efficiency improvement compared to imec's best baseline efficiency of 23.3% (in-house measurements). The clear agreement between cell results and photoconductance-based (contact) saturation current density measurements provides a sound verification of the characterization method proposed in [Deckers 2013]; and further refined in this dissertation, and in [Deckers 2014, Deckers 2014b].

4.1. Back surface field diffusion and oxidation

As performed in the present dissertation, the formation of a highly doped region comprises two main steps. The first main step is the deposition of a dopant source on the wafer surface, which we refer to as the deposition step. The second main step in the highly doped region formation is dopant drive-in.

The deposition step occurs in a diffusion furnace, and in the case of $POCl_3$ diffused junctions, the dopant source is a phosphosilicate glass (PSG). For the $POCl_3$ diffused junctions investigated in the present dissertation, all $POCl_3$ depositions were done for about 20 minutes at temperatures between 800 and 900°C.

The drive-in step was partly done in the diffusion furnace during the deposition step and, for some junctions, during a subsequent anneal in the diffusion furnace, at the deposition step temperature. Then, the PSG was etched, the wafers were cleaned (using an SPM – rinse – diluted aqueous HF/HCl – rinse – spin-dry procedure), and the wafers were consecutively processed in an oxidation furnace. During oxidation, a passivating oxide was formed and the dopants were further driven in. For the BSF oxidations discussed here, the passivating oxide was either a dry oxide formed using a 40 minute oxidation at 975°C, or the passivating oxide was a wet oxide formed using a 40 minute oxidation at 900°C. In a dry oxidation, the oxidizing species is O_2. In a wet oxidation, the oxidizing species is H_2O.

The baseline back surface field has the following figures of merit: $J_{0,diel} = 50\ fA \cdot cm^{-2}$, $J_{0,met} - J_{0,diel} = 230\ fA \cdot cm^2$, and for aluminum BSF contacts, $\rho_c = 5.8 \cdot 10^{-4} \Omega \cdot cm^2$. The oxide used for baseline back surface field passivation is formed via dry oxidation for 40 minutes at 975°C and is ca. $70\ nm$ thick. $J_{0,diel}$ was measured using Kane and Swanson's method on a passivated wafer, $J_{0,met} - J_{0,diel} =$ was measured at $\Delta p = 1 \cdot 10^{15} cm^{-3}$ using our test structure, and ρ_c was measured using circular transfer length measurements (cTLM). The oxide thickness was measured using single-wavelength ellipsometry. All measurements were done at room temperature.

All other back surface fields discussed in this section were made through the perturbation of one or more of the process parameters of the baseline back surface field.

Note that all saturation current densities reported in this thesis which are extracted from photoconductance measurements, are measured at room temperature and are reported assuming $n_i = 7.4 \cdot 10^9 cm^{-3}$. The exact value of the intrinsic carrier concentration n_i used for reporting saturation current densities is immaterial as

reworking reported saturation current densities obtained from QSSPC measurements to other n_i is readily feasible, as explained in section 3.2.4.

The SIMS profile for the baseline back surface field (BSF) is shown in Figure 4.1.1, along with the SIMS profiels for the baseline emitter and front surface field (FSF). All SIMS profiles are shown after dopant drive-in using thermal oxidation; and at the end of process, i.e. after the entire solar cell manufacturing process according to section 1.4.2 has been completed. The specification “at the end of process” is important because in our IBC silicon solar cell process, the emitter is formed before the BSF, and the BSF is formed before the FSF. Therefore, the emitter’s dopant profile in a finished solar cell is not just determined by the emitter depositon and drive-in characteristics, but also by the thermal budget associated with BSF and FSF formation. Similarly, the BSF profile is influenced by the thermal budget encountered during FSF formation. As a result, the specification “at the end of process” is critical.

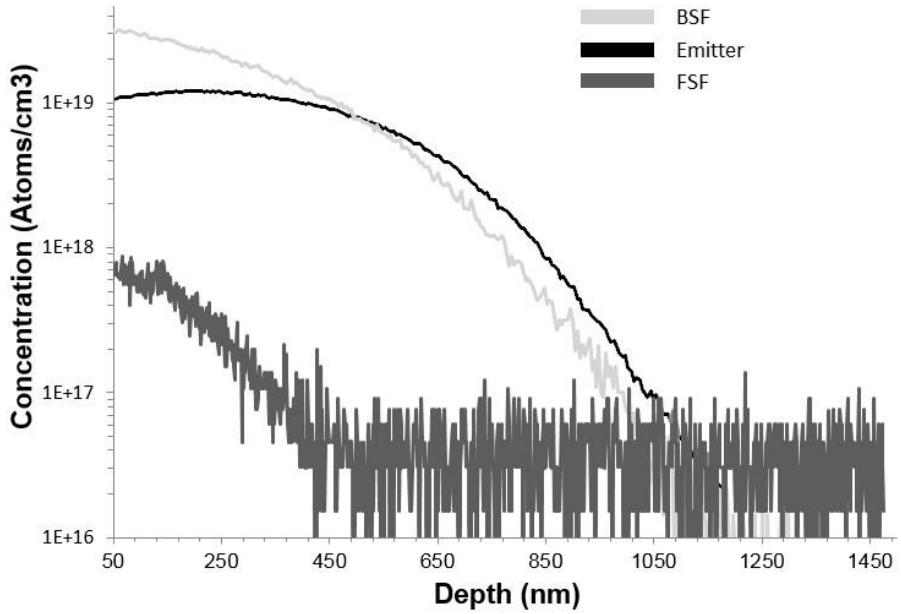

Figure 4.1.1. SIMS profiles for the BSF (phosphorous), emitter (boron) and FSF (phosphorous) as used in imec’s lithography-based baseline IBC silicon solar cell process (December 2013), at end-of-process conditions. The BSF and FSF diffusions investigated in this chapter are perturbations on the baseline BSF and FSF profile shown here.

As these saturation current densities are measured on dedicated test-structures instead of finished solar cells, the reporting at end-of-process conditions implies that the thermal budget associated with further process steps had to be simulated

in some way. The steps for which thermal budges simulation was necessary can be readily read from Figure 1.4.2.1. For each step, thermal budget simulation implies simply putting the respective wafers in a furnace at the appropriate temperatures and for the appropriate times, in the appropriate atmosphere.

For the reported emitter saturation current densities, the thermal budget associated with BSF and FSF formation was simulated. For the reported BSF saturation current densities, the thermal budget associated with FSF formation was simulated. FSF formation was the last process step such that thermal budget simulation was not necessary in that case. For the sake of completeness, we add that the baseline FSF was formed using a process that featured a $POCl_3$ deposition step between 800 and 900ºC, and a dry oxidation at 975 ºC.

In Figure 4.1.2, a plot of sheet resistance R_{sheet} as a function of contact resistance ρ_c is shown for a number of investigated n^+ diffused back surface fields. ρ_c and R_{sheet} were measured at the end of the process on cTLM test structures on n-type wafers. Note that the reported sheet resistances incorporate the effect of two n^+ diffusions (one on each wafer side) and the effect of bulk conductivity.

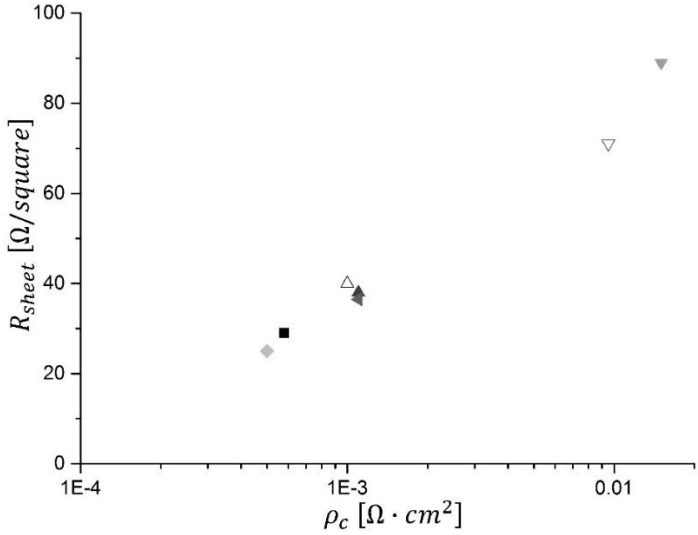

Figure 4.1.2. BSF sheet resistance as a function of BSF contact resistance. Each diffusion is represented by a unique symbol. Closed symbols represent junctions which were passivated, and further driven in, during a dry thermal oxidation. Open symbols represent junctions which were passivated, and further driven in, during a wet thermal oxidation.

For diffused junctions, the contact resistance of metal-semiconductor contacts is in one-to-one correspondence with the surface doping concentration; high (low) contact resistance corresponds to low (high) surface doping [Berger 1972b]. In addition, since conductivity is roughly proportional to carrier concentration, high

(low) sheet resistance corresponds to a low (high) integrated doping profile in the n^+ diffused region. As a result, the plot of sheet resistance versus contact resistance in Figure 4.1.2 is equivalent to a plot of the integrated doping profile versus surface concentration.

In Figure 4.1.3, $J_{0,diel}$ and $J_{0,met} - J_{0,diel}$ are shown as a function of ρ_c for Al:1%Si contacts on diffused n^+ silicon junctions. In Figures 4.1.2 and 4.1.3, identical symbols refer to the same sample. The trend of increasing sheet resistance, decreasing $J_{0,diel}$, and increasing $J_{0,met} - J_{0,diel}$ with increasing contact resistance is consistent with Gaussian profiles with various depths and surface concentrations. Within the narrow scope of the present experiment, deep (shallow) profiles with high (low) surface concentrations correspond to n^+ diffusions with low (high) ρ_c, low (high) R_{sheet}, low (high) $J_{0,diel}$, and high (low) $J_{0,met} - J_{0,diel}$. Note that these trends only apply to the narrow range of doping profiles used in our BSF experiments, and are not claimed to be general. This narrow range of doping profiles resulted from the fact that the investigated back surface fields were investigated as perturbations on a previously optimized back surface field. The optimization of a diffused BSF features a trade-off between $J_{0,met}$, $J_{0,diel}$ and ρ_c. A very detailed discussion of $J_{0,met}$ and $J_{0,diel}$ as a function of the surface concentration the diffusion depth for a much wider range of both phosphorous and boron diffusions can be found in [King 1990]. A discussion of contact resistance as a function of surface concentration for aluminum – silicon contacts can be found in [Berger 1972b].

Figure 4.1.3. shows a clear trade-off between contact resistance and contact saturation current density on the one hand, and saturation current density in passivated areas on the other hand. A reasonable trade-off are the diffusions that yield a contact resistance around $1\ m\Omega \cdot cm^2$. One of those back surface fields features a wet oxide. It has the following figures of merit: $\rho_c = 1\ m\Omega \cdot cm^2$, $J_{0,met} - J_{0,diel} = 235\ fA \cdot \mathrm{cm}^{-2}$, and $J_{0,diel} = 33\ fA \cdot \mathrm{cm}^{-2}$. Also, the thermal oxide of this back surface field has a thickness of around 300 nm, as opposed to oxide thicknesses of only ~60 nm for the dry oxides in this experiment. The wet oxide's higher thickness is advantageous since passivating silicon oxide layers between aluminum back contacts and the silicon substrate should be at least 100 nm thick for optimal back reflectance [Duerinckx 2014].

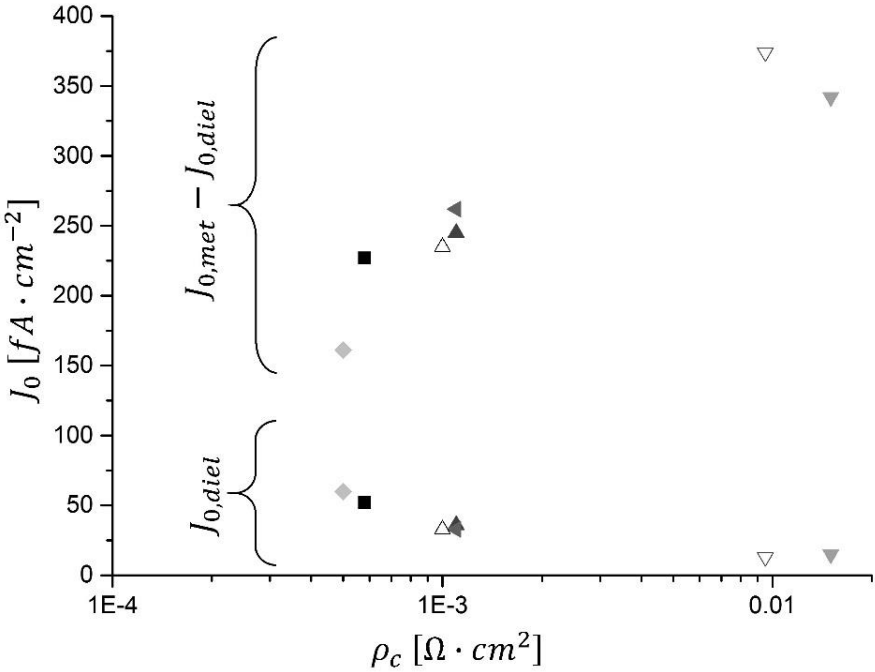

Figure 4.1.3. $J_{0,diel}$ and $J_{0,met} - J_{0,diel}$ as a function of ρ_c. Saturation current densities were extracted from a fit of inverse lifetime versus contact fraction at an injection level of $1 \cdot 10^{15} cm^{-3}$. Extraction of $J_{0,diel}$ using Kane and Swanson's [Kane 1985] method yielded values which are identical within ~10% to the values reported here.

4.2. Front surface field oxidation

In a subsequent experiment, the front surface field oxidation temperature was lowered by up to 120°C compared to the baseline front surface field oxidation temperature of 975°C, i.e. our front surface field oxidation experiments were executed in the temperature range of 855-975°C. The front surface field oxidation time, 20 minutes, was kept constant. Also, all gas flows were unaltered in this experiment.

The primary effect of this decreased oxidation temperature was a reduction in the front surface field oxide thickness from $\sim 20\ nm$ to $\sim 6\ nm$. The front surface field saturation current density was not affected; it was around $10\ fA \cdot cm^2$ for all front surface field oxidation temperatures.

The thinner front surface field oxide is very beneficial from an optical point of view as the $\sim 20\ nm$ thick passivating front surface field oxide in the baseline process is an optically parasitic layer in the SiN_x anti-reflective coating – SiO_2 passivation layer – silicon wafer stack at the front of the baseline IBC solar cells, resulting in increased front reflectance. The optically parasitic action of the SiO_2 passivation layer is related to the SiN_x layer used as an anti-reflective coating having a higher index of refraction than the intermediate SiO_2 layer. Therefore, the SiO_2 layer disrupts the graded-index effect associated with the SiN_x anti-reflective coating. Conversely, the $\sim 6\ nm$ thick passivation layer formed in a reduced-temperature front surface field oxidation has a negligible optical parasitic effect [Zielinski 2014].

Lowering the FSF oxidation temperature also lowers the thermal budget that the n^+ BSF receives during device manufacture. In fact, for the n^+ diffused regions with wet oxide passivation layers, the thermal budget is determined by the front surface field diffusion which occurs after the back surface field diffusion and oxidation (see section 1.4.2).

The thermal budget influences the doping profile steepness: exposing the diffusions to high temperatures for long periods tends to smear out the dopant concentration through diffusion of dopant species in the silicon lattice. Therefore, lowering the thermal budget allows to make doping profiles steeper, which can result in lower $J_{0,diel}$ but higher $J_{0,met}$ for the same surface concentration; or in lower ρ_c for the same integrated dopant concentration. Upon lowering the front surface field oxidation temperature by 120°C, the BSF contact resistance was lowered slightly to less than $0.9\ m\Omega \cdot cm^2$, as opposed to $1\ m\Omega \cdot cm^2$ for back surface fields exposed to the baseline front surface field oxidation. The back surface field's $J_{0,diel}$ and $J_{0,met}$ were not notably affected by lowering the FSF oxidation temperature. This could be attributable to one or a combination of the following effects: first, the

trends in $J_{0,diel}$ and/or $J_{0,met}$ with varying FSF oxidation temperature could be smaller than the precision and/or accuracy of our experiments; second, the BSF's thickness and surface concentration could be changing simultaneously when the FSF oxidation temperature is varied such that the BSF's shape (i.e. the BSF's thickness and depth) changes on an iso-$J_{0,diel}$ and/or iso-$J_{0,met}$ curve, see [King 1990].

4.3. Integration

A combination of a standard BSF diffusion, wet BSF oxidation and low temperature dry FSF oxidation was integrated in 2 cm x 2 cm lab-type IBC cells on n-type Czochralski silicon substrates made according to the baseline flow discussed in section 1.4.2. A comparison of solar cells manufactured according to the baseline process, and solar cells featuring the adapted BSF and FSF oxidations is shown in table 4.3.1.

Best cell	$J_{SC}\ [mA \cdot cm^{-2}]$	$V_{OC}\ [mV]$	$FF\ [\%]$	$\eta\ [\%]$
Baseline	41.7	690	81.2	23.3
Modified oxidations	41.8	694	81.1	23.5

Table 4.3.1. Comparison of the best baseline solar cell and the best solar cell featuring a wet BSF oxidation, and a low-temperature dry FSF oxidation.

The cells with modified BSF and FSF oxidations have a higher open circuit voltage, which is related to the significantly improved $J_{0,diel}$ of the BSF whereas $J_{0,met}$ is unchanged: $J_{0,diel} = 33\ fA \cdot cm^{-2}$ for cells with modified BSF and FSF oxidation versus $50\ fA \cdot cm^{-2}$ for baseline cells; $J_{0,met} - J_{0,diel}$ was $235\ fA \cdot cm^{-2}$ in both cases. Also, the cells with modified BSF and FSF oxidations have a higher short circuit current density. As argued below, we can attribute this short circuit current improvement to a combination of improved front reflectance and improved back reflectance.

Whether or not the back surface in a solar cell contributes to the measured reflectance at a given wavelength depends on the extinction coefficient of the incident light at that wavelength. The extinction length of a material is the characteristic distance over which most of the light traveling in that material is absorbed. The extinction length in silicon is only a few nanometers in the low wavelength range (around 300 nm), whereas it is hundreds of meters and more at high wavelengths, close to silicon's band gap (around 1100 nm) [Rajkanan 1979]. Because any low wavelength light that penetrates the silicon solar cell is absorbed close to the front surface, low wavelength light only probes the front reflectance of silicon solar cells. Conversely, high wavelength light is absorbed weakly, and can reflect from the back surface of silicon solar cells, and can escape through the front surface again. Therefore, high wavelength light can be used to probe both the front and back reflectance of silicon solar cells.

At low wavelengths (the left panel in Figure 4.3.1), the reflectance for cells with modified BSF and FSF oxidations is lower, which indicates improved front

reflectance due to the thinner FSF-passivating SiO_2 layer. At high wavelengths (the right panel in Figure 4.3.1), the reflectance is higher for the cells with modified BSF and FSF oxidations, which indicates improved reflectance related to the thicker back surface field oxide.

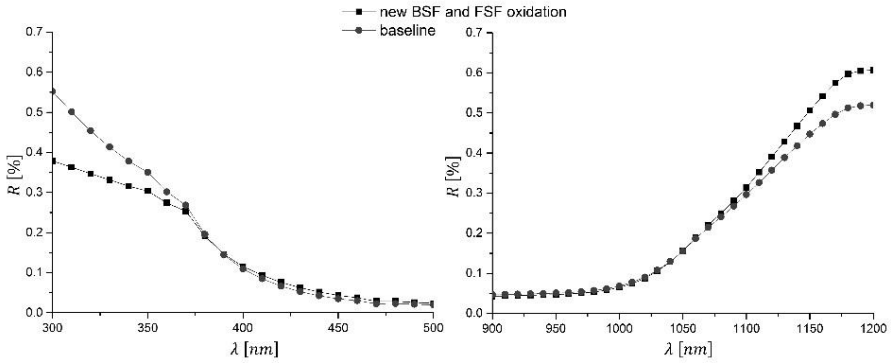

Figure 4.3.1. Reflectivity as a function of wavelength for a baseline solar cell, and for a solar cell featuring a wet BSF oxide and a thin, low temperature dry FSF oxide. The reflectivity is shown for low and high wavelengths in the left and right panels, respectively. The reflectivity in the intermediate wavelength region is identical for both samples and is not shown here.

The improved front and back reflectance result in better absorption of the incident light and this translates in improved current. The external quantum efficiency (EQE) is a spectrally resolved measure of this current improvement: it is the ratio of the number of minority carriers collected under short circuit conditions to the number of incident photons, as a function of the wavelength. The external quantum efficiency of a baseline solar cell and a solar cell with modified BSF and FSF oxidations is shown in Figure 4.3.2. The improved front and back reflectance result in EQE improvements in the low-wavelength and the high-wavelength regions, respectively.

Another a-priori possibility for the improved short circuit current in the solar cells with is modified BSF and FSF oxidations is reduced electrical shading due to the improved BSF saturation current density. Electrical shading is a recombination-related effect resulting in sub-optimal carrier collection above BSF regions in IBC silicon solar cells [Hermle 2008, Kluska 2010].

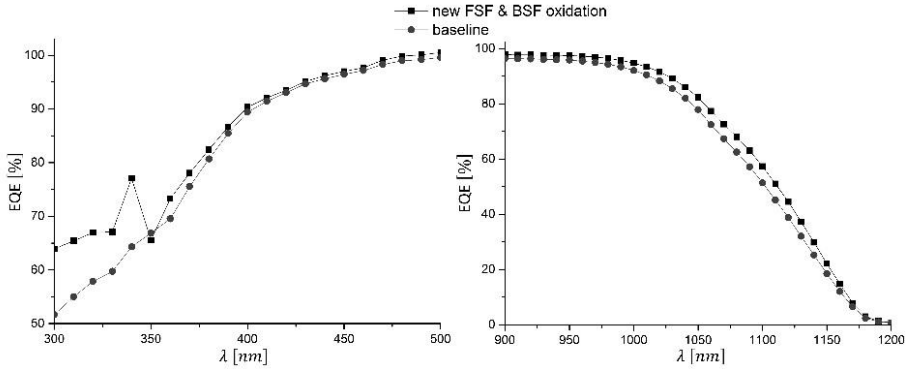

Figure 4.3.2. EQE for a solar cell with the baseline BSF and FSF oxidations, and for a solar cell with modified BSF and FSF oxidations. The low wavelength region is shown in the left panel and the high wavelength region is shown in the right panel. The EQE in the intermediate region is identical, and close to 100% for both cells.

In order to investigate the possibility that part of the current gain upon introducing modified BSF and FSF oxidations is due to reduced electrical shading losses, light beam induced current (LBIC) measurements were performed, featuring laser light with a wavelength of 800 nm. The reflectance of baseline and optimized solar cells was identical at this wavelength. Therefore, the LBIC measurement can be directly used to compare minority carrier collection in baseline and optimized cells since LBIC measurements are direct measurements of the carrier collection efficiency as a function of position.

The LBIC measurements, shown in Figure 4.3.3, show no difference in the carrier collection efficiency between baseline cells and cells with adapted BSF and FSF oxidations, which rules out the possibility of electrical shading effects lying at the basis of the observed difference in short circuit current density between baseline cells and cells with modified BSF and FSF oxidations. Therefore, the current gain observed upon modifying the front- and back surface field oxidations is due to a combination of improved front reflectance and improved back reflectance; as opposed to being due to reduced electrical shading.

In conclusion, the use of our $J_{0,met}$ test structure for a classical junction optimization problem allowed for further experimental confirmation of the characterization method proposed in this dissertation. Indeed, the consistency of the trends between contact resistance, contact saturation current density and saturation current density of the passivated junction is a strong experimental confirmation of this novel characterization method.

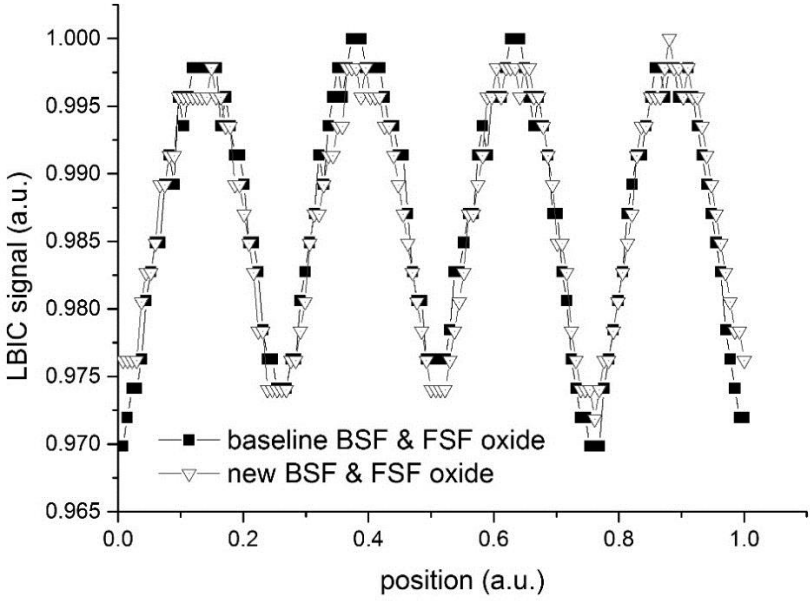

Figure 4.3.3. Normalized LBIC (Light Beam Induced Current) signal as a function of position, in arbitrary units; for IBC solar cells with imec's baseline BSF and FSF oxide, and for IBC solar cells with the new BSF and FSF oxide that was developed in the context of this thesis. Both solar cells have a nominal BSF contact fraction of 0.22%, relative to the total area.

5. Al_2O_3-passivated aluminum contacts on silicon

Efficient surface passivation is one of the enablers of high efficiency photovoltaic devices. Surface passivation schemes can be roughly divided into two categories. The first category is the passivation of non-contacted surfaces, i.e. the case in which no electrical current flows through the passivation layer. The second category is the passivation of contacted surfaces. For the passivation of contacted surfaces, passivation layers are applied between semiconductor and metal contact, and the passivation layer is designed to allow for electrical current to pass through while inhibiting minority carrier recombination at the metal-semiconductor interface. Both Plasma Enhanced Physical Vapor Deposition (PECVD) and Atomic layer deposited (ALD) Aluminum oxide (Al_2O_3) have proven to successfully passivate non-contacted silicon surfaces, see e.g. [Saint-Cast 2010]. Surface passivation is commonly attributed to a combination of chemical passivation (removal of surface states from the band gap; primarily related to dangling bond saturation), and field-effect passivation; related to Al_2O_3 generally being a negatively charged dielectric. The charge state of Plasma Enhanced Chemical Vapor Deposition (PECVD) aluminum oxide passivation layers on silicon may be influenced by the injection of electrons or holes from the silicon substrate through the application of a bias voltage [Töfflinger 2014].

Al_2O_3 is also used in conjunction with other dielectrics to form passivating stacks for highly doped silicon. For example, Al_2O_3-TiO_3 stacks have been found to successfully passivate non-contacted boron-diffused emitter surfaces [Suh 2014]. Al_2O_x-SiN_x stacks were found to adequately passivate both non-contacted n^+ and p^+ silicon in [Richter 2014].

The previous paragraphs relate to the use of ALD Al2O3 for the passivation of uncontacted surfaces. ALD Al_2O_3 has also gained significant interest for use as a passivation layer of metal contacts on silicon, see e.g. [Zielke 2011]. In this chapter, thin dielectric Al_2O_3 layers grown using thermal atomic layer deposition (ALD) are investigated for the passivation of the interface between aluminum contacts and n^+ or p^+ silicon. Specific attention is paid to the effect of the surface treatment prior to the formation of Al_2O_3 contact passivation layers: HF-last and HNO_3-last ALD Al_2O_3 contact passivation layers are investigated. ALD Al_2O_3 contact passivation layers are found to effectively passivate aluminum contacts on n^+ silicon surfaces, but they are found to be ineffective at passivating aluminum contacts on p^+ silicon surfaces. In addition, it is found that pin-holes associated with HF-last ALD Al_2O_3 contact passivation layers can improve the trade-off

between contact resistance and contact recombination associated with passivated contacts.

A schematic representation of an IBC silicon solar cell featuring MIS passivated BSF contacts is shown in Figure 5.1. The magnified area shows the passivated BSF contact which consists of a tunnel dielectric – metal stack on n^+ silicon. For the passivated contacts investigated in the present dissertation, the tunnel dielectric consists of a SiO_x-Al_2O_3 stack, which may or may not be perforated.

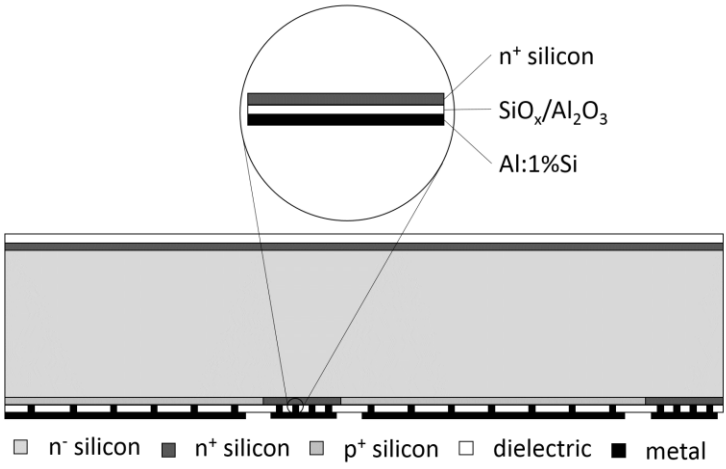

Figure 5.1. Schematic representation of an IBC silicon solar cell featuring passivated BSF contacts, in which the BSF contacts have been passivated using an MIS structure.

5.1. Effective lifetime and morphology[1]

In this section, we first discuss the passivation of n- and p-type silicon by thin aluminum oxide layers. We use contactless effective lifetime (QSSPC) measurements on symmetrical test structures to investigate the passivation quality. In particular, we investigate the effect of surface conditioning on the surface passivation quality. We conclude this section by discussing the morphology of thin Al_2O_3 layers in passivated aluminum contacts on silicon.

5.1.1. Effective lifetime

Effective lifetimes τ_{eff} are measured using quasi steady state photo conductance (QSSPC) measurements at room temperature. Effective lifetimes were measured on 160-170 µm thick, chemically polished, n- and p-type Czochralski silicon wafers passivated with thin Al_2O_3 passivation layers on both sides. The resistivity of the p-type wafers was ca. $2\ \Omega \cdot cm$, the resistivity of the n-type wafers was between 0.8 and $5\ \Omega \cdot cm$. The bulk lifetime τ_b of these wafers is at least $800\ \mu s$ for the p-type wafers and at least $1200\ \mu s$ for the n-type wafers, at an injection level of $1 \cdot 10^{15} cm^{-3}$. The bulk lifetime τ_b is at least two times higher than the observed effective lifetimes τ_{eff} of Al_2O_3 passivated wafers. As a result, the τ_{eff} reported here are good measures for the effective surface recombination velocity S_{eff} at the Al_2O_3 passivated silicon surface.

The closed symbols in Figure 5.1.1.1 are effective lifetimes of HF-last Al_2O_3 passivated wafers as a function of the number of ALD cycles. Effective lifetimes strongly increase with the number of ALD cycles: effective lifetimes range from ca. 10 µs for 3 ALD cycles to ca. $400\ \mu s$ for 25 ALD cycles. Remarkably, no significant difference in effective lifetimes was found between n- and p-type wafers passivated with the same number of ALD Al_2O_3 cycles. Since the n- and p-type wafers have about the same thickness and recombination in both types of wafers is dominated by surface recombination, this is a clear indication that the surface recombination velocity is independent of doping type, for the specific case considered in our experiment. The results of these effective lifetime tests are consistent with observations made in the literature [Loozen 2012]. Note that this is a remarkable observation since Al_2O_3 is well known to be a negatively charged dielectric and highly asymmetric electron and hole capture cross sections have

[1]This section is partly based on [Deckers 2014c].

been reported for traps at the Al_2O_3-Si interface [Werner 2012]. The identical effective lifetimes on n- and p-type silicon can be explained as by acknowledging that even just the oxide charge density at the SiO_x- Al_2O_3 interface ($-4 \cdot 10^{11} cm^{-2}$) [Rothschild 2010] is sufficient to cause inversion at the silicon surface of the lowly doped (ca. $1 \cdot 10^{15} cm^{-3}$) n-type wafers (see e.g. [Van Overstraeten 2000]). The surface of the p-type wafers is in accumulation as holes are attracted to the surface by the negative oxide charge. Therefore, holes are the majority carriers at the dielectric-silicon interface for both n- and p-type wafers, for the lowly doped wafers under investigation in this section. Note that in the following sections, we will be investigating contact recombination currents for wafers with a much higher surface doping concentration for which this is probably not the case.

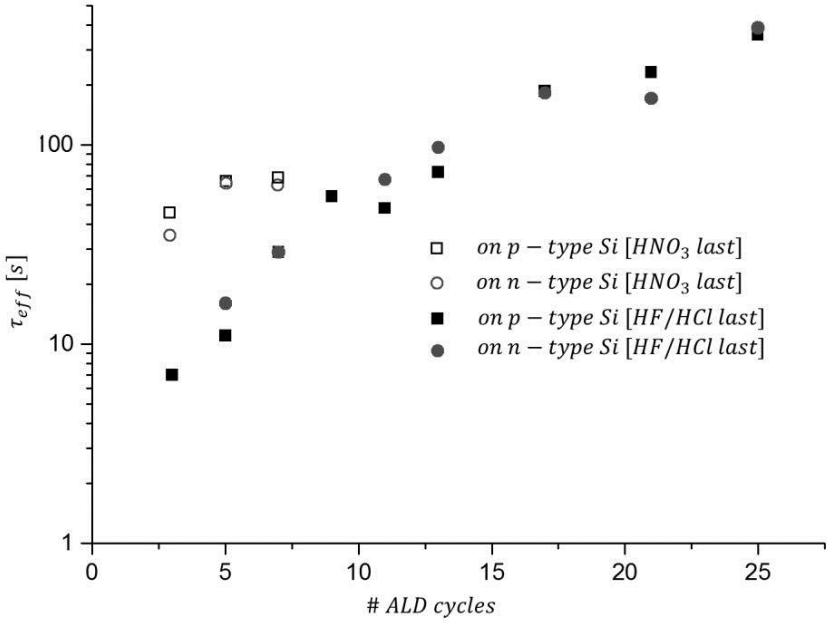

Figure 5.1.1.1. Effective lifetime of n- and p-type wafers passivated with thin Al_2O_3 layers, as a function of the number of ALD cycles. The Al_2O_3 layers were deposited shortly after either an HF dip or shortly after a dip in azeotropic HNO_3 at room temperature.

The open symbols in Figure 5.1.1.1 are effective lifetimes for Al_2O_3-passivated wafers, for Al_2O_3 layers deposited shortly after a dip in azeotropic HNO_3 at room temperature. The closed symbols in Figure 5.1.1.1 are effective lifetimes for Al_2O_3-passivated wafers, for Al_2O_3 layers deposited shortly after a dip in a diluted aqueous HF-HCl mixture at room temperature.

By comparison of the open and closed symbols in Figure 5.1.1.1, the effective lifetime is much higher for HNO_3-last wafers compared to HF-last wafers for the same number of ALD cycles. This is related to HF-last wafers being hydrophobic (i.e. featuring Si-H terminated surfaces) and HNO_3-last being hydrophilic (i.e. featuring Si-O-H terminated surfaces). ALD Al_2O_3 growth on hydrogen terminated silicon surfaces is well-known to result in non-uniform island growth, see e.g. [Vermang 2012]. This results in partially unpassivated surfaces for silicon wafers passivated with few ALD Al_2O_3 layers on HF-last surfaces. Conversely, the layer growth is smooth on the HNO_3-last silicon surfaces, which results in uniform layers, with uniform passivation.

5.1.2. Morphology

Figure 5.1.2.1 shows TEM micrographs of passivated aluminum contacts consisting of thin Al_2O_3 layers between silicon and aluminum. All Al_2O_3 layers shown in Figure 5.1.2.1 were grown in 7 ALD Al_2O_3 cycles and have a thickness of approximately 2 nm. The Al_2O_3 were grown on HF-last and HNO_3-last highly doped n^+ and p^+ silicon surfaces. The highly doped n^+ and p^+ silicon surfaces were formed using the BSF and emitter diffusion shown in Figure 4.1.1.

In Figure 5.1.2.1 a, the case of aluminum contacts passivated by Al_2O_3 on HF-last n^+ silicon, significant roughness in the form of small pyramids is observed. In between the pyramids, there is also significant short-range roughness. In Figure 5.1.2.1 c, the case of aluminum contacts passivated by Al_2O_3 on HNO_3-last n^+ silicon, no pyramids are detected but there is short range roughness present which looks similar to the intra-pyramid roughness which is present for aluminum contacts passivated by Al_2O_3 on HF-last silicon (Figure 5.1.2.1 a).

For Al_2O_3 passivated contacts on p^+ silicon, both for Al_2O_3 on HF-last (Figure 5.1.2.1 b) and HNO_3-last (Figure 5.1.2.1 d) p^+ silicon, the contact interface is much smoother compared to the interface of passivated n^+ silicon contacts. In the case of contacts passivated with Al_2O_3 on HF-last p^+ silicon (Figure 5.1.2.1 b), nano pyramids are present, but they are smaller and their density is much lower than in the case of Al_2O_3 passivated contacts on HF-last n^+ silicon. The smoothest contact interface is found for Al_2O_3 passivated HNO_3-last p^+ silicon contacts. In this case, the entire interface is comparatively flat and no nano pyramids are present.

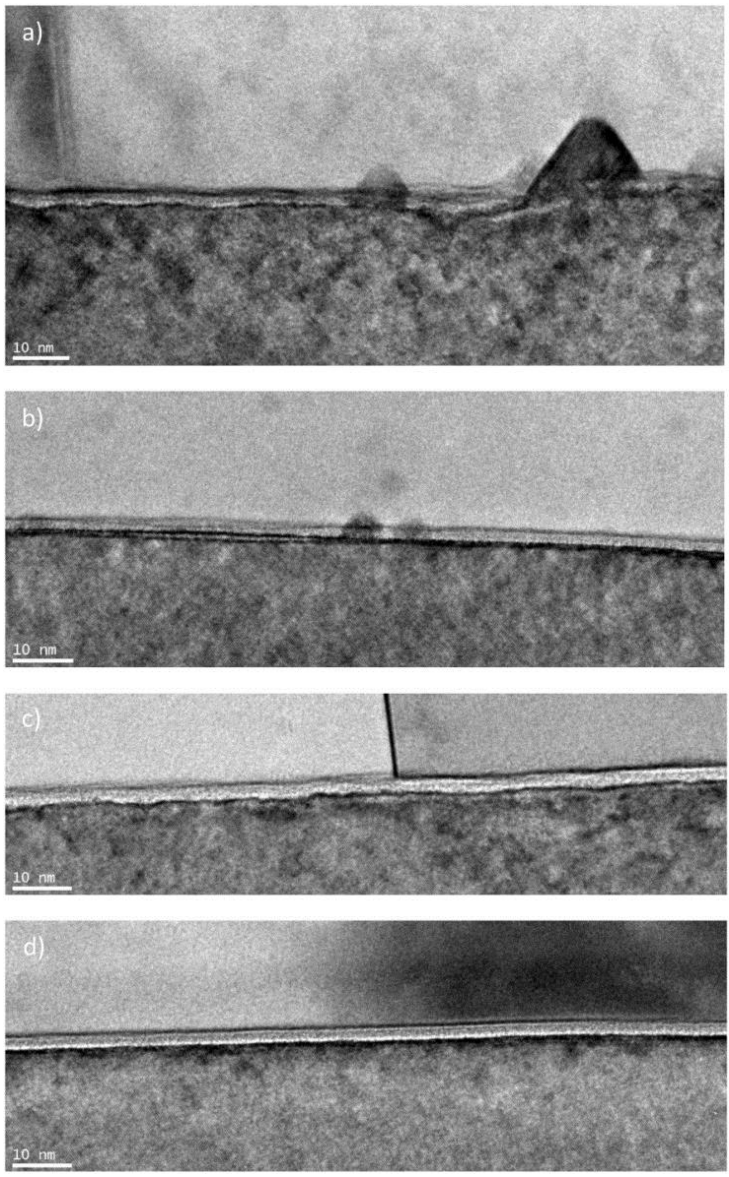

Figure 5.1.2.1. TEM micrographs of passivated contacts featuring thin Al_2O_3 layers between silicon and aluminum. All Al_2O_3 layers shown in this picture were grown using 7 thermal ALD cycles. The different pictures show passivated contacts on hydrophobic (HF-last) or hydrophilic (HNO_3-last) silicon with different doping types (p^+ or n^+). a) Al_2O_3 on HF-last n^+ Si, b) Al_2O_3 on HF-last p^+ Si, c) Al_2O_3 on HNO_3-last n^+ Si, d) Al_2O_3 on HNO_3-last p^+ Si.

A close-up of the pyramids found for the Al_2O_3 tunnel layers on HF-last n^+ silicon is shown in Figure 5.1.2.2. The pyramids are epitaxial Si but contain a high density of stacking faults and nanotwins. They most likely grew during the final forming gas anneal which is done after metal patterning. There is no dielectric stack on the pyramid's sides.

The silicon source for the epitaxial nano pyramids is the aluminum contact, which is actually 99% aluminum and 1% silicon. A solid solution of 1% silicon in aluminum is supersaturated at a temperature of 400°C [Murray 1984], which is the forming gas anneal temperature at the end of the process. This super saturation causes silicon to precipitate, preferably at low activation energy nucleation sides such as pin-holes in the thin ALD Al_2O_3 layers between the aluminum contact and a HF-last silicon wafer. The absence of epitaxial pyramids on HNO_3-last silicon is consistent with the growth of uniform, pinhole-free ALD Al_2O_3 layers on HNO_3-last silicon.

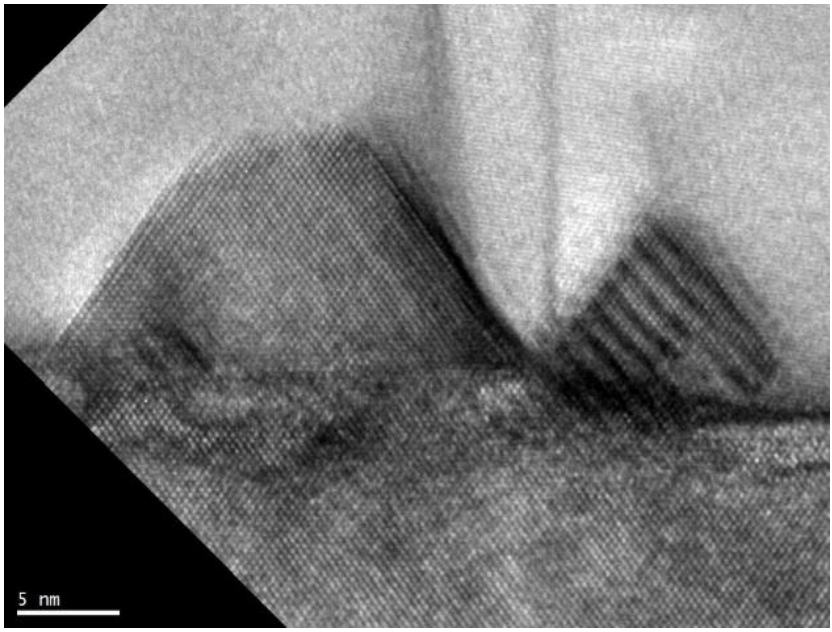

Figure 5.1.2.2. Close-up TEM micrograph of two nano pyramids found for Al_2O_3 tunnel layers on HF-last n^+ silicon. The small white bar in the lower left corner indicates the scale (5 nm).

The contact interface for both HF-last and HNO_3-last contacts on n^+ silicon features micro roughness in between the epitaxial nano pyramids, whereas no such roughness is observed for the contact interfaces on p^+ silicon. This could be due to interface reactions during wafer cleaning; all wafers went through a RCA cleaning process immediately after saw damage removal. Specifically the SC1

step for a (1 NH_4OH : 1 H_2O_2 : 5 H_2O) ratio, which has been used in this work, has been found to cause significant surface roughness in the context of pre-gate oxidation cleans during the manufacture of CMOS integrated circuits [Meuris 1992].

During the TEM measurement, the surface roughness of n^+ silicon surfaces is projected in the viewing direction. This projection causes the Al_2O_3 layer to be harder to observe and it is therefore difficult to determine the oxide layer thickness. Nevertheless, in the Al_2O_3 layers in Figure 5.1.2.1, a bright/gray/dark contrast is seen at the silicon- aluminum interface. The dark contrast is due to Ga contamination of the FIB (Focused Ion Beam) used during sample preparation. The bright/gray contrast cannot be interpreted in terms of composition since the bright contrast is likely caused by a focus effect at the rough interface. It is only possible to determine the total, combined, thickness of SiO_2 and Al_2O_3 stack from the total thickness of the bright-gray contrast, which is approximately 2 nm for the layers shown in Figure 5.1.2.1.

In order to determine the thickness of the ALD Al_2O_3 layers as a function of the number of ALD cycles, we use single wavelength ellipsometry at a wavelength of 633 nm on mirror polished boron doped Czochralski silicon wafers with a resistivity higher than 1 Ω·cm. The index of refraction of as-grown Al_2O_3 layers under investigation is taken to be 1.62, which is a result obtained from ellipsometry on thick Al_2O_3 layers. All thickness measurements were done with the purpose of obtaining a rough estimate of the layers' thickness. The thicknesses were extracted assuming that the only layer between silicon and the atmosphere was Al_2O_3, which is evidently an approximation since we did not take into account the thin SiO_x layer between Al_2O_3 and silicon. However, since the index of refraction of quartz is 1.54 at 633 nm [Ghosh 1999], which is close to the refractive index of as-grown Al_2O_3, we estimate that the relative error on the dielectric stack's physical thickness that results from making this approximation is less than 5%, even if the entire stack would consist of SiO_2 instead of Al_2O_3.

Figure 5.1.2.3 shows the thickness of Al_2O_3 layers deposited on mirror polished p-Si surfaces shortly after an HF-dip, as a function of the number of ALD cycles. For a low number of ALD cycles, these thicknesses are significantly thicker than expected from steady state growth rate measurements on thick layers, which yield a steady state growth rate of 0.137 nm/cycle. Also, the relative thickness discrepancy is the highest for the thinnest Al_2O_3 layers. This can be explained by the well-known presence of a thin SiO_x layer between Al_2O_3 and silicon, see e.g. [Bersch 2008, Simoen 2011]. This thin SiO_x layer could be formed either at room temperature in the atmosphere between HF dip and loading or while heating the wafers in the load lock of our ALD tool prior to deposition. Note that for ellipsometry

measurements on silicon wafers immediately after an HF dip, an 0.6 nm thick layer was measured assuming the index of refraction used in our Al_2O_3 thickness measurements. Therefore, we cannot exclude a significant relative error for our thickness measurements, especially for thickness measurements of the thinnest Al_2O_3 layers.

Also note that oxide thicknesses which are measured using different techniques do not correspond exactly. The measurement techniques reported in this section are: ellipsometry measurements on thick ALD Al_2O_3 layers and extrapolation to very thin layers, TEM measurements, and ellipsometry measurements on very thin layers. These discrepancies are suspected to be related to specific flaws of the respective measurement techniques, some of which have been discussed before.

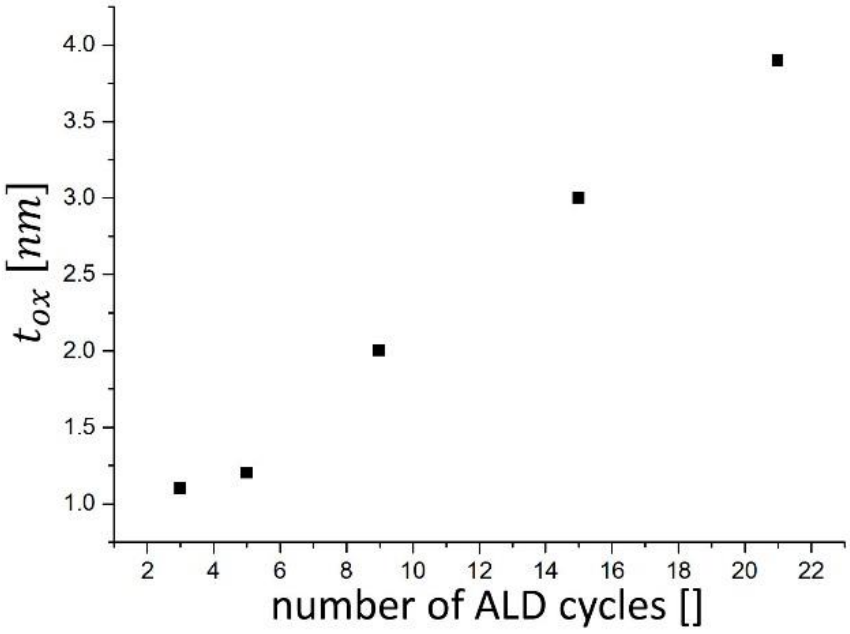

Figure 5.1.2.3. Passivation layer thickness from single wavelength ellipsometry as a function of the number of ALD cycles.

5.2. Contact recombination

$J_{0,met} - J_{0,diel}$ was extracted at each injection level from a linear fit of inverse effective lifetime as a function of the contact fraction (Equation 3.2.2.7). The investigated contact recombination currents are shown for ALD Al_2O_3-passivated aluminum contacts on highly doped n^+ and p^+ silicon junctions. The corresponding doping profiles are the BSF and emitter profiles shown in Figure 4.1.1 for n^+ and p^+ silicon, respectively.

$J_{0,met} - J_{0,diel}$ is shown in Figures 5.2.1 and 5.2.2 as a function of the excess carrier density (Δp) for HF-last Al_2O_3:Al contacts with various numbers of ALD Al_2O_3 cycles. In Figures 5.2.3 and 5.2.4, $J_{0,met} - J_{0,diel}$ is shown as a function of Δp for HNO_3-last Al_2O_3:Al contacts for several ALD Al_2O_3 cycles. Note that $J_{0,met} - J_{0,diel}$ for the unpassivated BSF contact is lower than $J_{0,met} - J_{0,diel}$ for the unpassivated emitter contact. Also, $J_{0,diel}$ is $\sim 40\ fA \cdot cm^2$ for the unpasisvated BSF and $J_{0,diel}$ is $\sim 50\ fA \cdot cm^2$, as obtained from Kane and Swanson's method on two-side passivated wafers.

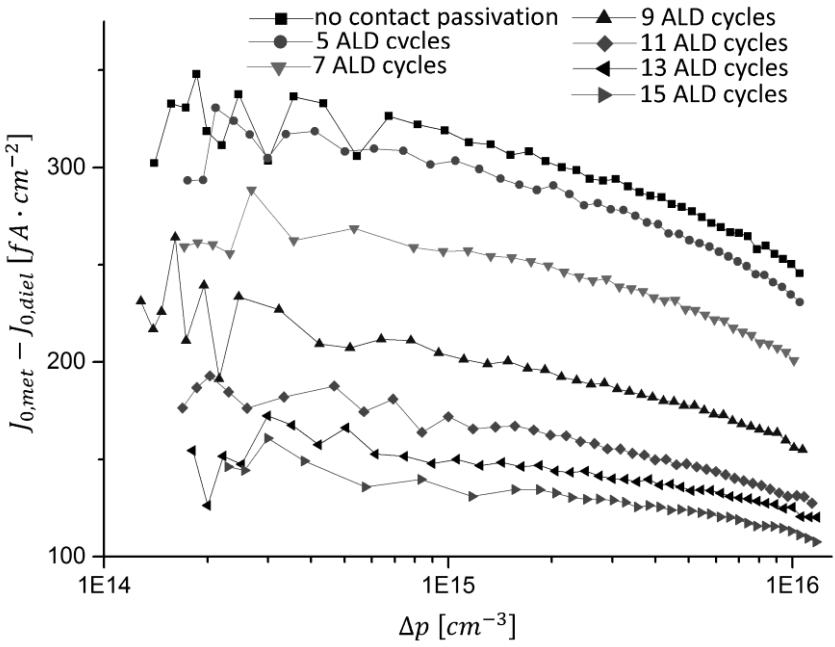

Figure 5.2.1. $J_{0,met} - J_{0,diel}$ as a function of injection level, for different numbers of Al2O3 ALD cycles on HF-last silicon for BSF (n^+ Si) contacts

Figure 5.2.1 shows $J_{0,met} - J_{0,diel}$ for HF-last Al_2O_3:Al contacts on a 45 Ω/square n^-n^+ junction (phosphorous doped), with a surface concentration of $3 \cdot 10^{19} cm^{-3}$. $J_{0,diel}$ was smaller than $50\ fA \cdot cm^{-2}$. We observe a steady decrease of $J_{0,met} - J_{0,diel}$ with increasing numbers of ALD cycles for all injection levels, which indicates that the contact on n^+ silicon is effectively passivated.

Figure 5.2.2 shows $J_{0,met} - J_{0,diel}$ for HF-last Al_2O_3:Al contacts on a 100 Ω/square n^-p^+ junction (Boron doped), with a surface concentration of $1 \cdot 10^{19} cm^{-3}$. For the emitter, $J_{0,diel}$ was less than $25\ fA \cdot cm^{-2}$. We do not observe decreasing emitter saturation current densities with increasing number of ALD cycles. This may be explained by the asymmetrical band structure and/or asymmetrical capture cross sections of the contact passivation layer, which we discuss in section 5.4.

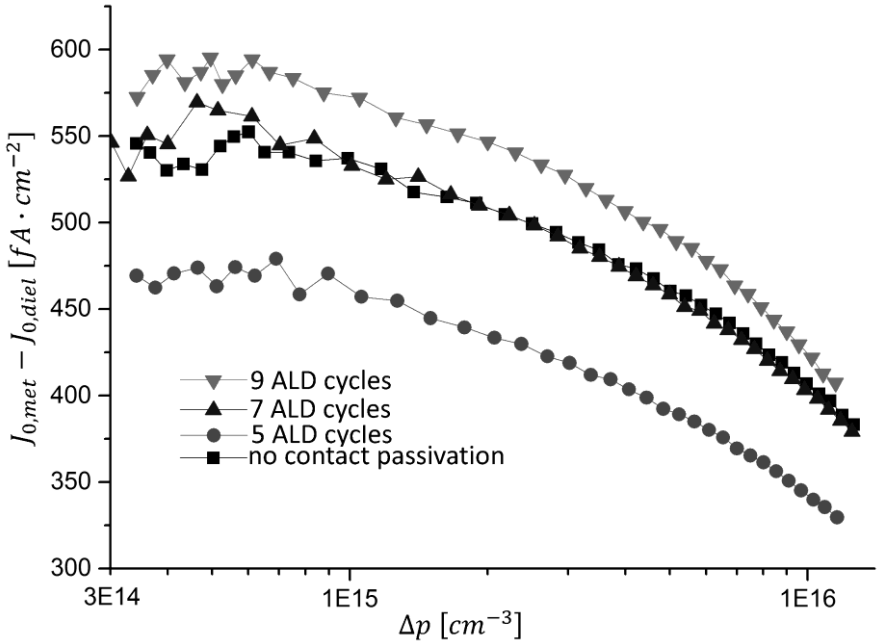

Figure 5.2.2. $J_{0,met} - J_{0,diel}$ as a function of injection level, for different numbers of Al_2O_3 ALD cycles on HF-last silicon for emitter (p^+ Si) contacts

In Figure 5.2.3, $J_{0,met} - J_{0,diel}$ is shown for HNO_3-last Al_2O_3:Al contacts on the same n^-n^+ junction that was used previously for the investigation of HF-last Al_2O_3:Al contacts. As before, a steady decrease of $J_{0,met} - J_{0,diel}$ with the number of ALD cycles is observed. However, the passivation is better for the same number of ALD cycles. This is explained by the absence of spikes through the passivation layer in the case of HNO_3-last Al_2O_3:Al contacts whereas HF-last Al_2O_3:Al contacts feature spikes through the passivation layer in the form of epitaxial silicon pyramids (Figure 5.1.2.1).

In Figure 5.2.4, $J_{0,met} - J_{0,diel}$ is shown for HNO_3-last Al_2O_3:Al contacts on the same n^-p^+ junction that was used previously for the investigation of HF-last Al_2O_3:Al contacts. Again, we do not observe decreasing emitter saturation current densities with the number of ALD cycles. The causes for this observation are discussed in section 5.4.

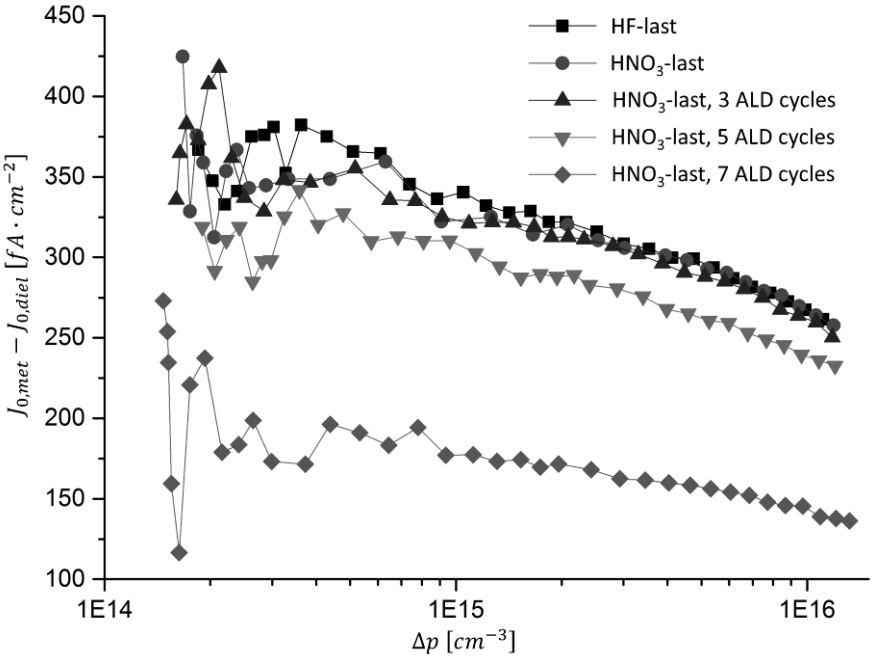

Figure 5.2.3. $J_{0,met} - J_{0,diel}$ for HNO_3-last Al_2O_3:Al BSF contacts as a function of the excess carrier density Δp for HNO_3-last n^+ silicon

$J_{0,met} - J_{0,diel}$ seemingly decreases with the injection level for all samples. This is most probably due to a parasitic effect similar to the effect of non-uniform excess carrier profiles on saturation current density extraction on blanket test structures reported by Kane and Swanson [Kane 1985]. In fact, in section 3.6 we showed that, for non-uniform excess carrier densities over wafer thickness, saturation current densities extracted using Equation 3.2.2.7 are underestimated by the factor pn_{met}/pn_a, in which pn_{met} is the pn product at the bulk side of the space charge region between contacted junction and bulk, and pn_a is the pn product in terms of the average injection level. The ratio of pn_{met} and pn_a decreases with increasing injection levels since the effective surface recombination velocity that describes junction recombination increases with injection level. As a result,

saturation current densities extracted using Equation 3.2.2.7 seemingly decrease with the injection level.

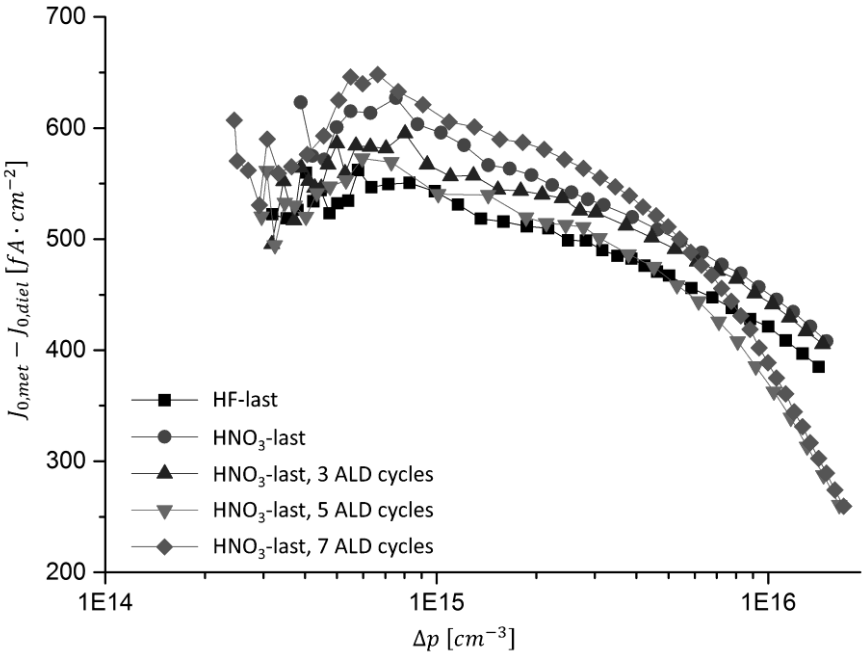

Figure 5.2.4. $J_{0,met} - J_{0,diel}$ for HNO_3-last Al_2O_3:Al emitter contacts as a function of the excess carrier density Δp for HNO_3-last p^+ silicon.

5.3. Contact resistance

In passivated contact design, a trade-off is made between contact passivation and contact resistance. In the previous section, we investigated the passivation of aluminum contacts on highly doped n^+ and p^+ silicon for two different surface pre-treatments. In this section, we investigate the other aspect that needs to be taken into account in the trade-off: contact resistance.

The contact resistance measurements performed in this dissertation are done using two methods. The first method is the circular transfer length method (cTLM). The second method is a simple current-voltage (IV) measurement between a tiny contact under test and an adjacent contact with similar properties but which is much bigger (see the inset in Figure 5.1.1.1). We now shortly discuss these two methods.

In the cTLM technique, contact resistance is extracted from multiple IV measurements on circular test structures which are described in [Schroder 2006] as "consisting of a conducting circular inner region of radius L, a gap of width d, and a conducting outer region." For $L \gg L_T$, with L_T the contact's transfer length; and for $L \gg d$; the expression for the test structure resistance, R_T, is particularly simple [Schroder 2006]:

$$R_T = \frac{R_S}{2\pi L}(d + 2L_T)C_f, \tag{5.3.1}$$

in which C_f is a correction factor given by:

$$C_f = \frac{L}{d}\ln\left(1 + \frac{d}{L}\right), \tag{5.3.2}$$

with R_s the semiconductor's sheet resistance, and $L_T = \sqrt{\rho_c/R_s}$, the contact's transfer length; with ρ_c contact resistance. Using Equations 5.3.1 and 5.3.2, contact resistance can be extracted from IV measurements as a function d, and optionally L.

Where contact resistances were too large for our particular cTLM test structure to be viable, the simple IV measurement between a tiny contact and a much larger contact was used. In this measurement, the measurement interpretation is even simpler than for the cTLM case. Because of its much larger size, the larger contact has negligible contact resistance compared to the tiny contact under test. Also, the resistance between the two contacts is neglected for simplicity. The latter assumption would result in an overestimate of contact resistance if the technique would be used to probe contacts with very small contact resistance. As the test structure's resistance (assumed to be) dominated by the contact resistance, the contact resistance is found from:

$$\rho_c = A_c \frac{dV}{dI}, \tag{5.3.3}$$

in which A_c is the contact's area, and dV/dI is the derivative of the current-voltage characteristic, measured around zero volts.

5.3.1. HF-last silicon

In Figure 5.3.1.1, we show the contact resistance of Al_2O_3 passivated contacts on our emitter (p^+ Si) and BSF (n^+ Si). The unpassivated BSF contact has a higher contact resistance than the unpassivated emitter contact even though the surface doping concentration is higher for the BSF than for the emitter. This is due to the higher Schottky barrier height of Al contacts on n^+ Si compared to Al contacts on p^+ Si. However, the contact resistance of BSF contacts increases much more slowly with the number of ALD cycles than the contact resistance of our emitter contacts. By comparison of Figures 5.2.1 and 5.2.2 with Figure 5.3.1.1, it is clear that ALD Al_2O_3 can provide very significant passivation of aluminum contacts on HF-last n^+ silicon for a relatively minor increase in contact resistance. Conversely, the presence of an ALD Al_2O_3 layer between Al and p^+ Si quickly results in excessive contact resistance while providing at most limited contact passivation. This can be explained by the fact the valence band offset of Al_2O_3 on silicon is higher than the conductance band offset of Al_2O_3 on silicon.

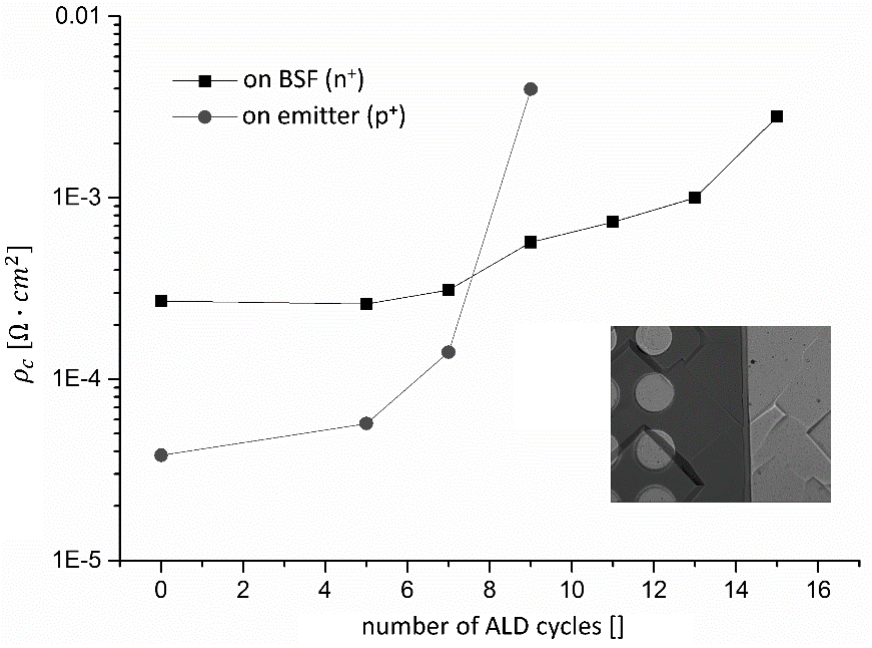

Figure 5.3.1.1. Contact resistance for Al_2O_3 passivated Al contacts on HF-last silicon as a function of the number of ALD cycles. The inset shows the test structure for the measurement of contact resistance for samples with very high contact resistance, for which the contact resistance is not measurable using our particular cTLM test structure.

We measured the temperature dependence of contact resistance at voltages below 5 mV between 25 and 100 ℃, which is shown in Figure 5.3.1.2, for two samples. These samples were chosen because they present a reasonable trade-off between contact resistance and contact passivation. It is clear that for these samples, contact resistance is not thermally activated. In [Deckers 2014], we noted that this is consistent with current transport through the dielectric which is dominated by direct tunneling tunneling through the SiO_x/Al_2O_3 passivation layer. Indeed, for small fields and thin oxides, the direct tunneling transport mechanism is expected (see e.g. [Sze 2007] p. 438). This should be contrasted with the trap assisted tunneling mechanism that has been found to be dominating at low operating voltages in (thicker) high-κ gate dielectric stacks in the context of complementary metal oxide semiconductor (CMOS) devices [Houssa 2000]. Other transport mechanisms, notably Poole-Frenkel emission and Fowler-Nordheim tunneling, are expected to be dominating at significantly larger electric fields, and for thicker oxides.

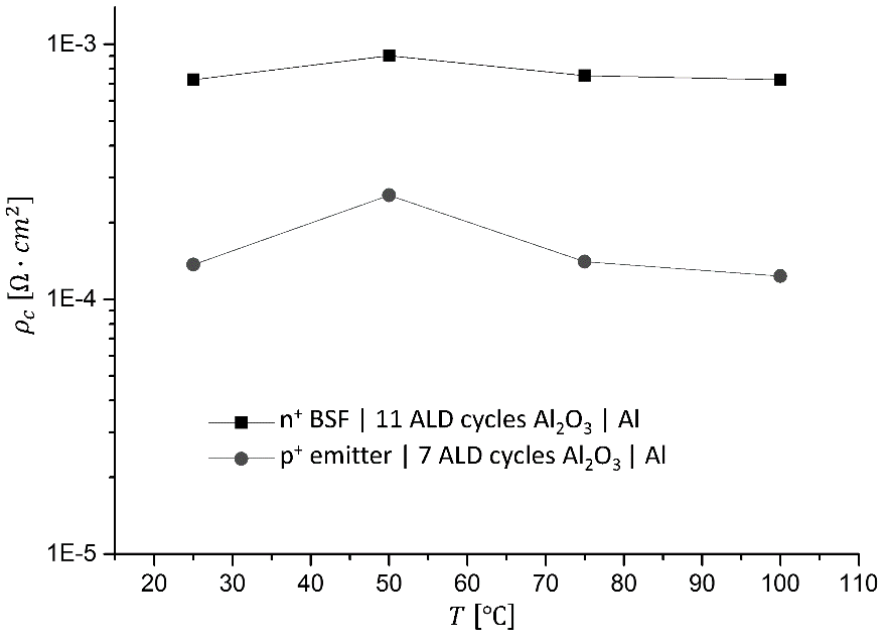

Figure 5.3.1.2. Contact resistance as a function of temperature for selected samples.

However, the TEM micrographs shown in section 5.1.2 indicate that the tunnel oxide is not continuous, but rather perforated. Therefore, it is actually likely that the contact resistance is determined by current flow through the perforations, as opposed to being dominated by a direct tunnel current through the thin dielectric contact passivation layer. Note that current transport dominated by direct tunneling through the space charge region associated with the aluminum-silicon junction in the perforations is consistent with the observed temperature independence of contact resistance.

5.3.2. HNO_3-last silicon

The contact resistance of ALD Al_2O_3 – passivated contacts on HNO_3-last silicon is shown in Figure 5.3.2.1. The contact resistance of all the HNO_3-last Al_2O_3 passivated contacts on silicon was too big to be measurable using our particular cTLM test structure. Therefore, we used the test structure shown in the inset of Figure 5.3.1.1 for all measurements, which yields an upper bound of the contact resistance.

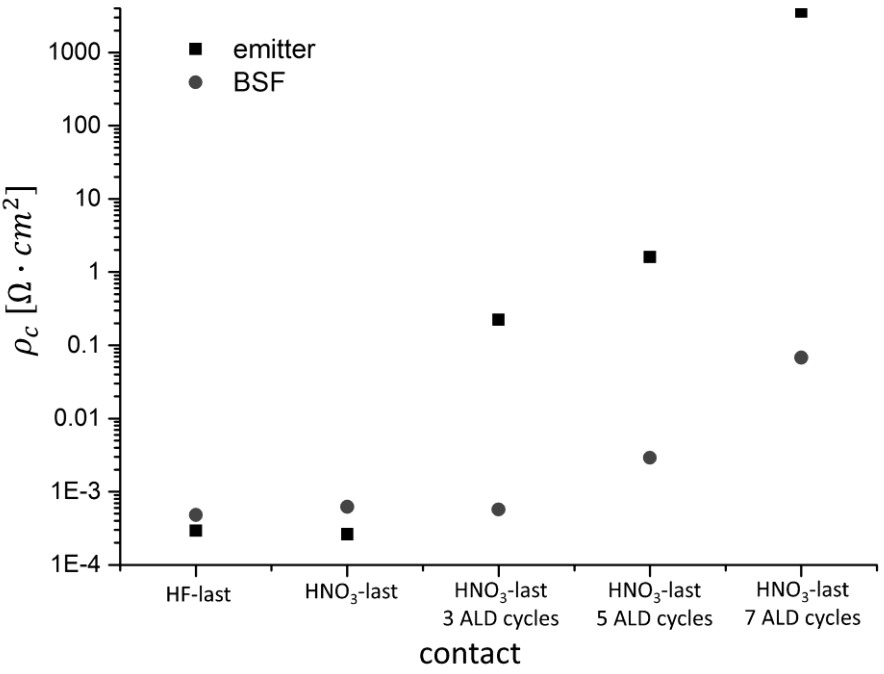

Figure 3.5.2.1. Upper bound on the contact resistance for ALD Al_2O_3-passivated aluminum contacts on HNO_3-last n^+ and p^+ silicon. The contact resistance of unpassivated aluminum contacts on HF-last and HNO_3-last n^+ and p^+ silicon is given as a reference.

By comparison of Figure 5.3.2.1 with Figure 5.3.1.1, the contact resistance for HNO_3-last Al_2O_3 passivated aluminum contacts is much higher than for HF-last Al_2O_3 passivated aluminum contacts, for the same number of ALD cycles. This is true for contacts on n^+ silicon and p^+ silicon. We suggest that this is due to the island growth of ALD Al_2O_3 during the first ALD cycles on the hydrogen-terminated HF-last silicon surfaces compared to the uniform growth of ALD Al_2O_3 on the hydroxyl-terminated HNO_3-last silicon. The associated perforations in the form of epitaxial nano-pyramids for HF-last Al_2O_3 passivated aluminum contacts form current paths which dominate the contact resistance for HF-last Al_2O_3 passivated aluminum contacts; conversely, the absence of these epitaxial nano pyramids in the case of HNO_3-last Al_2O_3 passivated aluminum contacts result in contact resistance being dominated by the tunneling current through the tunnel oxide, resulting in higher contact resistance.

5.4. Contact resistance and contact recombination

Our experiments yield several key observations on the passivation of Al-Si interfaces using Al_2O_3 on HF-last and HNO_3-last silicon. First, $J_{0,met}$ consistently decreases with increasing numbers of ALD cycles for passivated contacts on n^+ silicon. However, there was no appreciable contact passivation on p^+ silicon. Second, ρ_c consistently increases with the number of ALD cycles for contacts on both n^+ and p^+ silicon. Third, ρ_c increases much faster with the number of ALD cycles for p^+ silicon compared to n^+ silicon. Finally, $J_{0,met}$ decreases faster with the number of ALD cycles and ρ_c increases faster with the number of ALD cycles for Al_2O_3 passivated aluminum contacts for HNO_3-last silicon compared to HF-last silicon. These experimental observations are explained below.

5.4.1. Uniform layers

The passivation effect of a thin dielectric layer between metal contact and semiconductor is due to several effects. First, the silicon-metal interface is replaced by a silicon-dielectric interface, which reduces the density of states at the silicon surface, thereby reducing the surface recombination current. Apart from the density of states at the interface, the capture cross section of traps is another critical parameter that determines the surface recombination current. For plasma assisted ALD Al_2O_3 layers on (100) silicon interfaces, the capture cross section for holes in the lower band gap half is smaller than the capture cross section for electrons in the upper band gap half [Werner 2012]. Extrapolating this finding to the thermal ALD Al_2O_3 layers studied in this thesis, this partly explains why the investigated n^+ silicon surfaces are better passivated by Al_2O_3 than p^+ silicon surfaces.

Another reason for the passivation of a contacts by thin dielectric layers is that the dielectric forms a barrier that shields minority carriers from the metal. This is also an essential effect since minority carrier flow from the semiconductor into the contact is effectively a recombination current. The transfer coefficient for tunneling T_t, i.e. the tunnelling probability, of carriers through a rectangular barrier is approximately given by [Sze 2007] p. 440:

$$T_t \approx exp\left(-\frac{2d\sqrt{2qm^*\phi_T}}{\hbar}\right) \qquad (5.4.1.1)$$

in which d is barrier thickness, q is elementary charge, m^* is effective mass in the barrier, $q\phi_T$ is effective barrier height in eV, and $\hbar$ equals $h/2\pi$, with h Planck's constant.

In our qualitative analysis, we make the simplifying assumption that all electrons (holes) are situated at the top (bottom) of silicon's conduction (valence) band. As a consequence and in the context of our passivated contacts, the barrier height for electron flow through the dielectric corresponds to the conductance band offset ΔE_c between dielectric and silicon, and the barrier height for hole flow through the dielectric corresponds to the valence band offset ΔE_v between dielectric and silicon.

For passivated contacts on HNO_3-last silicon, contact resistance is determined by tunneling through the passivating dielectric stack. For passivated contacts on HF-last silicon, both tunneling and current transport through pinholes in the dielectric play a role. Here, the properties of the dielectric tunneling barrier are discussed. A first observation with respect to the dielectric tunneling layer is that the contact passivation layer under investigation is actually a SiO_x:Al_2O_3 stack, since it is well known that a thin SiO_x layer unavoidably grows between Al_2O_3 and silicon. The valence band offset ΔE_v of SiO_2 on Si is 4.35 to 4.54 eV and the conductance band offset ΔE_c of SiO_2 on Si is 3.15-3.5 eV. For Al_2O_3 on Si, ΔE_v is 2.95-3.75 eV and ΔE_c=2.08-2.8 eV [Bersch 2008]. For the purpose of our qualitative reasoning, we disregard the fact that SiO_2 and Al_2O_3 have different band offsets, but we use that for both SiO_2 and Al_2O_3, $\Delta E_v > \Delta E_c$. Therefore, the tunnelling probability through the SiO_x:Al_2O_3 stack is smaller for holes than for electrons, all other things equal. The contact resistance ρ_c is determined by the resistance to majority carrier flow. In Al_2O_3-passivated contacts on silicon, resistance to the flow of holes from silicon to metal is bigger than the resistance to the flow of electrons from silicon to metal since $\Delta E_v > \Delta E_c$. It therefore follows that contact resistance on our n^+ BSF is expected to increase slowly with the number of Al_2O_3 ALD cycles compared to contact resistance on our p^+ emitter. This corresponds to the experimental observation of contact resistance as a function of the number of Al_2O_3 ALD cycles.

The effective surface recombination velocity of the contact is determined by surface recombination at the Si-SiO_x:Al_2O_3 interface, by the tunneling probability of minority carriers from the semiconductor to the metal, and by recombination in pinholes, if present. We first focus on the properties of the Si-SiO_x:Al_2O_3 interface and then discuss the influence of pinholes to extend our conclusions to Al_2O_3 passivated aluminum contacts on HF-last silicon.

Since the capture cross section for holes in the lower band gap half is smaller than the capture cross section for electrons in the upper band gap half for Al_2O_3 – (100) silicon interfaces [Werner 2012], the surface recombination at the p^+ Si – Al_2O_3 interface is larger than the recombination current at the n^+ Si Al_2O_3 interface, all other things equal. This partly explains the worse passivation of p^+ silicon surfaces compared to n^+ silicon surfaces in our study.

An additional explanation for the observed trends of contact passivation and contact resistance can be found in the band structure of the aluminum-aluminum oxide-silicon contact. For Al_2O_3 on silicon, $\Delta E_v > \Delta E_c$ such that the transmission coefficient through the barrier is smaller for holes than for electrons, and the resistance to minority carrier flow is larger for the passivated n^+ BSF compared to the passivated p^+ emitter, all other things equal. This is beneficial for the passivation of the n^+ BSF compared to the passivated p^+ emitter. In addition, due to the asymmetric conduction and valence band offsets, $J_{0,met}$ of the passivated n^+ BSF is expected to decrease faster with the number of ALD cycles than $J_{0,met}$ of the passivated p^+ emitter. The above observations explain why we observed consistently improving n^+ BSF contact passivation with the number of ALD cycles, and we failed to observe such a trend for passivated contacts on our p^+ emitter.

Trapped charge in the ALD Al_2O_3 layers is also a factor which may affect the contact recombination properties. For thermal Al_2O_3 ALD layers, the charge carrier density was found to be $-4 \cdot 10^{11} cm^{-2}$ elementary charges at the SiO_x-Al_2O_3 interface and $-1 \cdot 10^{19} cm^{-3}$ elementary charges in the Al_2O_3 layer [Rothschild 2010]. The thickness of the layers we investigated was below 4 nm, which yields overall charge densities of $-4 \cdot 10^{11}$ to $-4.4 \cdot 10^{11}\ cm^{-2}$. The fact that the overall surface charge density is not expected to change significantly with the number of ALD cycles for the samples we investigated is consistent with our contact resistance measurements: increasing negative charge density in a tunnel barrier would increase the Schottky barrier height for passivated n^+ Si-Al contacts and it would decrease the Schottky barrier height for Al_2O_3 passivated p^+ Si-Al contacts. Therefore, if the surface charge would increase significantly with the number of ALD cycles in the investigated range, the contact resistance of Al_2O_3 passivated n^+ Si-Al contacts would tend to increase faster with the number of ALD cycles than contact resistance of Al_2O_3 passivated p^+ Si-Al interfaces. This contradicts our experimental observations, which motivates the interpretation of our experimental results in terms of band offsets, and a reduction in surface states.

The worse contact passivation of aluminum contacts on p^+ silicon compared to n^+ silicon by ALD Al_2O_3 layers is in apparent contradiction to experiments in [Hoex 2007, Hoex 2008]; in which excellent passivation of p^+ silicon surfaces by plasma assisted ALD Al_2O_3 was reported. Our failure to observe contact passivation on p^+ silicon surfaces by ALD Al_2O_3 layers is also at odds with experimental results reported in [Richter 2011]. In the next paragraphs, an attempt is made to explain the observed discrepancies.

The most remarkable difference between the layers investigated in [Hoex 2007] and the layers investigated in this work is their thickness. The thickness of our layers is kept very thin, less than 3 nm, as to allow a majority carrier tunnel current

to pass through. Conversely, the passivation layers in [Hoex 2007] were much thicker (30 nm), as they were not designed to allow current to tunnel through. The higher thickness implies more negative charge in the dielectric, which in turn implies a better field effect passivation of the negatively charged Al_2O_3 layer on the p^+ silicon surface. In addition, the extremely low thickness of our layers also implies that minority carriers can tunnel through, whereas the layers in [Hoex 2007] are much too thick for a tunnel current to pass through (by Equation 5.4.1.1, the tunneling probability of minority carriers through the SiO_x:Al_2O_3 stack decreases strongly with the layer thickness).

In [Richter 2011], very thin ALD Al_2O_3 layers, having thicknesses of less than a nanometer, are observed to passivate of p^+ silicon surfaces. However, the thin ALD Al_2O_3 layers studied in [Richter 2011] are not contacted; contrary to our samples on which we failed to observe the passivation of aluminum contacts on p^+ silicon by Al_2O_3 ALD layers. Therefore, the failure to observe contact passivation of aluminum contacts on p^+ silicon in our experiments may indicate that interactions between the metal layer and the dielectric could compromise the dielectric's passivating properties. However, it should be noted that other differences in the sample characteristics were present as well, including a difference in surface doping concentration. Therefore, definitely establishing the cause of the failure to observe contact passivation in our samples would require further research.

5.4.2. Non-uniform layers

In our analysis of non-uniform layers, we consider a special, simplified case, corresponding to a dielectric tunneling barrier with pinholes. Outside the pinholes, the tunneling barrier is perfectly homogeneous. We call the pinholes unpassivated areas, and the tunneling barrier covered surfaces are called passivated areas. In this case, the saturation current density of the contacted junction is approximately the area weighted sum of the saturation current densities of passivated and unpassivated areas:

$$J_{0,c} = J_{0,p} + C_u\left[J_{0,u} - J_{0,p}\right], \tag{5.4.2.1}$$

in which $J_{0,c}$ is the average saturation current density, $J_{0,p}$ is the saturation current density of passivated areas, $J_{0,u}$ is the saturation current density of unpassivated areas, and C_u is the ratio of the unpassivated area to the total area.

The resulting contact resistance of a non-uniform contact consisting of passivated and unpassivated areas is the area-weighed harmonic average of the contact resistances of passivated and unpassivated areas:

$$\frac{1}{\rho_c} = \frac{1}{\rho_p} + C_u \left[\frac{1}{\rho_u} - \frac{1}{\rho_p}\right], \quad (5.4.2.2)$$

in which ρ_c is the resulting contact resistance of the non-uniform contact, ρ_p is the contact resistance of the passivated areas, and ρ_u is the contact resistance of the passivated areas.

Because the dependence of ρ_c and $J_{0,c}$ on C_u is different, the occurrence of pinholes can yield an improved trade-off between contact resistance and contact recombination. Inspection of Equations 5.4.2.1 and 5.4.2.2 yields that especially when ρ_u is small compared to ρ_p, a small amount of pinholes can drastically lower the contact resistance while marginally impacting the contact saturation current density provided that $J_{0,u}$ is not much larger than $J_{0,p}$. This analysis, combined with the observation of pinholes for Al_2O_3 passivation layers on HF-last silicon, and the absence of pinholes for Al_2O_3 passivation layers on HNO_3-last silicon, qualitatively explains the dramatic dependence of contact resistance and contact passivation on the final surface treatment of the silicon wafer before ALD Al_2O_3 deposition.

Because the presence of pinholes can influence contact resistance and contact recombination in such a dramatic way, it is essential to control pinhole occurrence. Failure to do so can result in solar cells with excessively high contact resistance.

6. Conclusions

A novel test structure for contact recombination current measurements has been proposed. The test structure is based on lattices of point contacts with various contact fractions on which radio wave detected photoconductance measurements are performed. The test structure has the advantage of simplicity. Its most significant limitations are related to design rules for avoiding parasitic current flow through point contacts, and to design rules formulated to ensure constant excess carrier densities throughout the test structure's quasi neutral bulk. The test structure and the fundamental theory at its basis is outlined in section 3.2. Test structure manufacture for the characterization of MIS contacts on diffused junctions is outlined in section 3.3.

In order to avoid parasitic effects related to current flow through point contacts the contact's characteristic size must be smaller than the contact transfer length. Design rules related to avoid parasitic current flow through point contacts are treated in section 3.4. Failure to ensure that the contact's characteristic size is smaller than the contact's transfer length causes underestimations in extracted contact recombination currents. In addition, the point contacts in the test structure must be designed such that adjacent point contacts do not touch. For simple square lattices of circular point contacts, as used in this dissertation, this restriction limits the maximum theoretical contact fraction to $\pi/4$. However, practical maximum contact fractions are generally smaller as metallized areas are always bigger than the contact openings to provide a buffer for process limitations. For the lithographically defined test structures used in this dissertation, the maximum contact fraction is less than 20%, and is limited by design rules which require the metal point contacts to be significantly larger than the contact openings as to counter misalignment, over etch and over development.

The excess carrier density must be approximately constant throughout the test structure's quasi neutral bulk for a simple interpretation of the measurement results to apply. Excess carrier density variations are discussed in sections 3.5 and 3.6.

In order to avoid in-plane excess carrier density variations, contact size and pitch must be designed to be much smaller than the effective diffusion lengths in contacted and passivated areas, respectively. This is discussed in section 3.5.

Out-of-plane excess carrier density variations are discussed in section 3.6. Out-of-plane excess carrier density variations can be limited by using thin wafers such that the bulk diffusion length is much larger than wafer thickness. In addition, out-of-plane excess carrier density variations can be reduced by making symmetric

test structures as opposed to asymmetric test structures (section 2.3). However, in symmetric test structures the generation rate depends on the contact fraction, which has to be taken into account. Also, because of the partial shading in symmetric test structures, in-plane excess carrier density variations may be more pronounced. An additional consideration is related to bulk excess carrier density variations being smaller on a relative basis for smaller effective surface recombination velocities, all other things equal. Therefore, the test structure works better for better passivated contacts. In addition, since junction recombination is generally proportional to the pn product, junction recombination generally results in increasing effective surface recombination velocities for increasing injection levels such that excess carrier densities are more constant at lower excess carrier densities. As a result, contact recombination characteristics are more accurately extracted from the test structures at low excess carrier densities. At higher excess carrier densities, the increased effective surface recombination velocities result in higher excess carrier density variations, which result in seemingly decreasing saturation current densities with increasing excess carrier concentration. Finally, excess carrier density variations cause saturation current densities to be underestimated more when they are extracted using the high injection level technique compared to when they are extracted using the arbitrary injection level technique.

For saturation current densities extracted using the arbitrary injection level technique, the bulk doping level must be accurately known. Using incorrect bulk doping levels significantly distorts the extracted contact recombination currents at low excess carrier densities, but has no effect on contact recombination currents extracted at high excess carrier densities; thereby introducing artificial excess carrier density dependence in the extracted contact recombination currents. This is discussed in section 3.7.

In this dissertation, the focus is on surface recombination currents featuring unit ideality factors. The presence of significant space charge region recombination can give rise to ideality factors significantly bigger than one. The resulting effect on contact saturation current densities extracted using the arbitrary injection level technique is treated in section 3.8.

In lithographically defined test structures, contact diameter control is complicated due the use of relatively rough solar cell wafers. The use of relatively rough wafers requires relatively high illumination doses to ensure uniform resist development across the entire wafer. However, this introduces over-development. In addition, over-etch is unavoidable due to the relatively long etching times used to ensure uniform contact opening. Errors related to poor contact size control are treated in section 3.9.

For some contacting technologies, such as plated contacts, the use of line-shaped contact openings is desirable. Also, for some contact opening technologies such as laser-opened contacts, the contact recombination current is expected to depend on the contact shape. Therefore, test structures based on lattices of point contacts are not ideally suited for the study of some contacting technologies. Alternative test structure embodiments featuring line-shaped contacts are discussed in section 3.10.

In chapter 4, the $J_{0,met}$ test structure introduced in chapter 3 is applied to the optimization of diffused junctions. The use of this $J_{0,met}$ test structure for such a classical junction optimization problem allows for further experimental confirmation of the characterization method. The optimization has proven to be especially successful since the baseline efficiency of imec's IBC process was increased by 0.2% by merely modifying the BSF and FSF oxidations. Indeed, the consistency of the trends between contact resistance, contact saturation current density and saturation current density of the passivated junction is a strong experimental confirmation of this novel characterization method.

Finally, in chapter 5, thin dielectric Al_2O_3 layers grown using thermal atomic layer deposition (ALD) are investigated for the passivation of the interface between aluminum contacts and n^+ or p^+ silicon. Specific attention is paid to the effect of the surface treatment prior to the formation of Al_2O_3 contact passivation layers: HF-last and HNO_3-last ALD Al_2O_3 contact passivation layers are investigated. ALD Al_2O_3 contact passivation layers are found to effectively passivate aluminum contacts on n^+ silicon surfaces, but they are found to be ineffective at passivating aluminum contacts on p^+ silicon surfaces. In addition, it is found that pin-holes associated with HF-last ALD Al_2O_3 contact passivation layers can improve the trade-off between contact resistance and contact recombination associated with passivated contacts.

7. Suggestions for future work

The theoretical treatment in this dissertation is based on relatively simple analytical models to tackle the analysis of $J_{0,met}$ test structures based on lattices of point contacts one aspect at a time. This approach is advantageous because of its simplicity and transparency. However, an all-inclusive three dimensional model of the test structure could be useful to uncover phenomena related to the interaction of different non-ideal effects.

A three dimensional model could also be useful for quantitative modelling of non-ideal effects, for example those due to non-uniform excess carrier densities throughout the quasi neutral bulk. This might allow for extracting more accurate $J_{0,met}$ values from effective lifetime measurements on non-ideal samples. Alternatively, the Plagwitz model [Plagwitz 2006] could be used as a basis for more accurate contact recombination current extraction using our test structure.

The development of alternative test structure embodiments could allow for the application of the $J_{0,met}$ test structure to the characterization of line-shaped contacts. In addition, such alternative test structure embodiments could also be useful to speed up the measurement time. However, the realization of such alternative test structure embodiments would require the development of new measurement tools.

Test structures based on line-shaped contacts may also be useful in the field of DC contact recombination current measurements, as opposed to the AC contact recombination measurements performed in the present dissertation. The DC contact resistance of many passivated contacts is suspected to be higher than their AC contact resistance. Therefore, DC measurements may be useful in this context for reducing parasitic effects related to current flow through the metal contacts instead of through the semiconductor.

There is a great variety of material systems that show significant potential in the field of passivated contacts. We assert that the test structure proposed in the present dissertation, and its alternative embodiments, could proof to be useful characterization tools for further research in this field.

Symbols

k	Boltzmann's constant	$[cm^2 \cdot kg \cdot s^{-2}K^{-1}]$
C_{met}	contact fraction	$[\%]$
D	diffusion coefficient	$[cm^2 \cdot s^{-1}]$
E	electric field	$[V \cdot cm]$
E_F	Fermi level	$[eV]$
G	generation rate	$[cm^{-3}s^{-1}]$
J	current density	$[A \cdot cm^{-2}]$
$\mathrm{J_{mpp}}$	current density at maximum power point	$[A \cdot cm^{-2}]$
J_R	recombination current density	$[A \cdot cm^{-2}]$
J_0	saturation current density	$[A \cdot cm^{-2}]$
L_D	diffusion length	$[cm]$
L_T	transfer length	$[cm]$
n	free electron concentration	$[cm^{-3}]$
n_i	intrinsic carrier concentration	$[cm^{-3}]$
n_0	equilibrium free electron concentration	$[cm^{-3}]$
N_A	electron acceptor concentration	$[cm^{-3}]$
N_D	electron donor concentration	$[cm^{-3}]$
p	free hole concentration	$[cm^{-3}]$
p_0	equilibrium free hole concentration	$[cm^{-3}]$
P_{mpp}	output power at maximum power point	$[W]$
q	elementary charge	$[C]$
Q	$Q = S_{eq}/S_s$	[-]
R	recombination rate	$[cm^{-3}s^{-1}]$
R_s	sheet resistance	$[\Omega/square]$
S	conductance, also S_x, S_y or S_z when referring to a particular direction	$[\Omega^{-1}]$
	Also: pitch (in section 3.4)	$[cm]$
S_{eff}	effective surface recombination velocity also S_1 or S_2 when referring to a particular surface	$[cm \cdot s^{-1}]$
S_{eq}	sheet resistance of a wafer featuring a lattice of point contacts	$[\Omega^{-1} \cdot square]$
S_s	sheet conductance of a bare wafer	$[\Omega^{-1} \cdot square]$

t	time	$[s]$
T	temperature	$[K]$
V	quasi Fermi level splitting	$[V]$
V_{mpp}	output voltage at maximum power point	$[V]$
Δn	excess electron concentration	$[cm^{-3}]$
Δp	excess hole concentration	$[cm^{-3}]$
W	wafer thickness, approximately equal to bulk quasi neutral region thickness	$[cm]$
$\Delta\sigma$	photoconductivity	$[\Omega^{-1} \cdot cm^{-1}]$
η	efficiency	$[\%]$
μ	mobility	$\left[cm^2 \cdot V^{-1} \cdot s^{-1}\right]$
σ	conductivity	$[\Omega^{-1} \cdot cm^{-1}]$
τ_b	bulk lifetime	$[s]$
τ_{eff}	effective lifetime	$[s]$

Glossary

Arbitrary injection technique: The term “arbitrary injection technique” refers to the application of Equation 3.2.7 for $J_{0,met}$ extraction. The name derives from the fact that Equation 3.2.7 can be used at arbitrary injection levels, as opposed to Equation 3.2.10, the “high injection technique”, which is only applicable when the injection level is sufficiently high such that Kane and Swanson’s method [Kane 1985] is applicable.

BSF: Back surface field; highly doped region in a high-low junction on a solar cell’s non-illuminated side used for surface passivation and base contacting.

BSG: Boro-Silicate Glass - Glassy substance used as a boron source for the formation of p+ diffused regions.

CIGS: Copper Indium Gallium Selenide, an absorber material for thin-film solar cells.

Contact fraction C_{met} : The ratio of contacted area and total area.

cTLM: Circular Transfer Length Method, a method for contact resistance measurements

diffusion current: the component of the electrical current which is driven by a charge carrier concentration gradient.

drift current: the component of the electrical current which is driven by an electric field.

Dry oxide: oxide formed with O_2 being the oxidizing species. A dry oxide forming oxidation is called a dry oxidation.

Effective lifetime τ_{eff} $[s]$: Characteristic timescale of recombination processes. It is defined such that $\tau_{eff} \equiv \Delta p_a / R_{tot}$, in which Δp_a is the average excess carrier density over the thickness of the quasi neutral bulk, and R_{tot} is the total recombination rate per unit area.

Effective surface recombination velocity S_{eff} $[cm \cdot s^{-1}]$: A figure of merit for surface recombination in which the surface recombination current is described as: $J_R = qS_{eff}\Delta p$, with J_R the surface recombination current density, q elementary charge, and Δp the excess carrier density at the surface.

EQE [%]: external quantum efficiency; the ratio of the minority carrier flux collected by the solar cell under short circuit conditions and the photon flux reaching the solar cell surface.

Excess carrier density: The difference between the carrier density and the equilibrium carrier density, also called the injection level.

HF-dip: Short (typically 10s to 2 min) immersion of one or more wafers in a diluted aqueous HF-solution (typically 1-10 vol%). A small amount of HCl is commonly added to the solution (typically 1-10%).

High injection technique: The term “high injection technique” refers to the application of Equation 3.2.10 for $J_{0,met}$ extraction. The name derives from the fact that for Equation 3.2.10 to be relevant, $J_{0,tot}$ must be extractable using Kane and Swanson’s method [Kane 1985] from the effective lifetime data over a range of contact fractions. For Kane and Swanson’s method to be applicable, the injection level must be sufficiently high such that the slope of inverse lifetime versus the contact fraction is determined by junction recombination. Note that as used in this thesis, the term “high injection” does not necessarily refer to injection levels that are strictly larger than ten times the base doping level. In fact, as shown in sections 3.5 and 3.6, the high injection technique

should not be applied at “too high” injection levels because parasitic effects related to non-constant excess carrier densities are more significant at higher injection levels.

IBC solar cells: solar cells with a specific contacting layout in which all contacts are at the non-illuminated side of the solar cell, and the emitter and base contacts are shaped in a pattern that resembles two hands with interlocking fingers.

Ideality factor m: Figure of merit for recombination currents which describes their injection level dependence. In this dissertation, unit ideality factors are assumed unless mentioned otherwise.

Injection level: The difference between the carrier density and the equilibrium carrier density, also called the excess carrier density.

IQE $[\%]$: internal quantum efficiency - the ratio of the minority carrier flux collected by the solar cell under short circuit conditions and the photon flux reaching the solar cell’s active part.

Layperson: a person without professional or specialized knowledge in a particular subject.

Maximum power point: The point on a solar cell’s current-voltage characteristic at which the solar cell’s output voltage is at a maximum. The power delivered by the solar cell at the maximum power point is called $P_{mpp} = I_{mpp} \cdot V_{mpp}$.

MIS: a Metal-Insulator-Semiconductor structure

Passivated contact: The term passivated contact refers to the application of a technique to reduce the recombination current at the metal-semiconductor interface. Examples are metal – insulator – semiconductor contacts and semiconductor – insulator – semiconductor contacts. The term carrier-selective contact can be used interchangeably.

PL: photoluminescence – the process in which matter emits photons after the absorption of photons.

PSG: Phospho-Silicate Glass - glassy substance used as a phosphorous source for the formation of n^+ doped diffusions.

QSSPC: Quasi Steady State Photoconductance. A photoconductance measurement technique featuring an exciting light pulse that is much longer than the effective minority carrier lifetime such that the steady state approximation is valid. This measurement technique allows to obtain the effective lifetime as a function of the injection level.

RCA clean (Radio Corporation of America Clean): a silicon wafer cleaning process consisting of the following sequence: SC1 – water rinse – HF dip – water rinse – SC2 – water rinse – HF-dip – water rinse

Red.: Redacted; used in citations when certain bits and pieces of information were added to the citation in order to improve citation’s clarity.

Saturation current density J_0 $[fA \cdot cm^{-2}]$: A figure of merit for recombination currents, particularly for surface regions featuring highly doped regions between surface and semiconductor bulk. The recombination current at the surface and in the highly doped region is described as: $J_R = J_0 \exp(qV/mkT)$, in which J_R is the recombination current, q is elementary charge, V is the Fermi level splitting at the bulk-side of the space charge region between diffused region and semiconductor bulk, m is the ideality factor, k is Boltzmann’s constant, and T is absolute temperature.

SC1: Standard Clean 1, used in the RCA clean. It is performed in many variations in the Art. As used in the present dissertation, the SC1 clean consists of a 10 minute chemical treatment in a 1:1:5 NH_4OH:H_2O_2:H_2O solution at 70℃.

SC2: Standard Clean 2, used in the RCA clean. It is performed in many variations in the Art. As used in the present dissertation, the SC2 clean consists of a 10 minute chemical treatment in a 1:1:5 HCl:H_2O_2:H_2O solution at 80℃.

SPM: Sulfur-Peroxide-Mixture. Mixture of H_2O_2 and H_2SO_4. In the present dissertation, it is used for wafer cleaning: 10 minutes in a fresh solution (1:4 H_2O_2 and H_2SO_4) at a temperature between 90 and 120℃. The mixing process of H_2O and H_2SO_4 is highly exothermic such that this temperature is reached upon mixing of H_2O_2 and H_2SO_4 in a 1:4 ratio.

Something rotten in the state of this text: Allusion to a sentence from the first Act of Shakespeare's play "Hamlet". The original phrase is "something rotten in the state of Denmark". In English, the phrase "something rotten in the state of Denmark" is used to indicate "something which is not right, rife with errors from top to bottom, leading to suspicion of motive" [Wiktionary 2014].

Transfer length L_T $[cm]$: Characteristic length for current to flow in or out of a metal contact on a semiconductor. It is defined as $L_T = \sqrt{\rho_c / R_{sheet}}$, in which ρ_c is contact resistance and R_{sheet} is sheet resistance.

Wet oxide: Oxide formed with H_2O being the oxidizing species. A wet oxide forming oxidation is called a wet oxidation.

Publications

Peer-reviewed journal papers

J. Deckers et al., Avoiding parasitic current flow through point contacts in test structures for QSSPC contact recombination current measurements, IEEE Journal of Photovoltaics, 2015, vol. 5, issue 1, pp. 276-281; DOI: 10.1109/JPHOTOV.2014.2359731

J. Deckers et al., Excess carrier density variations in test structures for photoconductance-based contact recombination current measurements, IEEE Journal of Photovoltaics, in press.

J. Deckers et al., Comparing n- and p-type polycrystalline silicon absorbers in thin-film solar cells, Thin Solid Films, in press.

I. Abdo, C. Trompoukis, J. Deckers, et al., Integration of a 2-D Periodic Nanopattern Into Thin-Film Polycrystalline Silicon Solar Cells by Nanoimprint Lithography, IEEE Journal of Photovoltaics, 2014, Vol. 4, issue 5, pp. 1261-1267; DOI: 10.1109/JPHOTOV.2014.2339498

F. Dross, K. Baert, T. Bearda, J. Deckers, et al., Crystalline thin-foil silicon solar cells: where crystalline quality meets thin-film processing, Progress in Photovoltaics: Research and Applications 20(6), 2012, pp. 770-784; DOI: 10.1002/pip.1238

Peer-reviewed conference proceedings

J. Deckers et al., Aluminum oxide-aluminum stacks for contact passivation in silicon solar cells, Energy Procedia, 2014, pp. 656-664; DOI: 10.1016/j.egypro.2014.08.041

C. Dang, R. Labie, L. Tous, R. Russell, M. Recaman, J. Deckers, et al., nvestigation of Laser Ablation Induced Defects in Crystalline Silicon Solar Cells, Energy Procedia, 2014, pp. 649-655; 10.1016/j.egypro.2014.08.040

Patent applications

J. Deckers, Method for the extraction of recombination characteristics at metallized semiconductor surfaces, European patent application, filed on 24/09/2013 (comprises JP, US, & EP family members)

Conference proceedings – no peer review

J. Deckers et al., Injection Dependent Emitter Saturation Current Density Measurement under Metallized Areas Using Photoconductance Decay, in proc. 28th European Photovoltaic Solar Energy Conference and Exhibition, 2013, pp. 806 – 810; DOI: 10.4229/28thEUPVSEC2013-2BO.2.2

J. van Hoeymissen, C. Gritti, J. Deckers, et al., Embedded Porous Si Reflectors for Epitaxial Solar Cells: Stability, Optical Performance and Industrial Manufacturability, in proc. 5th European Photovoltaic Solar Energy Conference and Exhibition / 5th World Conference on Photovoltaic Energy Conversion, 2010, pp. 3602 – 3605; DOI: 10.4229/25thEUPVSEC2010-3BV.3.21

Contributions under peer review

J. Deckers et al., Out-of-plane excess carrier density variations in point contact lattice-based test structures for QSSPC contact recombination current measurements

J. Chen, J. Deckers et al., Investigation of laser ablation on boron emitters for n-type rear-junction PERT type silicon wafer solar cells

References

[Altermatt 2003] P. P. Altermatt et al., Reassessment of the intrinsic carrier density in crystalline silicon in view of band-gap narrowing, Journal of Applied Physics 93, 1598 (2003); doi: 10.1063/1.1529297

[Amkreutz 2014] D. Amkreutz et al., Conversion efficiency and process stability improvement of electron beam crystallized thin film silicon solar cells on glass, Solar Energy Materials & Solar Cells 123 (2014) 13-16; DOI: DOI: 10.1016/j.solmat.2013.12.021

[Baba 1995] T. Baba et al., 9.2% Efficiency thin-film polycrystalline silicon solar cell by a novel solid phase crystallization method, Proceedings of the 13th European Photovoltaic Solar Energy Conference, 1995, pp. 1708-1711

[Bagnall 2008] D. M. Bagnall and M. Boreland, Photovoltaic technologies, Energy Polyci 36, 12, December 2008, pp. 4390-4396; DOI: 10.1016/j.enpol.2008.09.070

[Baker-Finch 2011] S.C. Baker-Finch and K.R. McIntosh, Reflection of normally incident light from silicon solar cells with pyramidal texture, Progress in Photovoltaics 19 (4), pp. 406–416, 2011

[Bartels 1995] R. Bartels et al., Comparison of silicon oxynitride and silicon oxide as tunnel insulators in MIS-IL silicon solar cells, proceedings of the 13th European photovoltaic solar energy conference, 23-27 October 1995, Nice, France, pp. 1272-1275

[BAS 2014] British Antarctic Survey, BAS goes solar (http://www.antarctica.ac.uk/about_antarctica/environment/energy/solar.php; accessed on 15-09-2014)

[Basore 2013] P. A. Basore et al., All-aluminum Screen-printed IBC Cells: Design Concept, Presented at the 29th IEEE Photovoltaic Specialists Conference, Tampa, FL, 17-21 June 2013.

[Berger 1972] H. H. Berger, Models for Contacts to Planar Devices, Solid-State Electronics, Vol. 15, pp. 145-158, 1972

[Berger 1972b] H. H. Berger, Contact Resistance and Contact Resistivity, Journal of the Electrochemical Society: Solid-State Science and Technology, Vol. 119, No. 4, 1972, pp. 507-514

[Bersch 2008] E. Bersch et al., Band offsets of ultrathin high-κ oxide films with Si, Physical review B 78, 085114 (2008); DOI: 10.1103/PhysRevB.78.085114

[Beyer 1996] A. Beyer et al., Metal-insulator-semiconductor solar cells with silicon oxynitride tunnel insulator by using rapid thermal processing, Applied Physics Letters 68, 508 (1996); DOI: 10.1063/1.116382

[Borden 2008] P. Borden et al., Polysilicon tunnel junctions as alternates to diffused junctions, 23rd European Photovoltaic Solar Energy Conference, 1-5 September 2008, Valencia, Spain

[Bothe 2005] K. Bothe et al., Fundamental Boron-Oxygen-related Carrier Lifetime Limit in Mono- and Multicrystalline Silicon, Prog. Photovolt: Res. Appl. 13 (2005) 287-296; DOI: 10.1002/pip.586.

[Bullock 2013] J. Bullock et al., Passivation of aluminium-n+ silicon contacts for solar cells by ultrathin Al2O3 and SiO2 dielectric layers, Phys. Status Solidi RRL, 1-4 (2013); DOI: 10.1002/pssr.201308115

[Castañer 1994] L. Castañer et al., Series resistance in polysilicon contacted solar cells, Conference Record of the Twenty Fourth. IEEE Photovoltaic Specialists Conference, 5-9 Dec 1994, pp. 1489 - 1491 vol.2; DOI: 10.1109/WCPEC.1994.520232

[Cesar 2014] I. Cesar et al., Mercury: A Back Junction Back Contact Cell With Novel Design For High Efficiency And Simplified Processing, presented at SiliconPV 2014, 's Herthogenbosch, The Netherlands, March 25-27, 2014

[Chaar 2011] L. El Chaar et al., Review of photovoltaic technologies, Renewable and Sustainable Energy Reviews, Vol. 15, No. 5, June 2011, pp. 2165-2175; DOI: 10.1016/j.rser.2011.01.004

[Chase 2014] J. Chase, H1 2014 Levelised Cost of Electricity - PV, Bloomberg new energy finance, 4 February 2014

[Chapin 1954] D. M. Chapin et al., A New Silicon p-n Junction Photocell for Converting Solar Radiation into Electrical Power, Journal of Applied Physics 25, 676, 1954; DOI: 10.1063/1.1721711

[Chen 2014] J. Chen, Z. R. Du, B. Hoex, A. G. Aberle, P. Choulat, J. Deckers et al., Investigation of laser ablation for n-type PERT silicon wafer solar cells, to be published

[Chow 2010] T. T. Chow, A review on photovoltaic/thermal hybrid solar technology, Applied Energy 87 (2010), 365-379; DOI: 10.1016/j.apenergy.2009.06.037

[Clugson 1997] D. A. Clugston and P. A. Basore, PC1D version 5: 32-bit solar cell modeling on personal computers, Conference Record of the Twenty-Sixth IEEE Photovoltaic Specialists Conference, 1997, pp. 207-210

[Cousins 2010] P. J. Cousins et al, "Generation 3: Improved Performance at Lower Cost," in Proc. 35th IEEE Photovoltaics Specialist Conf., 2010, pp. 275-278

[Crabbé 1986] E. Crabbé et al., Majority and minority carrier transport in polysilicon emitter contacts, in Proceedings of the 32nd International Electron Devices Meeting, 1986, pp. 28-31; DOI: 10.1109/IEDM.1986.191102

[Cuevas 1996] A. Cuevas et al., Surface recombination velocity of highly doped n-type silicon, Journal of Applied Physics, 80 (6), 1996, pp. 3370-3375; DOI: 10.1063/1.363250

[Cuevas 1999] A. Cuevas, The effect of emitter recombination on the effective lifetime of silicon wafers, Solar Energy Materials & Solar Cells 57, 1999, pp. 277-290; DOI: 10.1016/S0927-0248(98)00179-2

[Debucquoy 2013] M. Debucquoy, private communication, 2013

[Deckers 2013] J. Deckers et al., Injection Dependent Emitter Saturation Current Density Measurement under Metallized Areas Using Photoconductance Decay, in proc. 28th European Photovoltaic Solar Energy Conference and Exhibition, 2013, pp. 806 – 810; DOI: 10.4229/28thEUPVSEC2013-2BO.2.2

[Deckers 2013b] J. Deckers, Method for the extraction of recombination characteristics at metallized semiconductor surfaces, European patent application, filed on 24/09/2013

[Deckers 2014] J. Deckers et al., Avoiding parasitic current flow through point contacts in test structures for QSSPC contact recombination current measurements, to be published

[Deckers 2014b] J. Deckers et al., Excess carrier density variations in test structures for photoconductance-based contact recombination current measurements, IEEE Journal of Photovoltaics, in press

[Deckers 2014c] J. Deckers et al., Aluminum oxide-aluminum stacks for contact passivation in silicon solar cells, Energy Procedia, 2014, pp. 656-664; DOI: 10.1016/j.egypro.2014.08.041

[Deckers 2015] J. Deckers et al., Out-Of-Plane excess carrier density variations in point contact lattice-based test structures for QSSPC contact recombination current measurements, to be published.

[De Ceuster 2013] D. De Ceuster et al., Trench process and structure for backside contact solar cells with polysilicon doped regions, US patent no. US 8,450,134 B2, May 28, 2013

[De Ceuster 2014] D. De Ceuster and P. J. Cousins, Solar cell with reduced base diffusion area, United States patent application US 2014/0190561 A1, July 10, 2014

[Dennis 2012] T. Dennis et al., Method of fabricating a solar cell with a tunnel dielectric layer, US patent no. US 8,334,161 B2, Dec. 18, 2012

[Dennis 2014] T. Dennis et al., Method of fabricating a solar cell with a tunnel dielectric layer, US patent no. US 8,709,851 B2, April 29, 2014

[Depauw 2009] V. Depauw, Transferable monocrystalline thin-films by annealing of macroporous silicon: Potential for solar cell applications, Ph.D. thesis, K.U.Leuven, 2009

[Duerinckx 2014] F. Duerinckx et al., Quantifying internal optical losses for 21% n-Si rear junction cells, to be presented at the 29th European PV Solar Energy Conference and Exhibition, 22-26 September 2014, Amsterdam, The Netherlands

[De Vos 1981] A. De Vos and H. Pauwels, On the Thermodynamic Limit of Photovoltaic Energy Conversion, Applied Physics 25, 119-125 (1981); DOI: 10.1007/BF00901283

[De Wolf 2012] S. De Wolf et al., High-efficiency Silicon Heterojunction Solar Cells: A Review, Green, Vol. 2, 2012, pp. 7-24; DOI: 10.1515/green-2011-0018

[DNA 2014] Electric supply generated from atomic power at lowest since Fukushima disaster, in Daily News and Analysis (http://www.dnaindia.com/world/report-electric-supply-generated-from-atomic-power-at-lowest-since-fukushima-disaster-2006322; accessed on 30/07/2014)

[DOE 2004] US Department of Energy, PV FAQ, 2004

[DOE 2014] US Department of Energy, Soft costs (http://www.energy.gov/eere/sunshot/soft-costs; accessed on 15-09-2014)

[Dong 2014] J. Dong et al., High-Efficiency Full Back Contacted Cells Using Industrial Processes, IEEE Journal of Photovoltaics, Vol. 4, No. 1, January 2014, pp. 130-133

[Dore 2014] J. Dore et al., Progress in Laser-Crystallized Thin-Film Polycrystalline Silicon Solar Cells: Intermediate Layers, Light Trapping, and Metallization, IEEE Journal of Photovoltaics, Vol. 4, Issue 1, 2014, pp. 33-39; DOI: 10.1109/JPHOTOV.2013.2280016

[Dziewior 1977] J. Dziewior and W. Schmid, Auger coefficients for highly doped and highly excited silicon, Applied Physics Letters 31, 346, 1977; DOI: 10.1063/1.89694

[EU 2014] The 2020 climate and energy package, (http://ec.europa.eu/clima/policies/package/index_en.htm; accessed on 30/07/2014)

[Falk 1998] A. R. Falk, Near ir absorption in heavily doped silicon-an empirical approach, International symposium for testing and failure analysis. ASM International, 1998, 2000.

[Fell 2013] A. Fell et al., Quokka version 2: selective surface doping, luminescence modeling and data fitting, Fell, Proc. 23rd Photovoltaic Science and Engineering Conf, 2013.

[Fell 2013b] A. Fell et al., Determination of injection dependent recombination properties of locally processed surface regions, Energy Procedia 38 (2013) pp. 22-31; DOI: 10.1016/j.egypro.2013.07.245

[Feldmann 2014] F. Feldmann et al., Passivated rear contacts for high-efficiency n-type Si solar cells providing high interface passivation quality and excellent transport characteristics, Solar Energy Materials & Solar Cells 120 (2014) 270-274; DOI: 10.1016/j.solmat.2013.09.017

[Feldmann 2014b] F. Feldmann et al., Efficient carrier-selective p- and n- contacts for Si solar cells, Solar Energy Materials and Solar Cells (2014); DOI: 10.1016/j.solmat.2014.05.039

[Feldmann 2014c] F. Feldmann et al., Carrier-Selective Contacts for Si Solar Cells, presented at the 4th International Conference on Silicon Photovoltaics, 's-Hertoghenbosch, March 26, 2014

[Felmann 2014d] F. Feldmann et al., Ion implantation into amorphous Si layers to form carrier-selective contacts for Si solar cells, Phys. Status Solidi RRL, 1-4, 2014; DOI: 10.1002/pssr.201409312

[Fellmeth 2011] T. Fellmeth et al., Recombination at Metal-Emitter Interfaces of Front Contact Technologies for Highly Efficient Silicon Solar Cells, Energy Procedia 8, 2011, pp. 115-121; DOI: 10.1016/j.egypro.2011.06.111

[Feltrin 2008] A. Feltrin and A. Freundlich, Material considerations for terawatt level deployment of photovoltaics, renewable Energy, vol 33, Issue 2, pp. 180-185, 2008

[First Solar 2014] First Solar, Press Release: First Solar to Deliver Diesel-PV Hybrid Solution to Rio Tinto in Australia, May 21 2014 (http://investor.firstsolar.com/releasedetail.cfm?ReleaseID=849440; accessed 15-09-2014)

[Fischer 1971] H. Fischer and R. Gereth, Electrochemically Passivated Contacts for Silicon Solar Cells, IEEE Transactions on Electron Devices, Vol. ED-18, No. 8, August 1971, pp. 459-464; DOI: 10.1109/T-ED.1971.17228

[Fischer 2003] B. Fischer, Crystalline Silicon Solar Cells Using Photoconductance and Quantum Efficiency Measurements, PhD dissertation, Konstanz University, March 2003

[Fthenkakis 2008] Fthenkakis et al., Emissions from Photovoltaic Life Cycles, Environ. Sci. Technol, vol. 42, No. 6, pp. 2168-2174, 2008

[Galbiati 2012] G. Galbiati et al., Large-Area Back-Contact Back-Junction Solar Cell With Efficiency Exceeding 21%, IEEE Journal of Photovoltaics, Proceedings of the 38th IEEE Photovoltaic Specialists Conference (PVSC), vol. 2, 2012; DOI: 10.1109/PVSC-Vol2.2012.6656742

[Gan 1990] J. Y. Gan and R. M. Swanson, Polysilicon emitters for silicon concentrator solar cells, Conference record fo the Twenty First IEEE Photovoltaic Specialists Conference, 1990, pp. 245-250

[Garcia-Alonso 2013] D. Garcia-Alonso et al., Silicon passivation and tunneling contact formation by atomic layer deposited Al2O3/ZnO stacks, Semiconductor Science and Technology 28 (2013) 082002; DOI: 10.1088/0268-1242/28/8/082002

[Ghannam 1992] M. Y. Ghannam et al., US patent no. 5,108,936; Method of producing a bipolar transistor having an amorphous emitter formed by plasma CVD, Date of Patent: 1992/04/28.

[Ghosh 1999] G. Ghosh, Dispersion-equation coefficients for the refractive index and birefrigence of calcite and quartz crystals, Optics communications, Vol. 163, Issues 1-3, 1999, pp. 95-102

[Green 1974] M. A. Green et al., Minority carrier MIS tunnel diodes and their application to electron- and photo-voltaic energy conversion- I. Theory, Solid-State Electronics, 1974, Vol. 17, pp. 551-561; DOI: 10.1016/0038-1101(74)90172-5

[Green 1990] M. A. Green, Intrinsic concentration, effective densities of states, and effective mass in silicon, J. Appl. Phys. 67 (6), 1990, pp. 2944-2954

[Green 2008] M. A. Green, Self-consistent optical parameters of intrinsic silicon at 300K including temperature coefficients, Solar Energy Materials and Solar Cells 92(11), 2008, pp. 1305-1310

[Green 2014] M. A. Green et al., Solar cell efficiency tables (version 44), Prog. Photovolt: Res. Appl. 22, 2014, pp. 701-710; DOI: 10.1002/pip.2525

[Gregg 2003] B. A. Gregg, Excitonic Solar Cells, Journal of Physical Chemistry B, 107 (2003) pp. 4688-4698

[Greulich 2014] J. Greulich et al., Analysing the lateral series resistance of high-performance metal wrap through solar cells, Solar Energy Materials & Solar Cells 124 (2014) 24-30; DOI: 10.1016/j.solmat.2014.01.032

[Guemyard 1995] C. A. Gueymard, SMARTS, A simple model of the atmospheric radiative transfer of sunshine: Algorithms and performance assessment, Technical Report No.FSEC–PF–270–95, Cocoa, Florida, Florida Solar Energy Center, 1995 (http://www.nrel.gov/rredc/smarts/; accessed on 19-09-2014).

[Heng 2013] J. B. Heng et al., Commercialization of Tunnel Oxide Junction Based Cell and Module with Efficiency and Good Reliability, Proceedings of the 28th European Photovoltaic Solar Energy Conference and Exhibition, pp. 952-955; DOI: 10.4229/28thEUPVSEC2013-2CO.3.3

[Hermle 2008] M. Hermle et al., "Shading Effects in Back-Junction Back-Contacted Silicon Solar Cells", proc. 33rd IEEE PVSEC, 12-16 May. 2008, St. Diego, CA

[Hezel 1984] R. Hezel et al., Silicon oxynitride films prepared by plasma nitridation of silicon and their application for tunnel metal-insulator-silicon diodes, Journal of Applied Physics, 56, 1756 (1984); DOI: 10.1063/1.334181

[Hoex 2007] B. Hoex et al., Excellent passivation of highly doped p-type Si surfaces by the negative-charge-dielectric Al2O3, Applied Physics Letters 91, 112107 (2007)

[Hoex 2008] B. Hoex et al., On the c-Si surface passivation mechanism by the negative-charge-dielectric Al2O3, Journal of Applied Physics 104, 113703, 2008

[Houssa 2000] M. Houssa et al., Trap-assisted tunnelling in high permittivity gate dielectric stacks, Journal of Applied Physics 87, 8615,2000; DOI: 10.1063/1.373587

[IEA 2009] International Energy Agency, World Energy Outlook 2009, 2009

[IEA 2013] International Energy Agency, World Energy Outlook 2013, Chapter 6: Renewable Energy Outlook

[IEA 2010] International Energy Agency, Technology Roadmap: Solar Photovoltaic Energy, 2010

[IMEC 1984] Dutch patent no. 8403005, assigned to IMEC VZW, Werkwijze voor het vervaardigen van een bipolaire heterojunctietransistor en bipolaire heterojunctie-transistor vervaardigd volgens de werkwijze, Filed on 1984/10/02

[IPM 2010] Solar powered oil rigs, Indiana Public Media moment of science (http://indianapublicmedia.org/amomentofscience/solar-powered-oil-rigs/; accessed on 15-09-2015)

[Johnson 2011] K. Johnson, Solar updates Marines arsenal, Associated Press, May 2011

[Kane 1985] D. E. Kane and R. M. Swanson, “Measurement of the Emitter Saturation Current by a Contactless Photoconductivity Decay Method”, in Proc. 18th IEEE Photovoltaics Specialist Conference, 1985, pp. 578-583

[Keevers 2007] M. J. Keevers et al., 10% efficient CSG minimodules, 22nd European Photovoltaic Solar Energy Conference, Milan, September 2007

[Keister 1999] J. W. Keister et al., Band offsets for ultrathin SiO_2 and Si_3N_4 films on Si(111) and Si(100) from photoemission spectroscopy, Journal of Vacuum Science & Technology B 17, 1831 (1999); DOI: 10.1116/1.590834

[Kelly 1978] H. Kelly, Photovoltaic Power Systems: A Tour Through the Alternatives, Science, Vol. 199, pp. 634-643, 1978

[King 1990] R. R. King, Studies of oxide-passivated emitters in silicon and applications to solar cells, Ph.D. dissertation, dept. Electrical Engineering, Stanford University, 1990, p. 6

[Kingon 2000] A. I. Kingon et al., Alternative dielectrics to silicon dioxide for memory and logic devices, Nature 406, 1032-1038 (31 August 2000); DOI: 10.1038/35023243

[Kluska 2010] S. Kluska et al., “Modeling and optimization study of industrial n-type high-efficiency back-contact back-junction silicon solar cells”, *Solar Energy Materials & Solar Cells* 94, 2010, pp. 568-577

[Kluska 2010] S. Kluska et al., “Modeling and optimization study of industrial n-type high-efficiency back-contact back-junction silicon solar cells”, Solar Energy Materials & Solar Cells 94, 2010, pp. 568-577

[Kopecek 2014] R. Kopecek and J. Libal, c-Si n-type technology break through or break down?, presented at the 4th nPV workwhop, 27-28 March 2014, ‘s-Hertogenbosch, Netherlands

[Kwark 1987] Y.H. Kwark and R. M. Swanson, N-type SIPOS and poly-silicon emitters, Solid-State Electronics Vol. 30, No. 11, pp. 1121-1125, 1987; DOI: 10.1016/0038-1101(87)90076-1

[Lanyon 1979] H.P.D. Lanyon and R.A. Tuft, Bandgap narrowing in moderately to heavily doped silicon, IEEE Transactions on Electron Devices, 26.7, 1979, pp. 1014-1018; DOI: 10.1109/T-ED.1979.19538

[Li 1978] S. S. Li, The dopant density and temperature dependence of hole mobility and resistivity in boron doped silicon, Solid-State Electronics, Vol 21, 1978, pp. 1109-1117

[Lindholm 1985] F. A. Lindholm et al., Heavily Doped Polysilicon-Contact Solar Cells, IEEE Electron Device Letters, Vol. EDL-6, NO. 7, July 1985, pp. 363-365; DOI: 10.1109/EDL.1985.26155

[Loozen 2012] X. Loozen, et al., “Passivation of a Metal Contact with a Tunneling Layer”, Energy Procedia 21, 75-83, 2012

[Masetti 1983] G. Masetti et al., Modeling of Carrier Mobility Against Carrier Concentration in Arsenic-, Phosphorus-, and Boron-Doped Silicon, IEEE Transactions on Electron Devices, Vol. ED-30, No. 7, 1983, pp. 764-769

[MSDS 2014] Science lab, cadmium material safety data sheet (http://www.sciencelab.com/msds.php?msdsId=9923223; accessed on 30/07/2014)

[MSDS 2014b] Science lab, silicon material safety data sheet (http://www.sciencelab.com/msds.php?msdsId=9924921; accessed on 30/07/2014)

[Manole 2005] M. Manole, et al., Effective methods to increase thermal stability of shallow emitter solar cells with aluminium front contacts, Proceedings of the 20th European Photovoltaic Solar Energy Conference, Barcelona, Spain, 2005

[Matsuura 1989] H. Matsuura, Hydrogenated amorphous silicon/ crystalline silicon heterojunctions: properties and applications, IEEE transactions on electron devices Vol. 36, No. 12, pp. 2908-2914, 1989

[Matsushita 1979] T. Matsushita et al., A silicon heterojunction transistor, Applied Physics Letters 35 (7), 1 October 1979, pp. 549-550; DOI: 10.1063/1.91174

[Meuris 1992] M. Meuris et al., The relationship of the Silicon Surface Roughness and Gate Oxide Integrity in HN4OH/H2O2 Mixtures, Japanese Journal of Applied Physics, Vol. 31 (1992) pp. L 1514-L 1517

[Misiakos 1993] K. Misiakos and D. Tsamakis, Accurate measurements of the silicon intrinsic carrier density from 79 to 340 K, Journal of Applied Physics 74, 3293 (1993); doi: 10.1063/1.354551

[Moldovan 2014] A. Moldovan, Simple applicable cleaning and conditioning of silicon surfaces with UV/ozone sources, presented at the 4th International conference on silicon photovoltaics, 's-Herthogenbosch, March 24-27, 2014

[Mueller 2012] J. Mueller et al., Reverse saturation current density imaging of highly doped regions in silicon: A photoluminescence approach, Solar Energy Materials & Solar Cells 106, 2012, pp. 76-79; DOI: 10.1016/j.solmat.2012.05.026

[Murray 1984] J. L. Murray and A. J. McAlister, The Al-Si (Aluminum-Silicon) System, Bulletin of Alloy Phase Diagrams, Vol. 5, No. 1, 1984, pp. 74

[Nagel 1999] H. Nagel, C. Berge and A. G. Aberle, "Generalized analysis of quasi-steady-state and quasi-transient measurements of carrier lifetimes in semiconductors," *Journal of Applied Physics*, Vol. 86, No. 11, pp. 6218-6221, 1999

[Ng 1979] K. K. Ng and H. C. Card, Asymmetry in the SiO_2 tunneling barriers to electrons and holes, Journal of Applied Physics 51, 2153 (1980); DOI: 10.1063/1.327888

[Ning 2001] T. H. Ning, History and Future Perspective of the Modern Silicon Bipolar Transistor, IEEE Transactions on Electron Devices, Vol. 48, No. 11, November 2011, pp. 2485-2491; DOI: 10.1109/16.960372

[Oh 2012] J. Oh et al., An 18.2%-efficient black-silicon solar cell achieved through control of carrier recombination in nanostructures, Nature Nanotechnology, Vol. 7, November 2012, pp. 743-748; DOI: 10.1038/nnano.2012.166

[O'Rourke 2009] S. O'Rourke et al., Solar Photovoltaic Industry – Looking through the storm, Deutsche Bank, 2009

[O'Rourke 2010] S. O'Rourke et al., Solar Photovoltaic Industry, 2010 global outlook 2010: Deja Vu?, Deutsche Bank, 2010

[Osvald 2004] J. Osvald, Comment on "Negative Schottky barrier between titanium and n-type Si(001) for low-resistance ohmic contacts", Solid-State Electronics 48 (2004), pp. 2347-2349; DOI: 10.1016/j.sse.2004.06.019

[Overstraeten 1998] R. Van Overstraeten and P. Heremans, Semiconductor Devices, Acco, 1998

[Pan 1993] Y. Pan and Y. Wang, Electrical properties of LPCVD Poly-Silicon Doped with oxygen atoms, Journal of Electronics (China), Vol. 10, No. 2, April 1993, pp. 181-187; DOI: 10.1007/BF02684545

[Pan 1993b] Y. Pan and Y. Wang, Study on the optical absorption of oxygen-doped polysilicon thin films, Optical Engineering, March 1993, Vol. 32, No. 3, pp. 589-592; DOI: 10.1117/12.61037

[Panasonic 2014] Panasonic press release, Panasonic HIT® Solar Cell Achieves World's Highest Energy Conversion Efficiency of 25.6% at Research Level, 10 April 2014 (http://panasonic.co.jp/corp/news/ official.data/data.dir/2014/04/en140410-4/en140410-4.html, accessed on 24-07-2014)

[Palik 1985] E.D. Palik (Ed.), Handbook of Optical Constants of Solids, Vols. I and II,Academic Press, New York, 1985/1991

[Parida 2011] B. Parida et al., A review of solar photovoltaic technologies, Renewable and Sustainable Energy Reviews, 15, pp. 1625-2636, 2011; DOI: 10.1016/j.rser2010.11.032

[Peibst 2014] R. Peibst et al., A Simple Model Describing the Symmetric I-V Characteristics of p Polycrystalline Si/n Monocrystalline Si, and n Polycrystalline Si/p Monocrystalline Si Junctions, IEEE Journal of Photovoltaics, Vol. 4, No. 3, May 2014, pp. 841-850; DOI: 10.1109/JPHOTOV.2014.2310740

[Peng 2013] J. Peng et al., Review on life cycle assessment of energy payback and greenhouse gas emission of solar photovoltaic systems, Renewable and Sustainable Energy Reviews 19, pp. 255-274, 2013; DOI: DOI: 10.1016/j.rser.2012.11.035

[Phipps 2008] G. Phipps et al., Indium and Gallium: long-term supply, renewable energy focus, July/August 2008, pp. 56-59

[Plagwitz 2006] H. Plagwitz and R. Brendel, Analytical model for the diode saturation current of point-contacted solar cells, *Progress in photovoltaics: Research and Applications* 14.1, pp. 1-12, 2006; DOI: 10.1002/pip.637

[PV Lighthouse 2014] PV Lighthouse (http://www.pvlighthouse.com.au/; accessed on 16-09-2014)

[Qiu 2010] Y. Qiu et al., 8.5% efficiency for thin-film polycrystalline silicon solar cells: a study of hydrogen plasma passivation, proceedings of the 25th European Photovoltaic Solar Energy Conference and Exhibition / 5th World Conference on Photovoltaic Energy Conversion, 6-10 September 2010, Valencia, Spain, pp. 3633-3637; DOI: 10.4229/25thEUPVSEC2010-3BV.3.28

[Rajkanan 1979] K. Rajkanan et al., Absorption coefficient of silicon for solar cell calculations, Solid-State Electronics Vol. 22, pp. 793-795, 1979; DOI: 10.1016/0038-1101(79)90128-X

[Raugei 2009] M. Raugei and P. Frankl, Life cycle impacts and costs of photovoltaic systems: current state of the art and future outlooks, Energy, vol. 34, pp. 392-399 (2009)

[Richter 2011] A. Richter, et al., Excellent silicon surface passivation with 5 Å thin ALD Al2O3 layers: Influence of different thermal post-deposition treatments, physica status solidi (RRL)-Rapid Research Letters, 5.5-6, pp. 202-204, 2011; DOI: 10.1002/pssr.201105188

[Richter 2014] A. Richter et al., Passivation of phosphorus diffused silicon surfaces with Al_2O_3: Influence of surface doping concentration and thermal activation treatments, Journal of Applied Physics 116, 2014, 243501; DOI: 10.1063/1.4903988

[Römer 2014] U. Römer et al., Recombination behavior and contact resistance of n^+ and p^+ poly-crystalline Si / mono-crystalline Si junctions, Solar Energy Materials and Solar Cells (2014); DOI: 10.1016/j.solmat.2014.06.003

[Rothschild 2010] A. Rothschild et al., ALD-Al2O3 passivation for solar cells: charge investigation, Proc. 25th European Photovoltaic Solar Energy Conference and Exhibition, 6-10 September 2010, Valencia, Spain, pp. 1382-1385

[Saito 2014] M. Saito and L. Twaronite (Reuters), Fukushima farmer takes on Tepco over wife's suicide, The Japan Times (http://www.japantimes.co.jp/news/2014/07/10/national/fukushima-farmer-takes-tepco-wifes-suicide/#.U9jyzrFZ6HQ; accessed on 30/07/ 2014)

[Saint-Cast 2010] P. Saint-Cast et al., High-Efficiency c-Si Solar Cells Passivated With ALD and PECVD Aluminum Oxide, IEEE Electron Device Letters, Vol. 31, No. 7, 2010, pp. 695-697; DOI: 10.1109/LED.2010.2049190

[Schenk 2006] A. Schenk et al., Physical Model of Incomplete Ionization for Silicon Device Simulation, Proceedings of the 2006 International Conference on Simulation of Semiconductor Processes and Devices, 6-8 September 2006, Monterey, CA, USA, pp. 51-54; DOI: 10.1109/SISPAD.2006.282836

[Schöfthaler 1994] M; Schöfthaler et al., Direct observation of a scaling effect on effective minority carrier lifetimes, Journal of Applied Physics 76, 4168, 1994; DOI: 10.1063/1.358450

[Schöfthaler 1995] M. Schöfthaler and R. Brendel, Sensitivity and transient response of microwave reflection measurements, *Journal of applied physics* 77.7, pp. 3162-3173, 1995; DOI: 10.1063/1.358670

[Schroder 2006] D. K. Schroder, "Semiconductor material and Device Characterization", 3rd edition, Wiley-IEEE press, 2006, pp. 144-146

[Schropp 2007] R. E. I. Schropp et al., Amorphous Silicon, Microcrystalline Silicon, and Thin-Film Polycrystalline Silicon Solar Cells, MRS Bulletin, Vol. 32, March 2007, pp. 219-224

[Schwägerl 2011] C. Schwägerl, Germany's Unlikely Champion Of a Radical Green Energy Path, Yale Environment 360, 09 May 2011 (http://e360.yale.edu/feature/germanys_unlikely_champion_of_a_radical_green_energy_path/2401/; accessed on 30/07/2014)

[Schwartzenegger 2010] A. Schwartzenegger, speaking at the Commonwealth Club in Santa Clara (California, USA) in support of AB32 and against prop 23, september 29, 2010 (https://www.youtube.com/watch?v=qxRn0_EH-DM; accessed on 12/08/2014)

[Seguini 2004] G. Seguini et al., Energy-band diagram of metal/Lu2O3/silicon structures, Applied Physics Letters, Vol. 85, No. 22, 29 November 2004, pp. 5316-5318; DOI: 10.1063/1.1828600

[Shah 2014] V. Shah et al., 2014 Outlook: Let the Second Gold Rush Begin, Deutsche Bank, 6 January 2014

[Shewchun 1974] J. Shewchun et al., Minority carrier MIS tunnel diodes and their application to electron-and photo-voltaic energy conversion – II. Experiment, Solid-State Electronics, Vol. 17, Issue 6, June 1974, ppl 563-572; DOI: 10.1016/0038-1101(74)90173-7

[Shewchun 1977] J. Shewchun et al., Theory of metal-insulator-semiconductor solar cells, Journal of Applied Physics 48, 765 (1977); DOI: 10.1063/1.323667

[Shockley 1956] W. Shockley, Transistor technology evokes new physics, Nobel Lecture, December 11, 1956

[Shockley 1961] W. Shockley and H. J. Queisser, Detailed Balance Limit of Efficiency of p-n Junction Solar Cells, Journal of Applied Physics, Vol. 32, No. 3, March 1961, pp. 510-519

[Simoen 2011] E. Simoen et al., “Impact of Forming Gas Annealing and Firing on the Al2O3/p-Si Interface State Spectrum”, Electrochemical and Solid-State Letters, 14 (9), 2011 H362-H364

[Sinton 1996] R.A. Sinton, A. Cuevas, and M. Stuckings, Quasi-Steady-State Photoconductance, A New Method for Solar Cell Material and Device Characterization, Proc. of the 25th IEEE Photovoltaic Specialists Conference, pp. 457-460, 1996

[Sinton 1996b] R.A. Sinton, and A. cuevas, Contactless determination of current–voltage characteristics and minority carrier lifetimes in semiconductors from quasisteadystate photoconductance data, Appl. Phys. Lett. 69, 2510, 1996; DOI: 10.1063/1.117723

[Sinton 2000] R.A. Sinton, and A. Cuevas, "A Quasi-Steady-State Open-Circuit Voltage Method for Solar Cell Characterization," 16th European Photovoltaic Solar Energy Conference, 2000

[Slotboom 1976] J. W. Slotboom and H. C. De Graaff, Measurements of bandgap narrowing in Si bipolar transistors, *Solid-State Electronics* 19.10, pp. 857-862, 1976; DOI: 10.1016/0038-1101(76)90043-5

[Smith 2014] D. D. Smith, Backside contact solar cell with formed polysilicon doped regions, US patent no. US 8,647,911 B2, Feb 11, 2014

[Sproul 1991] A. B. Sproul and M. A. Green, Improved value for the silicon intrinsic carrier concentration from 275 to 375 K, Journal of Applied Physics 70, 846 (1991); doi: 10.1063/1.349645

[Strasser 2013] T. Strasser et al., Integrating PV into the smart grid – implementation of an IEC 61850 interface for large scale PV inverters, in proceedings of the 2013 EU PVSEC, 2 october 2013

[Suh 2014] D. Suh and K. Weber, Effective silicon surface passivation by atomic layer deposited Al2O3/TiO2 stacks, Physica Status Solidi (RRL) - Rapid Research Letters, 8, 1, 2014; DOI: 10.1002/pssr.201308134

[Sze 2007] S. M. Sze and K. Ng Kwok, Physics of Semiconductor Devices, Third Edition, (Wiley, New York, 2007)

[Tanaka 1992] M. Tanaka et al., Development of New a-Si / c-Si Heterojunction Solar Cells: ACJ-HIT (Artificially Constructed Junction – Heterojunction with Intrinsic Thin-Layer), Japanese Journal of Applied Physics, Vol. 31, No. 11, November 1992, pp. 3518-3522; DOI: 10.1143/JJAP.31.3518

[Taylor 2010] S. Taylor, Timmico suspends solar-grade silicon production, Reuters, 17 March 2010 (http://www.reuters.com/article/ 2010/03/17/us-timminco-idUSTRE62G4IZ20100317; accessed on 31/07/ 2014)

[Taguchi 2014] M. Taguchi et al., 24.7% Record Efficiency HIT Solar Cell on Thin Silicon Wafer, IEEE Journal of Photovoltaics, Vol. 4, No. 1, January 2014, pp. 96-99; DOI: 10.1109/JPHOTOV.2013.2282737

[Tao 2004] M. Tao et al., Negative Schottky barrier between titanium and n-type Si(001) for low-resistance ohmic contacts, Solid-State Electronics 48 (2004), pp. 335-338; DOI: 10.1016/S0038-1101(03)00316-2

[Tao 2004b] M. Tao and J. Zhu, Response to “Comment on ‘Negative Schottky barrier between titanium and n-type Si(001) for low-resistance ohmic contacts”’ [Solid State Electron. 2004;48:335-8], Solid-State Electronics 48 (2004) 2351-2352

[Tao 2004c] M. Tao et al., Monoatomic layer passivation of semiconductor surfaces, US patent no. 6,784,114 B1, August 31, 2004

[Tarr 1985] N. G. Tarr, A Polysilicon Emitter Solar Cell, IEEE Electron Device Letters, Vol. EDL-6, No. 12, December 1985, pp. 655-658; DOI: 10.1109/EDL.1985.26264

[Thuy 2014] C. D. T. Thuy, private communication, 2014

[Töfflinger 2014] J. a. Töfflinger, et al., PECVD-AlOx/SiNx Passivation Stacks on Silicon: Effective Charge Dynamics and Interface Defect State Spectroscopy, Energy Procedia, 55, 845, 2014; DOI: 10.1016/j.egypro.2014.08.068

[Tous 2014] L. Tous, private communication,2014

[Trompoukis 2012] C. Trompoukis et al., Photonic assisted light trapping integrated in ultrathin crystalline silicon solar cells by nanoimprint lithography, Applied Physics Letters 101, 103901, 2012; DOI: 10.1063/1.4749810

[Tiedje 1984] T. Tiedje et al., Limiting Efficiency of Silicon Solar Cells, IEEE Transactions on Electron Devices, Vol. ED-31, No. 5, May 1984, pp. 711-716; DOI: 10.1109/T-ED.1984.21594

[Turekian 1961] K. Turekian and K. H. Wederpohl, Distribution of the Elements in Some Major Units of the Earth’s Crust, Geological Society of America Bulletin, v. 72, p. 175-192, February 1961; DOI: 10.1130/0016-7606(1961)72[175:DOTEIS]2.0.CO;2

[Turner 1999] J. Turner, A realizable Renewable Energy Future, Science, p. 687-689, 1999

[Vankemmel 1993] R. Vankemmel et al., A unified wide temperature range model for the energy gap, the effective carrier mass and intrinsic concentration in silicon, Solid-State Electronics Vol. 36, No. 10, pp. 1379-1384, 1993; doi: 10.1016/0038-1101(93)90046-S

[Van Kerschaver 2006] E. Van Kerschaver and G. Beaucarne, Back-contact Solar Cells: A Review, Prog. Photovolt: Res. Appl. 2006; 14:107-123 DOI: 10.1002/pip.657

[Van Overstraeten 2000] R. Van Overstraeten and P. Heremans, Semiconductor Devices, Acco, Leuven, 2000-2001

[Verlinden 2012] P. J. Verlinden et al., Simple power-loss analysis method for high-efficiency Interdigitated Back Contact (IBC) silicon solar cells, Solar Energy Materials & Solar Cells 106, 2012, pp. 37-41; DOI: 10.1016/j.solmat.2012.06.008

[Vermang 2012] Bart Vermang et al., Surface passivation for Si solar cells: a combination of advanced surface cleaning and thermal atomic layer deposition of Al2O3, 2012, Solid State Phenomena, 187, 357

[Vazsonyi 1999] E. Vazsonyi et al., Improved anisotropic etching process for industrial texturing of silicon solar cells, Solar Energy Materials & Solar Cells 57, 1999, pp. 179-188; DOI: 10.1016/S0927-0248(98)00180-9

[Verbruggen 2014] A. Verbruggen, Atoomenergie faalt over de hele lijn, Opiniebijdrage in De Tijd, 7 Augustus 2014 (accessed on 07/08/2014; http://www.tijd.be/opinie/analyse/Atoomenergie_faalt_over_de_hele_lijn.9531689-2336.art)

[Verlinden 2010] P. J. Verlinden, Power Loss Analysis Modelling of IBC cells - What is Jo?, seminar given on December 13, 2010, Heverlee (Leuven), Belgium.

[Verlinden 2012] P. J. Verlinden et al., Simple power-loss analysis method for high-efficiency Interdigitated Back Contact (IBC) silicon solar cells, Solar Energy Materials & Solar Cells 106, 2012, pp. 37-41; DOI: 10.1016/j.solmat.2012.06.008

[Warwick 2014] The University of Warwick, Ohmic Contact (http://www2.warwick.ac.uk/fac/sci/physics/current/postgraduate/regs/mpags/ex5/devices/hetrojunction/ohmic/; accessed on 15-09-2014)

[Werner 2012] F. Werner et al., Silicon surface passivation by Al2O3: Recombination parameters and inversion layer solar cells, Energy Procedia 27, 2012 pp. 319-324

[Wiktionary 2014] Wiktionary, Something is rotten in the state of Denmark (http://lmgtfy.com/?q=something+is+rotten+in+the+state+of+Denmark+wiktionary (first hit); accessed on 15-09-2014)

[Wooley 2001] Wooley et al., The Clean Air Act and Renewable Energy: Opportunities, Barriers, and Options, National Renewable Energy Laboratory, 2001

[Yablonovitch 1985] E. Yablonovitch et al., A 720 mV open circuit voltage SiO_x:c-Si:SiO_x double heterostructure solar cell, Applied Physics Letters 47, 1211 (1985); DOI: 10.1063/1.96331

[Yablonovitch 1985b] E. Yablonovitch and T. Gmitter, A Study of n+ - SIPOS:p-Si Heterojunction Emitters, IEEE Electron Device Letters, Vol. EDL-6, No. 11, November 1985, pp. 597-599; DOI: 10.1109/EDL.1985.26243

[Yoon 2001] S. Y. Yoon et al., Metal-induced crystallization of amorphous silicon, Thin Solid Films 383, pp. 34-38, 2001

[Young 2014] D. L. Young et al., Carrier selective, passivated contacts for high efficiency silicon solar cells based on transparent conducting oxides, presented at the 4th International Conference on Silicon Photovoltaics, SiliconPV, 2014

[Zhao 1990] J. Zhao et al., 24% efficient PERL structure silicon solar cells, Proc. 21st IEEE Photovoltaic Specialists Conference, Kissimmee, FL, USA, May 21-25, 1990, pp. 333-335; DOI: 10.1109/PVSC.1990.111642

[Zhao 1991] J. Zhao and M. A. Green, Optimized Antireflection Coatings for High-Efficiency Silicon Solar Cells, IEEE Transactions on Electron Devices, Vol. 38, No. 8, pp. 1925-1934; DOI: 10.1109/16.119035

[Zielinski 2014] B. Zielinski, private communication, May 2014

[Zielke 2011] D. Zielke et al., Contact passivation in silicon solar cells using atomic-layer-deposited aluminum oxide layers, Physica Status Solidi RRL 5, No. 8, 298-300 (2011); DOI: 10.1002/pssr.201105285

[Zielke 2014] D. Zielke et al., Organic-silicon heterojunction solar cells on n-type silicon wafers: The BackPEDOT contept, Solar Energy Materials and Solar Cells (2014); DOI: 10.1016/j.solmat.2014.05.022

[Zweibel 2010] K. Zweibel, The Impact of Tellurium Supply on Cadmium Telluride Photovoltaics, Science 328, 699, 2010; DOI: 10.1126/science.1189690